NOVEL NANOMATERIALS FOR LITHIUM ION BATTERIES AND LITHIUM SULFUR BATTERIES

A thesis presented for the award of the degree of

Doctor of Philosophy

From

University of Technology, Sydney

Faculty of Science

By Shuangqiang Chen, B. Sc., M. Eng.

December 2014

DEDICATION

This thesis is dedicated to my beloved wife, my parents, my brother and sister. With your concerns and helps, I have sufficient energy and strengths to fulfill my PhD research.

CERTIFICATION

I, Shuangqiang Chen, declare that the work in this thesis has not previously been submitted for a degree nor has it been submitted as part of requirements for a degree except as fully acknowledged within the text.

I also declare that the thesis has been written by me. Any help that I have received in my research work and the preparation of the thesis has been acknowledged. In addition, I declare that all information sources and literature used are indicated in the thesis.

Signature of student

Shuangqiang Chen

26-09-2014

Signature of supervisor

Professor Guoxiu Wang

ACKNOWLEDGEMENTS

I would like to convey my deeply appreciations to my respect supervisor, Prof. Guoxiu Wang, for his encouragements, understandings, invaluable advice, and constant supportings during my study at University of Technology, Sydney (UTS). I appreciate his constant motivation throughout this period and his support in professional careers.

I have my thanks to many people for constantly rendering helps during this research activity. Dr. Hao Liu, Dr. Bing Sun, Dr. Bei Wang, Dr. Ying Wang, Dr. Dawei Su, Dr. Xiaodan Huang, Dr. Zhimin Ao, Mr. Kefei Li, Mr. Jinqiang Zhang, Ms. Yufei Zhao and Mr. Anjon Kumar Mondal. Specical thanks go to Dr. Yueping (Jane) Yao for her support in many ways, letting me have enough time to complete those experiments.

I also wish to thank A/Prof. Alison Ung, Dr. Ronald Shimmon and Dr. Linda Xiao in Chemistry and Forensic Science for their friendly support and kind discussions during my study. I am very grateful to Dr. Waikong Yeoh from The University of Sydney for his assists on TEM analysis. I would to give my thanks to Prof. Shixue Dou, Prof. Huakun Liu, in University of Wollongong. I take this chance to mention my cordial thanks to China Scholarship Council (CSC) and Australian Research Council (ARC) through the ARC Linkage project (LP0989134), ARC Discovery Project (DP1093855) and Future Fellowship project (FT110100800) for financing my researches.

Finally, I would like to reserve my special and heartfelt thanks to my beloved wife Ms. Lingli Xu, a soul mate of my life. Her sweet loves and meticulous concerns give me endless strength and fearless courage to face many difficulties. She is the reason for my eternal happiness. I also would like to convey my significant thanks to my father, Mr. Liudang Chen, and my mother, Ms. Yin Jin, for their understanding, moral support and continuous encouragement throughout my life. The secret of my success is hidden in the hard work they did to financially support my education and live. I feel myself extremely fortunate to have such kind parents.

There is an active and passive role of many people who helped me to arrive at this milestone. I may have forgotten to mention their names, but the help they offered has certainly made a home in my heart.

TABLE OF CONTENTS

LIST OF FIGURES

LIST OF TABLES

LIST OF ABBRIEVIATIONS

Abbreviation	Full name
a.u.	Arbitrary unit
BET	Brunauer Emmett Teller
C rate	Current rate
CB	Carbon black
cm	Centimeter
EIS	Electrochemical impedance spectroscopy
EC	Ethylene carbonate
Eq.	Equation
FESEM	Field emission scanning electron microscopy
FT-IR	Fourier transform inferior red spectroscopy
EV	Electric vehicle
HEV	Hybrid electric vehicle
JCPDS	Joint committee on powder diffraction standards
nm	Nanometer
NMP	1-methyl-2-pyrrolidinone
PC	Propylene carbonate
PTFE	Polytetrafluoroethylene
PVDF	Polyvinylidene fluoride
SAED	Selected area electron diffraction
SEI	Solid electrolyte interphase
SEM	Scanning electron microscopy
TEM	Transmission electron microscopy
TGA	Thermogravimetric analysis
XRD	X-ray diffraction

LIST OF PUBLICATION

[1] **Shuangqiang, Chen**; Xiaodan, Huang; Hao, Liu; Bing, Sun; Waikong, Yeoh; Kefei, Li; Jinqiang, Zhang; Guoxiu, Wang; 3D Hyperbranched Hollow Carbon Nanorod Architectures for High-Performance Lithium-Sulfur Batteries. ***Advanced Energy Materials*** 2014, 4 (8), 1301761. Impact factor: 14.385. (**Selected as Frontispiece image, and reported by Materials Views China at June 12, 2014, VILEY**). Essencial science indicator (ESI) highly cited paper**.**

[2] Bing Sun, Xiaodan Huang, **Shuangqiang Chen**, Paul, Munroe and Guoxiu, Wang; Porous graphene nanoarchitectures: An efficient catalyst for low charge-overpotential, long life and high capacity lithium-oxygen batteries. ***Nano letters***, 2014. 14 (6), 3145–3152. Impact factor: 12.2. (**Top 10, most downloaded papers, May-June, 2014**)

[3] **Shuangqiang, Chen**; Peite, Bao; Xiaodan, Huang; Bing, Sun; Guoxiu, Wang; Hierarchical 3D mesoporous silicon@ graphene nanoarchitectures for lithium ion batteries with superior performance ***Nano Research*** 2014, 7, 85-94. Impact factor: 6.89. ESI highly cited paper.

[4] **Shuangqiang, Chen**; Peite, Bao; Linda, Xiao; Guoxiu, Wang; Large-scale and low cost synthesis of graphene as high capacity anode materials for lithium-ion batteries ***Carbon*** 2013, 64, 158-169. Impact factor: 6.16

[5] **Shuangqiang, Chen**; Peite, Bao; Guoxiu, Wang; Synthesis of Fe_2O_3-CNT–graphene hybrid materials with an open three-dimensional nanostructure for high capacity lithium storage ***Nano Energy*** 2013, 2, 425-434. Impact factor: 10.22.

[6] **Shuangqiang, Chen**; Xiaodan, Huang; Bing, Sun; Jinqiang,Zhang; Hao, Liu; Guoxiu, Wang; Multi-shelled hollow carbon nanospheres for lithium-sulfur batteries with superior performances ***Journal of Materials Chemistry A,*** 2014, 2, 16199-16207. (**Top 10, most downloaded papers, August-September 2014)**

[7] **Shuangqiang, Chen**; Waikong, Yeoh; Qi, Liu; Guoxiu, Wang; Chemical-free synthesis of graphene–carbon nanotube hybrid materials for reversible lithium storage in lithium-ion batteries ***Carbon*** 2012, 50, 4557-4565. Impact factor: 6.16.

[8] **Shuangqiang, Chen**; Yong, Wang; Hyojun, Ahn; Guoxiu, Wang; Microwave hydrothermal synthesis of high performance tin–graphene nanocomposites for lithium ion batteries ***Journal of Power Sources*** 2012, 216, 22-27. Impact factor: 4.67. 27 Citations. ESI highly cited paper.

[9] **Shuangqiang, Chen;** Peng, Chen; Yong, Wang; Carbon nanotubes grown in situ on graphene nanosheets as superior anodes for Li-ion batteries ***Nanoscale*** 2011, 3, 4323-4329. Impact factor: 6.9.

[10] **Shuang Qiang, Chen**; Yong, Wang; Microwave-assisted synthesis of a Co_3O_4–graphene sheet-on-sheet nanocomposite as a superior anode material for Li-ion batteries ***Journal of Materials Chemistry*** 2010, 20, 9735-9739. Impact factor: 6.6. 133 Citations ESI highly cited paper.

[11] **Shuangqiang, Chen**; Peng, Chen; Minghong, Wu; Dengyu, Pan; Yong, Wang; Graphene supported Sn–Sb@ carbon core-shell particles as a superior anode for lithium ion batteries ***Electrochemistry Communications*** 2010, 12, 1302-1306. Impact factor: 4.2. 79 Citations

[12] **Shuangqiang, Chen**; Bing, Sun; Xiaodan Huang; Waikong, Yeoh; Simon, Ringer; Guoxiu, Wang; Multi-chambered micro/mesoporous carbon nanocubes as new polysulfides reserviors for lithium-sulfur batteries with long cycle life ***Nano Energy***, 2015, Accepted. Impact factor: 10.22

[13] **Shuangqiang Chen**; Yufei, Zhao; Zhimin, Ao; Bing, Sun, Xiaodan, Huang; Xiuqiang, Xie; Guoxiu, Wang. Microwave-assisted synthesis of mesoporous Co_3O_4 nanoflakes for applications in lithium ion batteries and oxygen evolution reactions ***ACS Applied Materials & Interfaces*** **2015**, *7* (5), 3306–3313. Impact factor: 5.9

[14] **Shuangqiang Chen**; Bing Sun; Xiuqiang Xie; Hao Liu; Jinqiang Zhang; Yufei Zhao; Katja Kretschmer; Guoxiu Wang. Volume expansion controlled of Sn nanoparticles by mesoporous carbon nanocube for both lithium-ion batteries and sodium ion batteries. Under preparation.

[15] **Shuangqiang Chen**; Bing Sun, Yufei Zhao, Jinqiang Zhang; Xiuqiang Xie; Hao Liu; Katja Kretschmer; Guoxiu Wang. The free-standing and homogenous

CNT@Tin@Porous graphene composites with controllable CNT length and inner voids for both lithium-ion batteries and sodium ion batteries. Under preparation.

[16] Anjon Kumar Mondal, Dawei Su, **Shuangqiang Chen**, Xiuqiang Xie, and Guoxiu Wang; Highly Porous $NiCo_2O_4$ Nanoflakes and Nanobelts as Anode Materials for Lithium-Ion Batteries with Excellent Rate Capability ***ACS Applied Materials & Interfaces*** 2014 *6* (17), 14827-14835. Impact factor: 5.9.

[17] Xiaoyu, Cao; **Shuangqiang, Chen**; Guoxiu, Wang; Porous Carbon Particles Derived from Natural Peanut Shells as Lithium Ion Battery Anode and Its Electrochemical Properties ***Electronic Material Letters*** 2014, 10(4): 819-826**.** Impact factor: 3.977.

[18] Song, Bai; **Shuangqiang, Chen**; Xiaoping, Shen; Guoxing, Zhu; Guoxiu, Wang; Nanocomposites of hematite (α-Fe_2O_3) nanospindles with crumpled reduced graphene oxide nanosheets as high-performance anode material for lithium-ion batteries ***RSC Advances*** 2012, 2, 10977-10984. Impact factor: 3.7.

[19] Yiying, Wei; **Shuangqiang, Chen**; Dawei, Su; Bing, Sun; Jianguo, Zhu; Guoxiu, Wang; 3D mesoporous hybrid $NiCo_2O_4$@ graphene nanoarchitectures as electrode materials for supercapacitors with enhanced performances ***Journal of Materials Chemistry A*** 2014, 2 (21), 8103-8109. Impact factor: 6.6.

[20] Xiaodan, Huang; Bing, Sun; Kefei, Li; **Shuangqiang, Chen**; Guoxiu, Wang; Mesoporous graphene paper immobilized sulfur as a flexible electrode for lithium–sulfur batteries ***Journal of Materials Chemistry A*** 2013, 1, 13484-13489. Impact factor: 6.6.

[21] Anjon Kumar, Mondal; Dawei, Su; Ying, Wang; **Shuangqiang, Chen**; Guoxiu, Wang; Hydrothermal Synthesis of Nickel Oxide Nanosheets for Lithium-Ion Batteries and Supercapacitors with Excellent Performance ***Chemistry, an Asian journal*** 2013, 8, 2828. Impact factor: 4.572

[22] Xiaodan, Huang; Bing, Sun; **Shuangqiang, Chen**; Guoxiu, Wang; Self-Assembling Synthesis of Free-standing Nanoporous Graphene–Transition-Metal Oxide Flexible Electrodes for High-Performance Lithium-Ion Batteries and Supercapacitors

Chemistry–An Asian Journal 2014, 9, 206-211. Impact factor: 3.93 ESI, highly cited paper.

[23] Bing, Sun; Xiaodan, Huang; **Shuangqiang, Chen**; Jinqiang,Zhang; Guoxiu, Wang; An optimized $LiNO_3$/DMSO electrolyte for high-performance rechargeable Li-O_2 batteries ***RSC Advances*** 2014. Impact factor: 3.7

[24] Anjon Kumar, Mondal; Dawei, Su; Ying, Wang; **Shuangqiang, Chen**; Qi, Liu; Guoxiu, Wang; Microwave hydrothermal synthesis of urchin-like NiO nanospheres as electrode materials for lithium-ion batteries and supercapacitors with enhanced electrochemical performances ***Journal of Alloys and Compounds*** 2014, 582, 522-527. Impact factor: 2.39. ESI highly cited paper.

[25] Anjon Kumar, Mondal; Bei, Wang; Dawei, Su; Ying, Wang; **Shuangqiang, Chen**; Xiaogang, Zhang; Guoxiu, Wang; Graphene/MnO_2 hybrid nanosheets as high performance electrode materials for supercapacitors ***Materials Chemistry and Physics*** 2014, 143, 740-746. Impact factor: 2.13

[26] Anjon Kumar, Mondal; **Shuangqiang, Chen**; Dawei, Su; Hao, Liu; Guoxiu, Wang; Fabrication and enhanced electrochemical performances of MoO_3/graphene composite as anode material for lithium-ion batteries. ***International Journal of Smart Grid and Clean Energy*** 2013.

[27] Anjon Kumar, Mondal; Dawei, Su; **Shuangqiang, Chen**; Bing, Sun; Kefei, Li; Guoxiu, Wang; A simple approach to prepare nickel hydroxide nanosheets for enhanced pseudocapacitive performance ***RSC Advances*** 2014, 4 (37), 19476-19481. Impact factor: 3.7.

[28] Xiuqiang, Xie; Dawei, Su; **Shuangqiang, Chen**; Jinqiang,Zhang; Shixue, Dou; Guoxiu, Wang; SnS_2 Nanoplatelet@Graphene Nanocomposites as High-Capacity Anode Materials for Sodium-Ion Batteries ***Chemistry–An Asian Journal*** 2014, 9 (6), 1611–1617. Impact factor: 3.93.

[29] Bing, Sun; Xiaodan, Huang; Shuangqiang, Chen; Yufei, Zhao; Jinqiang,Zhang; Paul, Munroe; Guoxiu, Wang; Hierarchical macroporous/mesoporous $NiCo_2O_4$ nanosheets

as cathode catalysts for rechargeable Li-O_2 batteries. ***Journal of Materials Chemistry A***, 2014, **2**, 12053-12059. Impact factor 6.6.

[30] Jinqiang, Zhang; Bing, Sun; Xiaodan, Huang; **Shuangqiang**, **Chen;** Guoxiu, Wang; Honeycomb-like porous gel polymer electrolyte membrane for lithium ion batteries with enhanced safety. ***Scientific Reports*** 2014, 4. 6007. Impact factor: 5.078

[31] Yufei, Zhao; **Shuangqiang**, **Chen;** Bing, Sun; Dawei, Su; Xiaodan, Huang; Hao, Liu; Yiming, Yan; Kening, Sun; Guoxiu, Wang; Graphene-Co_3O_4 nanocomposites as electrocatalysts with high performance for oxygen evolution reaction. ***Scientific Reports*** 2014, 5, 7629. Impact factor: 5.078

[32] Jinqiang Zhang, **Shuangqiang Chen**, Xiuqiang Xie, Katja Kretschmer, Xiaodan Huang, Bing Sun, Guoxiu Wang Porous poly(vinylidene fluoride-co-hexafluoropropylene) polymer membrane with sandwich-like architecture for highly safe lithium ion batteries. ***Journal of Membrane Science*** 2014, 472: 133–140. Impact factor: 4.09

[33] Anjon Kumar, Mondal; **Shuangqiang, Chen**; Dawei, Su; Xiuqiang, Xie; Guoxiu, Wang; A facile microwave synthesis of mesoporous $NiCo_2O_4$ nanosheets as electrode materials for lithium ion batteries and supercapacitors. ***ChemPhysChem*** *2015,* 16, 169-175. Impact factor: 3.36

[34] Anjon Kumar, Mondal; Dawei, Su; **Shuangqiang, Chen**; Xiuqiang, Xie; Guoxiu, Wang; Mesoporous $MnCo_2O_4$ with a flake-like structure as advanced electrode materials for lithium ion batteries and supercapacitors. ***Chemistry - A European Journal***, 2015, 21, 1526-1532. Impact factor: 5.696

[35] Xie X., Su D., Zhang J., **Chen S.**, Mondal A., Wang G.; A comparative investigation on the effects of nitrogen-doping into graphene on enhancing the electrochemical performance of SnO_2/graphene for sodium-ion batteries. ***Nanoscale*** 2015, 7(7), 3164-72. Impact factor: 6.9

ABSTRACT

Rechargeable energy storage devices are being seen as having a crucial role in the powering of myriad portable electronic devices, electrical vehicles and hybrid electrical vehicles. The properties of electrode materials are of extreme significance for the electrochemical performances of both lithium-ion (Li-ion) batteries and lithium-sulfur (Li-S) batteries.

Tin-graphene nanocomposites were prepared by a combination of microwave hydrothermal and one-step hydrogen gas reduction. When applied as an anode material in Li-ion batteries, tin-graphene nanocomposite exhibited a high lithium storage capacity of 1407 mAh g^{-1}. The materials also demonstrated an excellent high rate capacity and a stable cycle performance. Graphene-carbon nanotube hybrid materials were successfully prepared that demonstrated high reversible lithium storage capacity, high Coulombic efficiency and excellent cyclability. Fe_2O_3-CNT-graphene nanosheet hybrid materials were synthesized using a chemical vapor deposition method, exhibiting a high specific capacity of 984 $mAh \cdot g^{-1}$ with a superior cycling stability and high rate capabilities.

High quality single crystalline graphene sheets were prepared by the ambient pressure chemical vapor deposition method using acetylene as the carbon source and coral-like iron with body-centered-cubic structure as the catalyst. It showed high lithium storage capacity and excellent cyclability. Hierarchical three-dimensional carbon-coated mesoporous Si nanospheres@graphene foam nanoarchitectures were successfully synthesized by a thermal bubble ejection assisted chemical-vapor-deposition and magnesiothermic reduction method. The materials exhibited superior electrochemical performances, including a high specific capacity of 1200 mAh/g at the current density of 1 A/g, excellent high rate capabilities and outstanding cyclability.

Mesoporous Co_3O_4 nanoflakes with interconnected architecture were successfully synthesized by means of a microwave-assisted hydrothermal and low-temperature conversion method. Co_3O_4 nanoflakes delivered a high specific capacity of 883 mAh/g at 0.1 C current rate and stable cycling performances even at higher current rates as anodes of Li-ion batteries.

The synthesis of graphitic hyperbranched hollow carbon nanorods encapsulated sulfur composites were employed as cathode materials for Li-S batteries. The sulfur composite

cathodes delivered a high specific capacity of 1378 mAh/g at 0.1 C current rate and exhibited a stable cycling performance.

Multi-shelled hollow carbon nanospheres-sulfur composites with a high percentage of sulfur loading (86 wt. %) were synthesized by an aqueous emulsion approach and *in-situ* sulfur impregnation, delivering a high specific capacity of 1350 mAh/g and excellent capacity retention. By adopting a dual confinement strategy, poly(3,4-ethylenedioxythiophene) (PEDOT) coated micro/mesoporous carbon nanocube encapsulated sulfur (P@CNC-S) composites were synthesized. The P@CNC-S composites exhibited superior performances, including a high specific capacity, extended cycle life and outstanding rate capabilities.

INTRODUCTION

The energy crisis, global warming, emissions of greenhouse gases and vehicle exhaust pollution caused by the combustion of fossil fuels, challenge the modern society on high living cost and increasing environmental problems. Renewable energy, including solar, wind and tidal, should be stored using different types of batteries and utilized for ever-increasing energy requirements. In recent decades, energy storage has been substantially researched and applied mainly to traditional rechargeable batteries (lead-acid batteries, nickel-cadmium batteries and nickel-metal hydride batteries), lithium-ion batteries and lithium sulfur batteries.[1-4] The drawbacks of traditional rechargeable batteries hinder the further development in the future, including toxic raw materials, self-discharge, and the memory effect. Lithium ion (Li-ion) batteries and lithium sulfur (Li-S) batteries with many advantages, including high capacities, low self-discharge feature and long cycling lifes, are regarded as the most promising rechargeable systems for the future energy storage market.

In the last two decades, Li-ion batteries have been widely used in digital portable devices, electric vehicles (EV) and hybrid electric vehicles (HEV) because of their relatively high capacity, rate capability, high voltage and long cycle life. Currently, graphite is the most common commercialized anode material for Li-ion batteries, but it can only deliver a limited capacity (372 mAh/g, theoretical capacity). There are many other problems that plagued Li-ion batteries, such as high cost, the low Coulombic efficiency in the first cycle and fast capacity decay.

Lithium-sulfur batteries have many exceptional features, such as high specific capacity (1673 mAh/g), low cost (abundant source) and environmental friendliness. That is recognized as attractive systems for large-scale energy storage. However, lithium-sulfur batteries suffer several drawbacks, including low sulfur loading in cathodes, the dissolution of polysulfides, and poor electronic conductivity of sulfur. Many efforts have been devoted to improving the performance of lithium-sulfur batteries. Although significant progress has been achieved in the last two decades, there are challenges still to overcome. These challenges need to be solved in order to reduce the energy crisis, global warming and environmental pollution.

This thesis mainly focuses on the synthesis of a series of new nanocomposites as anode materials for Li-ion batteries and cathode materials for Li-S batteries, with the aim of preparing suitable nanomaterials and improving their electrochemical performances. The aforementioned problems about Li-ion batteries and Li-S batteries will be carefully addressed via the synthesis novel nanocomposites. Meanwhile, the cost to manufacture the Li-ion batteries and Li-S batteries will also be reduced by the use cheap raw materials.

The content of each chapter is briefly outlined:

1. Chapter 1 mainly reviews the history of Li-ion batteries and Li-S batteries. The relative reaction mechanism and principles are also presented. For Li-ion batteries, the anode and cathode materials are both discussed, but this thesis mainly focuses on anode materials. For Li-S batteries, the concept and reaction mechanism are given, and the challenges for Li-S batteries are also mentioned. Recent achievements for both Li-ion batteries and Li-S batteries are shown in the literature review.
2. Experimental section, including material preparation, material characterization and electrochemical performance measurements, is presented in Chapter 2. Different synthesis approaches are introduced, and the corresponding preparation apparatuses are also shown. A series of characterization methods and analysis instruments are reviewed. Some images regarding analysis instruments are also presented in this chapter.
3. In Chapter 3, Sn-graphene nanocomposites, prepared by a combination of microwave hydrothermal synthesis approach and one-step hydrogen gas reduction method, are used to synthesize anode materials for Li-ion batteries. The influences of weight ratio between tin and graphene nanosheets on their morphologies and electrochemical performances are discussed. The reason for the good cycling performance is examined by analyzing the morphology changes of electrodes after cycles.
4. Graphene-carbon nanotube hybrid materials without using any chemical reagent are presented in Chapter 4. The weight ratios between carbon nanotube and graphene have critical influences on the product state. When applied as anode materials in lithium ion batteries, graphene-carbon nanotube hybrid materials demonstrate high reversible capacity, high Coulombic efficiency and excellent cyclability.

5. The synthesis of Fe_2O_3-CNT-graphene nanosheet (Fe_2O_3-CNT-GNS) hybrid materials via a chemical vapor deposition method is shown in Chapter 5. SEM and TEM observations show that the as-prepared materials consist of Fe_2O_3 nanorings, bamboo-like carbon nanotubes and graphene nanosheets, which form an open-ended three-dimensional architecture. For the first time, we observed the growth of bamboo-like carbon nanotubes with open tips, which were catalyzed by detecting iron nanorings. When applied as anode materials in lithium ion batteries, the Fe_2O_3-CNT-GNS hybrid materials exhibited high specific capacities, good cycling stabilities and high rate capabilities. The reason for the enhanced electrochemical performances is discussed.

6. The large-scale production of high quality single crystalline graphene sheets through an ambient pressure chemical vapor deposition method is shown in Chapter 6, where acetylene (C_2H_2) is used as the carbon source and coral-like iron with body-centered-cubic structure as the catalyst. A new horizontal "dissolution-deposition-growth" mechanism is proposed, and verified by high resolution TEM. When applied as anode materials in lithium ion batteries, graphene sheets exhibited a high lithium storage capacity and excellent cyclability. This chapter demonstrates that crystalline graphene produced on a large scale with low cost, opens an avenue for graphene applications in many fields.
7. In Chapter 7 the preparation of hierarchical three-dimensional C@Si@GF nanomaterials, successfully synthesized by a thermal bubble ejection assisted chemical-vapor-deposition and magnesiothermic reduction method, is presented. The morphology and structure are characterized by different analysis instruments. When applied as anode materials in lithium ion batteries, C@Si@GF nanocomposites exhibited superior electrochemical performances. Post-mortem analyses confirmed the well-maintained morphology of 3D C@Si@GF electrodes even after 200 cycles.
8. Mesoporous Co_3O_4 nanoflakes with interconnected architecture, successfully synthesized by means of a microwave-assisted hydrothermal and low-temperature conversion method, are shown in Chapter 8. Mesoporous Co_3O_4 nanoflakes exhibited excellent electrochemical performances as anode materials in lithium ion batteries

and as catalyst in oxygen evolution reaction (OER) under alkaline solutions. Post-mortem analyses of ex-situ FESEM images revealed that the particular structure had been well maintained after long-term charge/discharge cycling and verified the robust properties of the mesoporous Co_3O_4 nanoflakes electrode. The mesoporous Co_3O_4 nanoflakes also show both OER active properties and good catalytic stability during OER, even when cycled 1000 times.

9. The synthesis of graphitic hyperbranched hollow carbon nanorods encapsulated sulfur composites, employed as cathode materials for lithium-sulfur batteries, is shown in Chapter 9. The sulfur composite cathodes deliver a high specific capacity and exhibit stable cycling performance, which could be ascribed to the unique graphitic hyperbranched hollow carbon nanorods architecture and high length/radius aspect ratio of carbon nanorods. The impedance changes of the materials before and after cycles are also measured and discussed.
10. In Chapter 10, multi-shelled hollow carbon nanospheres encapsulated sulfur composites with a high percentage of sulfur loading (86 wt. %) are presented. When applied as cathodes in lithium-sulfur batteries, the composite materials delivered a high specific capacity of 1350 mAh/g and excellent capacity retention (92% for 200 cycles). Further measurements at high current densities also demonstrated significantly enhanced cyclabilities and rate capabilities.
11. Adopting a dual confinement strategy, homogenous PEDOT coated micro/mesoporous carbon nanocube encapsulated sulfur (P@CNC-S) composites are shown in Chapter 11. The P@CNC-S composites exhibited superior performances, including a high specific capacity, extended cycle life and outstanding high rate capabilities. Assisted by the analyses of ex-situ SEM, TEM and impedance spectra, the reasons for excellent cycling stabilities are discussed.

CHAPTER 1 LITERATURE REVIEW

1.1 Renewable energy storage

Today, energy storage devices are far more significant to modern society because of the emergence of many and varied cutting-edge information techniques and personal electronic devices, which have permeated every aspect of people's lives. From powering myriad portable electronic devices (mobile phones, laptops, tablet computers, etc.) to recharging electric vehicles and hybrid electric vehicles, the requirements for rechargeable energy storage in the future are increasing. Rechargeable energy storage can be categorized into several forms: 1) lithium-ion based batteries; 2) sodium-ion based batteries;[5] 3) supercapacitors;[6] and 4) other metal-ion based batteries (magnesium ion batteries and alkali metal-air batteries).[7-8] For Li-ion based batteries, there are three types of batteries (Li-ion batteries, Li-S batteries and Li-O_2 batteries) on which researchers are mainly focused. In this thesis the main efforts are devoted to studying the electrochemical performances of Li-ion batteries and Li-S batteries. Different kinds of nanomaterials are prepared and applied for subsequent measurements.

1.2 Lithium ion batteries

Lithium ion batteries, first developed by Sony Co. in 1991,[9] have been successfully commercialized for over 20 years. In order to avoid the formation of lithium dendrites for lithium batteries during cycles and for safety, Li-ion batteries are designed without lithium metal. In a typical Li-ion battery (as shown in Figure 1-1),[10] four parts are composed into a full Li-ion battery. The positive electrode (functioning as cathode, e.g. layered $LiCoO_2$), the non-aqueous lithium salt electrolyte (acting as Li^+ ions carriers, e.g. $LiPF_6$, which is dissolved in organic solvents, like propylene carbonate/ethylene carbonate, PC/EC) and the negative electrode (serving as anode, e.g. commercial graphite) are divided by a separator membrane. During the charging process, Li^+ ions deintercalate from the layered $LiCoO_2$ cathode, pass through the porous polymer separator via lithium salt electrolyte, and intercalate among graphite layers (anode). The electrons flow via the external circuit from the positive electrode to the negative electrode. During discharging, Li^+ ions experience the reverse process and the electrons flow in the opposite direction, as shown in Figure 1-1.

The redox reactions during charge/discharge processes are presented as follows:

$$LiCoO_2 \leftrightarrow Li_{1-x}CoO_2 + xLi^+ + xe^- \ (1<x<0) \qquad \text{(Cathode)}$$

$$6C + xLi^+ + xe^- \leftrightarrow Li_xC_6 \ (1<x<0) \qquad \text{(Anode)}$$

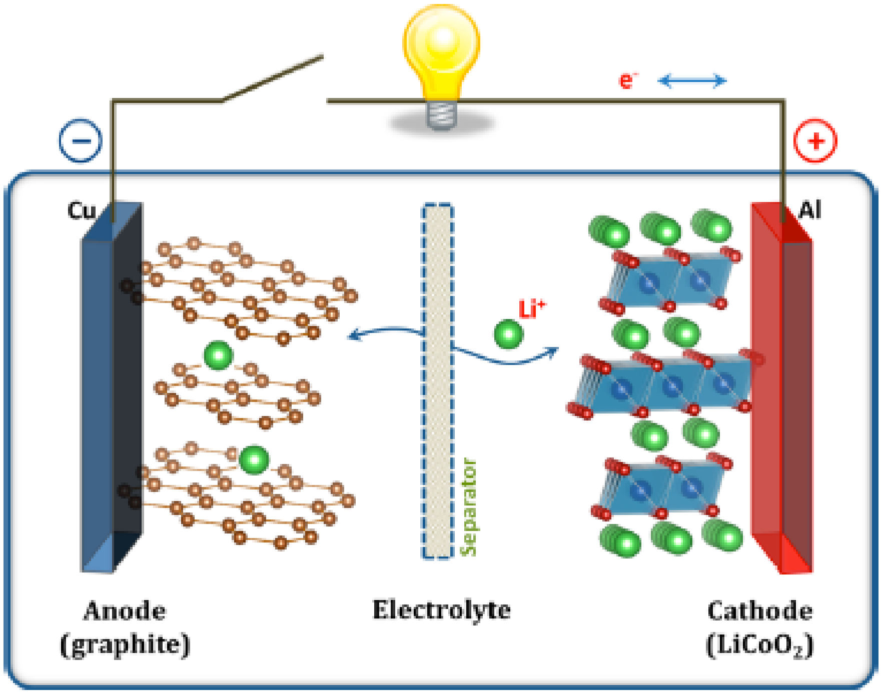

Figure 1-1 Schematic illustration for the first commercial Li-ion battery ($LiCoO_2/Li^+$ electrolyte/graphite).[11]

Besides the layered $LiCoO_2$ (widely used as cathode in commercial Li-ion batteries), a series of cathode materials, including layered lithium transition-metal oxide ($LiMO_2$, M=Ni, Mn or mixed metal with Co), lithium transition-metal phosphates ($LiMPO_4$, M= Fe, Ni, Mn or mixed metal with Co) and lithium transition-metal oxide spinels (LiM_2O_4, M=Mn, Ni, or mixed metal with Co), are developed as alternative electrodes to reduce the cost and lower their environmental influence. Alternatively, many nanomaterials, including carbon based materials (porous carbon, graphene and carbon nanotube), metal (Sn, In), metalloid (Si, Ge, Sb) and transition metal oxides, are applied as anode materials in Li-ion batteries. A schematic illustration about cathode and anode materials is shown in Figure 1-2. Moreover, compared with other anode materials, lithium metal is the most electropositive (-3.04 V versus standard hydrogen electrode) and lightest metal, making it the most potential material for Li-ion battery anodes with high energy density. However, due to the formation of lithium dendrites during cycling, and problems of moisture and oxygen sensitive features, fundamental research should be carried out to tackle those issues.

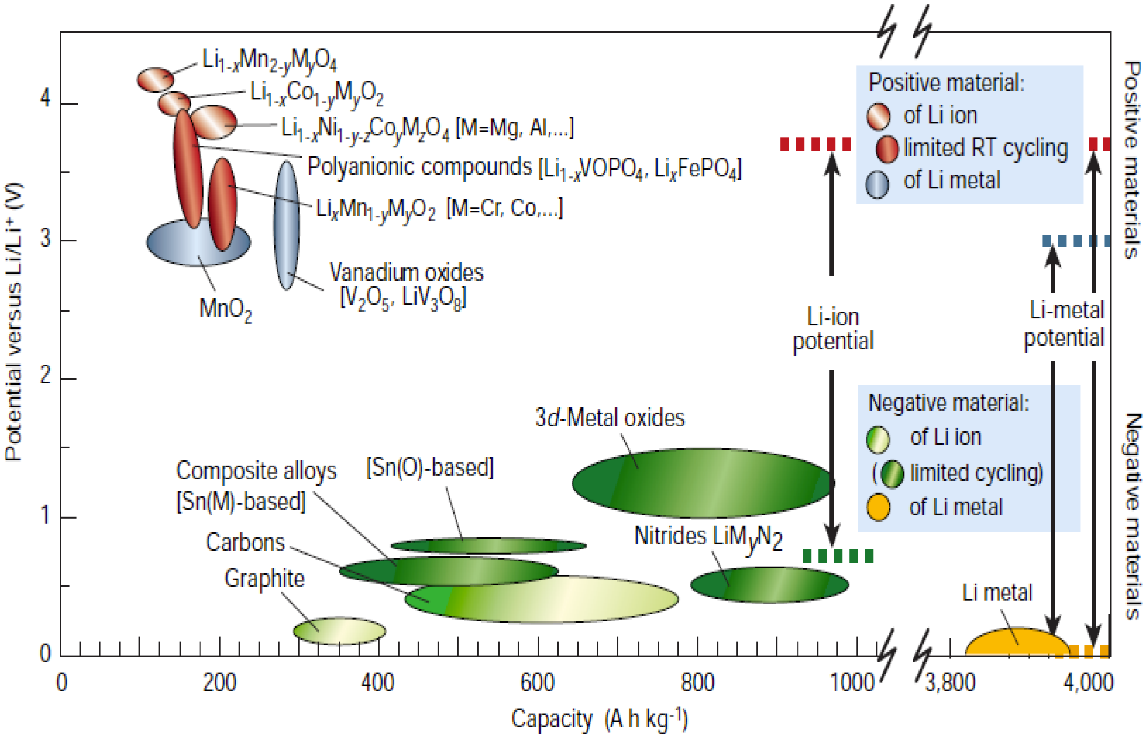

Figure 1-2 Voltage (V) versus capacity (Ah/kg) for positive and negative electrode materials.[12]

1.2.1 Cathodes

Since the successful commercialization by Sony Co. of Li-ion batteries, the layered $LiCoO_2$ cathode has dominated the cathode market for over 20 years because of its easy preparation process and stable cycling performances. However, there have been concerns about not only the high cost, but also its potential environmental pollution after discarding. Alternative cathodes should be developed to address these issues, by providing cathode materials with lower cost, higher capacity and more stable cycling performance. There are three categories in which the most researched cathodes fall: layered lithium transition-metal oxide ($LiMO_2$, M=Ni, Mn or mixed metal with Co); lithium transition-metal phosphates ($LiMPO_4$, M= Fe, Ni, Mn or mixed metal with Co); and lithium transition-metal oxide spinels (LiM_2O_4, M=Mn, Ni, or mixed metal with Co).

For layered lithium transition-metal oxides, major efforts have been devoted to developing high-performance cathodes (either individual lithium transition-metal oxides or lithium mixed transition-metals oxides). Replacing cobalt with the relatively cheaper and abundant transition metal Mn/Ni is a good strategy in tackling the cost problem and reducing the environmental pollution caused by toxic cobalt. Owing to its intrinsic structural instability, the delivered capacity of $LiCoO_2$ is only around 140 mAh/g, which is half of the theoretical capacity (274 mAh/g).[13] After substitution by Mn/Ni, the capacity can reach 240 mAh/g without apparent capacity decay, which is ascribed to the stable framework, and the valences of Mn^{4+}/Ni^{3+} are not changed during charge/discharge processes. Another approach to improve the performance of layered lithium transition metal oxides is the adjustment of metal ratios in the system ($LiCoO_2$- $LiNiO_2$- $LiMnO_2$). A schematic illustration of layered $LiMO_2$ is presented in Figure 1-3.

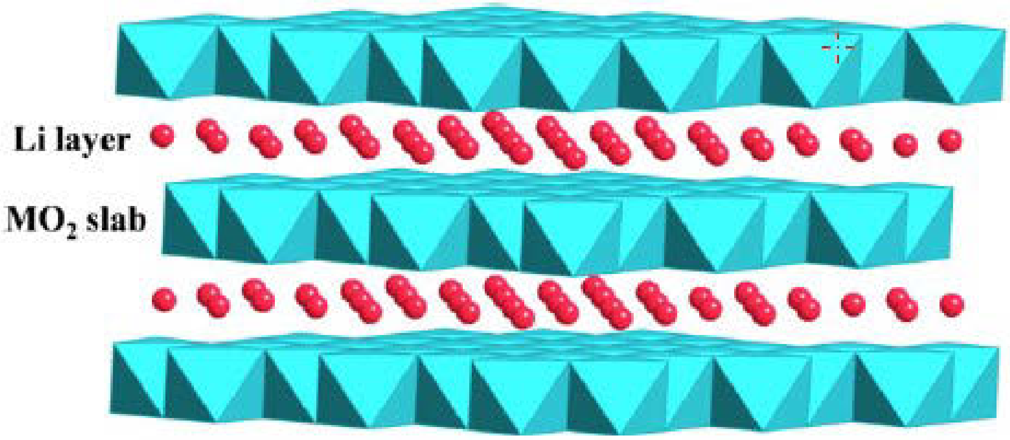

Figure 1-3 Schematic illustration of layered $LiMO_2$ crystal structure (blue: transition metal ions; red: Li-ions). [14]

The typical lithium transition-metal phosphate is $LiFePO_4$, which was first reported by Goodenough and co-workers in 1997. When applied as cathode materials, it shows many advantages, such as low cost, environmental friendliness and excellent thermal stability. Its crystal structure is composed of slightly distorted *hcp* anion oxygen arrays, where half of the octahedral sites are held by Fe and one eighth by Li. FeO_6 octahedra are corner-shared, while the LiO_6 octahedra are edge-shared. Three diffusion paths for Li-ions are proposed, which are also demonstrated by computational calculations. Only the channel along *b* axis is shown to have a much easier access than those channels along the *a* and *c* axis bridged by PO_4 tetrahydral. Although the rate capability in bare materials is not suitable for high-rate applications, modifications to $LiFePO_4$, including conductive carbon coating and reducing particle size to minimize Li-ion diffusion paths, make its high-rate capability more attractive. Replacing the Fe^{3+}/Fe^{2+} redox couple with another transition metal redox couple (Co, Mn, Ni) can improve the low voltage feature of $LiFePO_4$.[15-16] The high rate and stability properties of lithium metal phosphate oxides can also remain.

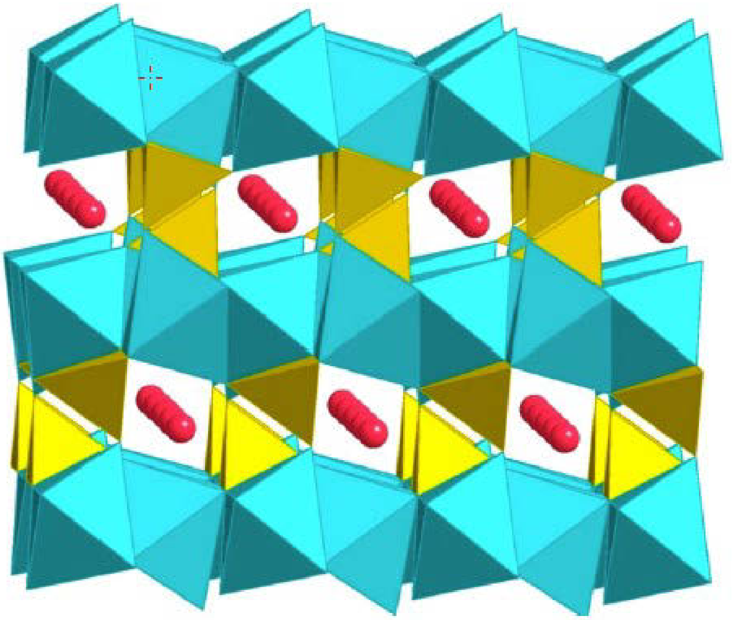

Figure 1-4 Schematic illustration of olivine-type $LiMPO_4$ crystal structure (blue: transition metal ions; red: Li-ions; yellow: P ions). [14]

The spinel LiM_2O_4 structure, as shown in Figure 1-5, was proposed by Thackeray and coworkers in 1983 as the cathode material for Li–ion batteries. The oxygen arrangement in LiM_2O_4 is the same as that of layered $LiMO_2$. The spinel structure is built with a three-dimensional MO_2 host and some vacancies in the transition metal layer, leaving tunnels for lithium ions. However, the original spinel materials face serious capacity fades for two reasons. One comes from the dissolution of Mn^{2+} in the electrolyte, which generates a disproportional reaction of Mn^{3+}. The other one is caused by new phases formed during cycling and the corresponding micro-strains. An alternative solution is doping the inactive ions (Al, Mg) or row transition metal ions (Ti, Cr, Fe and Cu) to alleviate the aforementioned dissolution of Mn^{2+} and improve the cycling performance.[17]

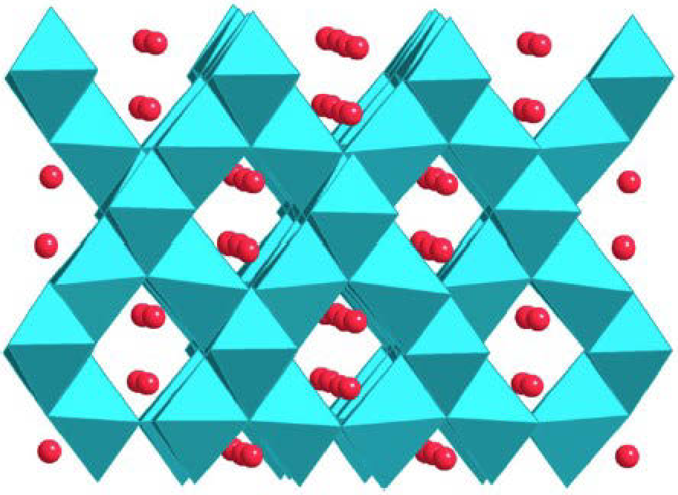

Figure 1-5 Schematic illustration of spinel LiM_2O_4 crystal structure (blue: M_2O_4 transition metal oxides; red: Li-ions).[14]

1.2.2 Anodes

For anode materials, lithium metal, which has the possible problem of forming lithium dendrites during cycling, is replaced with natural graphite for the successful commercialization of the lithium ion battery. Besides graphite, there are many alternative materials for anodes, such as carbon based materials (CNT, graphene and porous carbon), metal (Sn, In, etc.), metalloids (Si, Sb and Ge, etc.) and transition metal oxides (Fe, Mn, Ni, Cu and Co, etc.).

1.2.2.1 Graphite and other commercial anodes

Graphite with a stacking order of graphene layers is suitable to accommodate Li-ions with an intercalation mechanism, which can avoid the problem of forming Li dendrite. The theoretical capacity of graphite is 372 mAh/g, but for a practical anode, the specific capacity of graphite can only reach around 300 mAh/g, which cannot meet current requirements for EVs and HEVs. The intercalated Li ions in graphite show two states: one is intercalated with graphite, forming LiC_6, and the other arrangement is forming covalent Li_2 molecules, which can be observed in Figure 1-6.

Porous carbon materials, including microporous (pore size < 2 nm)/mesoporous (2 nm < pore size < 50 nm)/macroporous (pore size > 50 nm) materials, can provide extra capacities, which are much higher than that of graphite. The extra capacities come from those abundant porous structures, offering large surface area and providing more active positions to combine Li-ions. Moreover, many previous works have demonstrated that micro/mesopores can store large amounts of Li-ions (Figure 1-6b). Some Li-ions can be absorbed at the edge of graphite (if one layer of graphite can be viewed as graphene). For disordered carbon material, copious nanocavities can provide extra capacities (Figure 1-6d). Therefore, porous carbon materials often exhibit drastically enhanced capacities and good cycling performances, owing to large surface areas and small mechanical stresses of volume expansion/contraction during cycling.

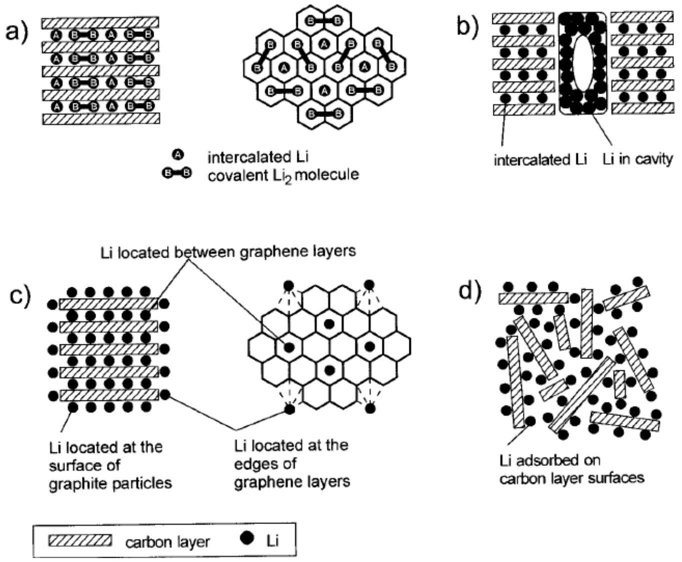

Figure 1-6 Schematic illustration of intercalation mechanism of Li ions and carbon based materials.[18]

1.2.2.2 Carbon nanotubes and graphene

Carbon nanotube, first prepared by Iijima in 1990, is a one-dimensional carbon material that can serve as anode material owing to its high surface area and extra volume inside its carbon tunnel. The Li-ions can be absorbed on the outside, the two edges and the inner tunnel of the CNT. Strains on the small diameters of CNTs are distributed across the hexagonal planar bonds, which cause de-localization of electrons and make it more attractive to Li-ions. The capacity range of CNTs is about 460-1100 mAh/g by different kinds of post-treatments (ball milling, acid oxidation-reduction). CNTs can also perform as host materials that carry different nanomaterials with enhanced electrochemical performances.

Graphene, first reported by Geim and Novoselov in 2004, is one layer and two-dimensional honeycomb carbon lattice with fascinating physical, chemical and mechanical features. Graphene can be wrapped into 0D fullerenes, rolled into 1D carbon nanotubes or stacked into 3D graphite, which are shown in Figure 1-7. When used as anode material for Li-ion batteries, graphene can, in theory, deliver a high capacity of 744 mAh/g, which is twice that of graphite. With the high surface area, intriguing electronic conductivity and porous structure, graphene is one of the most promising candidates for Li-ion battery anodes. Since Li^+ ions can be stored on both sides of the graphene planar, defects, edges and nanopores made by different treatment approaches, graphene with flexible and robust features has been widely used as host material to support metal or transition metal oxide nanomaterials. The enhanced capacities are ascribed to the relative synergic effects and buffer of volume changes during charge/discharge.

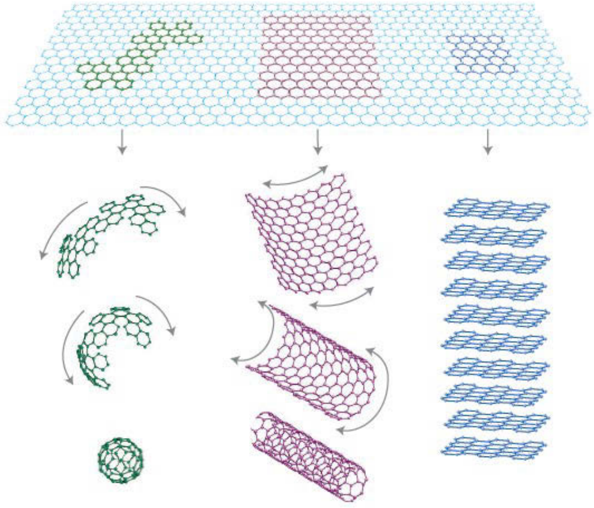

Figure 1- 7 A scheme diagram of graphene with capabilities of rolling into fullene, carbon nanotube or stacking as graphite. [19]

1.2.2.3 Metal and metalloid anodes

Lithium ions can form alloys with some metals (Sn, In, etc.) and metalloids (Si, Sb and Ge, etc.), as shown in Figure 1-8. The rechargeable anode materials experience large volume changes with the Li-alloy/dealloy mechanism during charge/discharge. For instance, the alloying reaction between Li and Si can generate a final product of $Li_{22}Si_5$ with the highest theoretical capacity of 4200 mAh/g. However, the volume expansion after forming the $Li_{22}Si_5$ alloy can reach 400%, which provokes serious electrode pulverization, followed by fast capacity decay. Similar things happen to other metal and metalloid, like Sn (generating $Li_{4.4}Sn$ alloy with a theoretical capacity of 994 mAh/g and a high volume expansion of 360%) and Ge (forming $Li_{4.4}Ge$ alloy with a theoretical capacity of 1620 mAh/g and a high volume expansion of 370%). The large volume changes during charge/discharge show fast capacity loss, making it difficult to meet the normal cycle life requirement. Many attempts have been made to confine the volume expansion via different approaches, such as carbon-coating, minimizing particle size, introducing flexible host (graphene or CNT) or encapsulated by other conductive materials. Efforts have also been devoted to improving electrochemical performances. Performing the largest value of those materials by means of special treatment or protection is still an intense topic. The Li-alloy mechanism is also suitable for the reaction between metal oxides and Li^+ ions, consisting of two steps: 1) M_xO_y +2yLi+ + $2ye^- \rightarrow xM + yLi_2O$; and 2) $M + zLi^+ + ze^- \leftrightarrow Li_zM$. The first reaction only happens in the first discharge, with the redox reaction then taking place between metal and Li^+ ions.

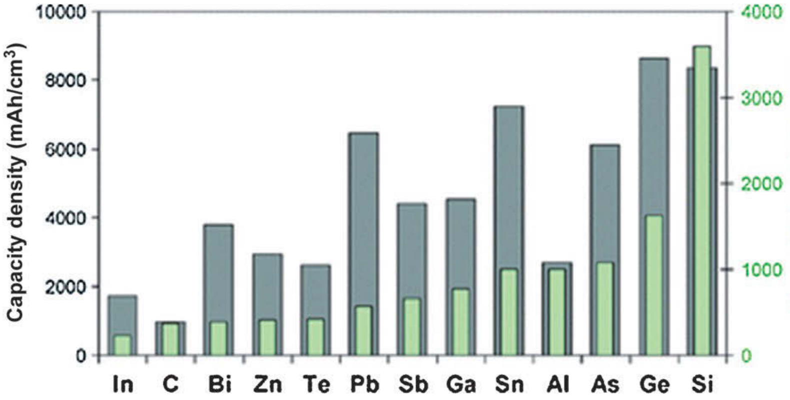

Figure 1- 8 The theoretical specific capacities and capacity densities for anode materials.[6]

1.2.2.4 Transition metal oxides

For transition metal oxides, there are two types of reaction mechanisms between transition metal oxides and Li^+ ions: 1) Insertion reaction mechanism: $MO_x + yLi^+ + ye^- \leftrightarrow Li_yMO_x$; and 2) Conversion reaction mechanism: $M_xO_y + 2yLi^+ + 2ye^- \leftrightarrow xM + 2yLi_2O$.

Some transition metal oxides, like TiO_2 and WO_2, are storing Li^+ ion via the aforementioned insertion reaction mechanism. Although these transition oxides are cheap and non-toxic, the amount of Li^+ ions inserting themselves into the vacancies of their structures is less than that of the transition metal oxide molecular, which means the insertion reaction-based transition metal oxide can only provide limited specific capacity. For instance, the theoretical specific capacity of TiO_2 is 335 mAh/g (lower than that of graphite), even though it can offer excellent rate capability.[20]

Other transition metal oxides that could react with Li^+ ions are followed by the conversion reaction mechanism, such as Fe, Co, Ni, Mn, Cu, Ru, Mo *etc*. Li_2O component will be generated after the conversion reactions between transition metal oxides and Li^+ ions, and then reversibly recovered to its initial state. With the high oxide state, transition metal oxides can deliver high specific capacities (more than 800 mAh/g) because of multiple electrons involved in the conversion reactions. The performances of specific transition metal oxides will be discussed in the following chapters. There is one disadvantage for transition metal oxides performing as anodes. Low Coulombic efficiency has always plagued transition metal oxides because of the unstable solid electrolyte interface (SEI). Unlike the uniform SEM layer of carbon based materials, the SEI layer on transition metal oxides is easily destroyed by the large volume changes during cycling. Therefore, to achieve reliable cycling performance and high Coulombic efficiency, there are several approaches, such as decreasing the particle size, forming the deliberated designed porous structure, loading on conductive and flexible host (graphene, CNT or porous carbon based materials).

1.3 Lithium sulfur batteries

1.3.1 Challenges and opportunities

Lithium-sulfur (Li-S) batteries, first developed by Herbert and Ulam in 1962, are regarded as the most promising rechargeable battery system. Li-S batteries can boost capacities fivefold over current commercial lithium-ion batteries, owing to the high theoretical capacity of sulfur (1673 mAh/g, energy density of ~2600 Wh/kg). Moreover, the Li-S battery is low cost, due to the natural abundance of sulfur (almost 3% of the Earth's mass), and environmentally friendly. The Li-S battery, as shown in Figure 1-9, is composed of cathode (sulfur composites with carbon additive and polymer binder), anode (Li metal) and electrolyte (lithium salts dissolved in mixtures of dioxolane-based solvent to give maximum performance of the sulfur utilization). Although many efforts have been devoted to improving the electrochemical performance of Li-S batteries, many challenges still remain. The large volume expansion (about 80%) during discharge can instigate electrode pulverization. The natural insulator of sulfur and discharged product (lithium sulfide) largely limits the rate capabilities of Li-S batteries. Additionally, the intermediate lithium polysulfides are soluble in electrolyte and freely migrate between cathode and anode, leading to the "shuttle effect". These drawbacks easily induce the fast capacity decay.

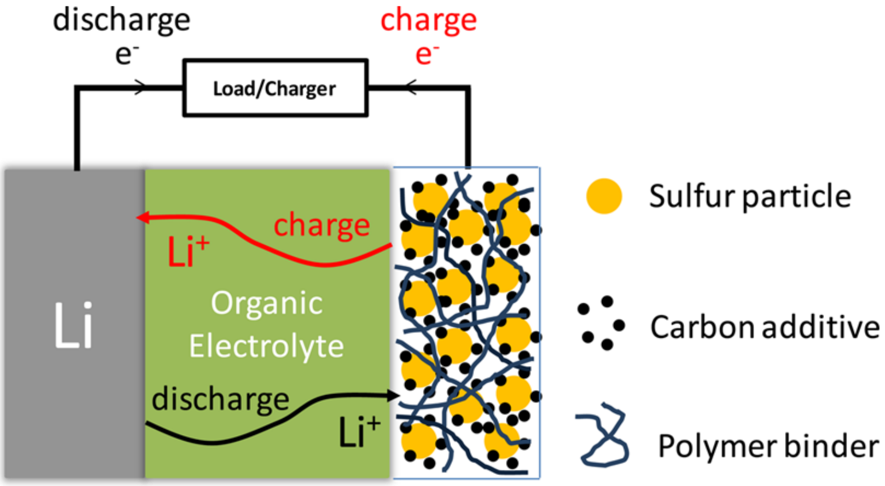

Figure 1- 9 A schematic illustration of Li-S batteries. [21]

The shuttle effect and electrochemical behavior of Li-S batteries are presented in Figure 1-10. The discharge reaction of a lithium-sulfur battery can be viewed in two main stages, with each stage comprising multiple reactions.[21-24] The first stage includes three reductive reactions in fast kinetics (Equation 1-3), relating to the transformation of cyclooctasulfur to long-chain soluble lithium polysulfides at high plateau (2.15-2.4V), and the following one contains two reductive reactions in relative slow kinetics (Equation 4-5),[25] involving the decomposition of lithium polysulfides to insoluble short-chain lithium sulfides at low and long plateau (2.0-2.1 V). By contrast, the charge reaction controlled by slow kinetics exhibits two main stages from lithium sulfides to lithium polysulfides at 2.3-2.4V (Equation 5-4) and 2.45-2.5 V (Equation 3-1), respectively. Sometimes, owing to slow oxidation kinetics, only one broad stage (Equation 5-1) can be observed in some reports.[26-28]

$$S_8 + 2e^- \leftrightarrow S_8^{2-} \quad \text{(Equation 1)}$$

$$3S_8^{2-} + 2e^- \leftrightarrow 4S_6^{2-} \quad \text{(Equation 2)}$$

$$2S_6^{2-} + 2e^- \leftrightarrow 3S_4^{2-} \quad \text{(Equation 3)}$$

$$S_4^{2-} + 4Li^+ + 2e^- \leftrightarrow 2Li_2S_2 \quad \text{(Equation 4)}$$

$$Li_2S_2 + 2Li+ +2e- \leftrightarrow 2Li_2S \quad \text{(Equation 5)}$$

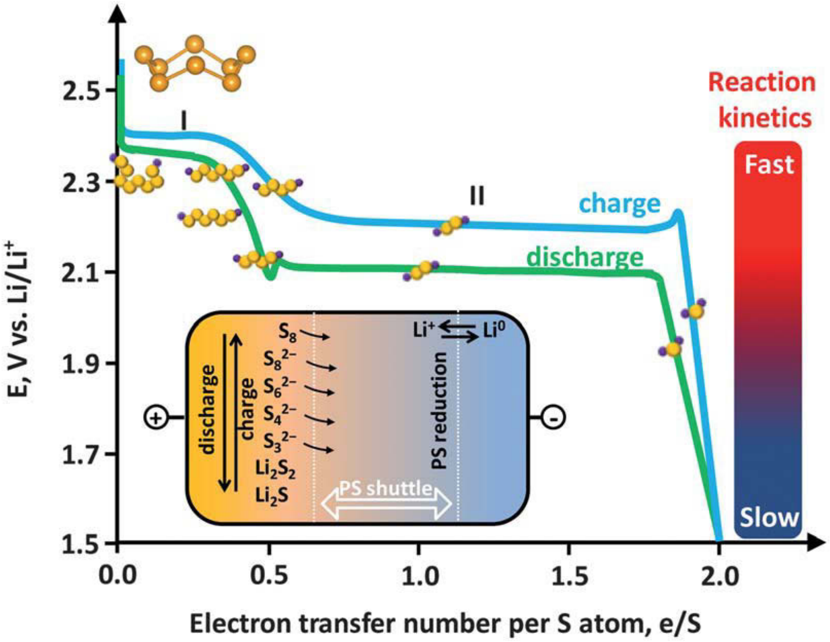

Figure 1-10 The electrochemical charge/discharge profiles of Li-S batteries and the shuttle effect.[21]

1.3.2 Cathodes

1.3.2.1 Sulfur composites

Despite many advantages, the practical application of Li-S batteries is hindered by rapid capacity decay. This is caused by the aforementioned reasons, including the insulating nature of sulfur, dissolution of lithium polysulfide ions (causing shuttle effect), large volume changes and the formation of lithium dendrite.[29-33] Furthermore, insoluble Li_2S_2 and Li_2S of the discharged products tend to precipitate on the surface of electrodes.[34] For traditional Li-S batteries, many approaches have been made in order to encapsulate sulfur. Conducting additives or graphitized carbon matrices are employed to improve the conductivity and to confine polysulfides dissolution.[31, 35-41] Various hollow (nanospheres[31, 42-44]), flexible (carbon paper[45] and graphene[46-49]) or tunnel carbon materials (carbon nanotube,[50-52] carbon nanofibers[30, 53] and highly ordered porous carbon matrix[54-55]) are also used to encapsulate sulfur and confine the shuttle effect originating from soluble lithium polysulfides, which is considered as the physical confinement.

Conducting polymers and amphiphilic polymers, including poly (3,4-ethylenedioxythiophene) (PEDOT),[56] polypyrrole (PPY),[57] polyethylene glycol (PEG),[38, 54] polyaniline (PANI)[58] and polyvinylpyrrolidone (PVP),[53, 59] have also been applied in order to restrain the dissolution of polysulfides ions through chemical interactions, which can be regarded as the chemical absorption strategy.[60-64]

Moreover, the addition of $LiNO_3$ in electrolyte also suppresses the shuttle effect and passivates the reactive lithium metal foil.[53] Combining the physical and chemical approaches as a dual sulfur confining tactic would open new opportunities to develop cathode materials with superior electrochemical properties. However, to date, only a few reports discuss the dual sulfur confining strategy.[28, 54]

Besides the improvements of electrode conductivity and the confinements of the shuttle effect, modification on sulfur composites and newly designed sulfur components have demonstrated enhanced electrochemical performances. Cui *et al.* prepared hollow sulfur nanospheres with the conductive polymer PEDOT coating, which achieved an initial capacity of 1267 mAh/g at 0.2 C, with a capacity retention ratio of 74% after 100 cycles and a reversible capacity of 739 mAh/g even after 300 cycles.[58] Long *et al.* reported a sustainable and efficient way of layer-by-layer catalyzing and depositing sulfur onto a nitrogen-contained mesoporous carbon framework, demonstrating a high reversible capacity of 939 mAh/g after 100 cycles at 0.2 C, and an excellent rate capability of 527 mAh/g up to 5 C.[55] Cheng *et al* developed a graphene-pure-sulfur sandwich structure by clamping pure sulfur between two well-prepared graphene membranes, and assembling with a commercial separator pre-coated with another graphene membrane, showing a resumed capacity of 950 mAh/g, with a capacity retention ratio of 90.3% after 100 cycles at a current density of 0.75 A/g.[48] Liu *et al.* designed a hybrid cathode with electrically connected graphite and lithium foil to control side-reactions on the surface of lithium foil, achieving a high capacity of 800 mAh/g for 400 cycles at a high current density of 1,737 mA/g, with a high Coulombic efficiency.[65] Moreover, a smart charging/discharging technique is also demonstrated to improve the cycling performance of Li-S batteries. Controlling the charging/discharging voltage can successfully stabilize the redox reactions in a highly reversible trace polysulfide shuttle zone, significantly enhancing the cycling performance and increasing the Coulombic efficiency.[66]

1.3.2.2 Lithium sulfide and lithium polysulfides

For a new configuration for Li-S batteries, the sulfur composite cathode is replaced by lithium sulfide (Li_2S) or lithium polysulfides, and the anode can use lithium metal-free materials, such as Si, Sn, transition metal oxides, and a series of carbon-based materials. Li_2S with a high theoretical capacity of 1166 mAh/g is recognized as being a promising candidate for Li-S battery cathodes, which can avoid the problem of lithium dendrites during cycling. However, there are some drawbacks with Li_2S, including low electronic and ionic conductivity, moisture and oxygen sensitivity, and tough synthesis conditions. Much work has been done to solve these disadvantages via ball-milling with porous carbon materials, coating with carbon shells (CVD method) and wrapping with graphene.[67-70] Lithium polysulfides (Li_2S_x, x=8, 6 or 4), the soluble intermediates for traditional Li-S batteries, can be also be applied as cathode materials for new configurations of Li-S batteries.[69] However, both Li_2S and lithium polysulfides should be charged first to activate the cathodes, which is different to the measurement process of sulfur cathodes.

1.3.3 Anodes

For most Li-S batteries, Li metal is employed as anode to supply Li^+ ions during cycling. The dissolved lithium polysulfides may deposit on the surface of Li metal and degrade the electronic conductivity. Moreover, there is a safety issue for Li metal anode owing to the possible formation of lithium dendrites during cycling. Additional carbon paper or graphene film can resist both the lithium dendrite penetration and the migration of dissolved lithium polysulfides. For a novel configuration to Li-S batteries, the Li^+ ions sources are transferred to cathodes (Li_2S or lithium polysulfides), which makes the lithium metal-free batteries possible and also improves the safety and cyclability of Li-S batteries.

CHAPTER 2 EXPERIMENTAL METHODE AND CHARACTERIZATION

2.1 Overview

The overall research routes for preparing different nanomaterials and their substantial applications are presented in Figure 2-1. There are three main procedures to all the nanomaterials: materials preparation; material characterizations of as-synthesized nanomaterials; and different applications on lithium-ion batteries or lithium-sulfur batteries. The nanomaterials are synthesized by four different approaches: chemical vapor deposition (CVD); wet-chemical synthesis (WCS); polymerization method (PM); and hydrothermal method (HM). Generally, the deliberately designed nanomaterials are firstly confirmed by a series of characteristic approaches, including X-ray diffraction (XRD), Raman spectroscopy, Fourier transform infrared (FTIR) spectroscopy, thermogravimetric analysis (TGA), Brunauer Emmett Teller (BET), atomic force microscopy (AFM), ultraviolet-visible spectroscopy (UV-vis), scanning electron microscopy (SEM), transmission electron microscopy (TEM) and high-resolution TEM (HR-TEM). After that, the as-synthesized nanomaterials are assembled as electrodes in a glove box for lithium ion batteries or lithium sulfur batteries. To further investigate the lithiation/delithiation mechanism and reasons for different electrochemical performances, some electrodes are further analyzed with *ex-situ* SEM, TEM approaches or electrochemical impedance spectroscopy (EIS).

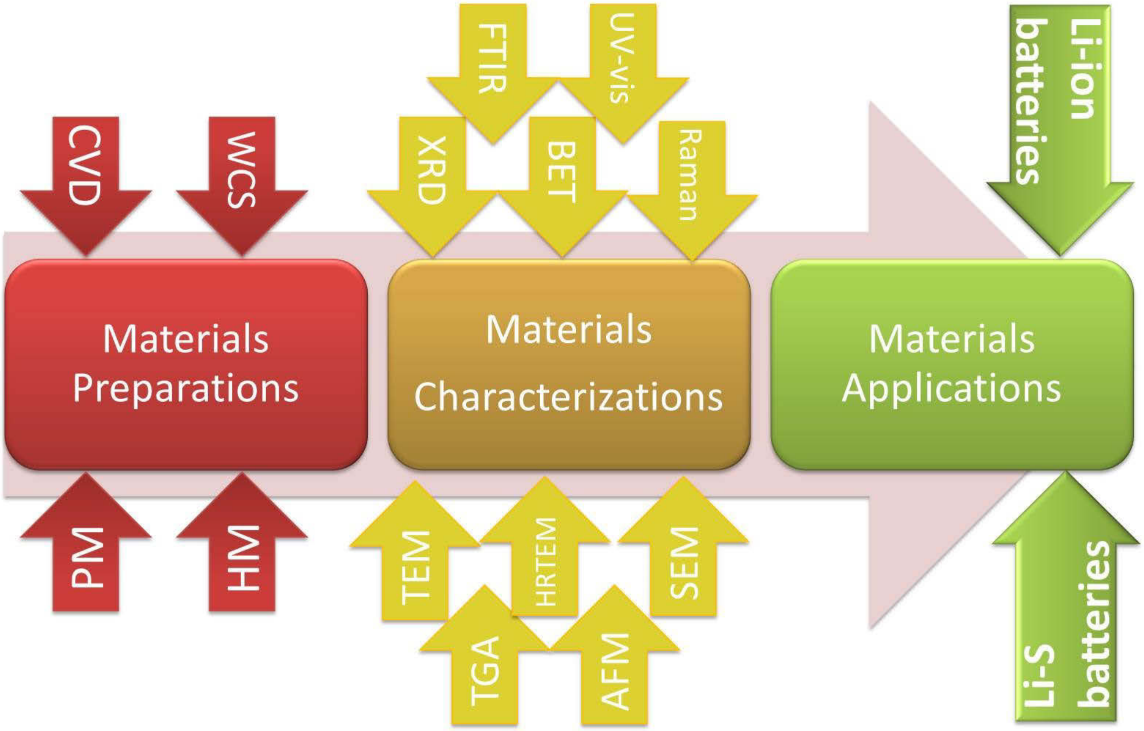

Figure 2-1 Schematic illustration for materials preparations, characterizations and applications.

A list of the names of materials and chemicals involved in the thesis, along with their formula, purity and supplier, is shown below in **Table 2-1**.

Table 2- 1 Materials and chemicals used in the research project.

Materials and chemicals	Formula	Purity	Supplier
1,2-Dimethoxyethane (DME, anhydrous)	$CH_3OCH_2CH_2OCH_3$	99.5%	Sigma-Aldrich
1,3-Dioxolane (DOX, anhydrous)	$C_3H_6O_2$	99.8%	Sigma-Aldrich
Carbon black	C	99%	Lexel
Citric acid	$HOC(COOH)(CH_2COOH)_2$	99.5%	Sigma-Aldrich
Cobalt(II) chloride hexahydrate	$CoCl_2 \cdot 6H_2O$	98%	Sigma-Aldrich
Cobalt(II) acetate tetrahydrate	$Co(NO_3)_2 \cdot 4H_2O$	98%	Sigma-Aldrich
Ethanol	CH_3CH_2OH	99.5%	Sigma-Aldrich

Iron(II) acetate	$Fe(NO_3)_2$	99.99%	Sigma-Aldrich
Acetylene/Ar	C_2H_2/Ar	10%	Air liquide
Ethylene glycol (EG, anhydrous)	$HOCH_2CH_2OH$	99.8%	Sigma-Aldrich
Graphite (natural flakes)	C	75%	Aldrich
Hydrazine hydrate	$NH_2NH_2 \cdot xH_2O$	50–60%	Sigma-Aldrich
Hydrochloric acid	HCl	37%	Sigma-Aldrich
Hydrogen peroxide solution	H_2O_2	30–32%	Sigma-Aldrich
L-cysteine	$HSCH_2CH(NH_2)CO_2H$	98%	Sigma-Aldrich
Lithium bis(trifluoromethane sulfon)imide (LiTFSI)	$CF_3SO_2NLiSO_2CF_3$	99.95%	Sigma-Aldrich
Lithium foil	Li	99.999%	Hohsen Corporation Japan
Lithium perchlorate	$LiClO_4$	99.99%	Aldrich
Lithium-ion battery electrolyte (LB-303)	1 M $LiPF_6$ in ethylene carbonate (EC) and dimethyl carbonate (DMC) (1:1 w/w)	–	Guotai-Huarong New Chemical Materials Co.Ltd, China
N-Methyl-2-pyrrolidinone (NMP, anhydrous)	C_5H_9NO	99.5%	Sigma-Aldrich
Poly(vinylidene difluoride) (PVdF)	$(CH_2CF_2)n$	–	Sigma-Aldrich
Potassium hydroxide	KOH	90%	Sigma-Aldrich
Potassium permanganate	$KMnO_4$	99%	Sigma-Aldrich
Propylene carbonate (PC, anhydrous)	$C_4H_6O_3$	99.7%	Sigma-Aldrich
Sodium borohydride	$NaBH_4$	99.99%	Sigma-Aldrich
Sodium nitrate	$NaNO_3$	99%	Sigma-Aldrich
Sodium sulfate (anhydrous)	Na_2SO_4	99%	Sigma-Aldrich
Sulfur	S	99.5%	Sigma-Aldrich

Sulfuric acid	H_2SO_4	95–98%	Sigma-Aldrich
Tetrabutylammonium borohydride ($TBABH_4$)	$(CH_3CH_2CH_2CH_2)_4N(BH_4)$	98%	Sigma-Aldrich
Tetraoctylammonium bromide (TOAB)	$[CH_3(CH_2)_7]_4N(Br)$	98%	Sigma-Aldrich
Tin	Sn	99%	Sigma-Aldrich
Tin(II) chloride dihydrate	$SnCl_2 \cdot 2H_2O$	98%	Sigma-Aldrich
Toluene (anhydrous)	$C_6H_5CH_3$	99.8%	Sigma-Aldrich

2.2 Material preparations

In this thesis, four different approaches are mainly applied to prepare various nanomaterials for lithium-ion batteries or lithium sulfur batteries: chemical vapor deposition; wet-chemical synthesis; a polymerization method; and a hydrothermal method.

Chemical vapor deposition is an extremely versatile technique using different chemical vapors as resources carried by high purity gases or mixed gases to produce high-purity, high-performance and uniform solid materials. An illustrated scheme is shown in Figure 2.2 and the quartz tube furnace is shown in Figure 2-3. There are mainly three kinds of CVD processes: atmospheric pressure chemical vapor deposition (APCVD); low pressure chemical vapor deposition (LPCVD); and water assisted or plasma assisted chemical vapor deposition (WACVD, PACVD). Normally, CVD precursors should hold several features, like high vapor pressure, ease of decomposition and being non-active to carrying gases. The typical precursor materials used for synthesizing graphene, carbon nanotubes or graphene-based nanocomposites are those like acetylene, methane and ethanol. The corresponding CVD processes can be categorized into the following: carbon coating, vapor-solid mechanism, dissolution-deposition-growth mechanism, tip-growth mechanism and bottom-growth mechanism. For carbon coating, most metal/metal oxides are able to decompose precursors or attract carbon atoms, and form a thin layer on the surface in limited duration time. For the vapor-solid mechanism, Si nanoparticles can be uniformly prepared via this method with SiH_4 as precursor. For the dissolution-deposition-growth mechanism, graphene nanosheets catalyzed by coral-like Fe can be achieved with a continuous supply of acetylene. For tip-growth and bottom-growth, different catalysts (Co, Ni and Fe), with competing carbon atom diffusion rates, can generate different types of carbon nanotubes with catalysts on the tip or at the bottom.

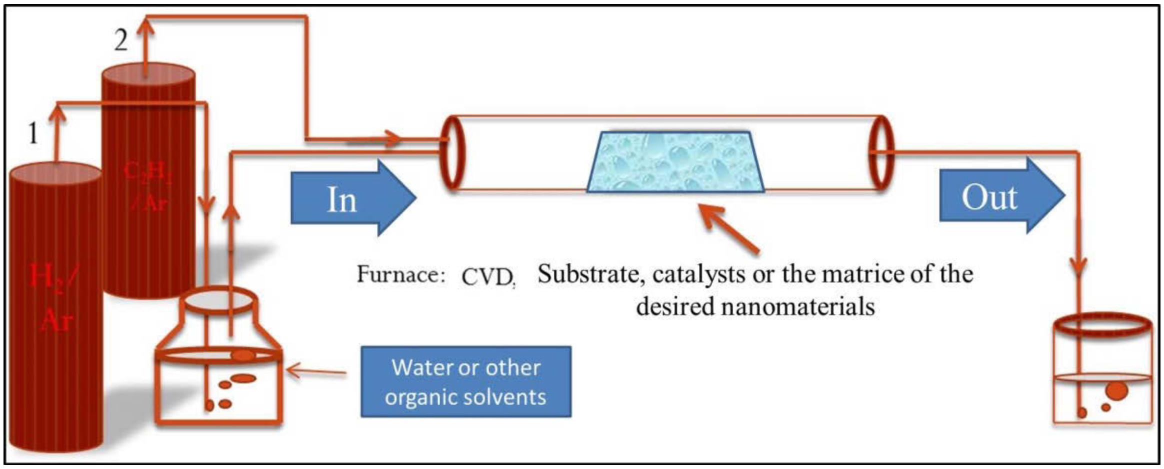

Figure 2- 2 The scheme for chemical vapor deposition with different gases supply and special furnace design.

Figure 2-3 The quartz tube furnace with additional gas routes and cooling system

Wet-chemical synthesis is used for preparing nanomaterials in aqueous solution, and the morphologies are controlled by adding different hydrophobic/hydrophilic solvent agents, further treated in a Muffle furnace, as shown in Figure 2-4. The polymerization process is applied to synthesize conductive polymers as chemical absorption forces to lithium polysulfides in lithium sulfur batteries. The hydrothermal method is carried out by microwave-assisted single-mode synthesizer with an accurate control of pressure and temperature, as shown in Figure 2-5, preparing graphene-based nanocomposites or porous nanomaterials. The details for synthesizing different kinds of nanomaterials will be specifically described in particular chapters.

Figure 2-4 Muffle furnace.

Figure 2- 5 Single-mode microwave synthesizer with pressure and temperature controllers

2.3 Material characterizations

2.3.1 X-ray diffraction analysis

X-ray diffraction, a non-destructive, effective and versatile technique, relies on the dual wave/particle nature of X-rays to obtain information about the structure of crystalline materials, including atomic arrangement, crystal size, and imperfections. Figure 2-6 shows the schematic illustration of the phenomenon of XRD, demonstrating that the atomic planes of a crystal cause an incident beam of X-rays to interfere with one another as they leave the crystal, which is determined by Bragg's Law. Bragg's Law is expressed by the equation:

$$2d\sin\theta = n\lambda \qquad \text{Equation 2-1}$$

In the equation, d is the space distance between diffracting planes, θ represents the incident angle, n is any integer, and λ is the wavelength of the X-ray beam. As-obtained XRD patterns of particular nanomaterials can be compared with the standard database (JCPDS cards) and matched to possible catalogues and phases. Moreover, the particle size of as-prepared nanomaterials can be estimated according to the Scherrer equation:

$\tau = K\lambda / \beta\cos\theta$ Equation 2-2

Where τ is the mean size of the ordered domains (either smaller or equal to the actual size); K is a dimensionless shape factor. Normally, it has a typical value of 0.89, but it is varied with different actual shapes of crystallite. λ is the X-ray beam wavelength. θ is the aforementioned Bragg angle. β is the line broadening at full width at half maximum. All the XRD patterns in this doctoral work are obtained on the Siemens D5000 diffractometer, which facilitates automatic measurements up to 40 samples, and the instrument is operated at 40 KV and 30 mA with a monochromatized Cu Ka radiation (where λ is equal to 0.15406 nm) at a scan speed of 1 degree per min. Optical photo of the XRD instrument is shown in Figure 2-7.

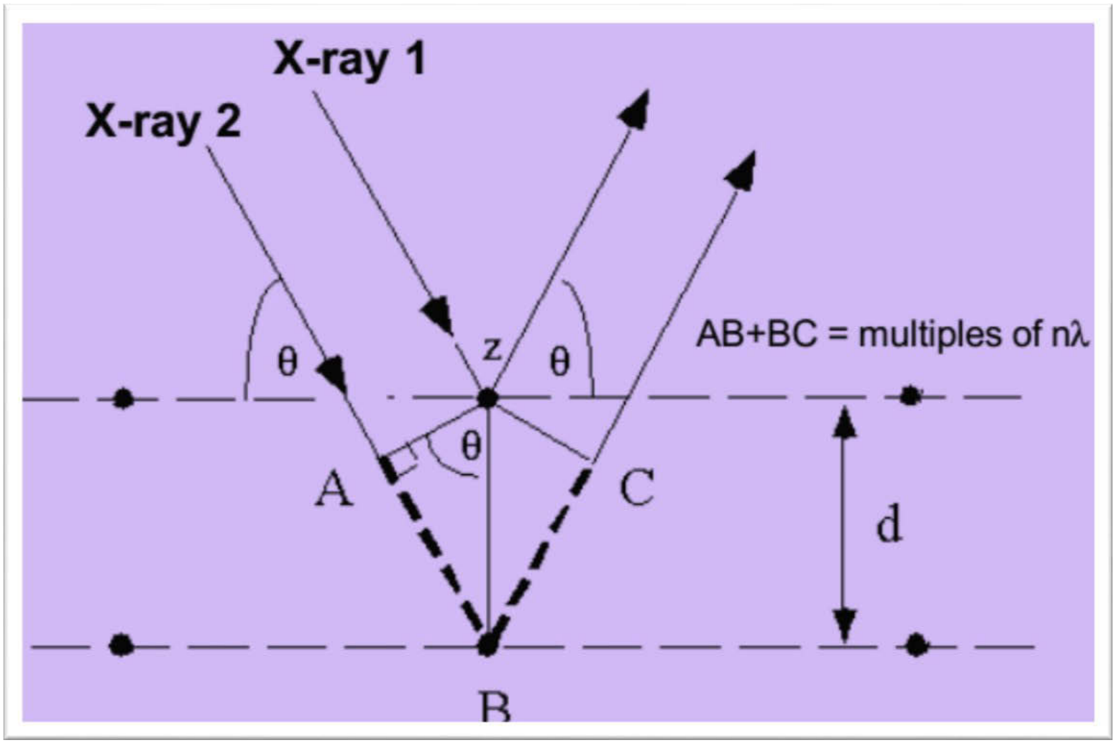

Figure 2- 6 Scheme for the theory of Bragg's Law.[71]

Figure 2- 7 Siemens D5000 diffractometer for XRD measurements.

2.3.2 Brunauer Emmer Teller

Brunauer-Emmer-Teller method, proposed by Stephen Brunauer, Paul Hugh Emmett, and Edward Teller in 1938, served to measure the physical adsorption/desorption of gas molecules on the surface of solid materials in order to measure a specific area.[72] The BET theory is recognized as deriving from the Langmuir theory, yet considers multilayered gas molecular absorption, which benefits the measuring of mesoporous nanomaterials with multilayered architecture. The surface area by BET method is achieved by measuring the nitrogen adsorption at liquid nitrogen temperature before the materials are completely dried with heat and vacuum. The instrument used in this doctoral work, shown in Figure 2-8, is a 3 Flex surface characterization analyser produced by Micromeritics with three available ports, using a Quadrasorb SI analyser at 77 K. The as-obtained surface area was evaluated by the experimental points at a relative pressure of P/P_0=0.05–0.25. The pore size distribution was calculated by the Barrett–Joyner–Halenda (BJH) method.

Figure 2-8 The 3 Flex surface characterization analyser instrument produced by Micromeritics.

2.3.3 Raman spectroscopy

Raman spectroscopy, named after C. V. Raman, is a non-destructive and fast-detecting spectroscopic technique, relying on a laser in a range of visible, near infrared, and near ultraviolet to observe vibrational, rotational and other low-frequency modes. The specific vibrational information obtained in Raman spectroscopy is specific to the molecules' chemical bonds and symmetry, which provide sufficient information to identify a specific molecular. In this thesis, Raman spectroscopy is mainly used to detect the ordered or defected information of carbon nanotube and graphene, and their composites. Since it is based on the scattering technique, a specimen can be easily measured without excessive protection and can be placed on the surface of a silicon wafer or mica. Figure 2-9 illustrates a Renishaw inVia Raman spectrometer system, used for this thesis (Gloucestershire, UK), equipped with a Leica DMLB microscope (Wetzlar, Germany) and a 17 mW at 633 nm Renishaw helium neon laser.

Figure 2-9 The Renishaw inVia Raman microscope equipped with a Leica DMLB microscope (Wetzlar, Germany) and a 17 mW at 633 nm Renishaw helium neon laser.

2.3.4 Fourier transform infrared spectroscopy

Fourier transform infrared spectroscopy, using time-domain or space-domain measurements of electromagnetic radiation (especially infrared radiation), is used to perform qualitative and quantitative analysis of organic compounds or carbon based materials with organic groups. It can also confirm the chemical structure of many unknown organic compounds and materials based on the analysis of the fingerprint of those samples. The as-obtained spectrum represents the molecular absorption and transmission. FTIR spectra are obtained by Nicolet Magna 6700 FTIR spectrometer to analysis the oxidized graphite and the reduction of graphene oxide and the corresponding composites.

2.3.5 Ultraviolet-visible spectroscopy

Ultraviolet-visible spectroscopy, using electromagnetic radiation in the range of ultraviolet to visible and adjacent light, is a technique that acquires the absorption or reflectance spectroscopy. Molecules in specimens containing π-electrons or non-bonding electrons excite the electrons to higher anti-bonding molecular orbitals after absorbing the energy from the ultraviolet or visible lights. This technique is mostly used in analytical chemistry for qualitative measurements. The UV-vis absorption spectra, using the Beer-Lambert Law, in this thesis are measured by a Carry 300 UV/vis spectrophotometer.

2.3.6 Thermogravimetric analysis

Thermogravimetric analysis, based on the changes in physical and chemical properties with the increase of temperature, is a technique to determine the physical and chemical features of samples. The TGA instrument continuously measures the weight of a sample when the sample is heated to high temperature (800-1200 °C). The analysis of TGA plots can deduce the decomposed temperature of the sample and the weight increase or decrease percentages, which is extremely useful when confirming the percentage of carbon in electrode materials or the sulfur content in carbon-sulfur composites. In this doctoral work, the TGA instrument is Simultaneous TG-DTA (SDT 2960) with the alumina or platinum plates as the sample holder. The operating temperature range is between room temperature and 1000 °C in air or N_2 atmosphere with a temperature increase rate of 5-10 C min^{-1}.

2.3.7 Atomic force microscopy

Atomic force microscopy, equipped with a cantilever with a sharp tip to scan the specimen surface and a laser to reflect the vibration or movement of the sharp tip, is a kind of high-resolution scanning probe microscopy. There are three modes to image: contact mode, tapping mode and non-contact mode. In order to protect the tip, we normally use the tapping mode, and the laser beam deflection is collected by a position-sensitive detector. We apply this technique mainly to detect the thickness of graphene, which is obtained by either chemical-exfoliation or chemical vapor deposition method. The AFM measurements are performed on the Dimension 3100 SPM with a tapping mode.

2.3.8 Scanning electron microscopy

Scanning electron microscopy, invented by Manfred von Ardenne in 1937, relies on the detection of signals irritated by the electron beam to produce digital images with a high-resolution to around 1 nm. The electrons interact with surface atoms in the specimen, delivering various information about properties of samples, including morphologies, components and element percentages. Furnished with energy dispersive X-ray spectroscopy (EDS) detectors, the SEM instrument has the ability to perform elemental analysis.

Equipped with cathodoluminescence microscope (CL) systems, the SEM instrument can accurately distinguish the intensity and spectrum of electron-induced luminescence. Moreover, the SEM instrument can also merge a multi-piece color image with different signals into one signal color image, vividly illustrating the structure and composition of the specimen. The morphologies and elemental analysis of nanomaterials in this doctoral work are performed on the field emission scanning electron microscope (JSM-6700F, 20kV, and field emission SEM, Zeiss Supra 55VP with a voltage of 20kV and 20-30 mm aperture, as shown in Figure 2-10) with an in-lens secondary detector. Appropriate treatments, like depositing a thin carbon or gold layer on the surface, will be proceeded when the conductivity of specimens is low, such as sulfur and some polymer precursors.

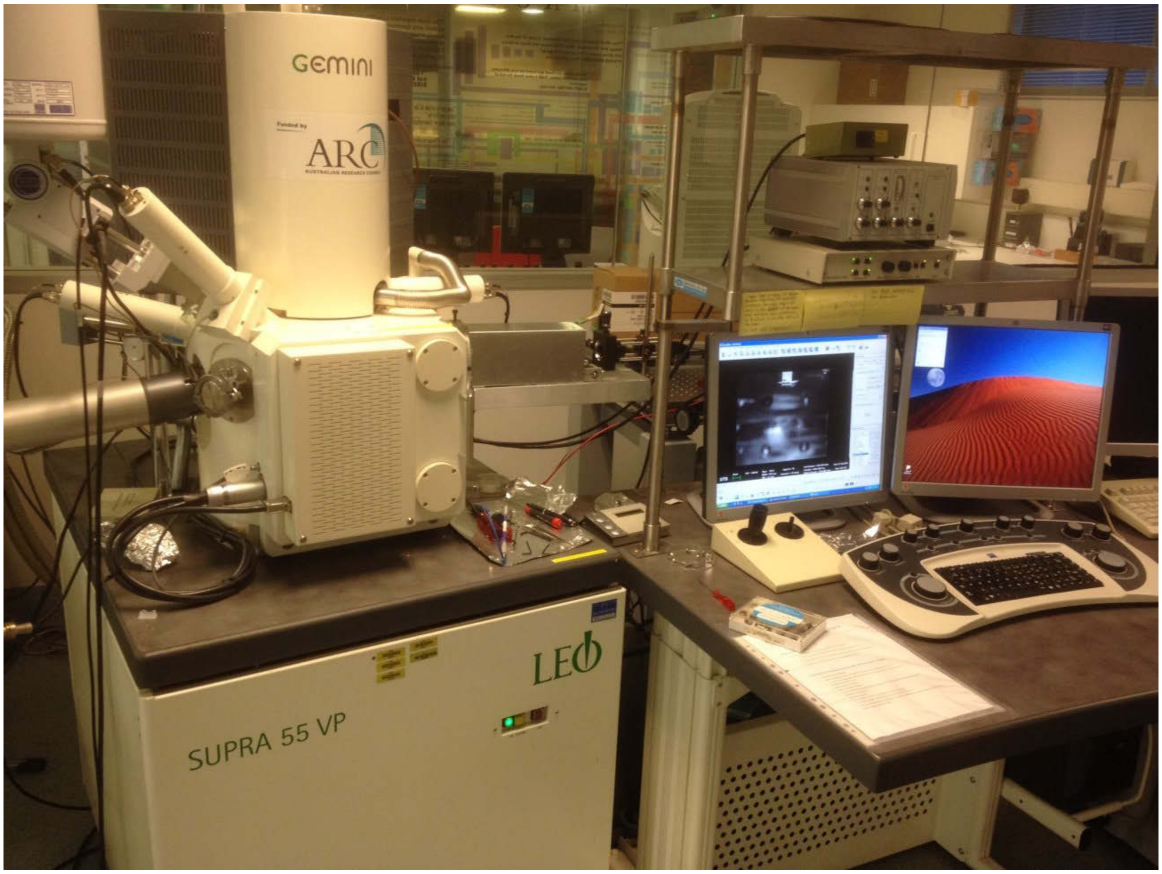

Figure 2-10 The field emission scanning electron microscopy in a mode of Supera 55 VP produced by Zeiss and equipped with EDS detector.

2.3.9 Transmission electron microscopy

The transmission electron microscopy was built by Max Knoll and Ernst Ruska in 1931—they also developed in 1933 the first TEM with a resolution higher than that of light—is a microscopy technique using a high-voltage beam of electrons transmitted through a thin specimen, and a sensor such as a CCD camera to detect the interacted electrons within the specimen. In this doctoral work, the transmission electron microscopy (TEM, JEOL JEM-2010FS) instrument is shown in Figure 2-11. It is equipped with energy dispersive X-ray spectroscopy detectors for elemental analysis, which is beneficial in confirming the components in the nanomaterials, especially for sulfur distribution in sulfur cathodes, and metal oxides anchored on graphene nanosheets. Moreover, the phase feature for crystalline samples can be captured by selected area electron diffraction (SAED), which can illustrate a pattern of dots for a single crystal or a series of rings for a polycrystalline or amorphous solid materials. The specimen preparation procedure follows a standard approach, diluting the specimen in ethanol or acetone. With the assistance of an ultrasonic wave, the specimens are quickly dropped onto the carbon supported films in copper grids. In order to discover the mechanism of charge/discharge in cells, rechargeable electrodes are sometimes re-observed by TEM and SEM to evaluate the morphology changes of those electrodes.

Figure 2- 11 TEM instrument (JEM-2010FS) equipped with EDX detector.

2.4 Electrode preparation and batteries assembly

2.4.1 Lithium ion batteries

The working electrodes for lithium ion batteries are made from 80 wt.% of active materials, 10 wt.% of the conductive agent (acetylene black), and 10 wt.% of the binder (polyvinylidene difluoride) in N-methyl-2-pyrrolidone (NMP). The mixture is stirred with an adjustable high-speed electric agitator, forming a black slurry. Then, the slurry is homogenously pasted using a doctoral blade onto Al foil for cathode or Cu foil for anode and dried in a vacuum oven at 80 ℃. To test the electrochemical performance, CR2032 coin cells are used and assembled in an argon-filled glove box (Mbraun, Unilab, Germany), in which both the moisture and oxygen contents are controlled to be less than 0.1 ppm. Lithium foil is used as the counter electrode and a porous polypropylene is used as separator. The electrolyte is 1M $LiPF_6$, which is dissolved in a 1:1 (weight ratio) mixture of ethylene carbonate and diethyl carbonate. A scheme to illustrate the components of lithium ion batteries is presented in Figure 2-12.

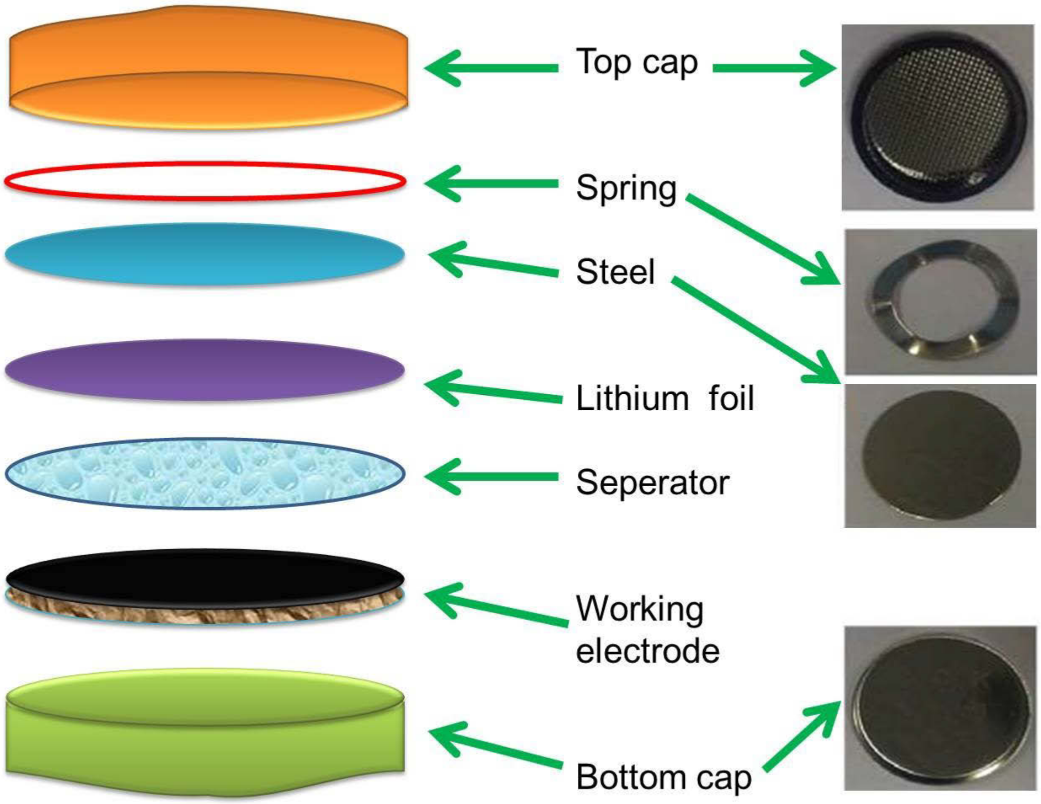

Figure 2-12 Schematic illustration for the components for lithium ion batteries.

2.4.2 Lithium sulfur batteries

The working electrodes for lithium sulfur batteries are also made from 80 wt.% of active materials, 10 wt.% of carbon black, and 10 wt.% of the binder (PVDF) dissolved in NMP solvent. The following steps are similar to the treatment of lithium ion batteries, such as stirring with an adjustable high-speed electric agitator to form black slurry, pasting onto to Al foil with a doctoral blade and drying in a vacuum oven at 80 ℃. The mass of each electrode on the aluminium current collector is around 2.5 mg/cm^2. The sulfur cathode and Li foil anode are assembled as CR2032 coin cells in an argon-filled glove box (Mbraun, Unilab, Germany), in which both the moisture and oxygen contents are controlled to be less than 0.1 ppm. Lithium foil is used as both the counter electrode and reference electrode. The electrolyte for Li-S batteries is composed of 1 M lithium bis(trifluoromethanesulfonyl) imide and 0.1M lithium nitrate ($LiNO_3$) in 1,3-dioxolane and 1,2-dimethoxyethane (volume ratio 1:1). Electrochemical measurements are performed on a LAND-CT2001C and Neware battery test system. The cells are galvanostatically discharged and charged in a voltage range of 1.7–2.6 V at a current density of 167.3 mA·g^{-1} (0.1 C). Higher current rates (0.5 C, 1 C, 5 C or 10 C) are also applied to evaluate the rate capabilities. The CV is measured on a CHI 660E electrochemical workstation at a scan rate of 0.1 mV·S^{-1}.

Figure 2-13 The argon-filled glove box (Mbraun, Unilab, Germany).

2.5 Electrochemical performance characterization

The electrochemical performances of lithium ion batteries and lithium sulfur batteries with different kinds of nanomaterials are mainly evaluated using three types of measurement approaches:

galvanostatic charge and discharge, cyclic voltammetry and electrochemical impedance spectroscopy.

2.5.1 Galanostatic charge and discharge

Two important factors to evaluate the performances of one battery are the specific capacity and cyclability, which can be measured by the galvanostatic charge/discharge method. This method is conducted at a constant charge/discharge current density. The specific capacity is calculated with the following equation:

$$C = Q/m = (I*t)/m$$

Where Q is the charge/discharge capacity, I is the current value, t is the charge/discharge time and m is the mass of the electrode. The cyclability can be evaluated with the capacity retention ratio after one particular period. The cut-off voltage (anode materials) for lithium ion batteries of galvanostatic testing is 0.01-3 V, and the cut-off voltage of sulfur cathode for lithium sulfur batteries is 1.7-2.6 V. In order to test the electrochemical properties of nanomaterials at high current rates, step-wise current densities are applied to electrodes. The galvanostatic charge/discharge measurements are performed on a computer-controlled Neware battery test system and Land battery test machines, as shown in Figure 2-14.

Figure 2- 14 The computer-controlled Neware battery test system.

2.5.2 Cyclic voltammetry

Cyclic voltammetry is a typical potentiodynamic electrochemical measurement that captures information about potential, current, impedance and time etc. CV in the electrochemistry area is usually applied in order to study the electrochemical behaviors of the electrodes versus the reference electrode at different reaction positions. For instance, the CV method is used to reveal the reaction behaviors at different potentials, which can be compared with the charge/discharge profiles by the galvanostatic charge/discharge approach. The instrument used for CV is an electrochemical workstation produced by CH instruments, as shown in Figure 2-15.

Figure 2-15 The CH instruments (CHI 660D) for CV and EIS testing.

2.5.3 Electrochemical impedance spectroscopy

Electrochemical impedance spectroscopy, also known as dielectric spectroscopy, is an effective experimental method to characterize electrochemical behaviors. The impedance of a system is measured using this technique over a series of frequencies, which is often expressed graphically as a Nyquist plot. The EIS technique can provide much information about reaction mechanisms during electrochemical processes. Ohmic resistance R_{Ω} can be revealed in series after measurements of electrode impedances during cycles, which is shown by the schematic Nyquist plots. The electrochemical impedances of electrodes of both lithium ion batteries and lithium sulfur batteries are all measured before and after a cycling test to compare the changes of electrochemical resistances of the electrodes, which can provide estimations on the changes of internal resistance (electrolyte resistance and charge-transfer resistance). The EIS technique is an effective and helpful tool to further understand the internal electrochemical processes and explain corresponding electrochemical phenomena. In this doctoral thesis, EIS data are also collected on a CHI 660 D electrochemical workstation (as shown in Figure 2-15).

CHAPTER 3 TIN-GRAPHENE NANOCOMPOSITES FOR LITHIUM ION BATTERIES

3.1 Introduction

Lithium-ion batteries are widely used as the power sources for portable electronic devices, owing to their high energy density, high voltage and long cycle life than other rechargeable batteries. The electrochemical performances of lithium ion batteries are determined by both cathode materials and anode materials. For large-scale applications such as electric vehicles, new electrode materials must be developed to meet the increasing demand for high energy density and power density.

Carbon-based materials are the commercial anode materials for Li-ion batteries [49] with a limited theoretical capacity of 372 mAh g^{-1}, which cannot meet the demand for high specific capacities. Metal and metal oxides, such as silicon (Si) [73], tin (Sn) [74], cobalt oxide (Co_3O_4) [75-79], and nickel oxide (NiO) [78-81], have been considered as promising alternative anode materials for reversible lithium storage. In particular, metallic tin and tin based anode materials [82-86] are one of the attractive replacement materials for lithium ion batteries due to their high theoretical capacity ≥ 992 mAh g^{-1}. On the other hand, tin and tin based anode materials do not encounter solvent intercalation during discharge/charge cycling, leading to greatly reduced irreversible capacity loss, while large volume variation always occurs in tin based anode materials during lithiation and de-lithiation processes, which causes pulverization of the electrode [87-89]. In order to overcome this problem, many methods have been developed to buffer or prevent volume changes such as CNTs-encapsulation [88, 90], formation of core-shell nanostructures [73, 91-94], and decrease of particle size [95].

Graphene, discovered by Geim [19] in 2004, is an allotrope of carbon with a structure of one-atom-thick planar sheet of sp^2-bonded carbon. Many studies have demonstrated that graphene posesses outstanding physical, chemical and mechanical properties [96-100]. It has been proved that lithium ions could be absorbed on the two sides of graphene nanosheet, which increases the theoretical capacity to 744 mAh g^{-1}, according to the formation of Li_2C_6. [101-105] Graphene nanosheet (GNS)-based materials have been investigated for lithium storage. Ji and co-worker [106] prepared a multilayer nanoassembly of Sn-nanopillar with graphene, which formed three-dimensional (3D) structure without polymer binder and carbon black. The initial reversible specific capacity reached 734 mAh g^{-1}. The specific capacity maintained 679 mAh g^{-1} after 30 cycles. Li and coworkers [107] reported that graphite oxide (GO) was simply reduced by Sn^{2+} ion, forming SnO_2/graphene anode materials with different weight ratios. It was found that different ratios between Sn^{2+} and GO led to different morphologies and specific capacities. In particular, the specific capacity reached 541.3 mAh g^{-1} at a current density of 200 mA g^{-1} in a voltage range of 1.5 V - 0.01 V. Kim and co-workers [108] developed a SnO_2/graphene composite via loading Sn particles on GO, then reduced by NH_4OH and hydrazine at 80 ℃ for 8 h. The first reversible specific capacity was about 852 mAh g^{-1} and retained 634 mAh g^{-1} after 50 cycles at a current density of 100 mA g^{-1} between 0.001 V and 3.0 V. When the current density was increased to 2000 mA g^{-1}, the reversible specific capacity was 389 mAh g^{-1}.

Microwave-assistant hydrothermal synthesis (MAHS) method has many advantages such as fast heating, high yield rate, and good homogeneity. Both cathode and anode materials for lithium ion batteries with novel structures and special morphologies have been prepared by the MAHS method and demonstrated improved properties.[109-111] Most of previous reports involved in the preparation of SnO_2-graphene nanocomposites. Zhong et al. synthesised SnO_2-graphene composites and achieved a stable capacity of 590 mA g^{-1} at a current density of 100 mAh g^{-1}.[111] Zhu and coworkers developed SnO_2-graphene composites, in which tin oxide particles (100-200 nm) were uniformly anchored on the surface of graphene.[112] Herein, we report a simple and novel synthetic route to prepare Sn-graphene nanocomposites using a combination of microwave hydrothermal reaction and H_2 reduction. The homogeneous dispersion of Sn nanoparticles on graphene nanosheets were achieved by the MAHS method. The as-prepared Sn-graphene nanocomposites exhibited a better electrochemical performance for lithium storage in lithium ion batteries than that of the previously reported results.

3.2 Experimental

3.2.1 Preparation of Sn-Graphene nanocomposites

Graphene oxide (GO) was prepared according to the previously published procedure[113]. Two batches of Sn-graphene nanosheets (Sn-GNS) composites were synthesized with weight ratios of 1:1 and 1:4, which are defined as Sn-GNS-1 and Sn-GNS-2, respectively. For the preparation of Sn-GNS composites, 20 mL 0.0072 M $SnCl_4 \cdot 5H_2O$ aqueous solution was added into the two certain amount of GO (14 mL and 56 mL, 2mg mL^{-1}) solutions. After mixing by ultrasonic probe for 1h, then the solutions were transferred to another beaker, and excessive amounts of urea was added into the solutions, Then, the solutions were heated in the single mode of microwave reactor (NOVA I microwave synthesizer with a magneton stirring and monitoring the real preasure in the vessel) at 120 °C for 20 min, the predecessors of SnO_2-GO were obtained. The precipitates were collected by centrifugation and washed with de-ionized water for several times. The dried precursors (SnO_2-GO-1 and SnO_2-GO-2) and GO were heated at 300°C for 2h in a quartz tube furnace under a flowing gas mixture of H_2 in N_2 (H_2: 10%, N_2: 90%) at a flow rate of 80 sccm, respectively. The actual ratios of tin : graphene have been determined by the CHN elemental analysis. The Sn-GNS-1 consists of 51.4 wt% carbon, which is close to the weight ratio Sn:C = 1:1. The Sn-GNS-2 sample consists of 80.7 wt% carbon, corresponding to the weight ratio Sn:C = 1:4.

3.2.2 Characterization of Sn-Graphene nanocomposites

Sn-graphene nanocomposites and GNS were characterized by X-ray diffraction (XRD, Rigaku D/max-2550V, Cu Kα radiation), field-emission scanning electron microscopy (FE-SEM, JSM-6700F), and transmission electron microscopy/selected area electron diffraction (TEM/SAED, JEOL JEM-200CX and JEM-2010F).

3.2.3 Electrochemical measurements

For electrochemical testing, the working electrodes were made by mixing 80 wt. % active material, 10 wt. % acetylene black, and 10 wt. % binder (polyvinylidene difluoride) in NMP to form a slurry. Then, the slurry was coated on copper foil and dried in a vacuum oven at 65 °C for 12h. Swagelok cells with a diameter of 12 mm were assembled in an argon-filled glove-box (Mbraun, Unilab, Germany), in which both the moisture and oxygen contents were controlled to be less than 0.1 ppm. Lithium foil was used as the counter electrode and the electrolyte was 1M $LiPF_6$ in a 1:1 (weight ratio) mixture of ethylene carbonate and diethyl carbonate. Electrochemical measurements were performed in a LAND-CT2001C battery test system. The cells were galvanostatically discharged and charged in the fixed voltage range of 0.005-3.0 V, with a current density of 80 mAh g^{-1} (0.1 C). Higher current densities (0.5 C, 1 C, 2 C and 5 C) were also used to test the high rate capability.

3.3 Results and discussion

The properties of the graphene oxide (GO), SnO_2-graphene oxide (SnO_2-GO), Sn-GNS-1, and Sn-GNS-2 were characterized by X-ray diffraction (XRD) and the XRD patterns were showed in Figure 3-1. The characteristic peak of graphene oxide at 11.5° corresponds to the (002) planes of graphite oxide, indicating that the interplanar spacing of d_{002} had been expanded to 0.769 nm after oxidation. This is ascribed to the oxygen-containing functional groups that were attached, which has been previously confirmed by FTIR[32]. After heating by a single mode of microwave, the precursors were converted to SnO_2-GO, the characteristic peaks of GO were reserved and the other diffraction peaks can be indexed to the tetragonal rutile SnO_2 phase with lattice parameters a=4.738 Å and c=3.188 Å (JCPDS 21-1250). The broad diffraction peaks of SnO_2 indicate that the SnO_2 particles have small crystal size. The third and the firth XRD patterns are Sn-GNS nanocomposites with weight ratios of 1:1 and 1:4, respectively. The sharp diffraction lines reflect good crystallite of Sn obtained by H_2 reduction, moreover, he characteristic (002) diffraction peak of GO has shifted from 11.4° to 26.3°, confirming the reduction of graphene oxide to graphene nanosheets.

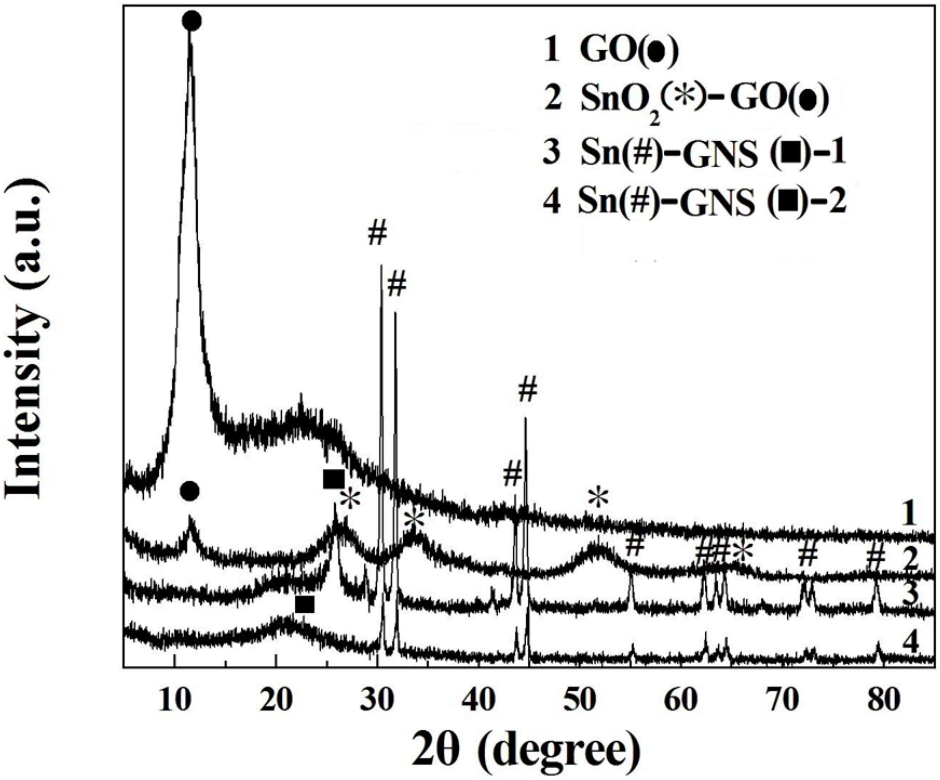

Figure 3- 1 Powder X-ray diffraction (XRD) patterns of graphite oxide (GO), SnO_2-graphene oxide (SnO_2-GO), Sn-graphene nanosheets (Sn-GNS-1), Sn-graphene nanosheets (Sn-GNS-2).

A schematic representation of the synthesis process was given, which can be observed in Figure 3-2. The natural graphite powders were oxidized and exfoliated to graphene oxide by using the modified Hummers method [114]. When $SnCl_4$ and urea were added into graphene oxide solution, Sn^{4+} ions attached to the both sides of the basal plane of graphene oxide nanosheets, owing to the negatively charging nature of graphene oxide. Under microwave irradiation at 120℃, $Sn(OH)_4$-GO precursors were formed initially and then converted to SnO_2-GO due to the effect of microwave energy. During the heat treatment in H_2 atmosphere, GO and SnO_2 nanoparticles were simultaneously reduced by H_2 at 300℃ to GNS and Sn nanoparticles. Therefore, the one-step H_2 reduction [115-117] can produce Sn-GNS nanocomposites with a uniform distribution of Sn nanoparticles on GNS.

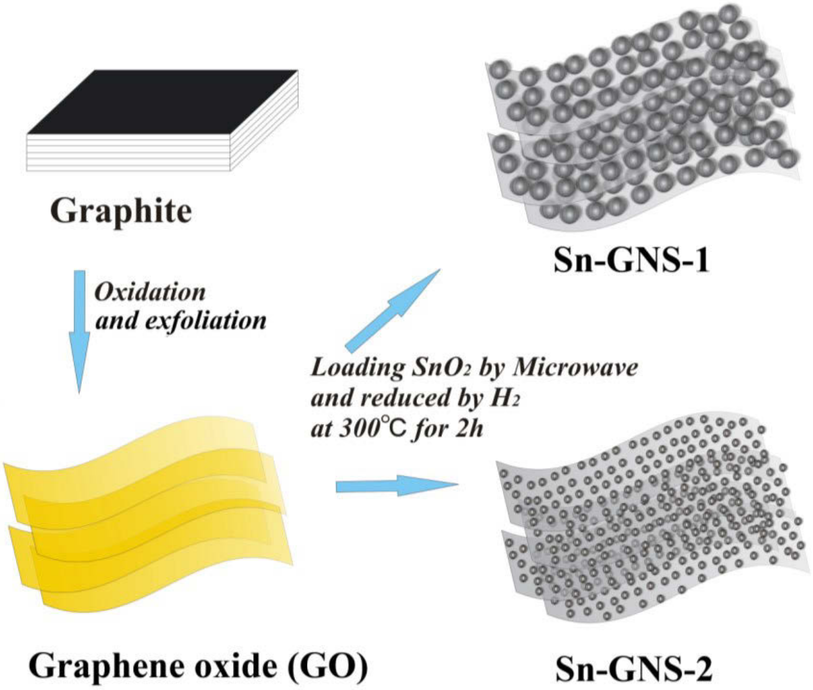

Figure 3- 2 A schematic illustration for the preparation process of Sn-graphene nanosheets (Sn-GNS) nanocomposites.

The morphologies of Sn-GNS nanocomposites were observed by FESEM (as shown in Figure 3-3). When the ratio of Sn and GNS was reduced to 1:4, smaller Sn nanoparticles with a uniform size of 10-20 nm were obtained (as shown in Figure 3-3b). Since the melting point of Sn nanoparticles is 231.9 ℃, SnO_2 nanoparticles were reduced to Sn nanoparticles by H_2 at 300℃, since Sn droplets adopt the sphere-like shape with the influence of the surface tension. Meanwhile, GO and SnO_2 nanopariticles were reduced simultaneously, which would be advantageous in maintaining the stability of the Sn-GNS nanocomposites.

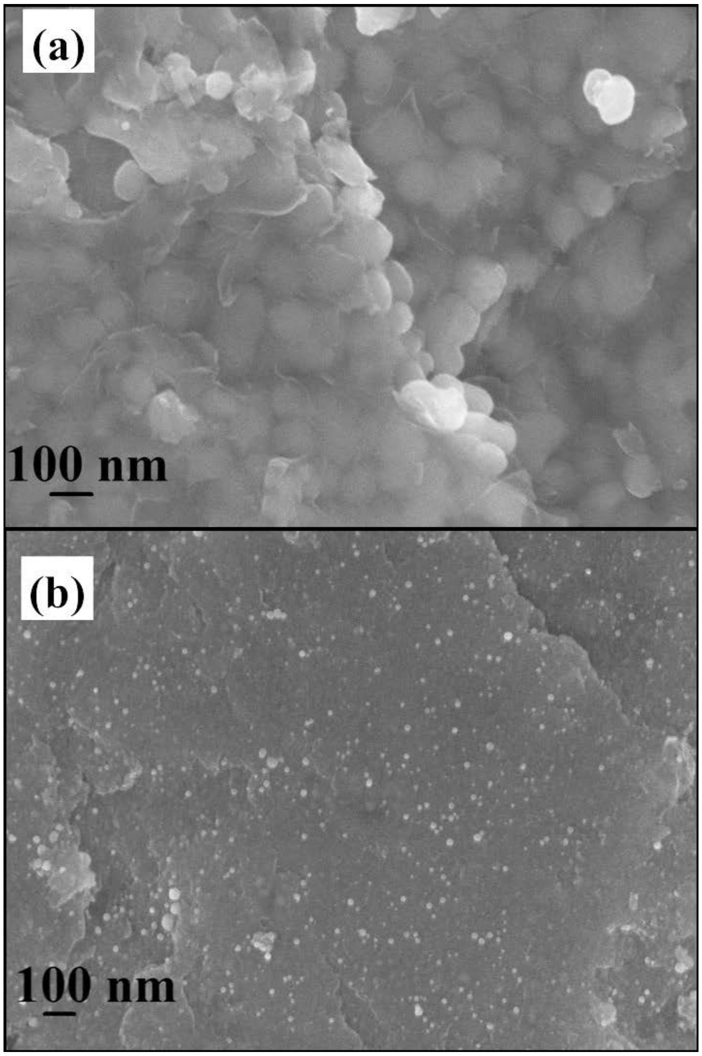

Figure 3- 3 SEM images of Sn-graphene nanosheets nanocomposites: (a) Sn-graphene nanosheets (Sn-GNS-1), (b) Sn-graphene nanosheets (Sn-GNS-2).

In order to characterize the microstructure of GNS, transmission electron microscope (TEM) and high resoultion transmission electron microscope (HRTEM) were used and the images of GNS were showed in Figure 3-4(a) and (b), respectively. Under the electron beam, GNS exhibit a transparent feature with a winkle structure and a thickness of 3-5 nm, which corresponds to ~ 8-15 layers of single graphene nanosheets stacking together. The high magnification TEM images of Sn-GNS-1 (with a weight ratio of 1:1) nanocomposite were exhibited in Figure 3-4(c) and (d). The Sn particles, with the diameters of 60-120 nm, scattered on the surfaces of graphene nanosheets. A large amount of Sn nanoparticles, with diameters of 10-20 nm, were also observed on the surfaces of GNS. Under the heat treatment at 300 ℃, Sn nanoparticles become spherical with some aggregations. Furthermore, the aggregation phenomenon may also result from the high ratio of Sn-GNS (1:1), however, when the weight ratio of Sn and GNS was reduced to 1:4, the Sn nanoparticles obtained are much smaller and uniformly distributed on graphene nanosheets (as shown in Figure 3-4(e) and (f)).

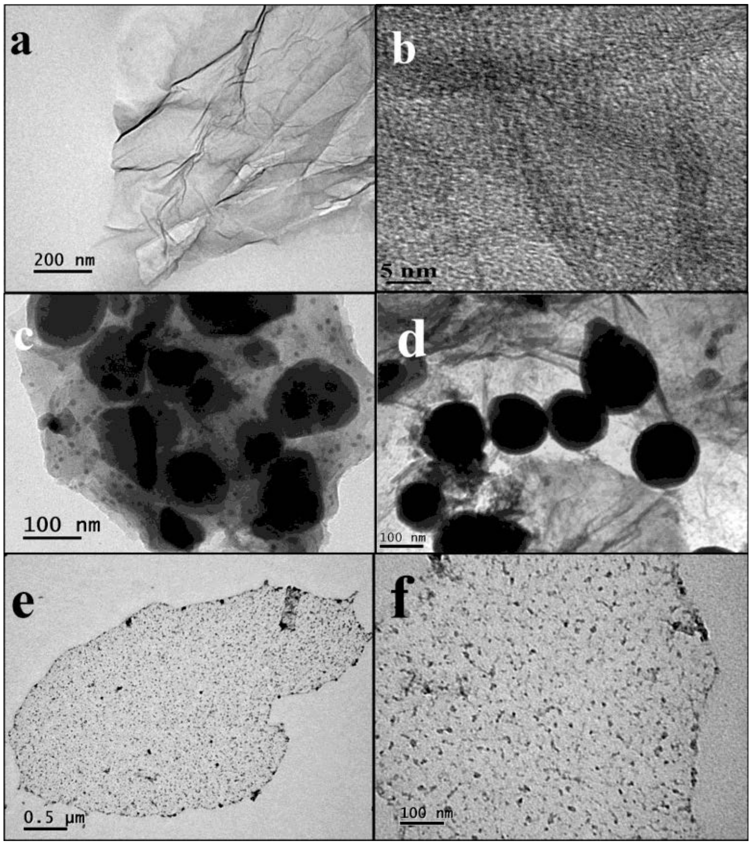

Figure 3- 4 (a) TEM image of graphene nanosheets (GNS), (b) HRTEM image of graphene nanosheets (GNS), (c-d) TEM images of Sn-graphene nanosheets (Sn-GNS-1), (e-f) TEM images of Sn-graphene nanosheets (Sn-GNS-2).

The electrochemical performances of GNS and Sn-GNS nanocomposites were tested by galvanostatical charge and discharge cycling in the voltage range of 0.005-3V (at a current density of 80 mA g^{-1}). Figure 3-5(a) shows the voltage profiles of GNS, Sn-GNS-1 and Sn-GNS-2 electrodes in the first cycle. The initial discharge and charge capacities of the GNS electrode are 1787 mAh g^{-1} and 904 mAh g^{-1}, corresponding to a Coulombic efficiency of 50.6%. The high lithium storage capacity could be attributed to a large number of active sites such as edge-type sites, nano-cavities, or other defects in graphene nanosheets. There is a considerable capacity loss in forming solid electrolyte interphase (SEI) layers on the surface of GNS. The Sn-GNS-1 and Sn-GNS-2 electrodes delivered discharge capacities of 1776 and 2136 mAh g^{-1} and the charge capacities of 1206 and 1407 mAh g^{-1} with the Coulombic efficiencies of 67.9% and 65.9%, respectively. The high specific capacities of Sn-GNS composites could be ascribed to the contributions of Sn nanoparticles and the 3D stacking structure. There are a large amount of defects or nano-cavities in GNS induced during the oxidation and reduction processes. It has been proposed that Li^+ ions could be adsorbed either on the surface or on the edge planes of the GNS.[118] In the first cycle, the irreversible capacities loss for Sn-GNS-1 and Sn-GNS-2 electrodes could be caused by the formation of the SEI layers on the surface of the electrodes, the large volume expansion of Sn nanoparticles, different content of Sn nanoparticles, and different surface areas of Sn-GNS nanocomposites. Moreover, the small plateaus at the end of the discharge process for Sn-GNS-1 and Sn-GNS-2 electrodes should be ascribed to the reaction of lithium with Sn nanoparticles. This phenomenon has been reported in the previous publications [94, 119]. The cycle performances of the GNS, Sn-GNS-1 and Sn-GNS-2 samples are shown in Figure 3-5(b). After 30 cycles, the specific capacities of GNS, Sn-GNS-1 and Sn-GNS-2 electrodes are 582 mAh g^{-1}, 771.8 mAh g^{-1} and 1100 mAh g^{-1}, respectively. These correspondes to the capacity retention ratios of 64.3%, 63.9% and 78.1%. Therefore, Sn-GNS-2 electrode demonstrated the best cycle performance. The better cycling performance of the sample Sn-GNS-2 could be attributed to small Sn nanoparticles and the synergistic effect of the Sn-GNS 3D nanoarchitecture. Sn nanoparticles with a high theoretic specific capacity of 992 mAh/g provide most of the capacities, and GNS with a low Coulombic efficiency of 50% only offer 40% of capacities. The volume change of Sn nanoparticles can be effectively buffered by flexible graphene nanosheets, which maintains the integrity of the electrode on charge and discharge cycling. In order to examine the tolerance of the Sn-GNS nanocomposite electrode towards different current densities, the Sn-GNS-2 electrode was cycled at different current densities (0.1 C, 0.5 C, 1 C, 2 C, and 5 C) and reversed back to low current densities (Figure 3-5(c)). As expected, the capacity decreases with increasing current densities. It should be noted that when the current density was reversed back to a low current density, the capacity almost recover to the original value. This indicates that the Sn-GNS nanocomposites are quite tolerant to the high current charge and discharge.

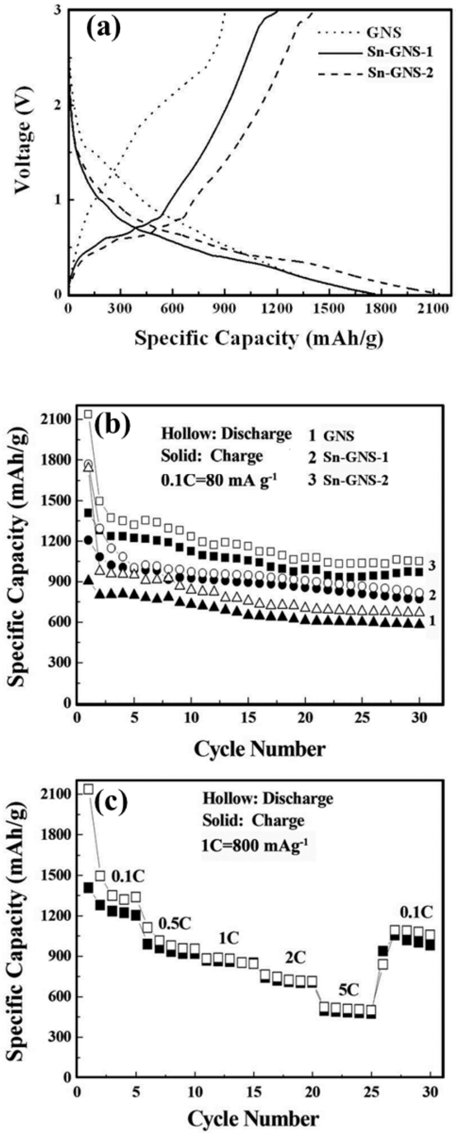

Figure 3- 5 Electrochemical performances of graphene nanosheets and Sn-graphene nanosheets nanocomposites, (a) The first cycle discharge (lithium insertion) and charge (lithium extraction) curves of the three materials, (b) Cycling performances at 0.1 C of GNS, Sn-GNS-1 and Sn-GNS-2, (c) Cycling performance at stepwise current densities of Sn-GNS-2.

The voltage profiles of Sn-GNS-2 nanocomposite electrode at different current densities in the first cycle can be seen in the Figure 3-6(a). The electrode delivered specific discharge capacities of 1247, 1106, 946 and 876 mAh g^{-1} at current densities of 0.5 C, 1 C, 2 C and 5 C, respectively. After 30 cycles, the specific capacity of Sn-GNS-2 at a current density of 1600 mA g^{-1} maintained at 542 mAh g^{-1} and the reversible capacity at a current density of 4000 mA g^{-1} maintained at 423 mAh g^{-1}. The shapes of voltage profiles are similar for four pairs of discharge and charge curves. In order to further illustrate the cycle performances of Sn-GNS-2 nanocomposite electrode at different current densities, the electrochemical cycle performances are tested and showed in Figure 3-6(b). The Sn-GNS nanocomposites electrodes have demonstrated a good rate performance under high current charge and discharge cycling. The capacity and retention ratio of Sn based materials are comparied in Table 3-1.

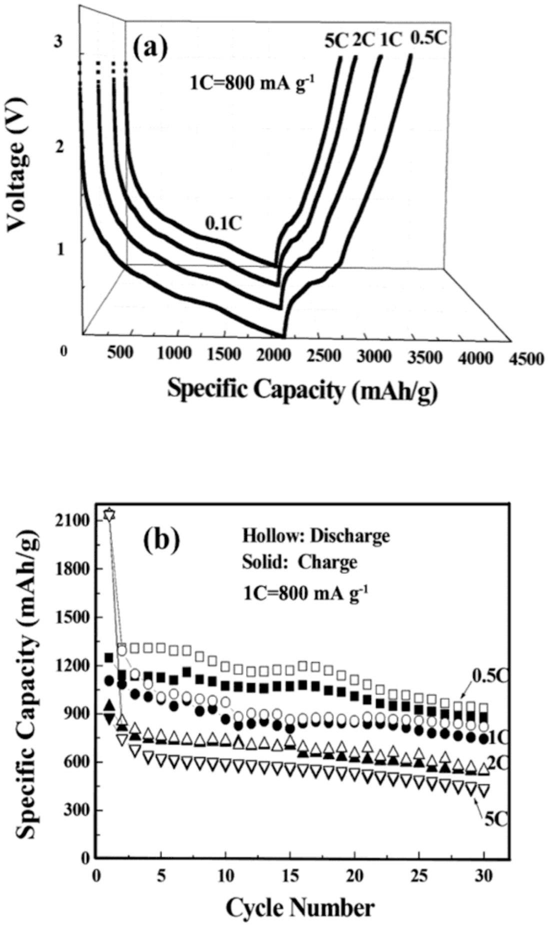

Figure 3- 6 The first cycle discharge and charge curves at large current densities of 0.5 C, 1 C, 2 C and 5 C of Sn-GNS-2, (f) Cycling performances at large current densities of Sn-GNS-2.

Table 3- 1 The comparison of electrochemical performances of different Sn-graphene basd materials

Materials	Initial capacity (mAh/g)	Final capacity (mAh/g)	Retention ratio (mAh/g)	Rate capacity (mAh/g)
Sn/graphene[106]	734	679	92% (30 cycles)	576 (1 A)
SnO_2/graphene[120]	541.3	377	69.3% (30 cycles)	---
SnO_2/graphene[108]	852	634	74% (50 cycles)	389 (2 A)
This thesis	1407	1100	78.1% (30 cycles)	423 (4 A)

After 30 cycles, the Sn-GNS electrodes were examined by TEM analysis. The TEM images of two Sn-GNS nanocomposite electrode after cycling can clearly illustrate the properties of the two electrodes. From Figure 3-7(a), the pulverization and cracking of Sn nanoparticles can be easily identified. This could be due to relatively large particle size of Sn (60-120 nm) in the Sn-GNS-1 sample, which cannot endure large volume change on cycling. On the contrary, there is no apparent crack on Sn nanoparticles in the sample Sn-GNS-2 electrode after cycling test (as shown in Figure 3-7(b)), which could be credited to the much smaller size of Sn nanoparticles (5-15 nm). Therefore, it is essential to obtain small Sn nanoparticles and uniform distribution on GNS to achieve good electrochemical performance.

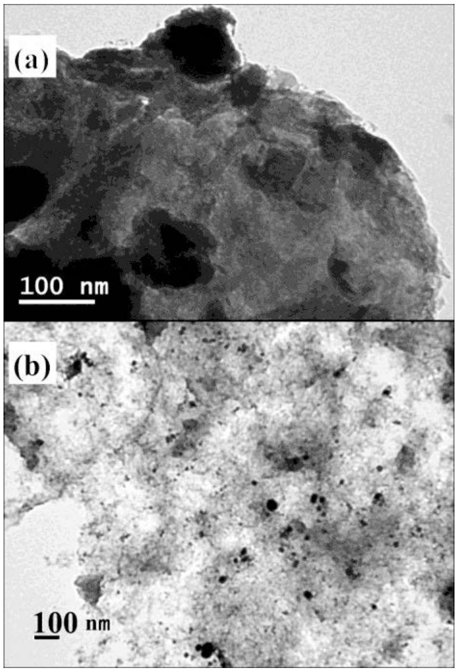

Figure 3- 7 (a) The TEM image of Sn-graphene nanosheets (Sn-GNS-1) after cycling test, (b) TEM image of Sn-graphene nanosheets (Sn-GNS-2) after cycling test.

3.4 Conclusions

We have developed a microwave hydrothermal synthesis approach for the preparation of Sn-GNS nanocomposites with different weight ratio using hydrogen gas reduction. Altering the weight ratio between tin and graphene has critical influences on their morphologies. Field emission scanning electron microscope and transmission electron microscope analysis reveals that tin nanoparticles homogeneously distribute on the surface of graphene nanosheets. There is no apparent pulverization and cracking of Sn nanoparticles for Sn-graphene nanosheets nanocomposite after cycling test. The Sn-graphene nanosheets with weight ratio of 1:4 (Sn-GNS-2) exhibits a high initial reversible specific capacity of 946 mAh g^{-1} at large current density of 1600 mA g^{-1} and a high specific capacity of 542 mAh g^{-1} has been maintained after 30 cycles, which demonstrates that the Sn-GNS-2 electrode has an excellent high rate capacity and a stable cycle performance. The superior electrochemical performance should be attributed to the high specific surface area of tin nanoparticles and the synergetic effect of the combination of Sn nanoparticles and highly conductive graphene nanosheets.

CHAPTER 4 GRAPHENE-CARBON NANOTUBES HYBRID MATERIALS FOR LITHIUM ION BATTERIES

4.1 Introduction

Carbon nanotube (CNT), one of the carbon allotropes, has been investigated for more than two decades since it was discovered by Ijima in 1991 [121], owing to its unique electrical, thermal, and mechanic properties [122-130]. The special sp^2 structure and eminent electrical properties lead to many technological applications, such as field-effect transistors [131], drug-delivery [132-133], hydrogen storage [134-135] and energy storage and conversion [136]. All of these applications require CNTs to be processed in bulk scale. The major approach is to dissolve or disperse CNTs in aqueous solution through chemical functionalisation [17-19], including esterification or amidation of oxidized nanotubes, and side-wall covalent attachment of functional groups. Nevertheless, acidic solution [137-138] (Sulphuric acid, Nitric acid), organic solvents [139-142] (N, N-dimethylformamide, N-methylpyrrolidinone, hexamethylphosphoramide, surface active agent) and toxic reagents[143-145] are commonly used to dissolve CNTs in aqueous solution. These are not environmentally friendly approaches to obtain homogenous and functionalised CNTs. Therefore, a chemical free technique is needed for processing CNTs.

Graphene, discovered by Novoselov and Geim in 2004 [19, 146-148], is a two-dimensional (2D) one-atom-thick planar sheet of sp^2-bonded carbon. Graphene is a promising material for energy storage due to its superior electronic conductivity, good thermal stability, remarkable structural flexibility, and high specific surface area [98, 149-150]. However, graphene nanosheets (GNS) tend to agglomerate in the dry state, which induces the loss of the merits of 2D GNS. Many methods have been developed to solve this problem, including the insertion of metal nanoparticles [151], combination with other carbon materials and *in-situ* growth of carbon nanotubes [152-154]. However, all of these techniques are environmentally unsound, requiring the use of strong oxidizing agents to treat CNTs [137, 155], toxic chemical reagents to produce metal oxides or high temperature and high pressure to grow carbon materials on graphene nanosheets.

Graphene oxide (GO) can be produced by exfoliation of chemically oxidized natural graphite in a large scale. GO, with the hydrophilic oxidation group, can be readily dispersed into water to form stable colloidal suspensions. Recent studies [156-159] have proved that it is possible to disperse multi-walled and single walled CNTs in aqueous solution via non-covalent interactions without any surfactant agents and polymer dispersants. By changing the weight ratio between GO and CNT, a hydrogel of GO/CNT can form, which indicates the strong π-π interactions. Herein, we report a chemical-free method to prepare graphene-carbon nanotube hybrid materials and application in lithium ion batteries. The dispersion of multi-walled carbon nanotubes in graphene oxide solution was achieved through π-π interactions. After reduced by thermal treatment, graphene-carbon nanotube hybrid materials were obtained, which have a uniform nanostructure. The as-prepared graphene-carbon nanotube hybrid materials demonstrated a good electrochemical performance in lithium ion batteries.

4.2 Experimental

4.2.1 Preparation of Graphene-CNT nanocomposites

Graphene oxides (GO) were prepared according to the previously reported procedure. [113] The multi-walled carbon nanotubes (MWCNTs, 10-20 nm) were purchased from Sigma-Aldrich, without any further treatment. In a typical synthesis process: 2 mg mL^{-1} graphene oxide colloid (20 mL) was ultrasonically treated for 1h and a certain amount of pristine MWCNTs was added into 20 mL de-ionized water and ultrasonically treated for 1h, respectively. Then the GO colloid solution was added into MWCNTs dispersion with the GO: MWCNTs weight ratios of 2:1 and 1:1. After then, the mixtures were treated by pulsed sonication for 2h (5s on and 5s off) in an ice bath using a Branson S-450D sonifier with a horn of 13 mm in diameter (40% amplitude). A homogenous and opaque brown aqueous dispersion was obtained for GO-MWCNTs with the weight ratio of 2:1. However, the precipitation occurred for GO-MWCNTs with the weight ratio of 1:1. The two precursors were collected by vacuum filtration with a membrane filter (47 mm in diameter, 0.2 μm pore size, Whatman) and repeatedly washed with de-ionized water. They were dried in the vacuum oven at 60 °C for 12h. Finally, the GO-MWCNTs powders were placed in furnace and heated to 300 °C for 2 h in nitrogen. During this process, the precursors were reduced to graphene nanosheets/carbon nanotubes (GNS-CNT). The graphene nanosheets/carbon nanotubes hybrid materials with different weight ratios of 1:1 and 2:1 were abbreviated as GNS-CNT-1 and GNS-CNT-2, respectively. Bare graphene nanosheets were also prepard using the same procedure.

4.2.2 Characterization of Graphene-CNT nanocomposites

The as-prepared materials were characterised by X-ray diffraction (XRD, Rigaku D/max-2550V with Cu Kα radiation) operated at 40 KV and 50 mA, and Raman spectroscopy (HR Micro Raman spectrometer, Horiba JOBIN YVON US/HR800 UV) using 632.8 nm wavelength laser. UV/Vis absorption spectra were measured using a Carry 300 UV/Vis spectrophotometer (Varian). The morphologies of the as-obtained hybrid materials and GNS were investigated by field-emission scanning electron microscopy (FE-SEM, JSM-6700F), and transmission electron microscopy/selected area electron diffraction (TEM/SAED, JEOL JEM-200CX and JEM-2010F). Microstructures of hybrid materials were analysed using high-resolution transmission electron microscope (HRTEM) on a JEM-2010 apparatus with an acceleration voltage of 200 kV. Nitrogen adsorption-desorption measurements were conducted to determine the Brunauer–Emmett–Teller (BET) specific surface areas of GNS, MWCNTs, GNS-CNT-1 and GNS-CNT-2 using a Quadrasorb SI analyzer at 77 K. The Brunauer–Emmett–Teller (BET) surface area was calculated using experimental points at a relative pressure of P/P_0=0.05–0.25. The pore size distribution was derived from the desorption branch using the Barret–Joyner–Halenda (BJH) method.

4.2.3 Electrochemical measurements

For electrochemical testing, the working electrodes were made from 80 wt. % (weight percent) of active material, 10 wt. % of the conductivity agent (acetylene black), and 10 wt. % of the binder (polyvinylidene difluoride). Lithium foil was used as the counter electrode. Swagelok cells with a diameter of 12 mm were assembled for testing. The electrolyte was 1M $LiPF_6$ in a 50:50 w/w mixture of ethylene carbonate and diethyl carbonate. The cells were assembled in an argon-filled glove box (Mbraun, Unilab, Germany), in which both the moisture and oxygen contents were controlled to be less than 0.1 ppm. Electrochemical measurements were performed in a LAND-CT2001C battery test system. The cells were discharged and charged galvanostatically in the fixed voltage range of 0.005-3.0 V.

4.3 Results and discussion

A schematic illustration of the formation process of GNS-CNTs hybrid materials was proposed and shown in Figure 4-1. GO colloid solution is stable with a brown color. When GO solution was mixed with the MWCNTs suspension under ultrasonic processing, we observed two different phenomena. A homogeneous dispersion with a dark brown color was obtained for the mixture of GO and MWCNTs with a weight ratio of 2:1, which is very stable. No precipitate was observed for six months. On the other hand, precipitation was observed for the mixture of GO and MWCNTs with a ratio of 1:1. Graphene oxide is hydrophilic in nature, owing to attached hydroxyl and carboxyl groups. Therefore, GO can form a stable suspension in water. On contrary, carbon nanotube is hydrophobic in nature. MWCNTs cannot be dispersed and precipitate in water. If small amount of MWCNTs are added into the GO aqueous solution (GNS:CNT = 2:1, GNS-CNT-2 sample), MWCNTs are attracted on the surfaces of GO due to strong π- π interaction. The hybrid materials will not precipitate because there are enough suspended GO nanosheets to hold MWCNTs; If a large amount of MWCNTs are added into the GO aqueous solution (GNS:CNT = 1:1, GNS-CNT-1 sample), individual suspended GO nanosheets will be attracted by MWCNTs and form precipitation. Therefore, Depending on the ratio between GO and CNTs, either stable suspension or precipitation can form. Similar phenomena were also observed by previous investigations. It has been reported that sonicating the mixture of GO dispersion and CNTs powder (0.05 wt%, respectively) resulted in the formation of a black suspension, which is very stable. When the content of GO and CNTs was increased to 0.5 wt%, a GO/CNTs hydrogel was formed [42, 43]. Tung and co-workers demonstrated that GO and CNTs with a weight ratio of 1:10 were directly dispersed into anhydrous hydrazine, forming a stable solution [20]. Therefore, the formation of GNS-CNTs hybrid materials is one of the best strategies to prevent the re-stacking of graphene nanosheets, in which CNTs were sandwiched between GNS with a three-dimensional (3D) nanoarchitecture (as illustrated in Figure 4-1).

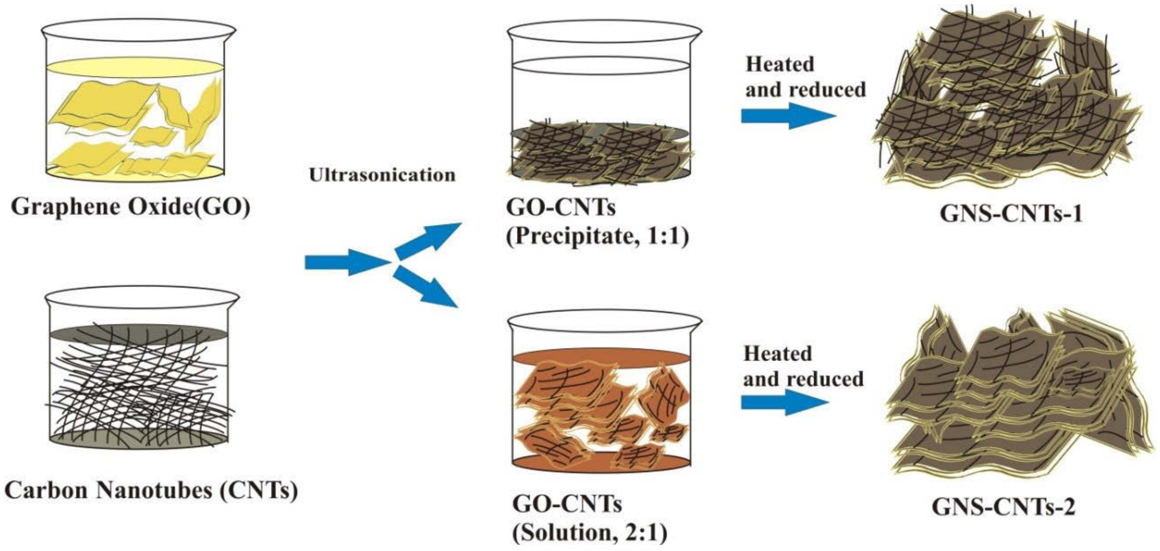

Figure 4- 1 A schematic illustration of the formation process of GNS-CNTs hybrid materials.

X-ray diffraction (XRD) patterns of graphene oxide (GO), GNS, MWCNTs, GNS-CNT-1 and GNS-CNT-2 are shown in Figure 4-2(a). The characteristic (002) diffraction peak of graphene oxide appears at around 2θ = 9.67 ° with the interplanar distance of 0.914 nm. Compared with the interplanar distance about 0.335 nm of natural graphite, the oxygen-containing functional groups on the graphene oxide enlarged the interplanar distance. When the graphene oxide was reduced by heat treatment at 300 °C for 2h in N_2, the characteristic (002) diffraction peak shifts back to 23.85 ° with the interplanar distance of 0.372 nm, indicating the reduction from GO to GNS. MWCNTs show a (002) diffraction peak at 2θ=26.09° and (101) diffraction peak at 43.2°. The GNS-CNTs hybrid materials exhibit similar features, which can be observed in the Figure 4-2(a).

Figure 4-2(b) shows the Raman spectra of GNS, GNS-CNT-1, GNS-CNT-2 and MWCNTs. There are three main Raman peaks associated with different characteristics of carbon materials. The D band is related to the defect mediated zone-edge (near K-point) phonons, which can determine the defects, edges and disordered carbon. The G band (1580 cm^{-1}) reflects the in-plane vibration of sp^2 carbon atoms in graphitic materials, which is doubly degenerated E_{2g} mode at the Brillouin zone centre. The intensity of G band increases with the thickness of graphene nanosheets. The 2D band is associated with the second order double resonant Raman scattering from zone boundary, K + ΔK phonons [160]. Ni *et al* [49] reported that the intensity of the G band rises almost linearly with the increase of the graphene thickness (when the number of layers of graphene exceeds a certain value, the intensity of G band declines), and the intensity ratio of D and G band (I_D/I_G) can be used to estimate the amount of defects and disorder in the carbon materials. By analysing Raman spectra, we can distinguish the differences among GNS, MWCNTs and GNS-CNT hybrid materials. The 2D band of GNS is very weak, indicating exist of defects and disordered structure in GNS. However, MWCNTs and GNS-CNT hybrid materials show strong 2D band. The intensity ratios of D and G band ($\mathrm{I_D/I_G}$) for GNS, MWCNT, GNS-CNT-1 and GNS-CNT-2 samples are 1.16, 1.33, 1.29 and 1.31, respectively. This implies that there are large amount of disordered structures and defects in GNS and the graphene layers are more separated in the GNS-CNT-2 sample. The G band originates from the stretching of C-C bond, corresponding to the ordered sp^2 bonded carbon [155, 161-162]. The G bands of MWCNT and GNS are located at 1576.8 $\mathrm{cm^{-1}}$ and 1602 $\mathrm{cm^{-1}}$, respectively. However, there are a few peaks with different intensities between 1583 $\mathrm{cm^{-1}}$ and 1602 $\mathrm{cm^{-1}}$ for GNS-CNT hybrid materials, which could be ascribed to the lattice vibration of sp^2 bonds in GNS and MWCNT. Similar results have been observed previously [163-164], further indicating the semiconducting and metallic properties (contributed by carbon nanotubes and graphene nanosheets). The features of D and G bands indicates the substantial decrease of the size of the in-plane sp^2 domains, the decrease of edge planes and the degree of disorder in the as-prepared GNS-CNT hybrid materials.

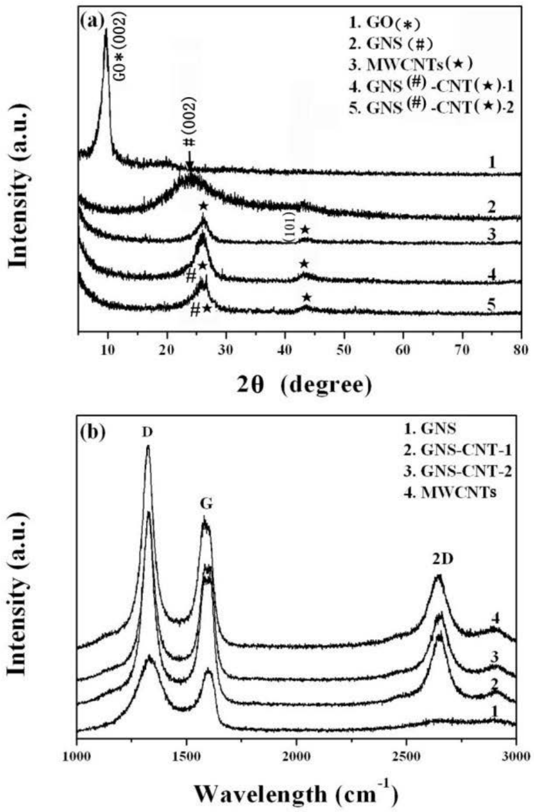

Figure 4- 2 (a) XRD patterns of graphene oxide (GO), graphene nanosheets (GNS), Multi-walled carbon nanotubes (MWCNTs), GNS-CNT-1 and GNS-CNT-2, (b) Raman spectra of GNS, MWCNTs, GNS-CNT-1 and GNS-CNT-2.

MWCNTs, GO, GO-CNT-1 and GO-CNT-2 were further characterized by UV-Vis spectroscopy. Figure 4-3(a) shows the UV-vis spectra of the four samples at a concentration of 0.1 mg mL^{-1}. MWCNT suspension is exhibited a broad absorption at around 230nm with the high energy of ultraviolet, which is related with the plasmon resonances in the free electron cloud of the nanotube π electrons (155-310 nm, 4.0-8.0 ev) and $\pi+\sigma$ plasmon (40-125 nm, 10-30 ev) [49, 50]. GO also has π electrons among different layers and shows the broad absorption at the same position of MWCNT. Therefore, with the precursor composites of MWCNT and GO, similar broad absorptions can be observed in the GO-CNT composites (the peak of GO-CNT-1 is more broad than the GO-CNT-2, which might has some relation with the different weight ratio), which is contributed by the combined actions from MWCNT and GO.

The porous structure and surface area of the GNS-CNT-2 hybrid material was investigated by nitrogen adsorption and desorption isotherms (as shown in Figure 4-3b). The specific surface area was measured by the Brunauer-Emmett-Teller (BET) method. The specific areas of GNS, MWCNTs, GNS-CNT-1 and GNS-CNT-2 are shown in Table 4-1. The specific BET surface area of GNS, GNS-CNT-1, GNS-CNT-2 and MWCNTs are 436.7 $m^2 g^{-1}$, 240.4 $m^2 g^{-1}$, 399.5 $m^2 g^{-1}$, and 22.4 $m^2 g^{-1}$, respectively. The bare GNS has a very large specific surface area; while the BET surface area of MWCNTs is the smallest. Therefore, when the weight ratio of MWCNTs in the hybrid materials increases, the specific surface area decreases. The BET analysis revealed that the GNS-CNT-2 sample has a large surface area of 399.5 $m^2 g^{-1}$. Furthermore, the prominent hysteresis loops at relative pressure of 0.4 to 1.0 suggests that the hybrid material has a mesoporous structure. The total pore volume of the GNS-CNT-2 sample was determined to be 0.299 mL g^{-1}. The average pore size of GNS-CNT-2 was measured to be 31.837 Å. While the average pore size of GNS and MWCNTs are 41.389 Å and 19.364 Å, respectively. The changes of average pore size and BET surface area are related to a certain amount of carbon nanotubes loaded on the surface of graphene nanosheets. The detailed BET surface area and pore size for each sample are shown in the Table 4-1. This mesoporous 3D nanostructure could provide more reactive sites for lithium storage and buffer the large volume change during lithium ion insertion/extraction process, leading to its improved performance as an anode material in Li-ion batteries.

Table 4- 1 The specific BET surface areas and average pore size of GNS, GNS-CNT-1, GNS-CNT-2 and MWCNTs.

Samples	**BET Surface Area($m^2 g^{-1}$)**	**Average pore size (Å)**
GNS	436.7	41.389
GNS-CNT-1	240.3	28.541
GNS-CNT-2	399.5	31.837
MWCNTs	22.4	19.364

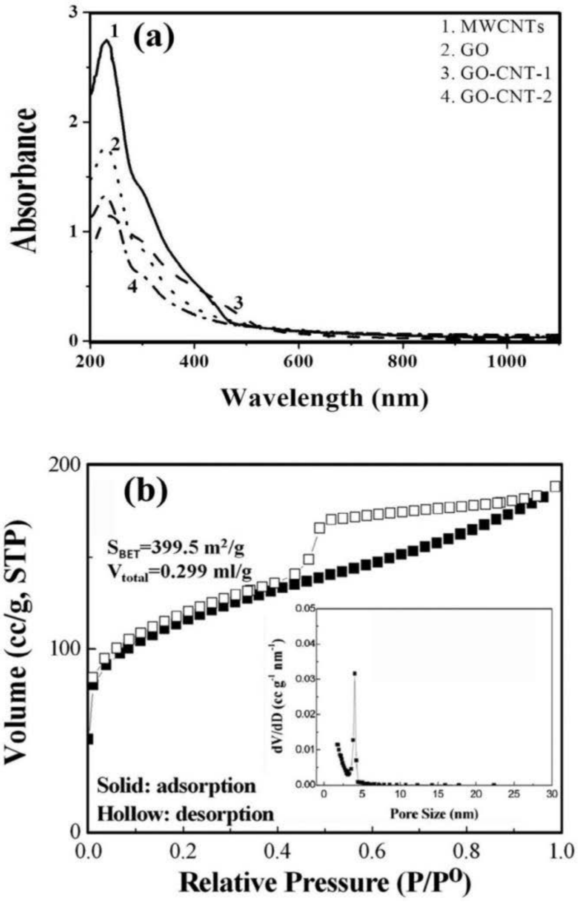

Figure 4- 3 (a) UV/Vis absorption spectra of MWCNT, GO, GO-CNT-1 and GO-CNT-2, (b) Nitrogen adsorption-desorption isotherm and insert image is pore size distribution of GNS-CNT-2.

Figure 4-4 (a) – (d) shows FESEM images of GNS-CNT-1 and GNS-CNT-2 samples at low and high magnifications. In general, MWCNTs and GNS form a homogeneous hybrid material, in which graphene nanosheets wrap around carbon nanotubes. Since bare graphene nanosheets are transparent with a crumpled and rippled structure. Some MWCNTs can be observed through the transparent graphene nanosheets. In Figure 4-4 (b) and (d), we can identify that some MWCNTs extrude from the wrapped structure, which is due to longer length of MWCNTs than GNS. The microstructure of GNS-CNT hybrid materials were further analysed by TEM and HRTEM. Figure 4-5(a) shows a low magnification TEM image of GNS-CNT-s sample. It is evident that graphene nanosheets wrapped many carbon nanotubes and formed a bulk of agglomerate. A HRTEM reveals the detailed nanostructure of GNS-CNT-1 sample (as shown in Figure 4-5(b)). Two layers of graphene nanosheets wrap around the carbon nanotube, in which MWCNTs curled along the edge of graphene nanosheets. Figure 4-5(c) shows a low magnification TEM image of the GNS-CNT-2 sample. A more homogeneous structure was achieved for this sample, in which individual MWCNTs were well dispersed in graphene nanosheet matrix. The corresponding HRTEM image (Figure 4-5(d)) illustrates that five layer graphene nanosheets wrap around the carbon nanotube. The average d-spacing of GNS was determined to be 0.372 nm, which is consistent with the XRD result.

Two mechanisms have been proposed to explain in the interactions between GO and CNT in the aqueous suspension. According to the mechanism raised by Li *et al*, GO moved to MWCNTs during sonication and strong intermolecular forces become much stronger. Then, GO molecules curl up and wrap around the MWCNTs [45]. However, this phenomenon only occurred on the edge of graphene oxide nanosheet. The other mechanism is related to the π-π interactions, which plays the major role in the interactions between the basal plane of GO and MWCNTs. The hydrogen bonds could also contribute towards attracting MWCNTs.

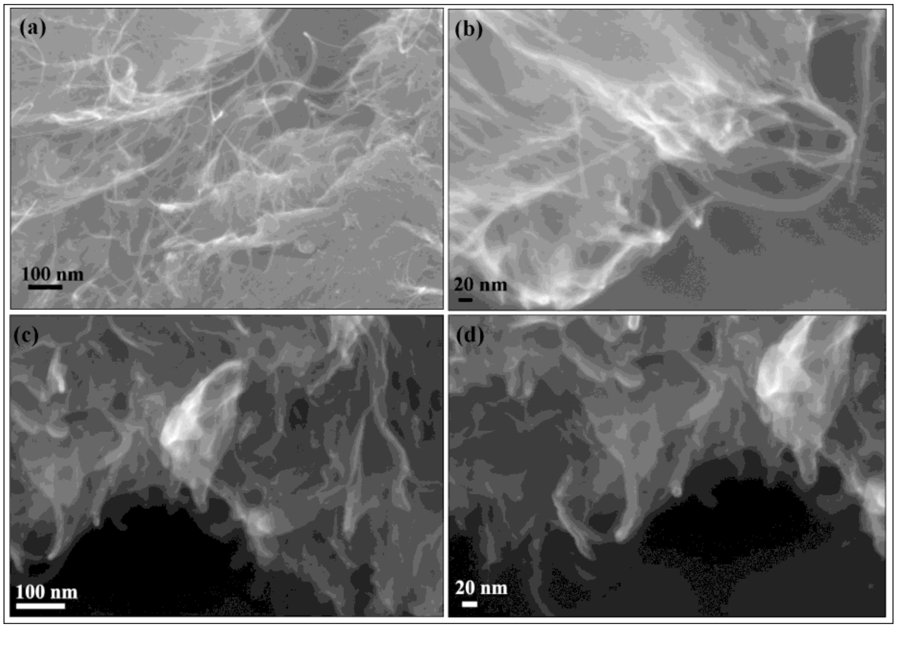

Figure 4- 4 Low and high magnification SEM images of GNS-CNT-1 (a, b) and GNS-CNT-2 (c, d).

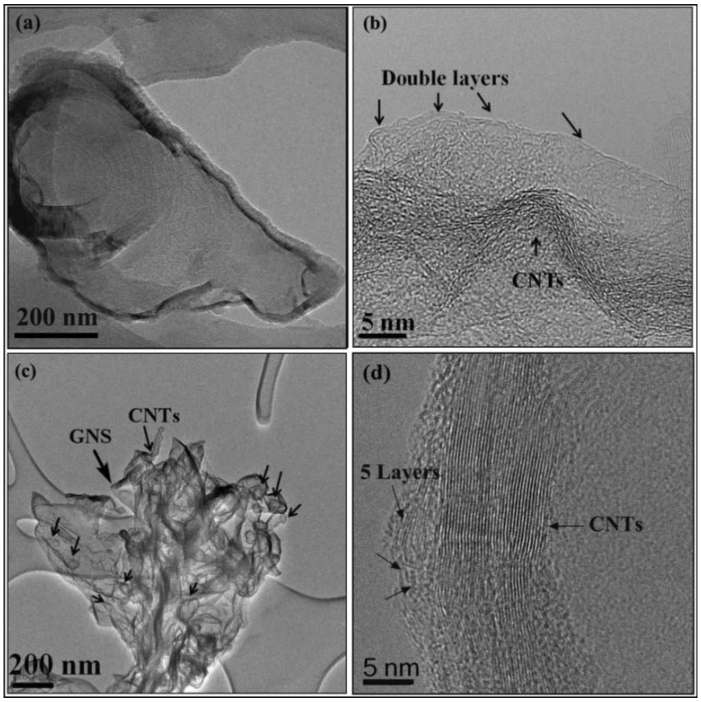

Figure 4- 5 Low and High resolution TEM images of GNS-CNT-1(a, b) and GNS-CNT-2 (c, d).

The electrochemical performances of the as-prepared GNS-CNT hybrid materials were tested by galvanostatical charge and discharge cycling in the voltage range of 0.005-3 V. Figure 4-6 (a), (b) and (c) show the voltage profiles of GNS, GNS-CNT-1 and CNT-CNT-2 electrodes in the 1st and 100th cycles, respectively. The first discharge specific capacities for three samples are around 1550 mAh g^{-1}. However, the reversible specific capacities are different. The first rechargeable specific capacity of GNS is 431.9 mAh g^{-1}, the large irreversible capacity loss may be related to the large specific surface area of GNS and the formation of solid electrolyte interface (SEI) on the electrode. The initial reversible capacity of the GNS-CNT-1 electrode is 548 mAh g^{-1}. The large irreversible capacity indicates the formation of solid electrolyte interface (SEI) on the surface of GNS-CNT-1 electrode. The specific capacity retained 401 mAh g^{-1} with a high Coulombic efficiency of 97.6% in the 100th cycle. The GNS-CNT-2 sample exhibited better electrochemical performance with a reversible capacity of 618 mAh g^{-1} in the first cycle, 485 mAh g^{-1} in the 100th cycle with a high Coulombic efficiency of 98.5%.

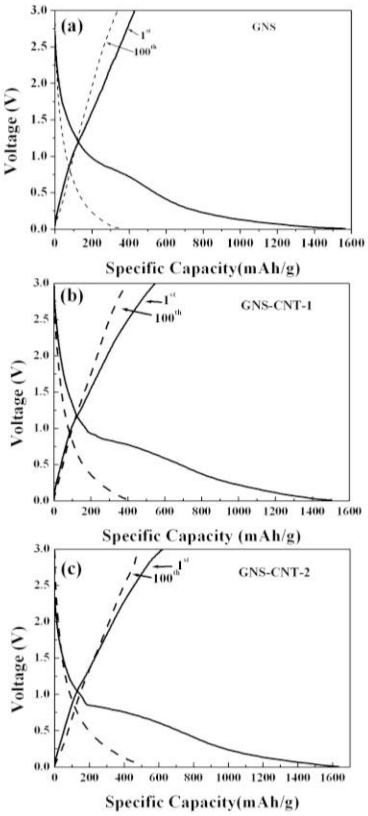

Figure 4- 6 (a) Charge-discharge profiles of the electrodes in the 1st and 100th cycles (a) GNS, (b) GNS-CNT-1 and (c) GNS-CNT-2. Current density: 74.4 mA g^{-1}.

The cycling properties of the GNS and GNS-CNT hybrid materials are shown in Figure 4-7(a). The Coulombic efficiencies of bare GNS in the first 10 cycles are low and the specific capacity decreased quickly. This could be related to the high surface area, defects and disordered structures in GNS. Large amount of Li^+ ions cannot be extracted from those cavities, inducing the irreversible capacity loss. The Coulombic efficiency of GNS-CNT-1 is better than that of GNS. Although the rechargeable specific capacities decrease in the first 40 cycles, cycling performances are stable after 40 cycles, with a high Coulombic efficiency. This should be credited to the intermingling MWCNTs and relative ordered structure of the GNS-CNT hybrid material. The GNS-CNT-2 electrode demonstrated the best cycling performance. The specific capacity declined in the first few cycles, which is ascribed to the formation of solid electrolyte interfaces, the absorption of carbon nanotubes on the surfaces, the consumption of the disordered carvities and edges of reduced graphene nanosheets. Nevertheless, the cycling performance stabilized in the subsequent cycles, due to the full diffusion of electrolyte into mesoporous structure in the electrode. The good electrochemical performance of GNS-CNT hybrid materials could be credited to the uniform 3D nano-architecture and the synergistic effect between graphene nanosheets and carbon nanotubes. The morphologies of the GNS-CNT hybrid materials have influences on their lithium storage properties. The weight ratios between GNS and MWCNTs affect the specific surface area and microstructure of the hybrid materials. Although GNS has high specific surface area, large amount of defects and disordered structures exist in GNS, which induces an inferior electrochemical performance. When small amount of MWCNTs are added in GNS (GNS:CNT = 2:1), GNS and MWCNTs can form a 3D nanostructure. Therefore, the GNS-CNT-2 electrode demonstrated the best electrochemical performance. However, when large amount of MWCNTs are added in GNS, the precursor forms precipitation and the BET surface area decreases, leading to a degraded electrochemical performance. Therefore, the ratio between GNS and MWCNTs is one of crucial factors affecting electrochemical properties of resultant hybrid materials.

In order to examine the tolerance of the GNS-CNT-2 electrode towards different current rates, the GNS-CNT-2 electrodes were cycled at varied current rates (0.5 C and 1 C, 1 C=744 mA g^{-1}). Figure 4-7(b) shows the specific capacities of the GNS-CNT-2 electrode at different current rates in the 100 cycles. The Coulombic efficiency of the GNS-CNT-2 electrode at 0.5 C is not high in the initial cycle. However, it quickly increased to more than 98.5% in the subsequent cycles, indicating that the cycling performance of GNS-CNT-2 is stable. The specific capacity retained 429 mAh g^{-1} after 100 cycles with a high capacity retention ratio of 97.7%. The GNS-CNT-2 electrode exhibits a discharge specific capacity of 330 mAh g^{-1} after 100 cycles at 1 C rate and maintained a high Coulombic efficiency. The electrochemical performances of the GNS-CNT-2 sample in different current densities illustrate the excellent cycling behaviour and the capability of high capacity retention. The electrochemical performances of GNS-CNT hybrid materials are compared with other graphene based materials, which is shown in Table 4-2. Compared to the bare graphene, the GNS-CNT hybrid materials demonstrate higher rechargeable capacity and better cycling performances, which are ascribed to the synergistic effect from GNS and CNT. As the bare graphene nanosheets are easily re-stacked due to the strong van der Waals' force, with the assist of CNT, GNS-CNT hybrid materials can maintain the good performance of graphene and the good conductivity of CNT.

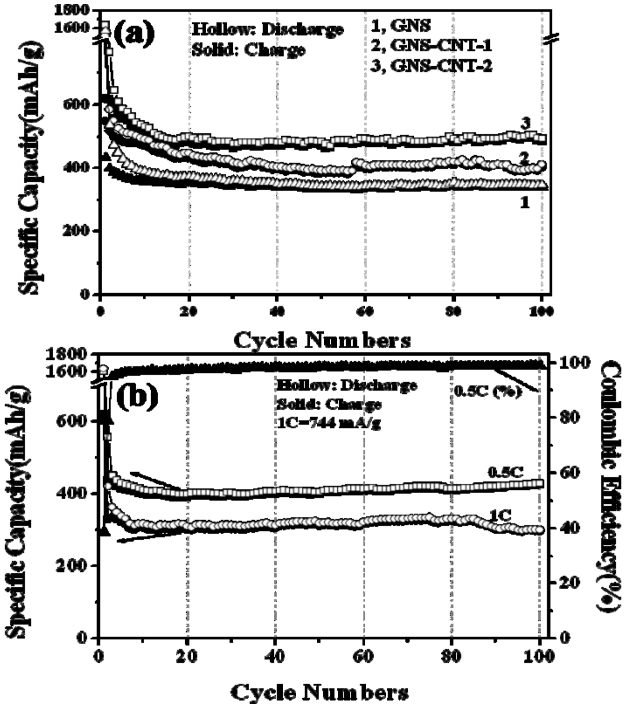

Figure 4- 7 (a) Cycling performances of the GNS, GNS-CNT-1 and GNS-CNT-2 electrodes in the 100 cycles, (b) Charge/discharge cycling performances of the GNS-CNT-2 electrodes at different current densities (0.5 C and 1 C) and the Coulombic efficiencies at current density of 372 mA g^{-1}.

Table 4- 2 The comparison of electrochemical performances of different graphene basd materials.

Materials	Initial capacity (mAh/g)	Final capacity (mAh/g)	Retention ratio (mAh/g)	Rate capacity (mAh/g)
CNF/G[165]	667	606	91% (30 cycles)	189 (6 mA/cm^2)
GNS[166]	672	502	74.7% (30 cycles)	554 (1 mA/cm^2)
N-doped GNS[167]	1043	872	83.6% (30 cycles)	493 (0.5 A/g)
This thesis	618	485	78.5% (100 cycles)	469 (0.37 A/g)

4.4 Conclusions

In conclusion, we have successfully synthesised graphene nanosheet/carbon nanotube hybrid materials facilitated by the π- π interaction without using any chemical reagent. The different ratios between graphene oxide and carbon nanotubes had critical influences on their states in aqueous solution and the final products' morphologies. FESEM and TEM analysis confirmed the 3D nanoarchitecture with the wrapping of graphene nanosheets around individual carbon nanotubes. The GNS-CNT-2 sample exhibited a high initial reversible specific capacity of 439 mAh g^{-1} at a current density of 372 mA g^{-1} and a high capacity of 429 mAh g^{-1} had been maintained after 100 cycles with a high Coulombic efficiency of 98.5% (from the 2nd to 100th cycles). The good electrochemical performance could be attributed to the homogeneous three-dimensional nanostructure and the synergistic effect of the combination between graphene nanosheets and carbon nanotubes.

CHAPTER 5 Fe_2O_3-CARBON NANOTUBE-GRAPHENE HYBRID NANOMATERIALS WITH AN OPEN THREE DIMENSIONAL FEATURE FOR LITHIUM ION BATTERIES

5.1 Introduction

In order to meet the increasing demand for sustainable energies, various types of energy storage devices have been developed, such as lithium ion batteries [168-169], lithium air batteries [170-172], supercapacitors [173-175] and lithium ion capacitors [176-178]. Among them, lithium ion batteries are considered to be the most practical power sources for electric vehicles, hybrid electric vehicles and plug-in hybrid electric vehicles. However, the specific capacity, energy density and cycle life of lithium ion batteries require improvement. Many new anode materials have been developed to increase lithium storage capacity, including graphene nanosheets (GNS) [19, 146-147, 179-181], carbon nanotubes (CNTs) [121, 182-184] and loading metal nanoparticles (Si [185], Sn [186], Sb [94] and Ge [187]) or metal oxides (Co [90], Fe [188], Sn [108, 189], Mn [190], Cu [191-192] and Ni [193]) on GNS or CNTs matrix [101].

Hermatite (α-Fe_2O_3) anode material has been extensively investigated owing to its high specific capacity, eco-friendliness and low cost. Liu et al. [194] prepared one-dimensional fiber-like Fe_2O_3 with macroporous nanostructure using a wet spinning method, which exhibited a discharge capacity of 2750 $mAh\cdot g^{-1}$ in the first cycle, then decreased to 732 $mAh\cdot g^{-1}$ in the 50th cycle with a capacity retention of 27%. Two-dimensional Fe_2O_3 with a mesoporous structure synthesized by Sun et al. [195] showed a reversible specific capacity of 1360 $mAh\cdot g^{-1}$ in the initial cycle, then decreased to 1293 $mAh\cdot g^{-1}$ in the 50th cycle with a capacity retention of 95%. GNS supported Fe_2O_3 nano-rices composites with three-dimensional structure were prepared by Zou et al. [196] using a microwave-assisted hydrothermal technique. This nanocomposite demonstrated a reversible capacity of 1184 $mAh\cdot g^{-1}$, maintained 734 $mAh\cdot g^{-1}$ at the 40th cycle, and retained 62% of the initial capacity.

Herein, we reported the synthesis of 3D Fe_2O_3-CNT-GNS hybrid materials with an open architecture. The hybrid materials consist of CNTs grown on graphene nanosheets, in which CNTs have a bamboo-like morphorlogy and open tips capped with Fe_2O_3 nanorings. A modified "tip-growth" mechanism for growing bamboo-like CNTs and a unique lithiation process were proposed. Fe_2O_3-CNT-GNS hybrid materials exhibited a high lithium storage capacity with a superior cycling stability and high rate performance.

5.2 Experimental

5.2.1 Synthesis and characterizations

Graphene oxides (GO) were prepared according to the previously reported procedure [113]. A typical process for preparing Fe_2O_3-CNT-GNS hybrid materials is as follows: 2 $mg \cdot mL^{-1}$ graphene oxide colloid (50 mL) was ultrasonically treated for 2 h (10 s on and 10 s off) in an ice bath using a Branson S-450D sonifier with a horn of 13 mm in diameter (40% amplitude). 72.1 mg $Fe(NO_3)_3 \cdot 9H_2O$ was added to GO aqueous solution with magnetic stirring for 2 h and ultrasonicated for 1h to form a solution. Then the mixture was dried at 80 ^oC in a vacuum oven for 12 h, the solvent (H_2O) was evaporated and $Fe(NO_3)_3 \cdot 9H_2O$-graphene oxide ($Fe(NO_3)_3$-GO-1) was obtained. 144.3 mg $Fe(NO_3)_3 \cdot 9H_2O$ was added in the same amount of GO solution.

The precursors were heated to 550 ℃ at a heating rate of 5 $℃ \cdot min^{-1}$ in a tube furnace with Ar flow at 200 sccm. Then C_2H_2 gas (C_2H_2: 10%, Ar: 90%) was introduced for 10 min at 50 sccm before the furnace was gradually cooled in Ar to room temperature. After then, the products were heated to 400 ℃ for 2 h in air to obtain the final materials. For comparison, 200 mg Fe_2O_3 nanoparticles and 50 mg GNS were also prepared under the same experimental condition without acetylene.

The as-prepared materials were characterized by X-ray diffraction (XRD, Rigaku D/max-2550V with Cu Kα radiation) operated at 40 KV and 50 mA, and Raman spectroscopy (HR Micro Raman spectrometer, Horiba JOBIN YVON US/HR800 UV) using a 632.8 nm wavelength laser. The morphologies of the as-obtained hybrid materials and GNS were investigated by field-emission scanning electron microscopy (FE-SEM, JSM-6700F), and transmission electron microscopy/selected area electron diffraction (TEM/SAED, JEOL JEM-200CX and JEM-2010F) equipped with an energy-dispersive X-ray spectrometer (EDX).

5.2.2Electrochemical measurements

The working electrodes were made from 80 wt. % of active materials, 10 wt. % of the conductive agent (acetylene black), and 10 wt. % of the binder (polyvinylidene difluoride). The mixture was stirred by an adjustable high-speed electric agitator. The working electrodes were dried in a vacuum oven. CR2032 coin cells were assembled in an argon-filled glove box (Mbraun, Unilab, Germany), in which both the moisture and oxygen contents were controlled to be less than 0.1 ppm. Lithium foil was used as the counter electrode. The electrolyte (Zhangjiagang Guotai-Huarong New Chemical Materials Co., Ltd.) was 1M $LiPF_6$ in a 1:1 (weight ratio) mixture of ethylene carbonate and diethyl carbonate. Electrochemical measurements were performed using a LAND-CT2001C battery test system. The cells were discharged and charged galvanostatically in the fixed voltage range of 0.005-3.0 V with a current density of 74.4 $mA \cdot g^{-1}$ (0.1 C). Higher current rates (0.5 C, 1 C or 5 C) were also used to test the electrochemical performance. After 100 cycles, the electrode materials were taken out from those coin cells in glove box, washed by ethylene carbonate to remove electrolyte. The cycled electrode materials were analyzed by SEM, TEM, elemental mapping and EDX. Cyclic voltammetry was measured on a CHI 660D electrochemical workstation at a scan rate of 0.1 $mV \cdot S^{-1}$.

5.3 Results and discussion

The synthesis process of Fe_2O_3-CNT-GNS hybrid materials is shown in Figure 5-1. In the first step, $Fe(NO_3)_3 \cdot 9H_2O$ solution was added in graphene oxide nanosheet (GO) suspension. Since GO nanosheets contain carboxylic acid groups on the edge sites, and epoxy and hydroxyl moieties on the basal plane, the positively charged Fe^{3+} are attached to those negatively charged functional groups. During the second step of chemical vapor deposition (CVD), Fe^{3+} ions were reduced to Fe nanoparticles by acetylene and then the growth of CNTs on graphene nanosheets were simultaneously catalyzed. GO nanosheets were also reduced to graphene nanosheets during this process. In order to oxidize Fe to Fe_2O_3, the CVD products were heat treated at 400 ^{o}C for 2 h to obtain Fe_2O_3-CNT-GNS hybrid materials.

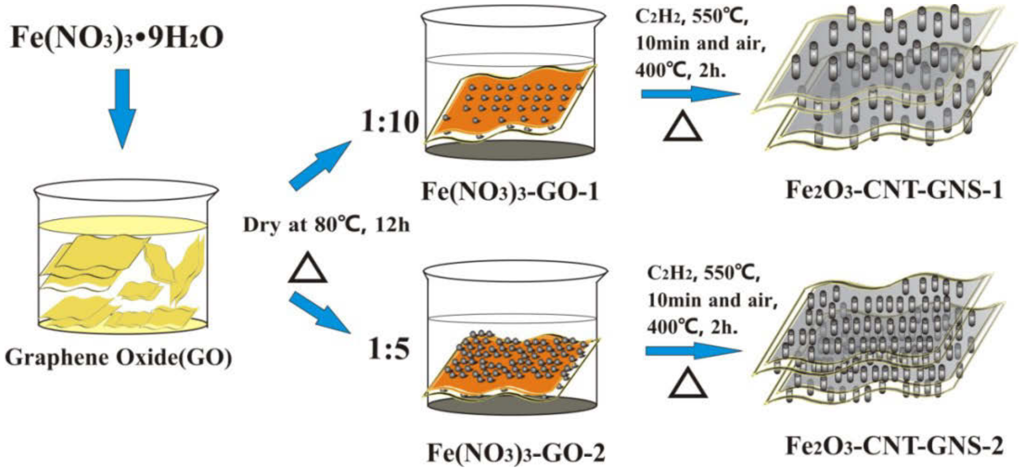

Figure 5- 1 A schematic diagram for the preparation of Fe_2O_3-CNT-GNS hybrid materials

The as-synthesized materials were characterized by X-ray diffraction, which are shown in Figure 5-2(a). A strong characteristic (002) diffraction peak of GO shows at $2\theta = 9.67°$ with an interplanar distance of 0.914 nm, which is larger than that of graphite (0.335 nm). In comparison, graphene nanosheets (GNS) were also obtained under the similar experimental condition without acetylene. The characteristic (002) diffraction peak shifts from 9.76° to 24.2° with the interplanar distance of 0.367 nm. This indicated that GO nanosheets were successfully reduced to GNS. Rhombohedral phase of hematite (α-Fe_2O_3, JCPDS No. 79-0007) is indexed as the diffraction peaks of (012), (104), (110), (113), (024) (116), (214) and (300).

Raman spectroscopy measurement was performed to characterise GNS and CNTs (Figure 5-2(b)). The I_D/I_G values of GNS, Fe_2O_3-CNT-GNS-1 and Fe_2O_3-CNT-GNS-2 are 1.03, 1.14 and 1.2, respectively. The intensity ratio of D and G band (I_D/I_G) can be used to estimate the amount of defects and disorder in carbon materials. The increase of I_D/I_G value for Fe_2O_3-CNT-GNS, implies that there are more defects and nanocavities in Fe_2O_3-CNT-GNS hybrid materials. This could be owing to bamboo-like morphorlogy with cracks, nanocavities and graphene layers inside CNTs. Through thermogravimetric analysis (TGA) and compared with previous reports [113, 197-198], the percentages of Fe_2O_3 in hybrid materials were determined to be 30.9 wt% and 50.1 wt% for Fe_2O_3-CNT-GNS-1 and Fe_2O_3-CNT-GNS-2, respectively.

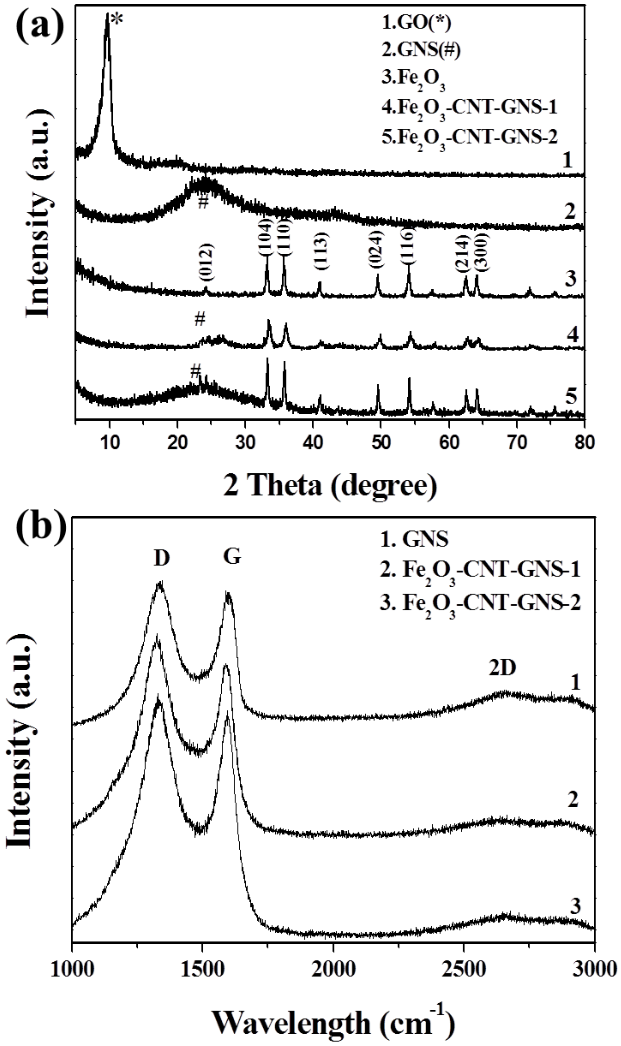

Figure 5- 2 (a) X-Ray diffraction (XRD) patterns of GO, GNS, Fe_2O_3, Fe_2O_3-CNT-GNS-1 and Fe_2O_3-CNT-GNS-2. (b) Raman spectra of as-prepared GNS, Fe_2O_3-CNT-GNS-1 and Fe_2O_3-CNT-GNS-2.

The low and high magnification FESEM images of Fe_2O_3-CNT-GNS-1 and Fe_2O_3-CNT-GNS-2 samples are shown in Figure 5-3. The magnified views marked by white squares in (a) and (c) are shown in Figure 5-3(b) and (d), respectively. As shown in Figure 5-3(b) and (d), carbon nanotubes grew on both sides of GNS. The amount of CNTs in the Fe_2O_3-CNT-GNS-2 is almost double that of the Fe_2O_3-CNT-GNS-1 sample. The individual GNS shows a wavy and crumpled feature with an area of about 36 μm^2. In comparison, the morphologies of bare GNS and Fe_2O_3 nanoparticles are shown in Figure 5-4.

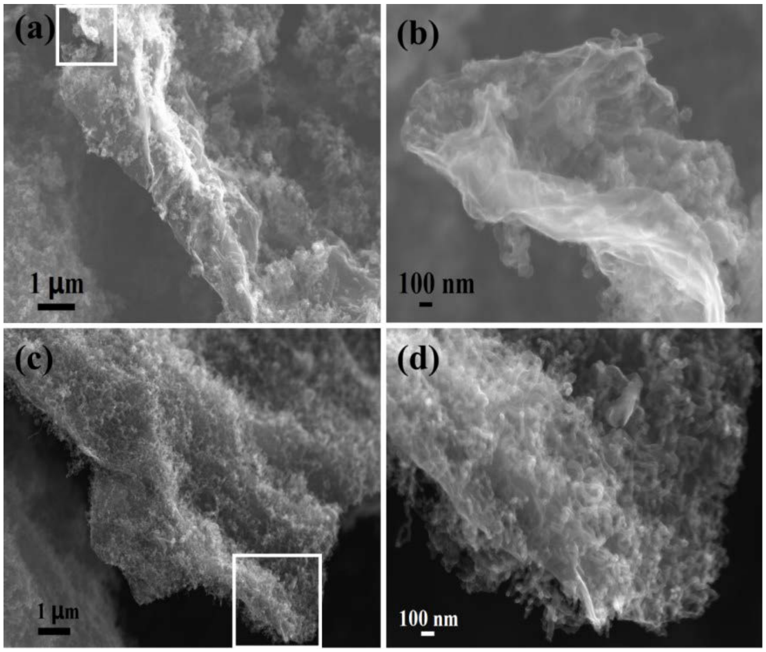

Figure 5- 3 Low and high magnification SEM images showing morphologies of Fe_2O_3-CNT-GNS-1 (a, b) and Fe_2O_3-CNT-GNS-2 (c, d). (b) and (d) are the magnified views, marked by a white square in (a) and (c), respectively

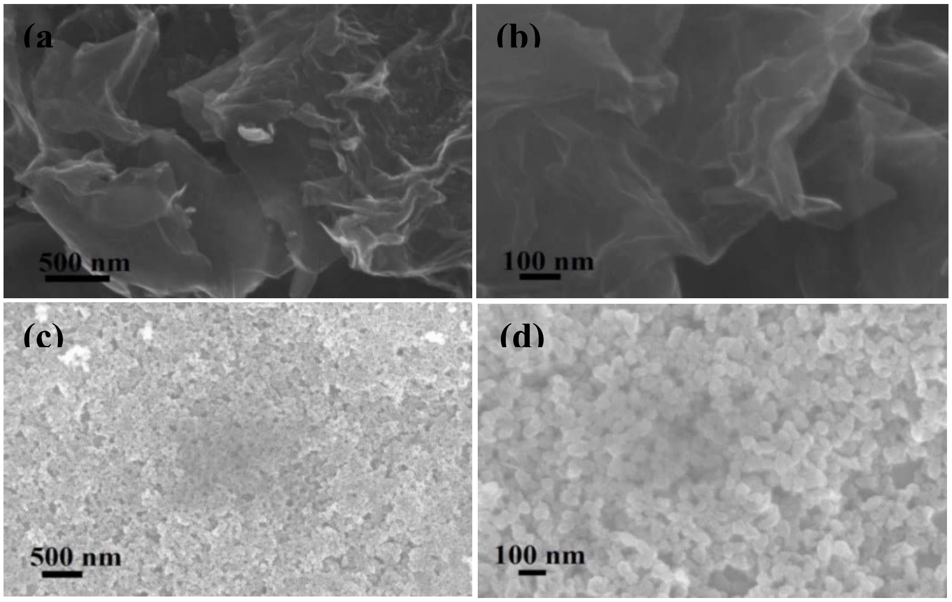

Figure 5- 4 Low and high magnification SEM images showing the typical morphologies of GNS (a, b) and Fe_2O_3 nanoparticles (c, d).

The crystal structure and morphology of Fe_2O_3-CNT-GNS hybrid materials were further analyzed by transmission electron microscopy (TEM) and high resolution TEM (HRTEM).

Figure 5-5 shows low and high magnification TEM images of two Fe_2O_3-CNT-GNS samples. As shown in Figure 5-5(a) and (c), the hybrid materials consist of transparent graphene nanosheets and abundant CNTs, which form 3D porous nano-networks. The high magnification TEM images shown in Figure 5-5(b) and (d) clearly illustrate the hollow structure of CNTs. Carbon nanotubes grew on the basal planes of GNS, catalyzed by iron anchored on graphene, which can effectively prevent the restacking of graphene nanosheets. Figure 5-5(e) and (f) present HRTEM images of tips of CNTs, marked by white squares in Figure 5-5(b) and (d). It can be seen that Fe_2O_3 nanorings are capped on the tips of individual CNTs. The corresponding fast Fourier transformed (FFT) patterns are shown as the insets in Figure 5-5(e) and (f), which depict the rhombohedral phase of hermatite and typical diffuse rings of CNTs.

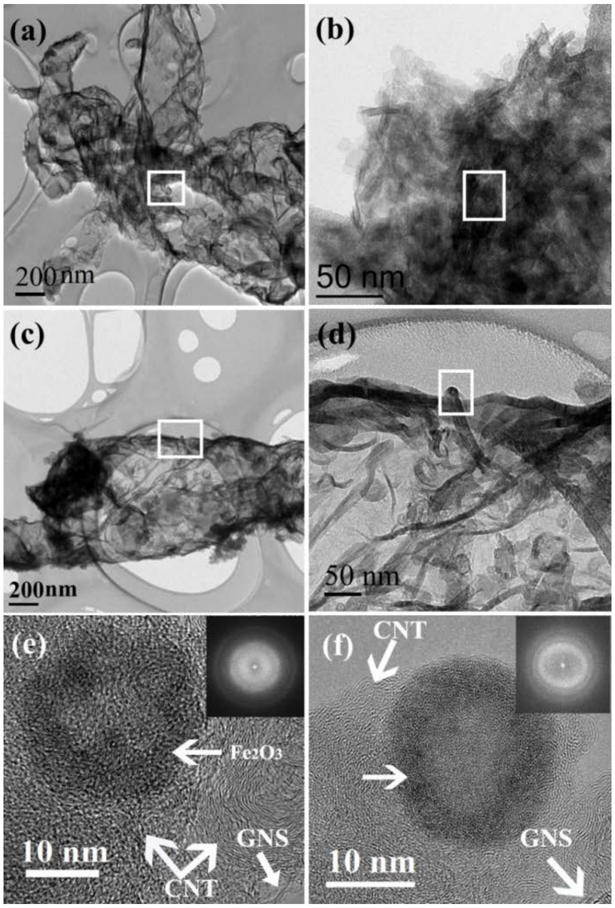

Figure 5- 5 Low and high magnification TEM images showing structures of Fe_2O_3-CNT-GNS-1 (a, b) and Fe_2O_3-CNT-GNS-2 (c, d). (b) and (d) are the magnified views, marked by a white square in (a) and (c), respectively. HRTEM images of Fe_2O_3-CNT-GNS-1 (e) and

Fe_2O_3-CNT-GNS-2 (f), showing Fe_2O_3 nanorings anchored on the tips of CNTs. (e) and (f) are the magnified views, marked by a white square in (b) and (d), respectively. The inset images in (e) and (f) are the fast Fourier transformed (FFT) patterns of Fe_2O_3-CNT-GNS-1 and Fe_2O_3-CNT-GNS-2, illustrating the rhombohedral phase of hematite.

The nanostructures of individual carbon nanotubes were examined particularly by TEM analysis. As shown in Figure 5-6(a) and (b), the as-grown carbon nanotubes have bamboo-like morphology and structure. The black-arrows in Figure 5-6(a) and (b) indicate many cracks on the walls of CNTs, which could be related to the lattice distortion during the catalysis growth process. Interestingly, these cracks and bamboo-like structures on carbon nanotubes follow the periodic-law, in which the distances between every two nodal points are almost the same. Furthermore, graphene layers appear at each nodal point inside carbon nanotubes. These unique features resemble natural bamboo. As reported previously, the growth of CNTs follow the “tip-growth” mechanism[181]. During the growing process, carbon diffuses into Fe atoms and the solid carbon starts to precipitate when Fe-C solid state solution is saturated. When the surface diffusion force between Fe atom and CNT is weaker than the bulk diffusion force, Fe atoms gradually depart from CNTs, which promotes the continuing growth of CNTs. Several factors could influence the formation of bamboo-like CNTs. These include vapour pressure-driven movement of metal catalyst[199], introduced pentagon defects on CNTs[183], unstable gas-flow, and turbulence of carbon source gas, resulting in lattice distortion of CNTs. Based on the above analysis, we proposed a modified “tip-growth” mechanism for the growth of bamboo-like CNTs, which is shown in Figure 5-7. Driven by the flowing gas or turbulence, Fe nanorings could keep rolling and somersaulting during catalyzing of the CNTs. The two sides of Fe nanorings can catalyze the CNTs growth, while the two arcs of Fe nanorings induce an arc-type catalyzing trajectory. Therefore, when Fe nanorings roll, arc-type carbon layers will grow inside CNTs. Consequently, bamboo-like structure formed with graphene layers inside CNTs. The TEM images and Energy dispersive X-ray (EDX) spectrum of Fe nanorings are detected. As shown in Figure 5-6(a) and (b), the black arrows indicate cracks on the bamboo-like carbon nanotubes and the white arrows point to graphene layers inside CNTs. The cracks on the side wall of the bamboo-like carbon nanotubes can provide direct paths for Li ion diffusion and the arc-like graphene layers can store more Li ions, which could enhance the reversible lithium storage.

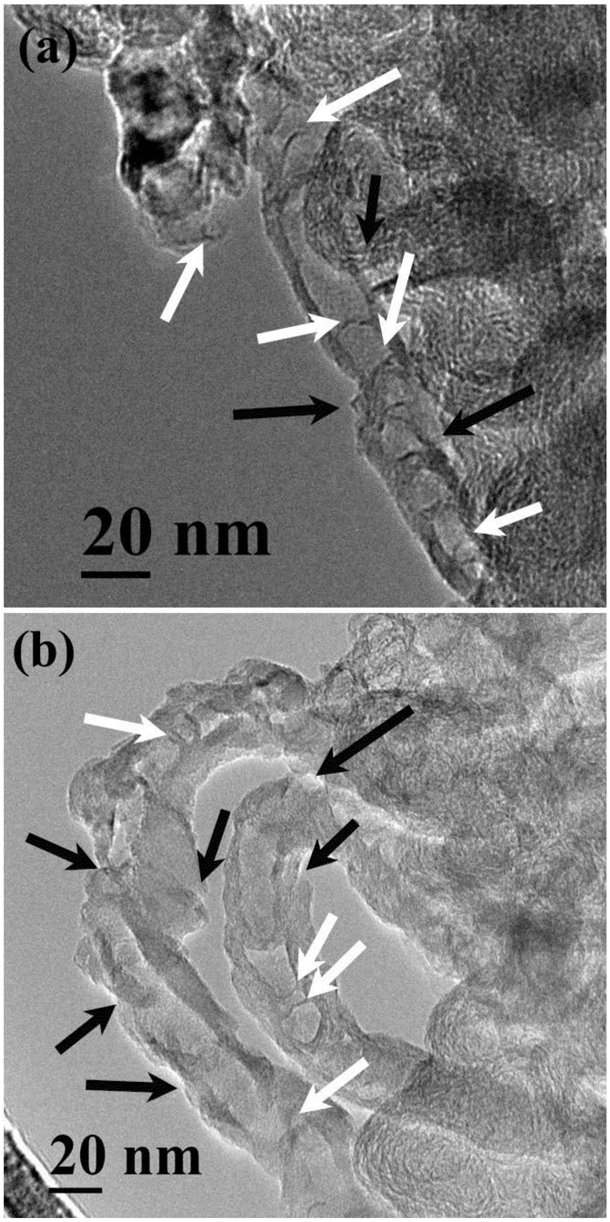

Figure 5- 6 The typical nanostructures of carbon nanotubes of Fe_2O_3-CNT-GNS-1 (a) and Fe_2O_3-CNT-GNS-2 (b). The black arrows show the cracks on bamboo-like carbon nanotubes and the white arrows show the several layers of graphene catalyzed by rolling Fe nanorings.

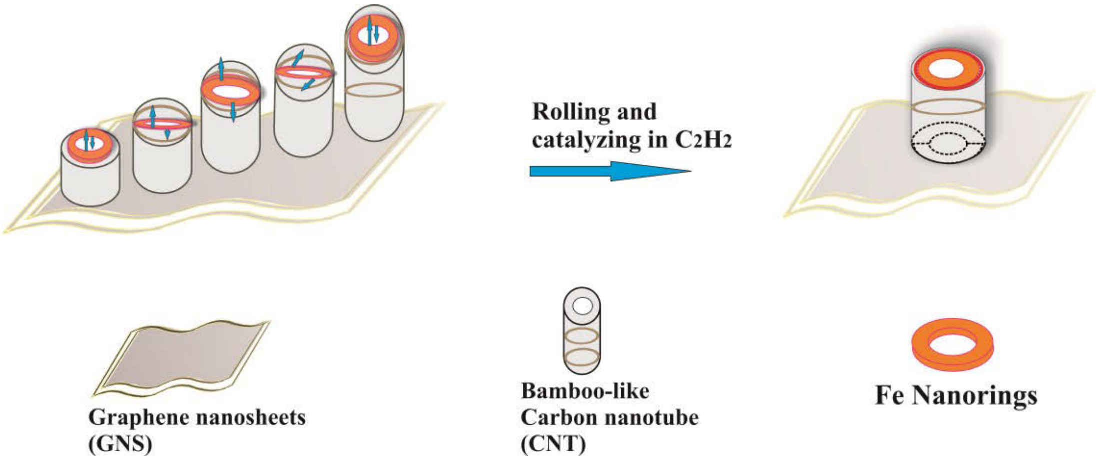

Figure 5- 7 The modified "tip-growth" mechanism of Fe nanorings catalyzing CNTs. Driven by the airflow or turbulence, Fe nanorings keep rolling and turning during catalyzing of CNTs. The two sides of Fe nanorings can catalyze the CNTs growth, while the two arcs of Fe nanorings induce an arc-type catalyzing trajectory, then a bamboo-like structure is formed with graphene layers inside CNTs

EDX spectra and elemental mapping images were performed to analyze the elemental distribution in Fe_2O_3-CNT-GNS hybrid materials. Figure 5-8 shows the TEM image and EDX mappings of C, Fe and O. According to the EDX mapping image, Fe_2O_3 nanorings are confirmed on the tips of CNTs with a diameter of about 20 nm.

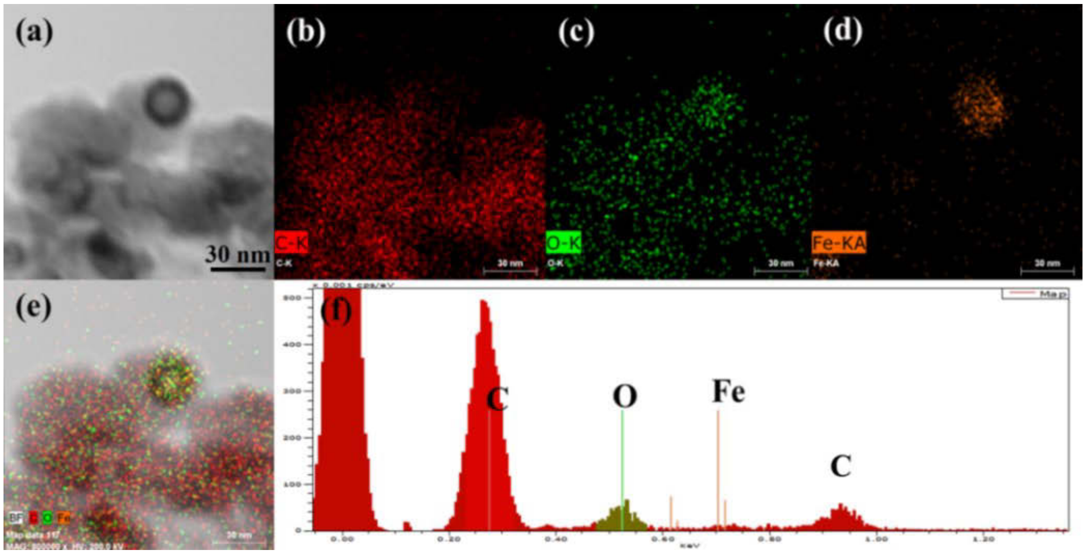

Figure 5- 8 TEM image of Fe_2O_3-CNT-GNS-2 (a) and corresponding elemental mapping images (b, c, d and e). (f) The corresponding EDX spectrum of Fe_2O_3-CNT-GNS-2

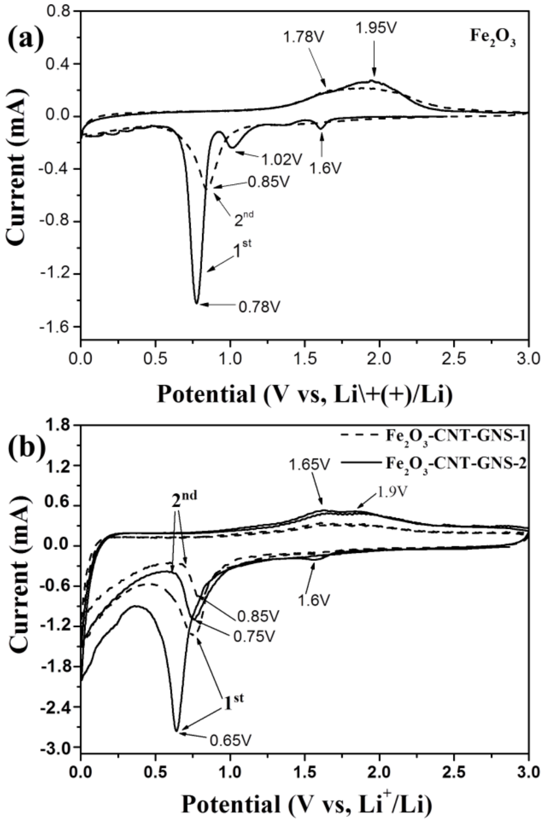

Figure 5- 9 Cyclic voltammogram (CV) profiles of bare Fe_2O_3(a), Fe_2O_3-CNT-GNS-1 and Fe_2O_3-CNT-GNS-2 hybrid materials (b) in the first two cycles with a scan rate of 0.1 $mV \cdot S^{-1}$.

The electrochemical behaviours of Fe_2O_3 and Fe_2O_3-CNT-GNS hybrid materials with a bamboo-like 3D structure were tested by cyclic voltammogram (CV, Figure 5-9a and b) with a scan rate of 0.1 mV/s. There are three main cathodic peaks in the initial negative scan for bare Fe_2O_3 at ~1.6, 1.02 and 0.78 V in Figure 5-9(a), including three lithiation steps with different iron states[195, 200-201]. The first small peak reflects formation of Li-intercalated hexagonal phase and the second peak is relevant to formation of Li-intercalated cubic phase, the sharp peak at 0.78V shows reduction of Fe^{2+} to Fe^0 and decomposition of electrolyte leading to the formation of solid electrolyte interface (SEI)[202]. However, there is only one main broad peak left at around 0.85 V in the second cycle, reflecting irreversible phase transformation during Li-ion insertion. The positive scan shows two hump-like anodic peaks at 1.78 and 1.95 V, indicating two steps of oxidation reaction of Fe (from Fe^0

to Fe^{2+}, then from Fe^{2+} to Fe^{3+}, respectively), while only one main broad peak with a little decrease in peak intensity at 1.78V is left at the second cycle, reflecting irreversible phase transformation during the lithium extraction. The shape and intensity of bare Fe_2O_3 are different in the twice scan, indicating low Coulombic efficiency. The electrochemical behaviours of Fe_2O_3-CNT-GNS hybrid materials in Figure 5-9(b) are similar to that of bare Fe_2O_3, except migration phenomena of reduction/oxidation peaks contributed by GNS and CNTs. There are three main cathodic peaks for Fe_2O_3-CNT-GNS-2 hybrid materials (1.6, 0.85 and 0.65V) and two main broad peaks in oxidation reaction (1.65 and 1.85V) in first scan. Similarly, the main reduction/oxidation peaks show at around 0.8V and 1.65V with a little decrease of peak intensities, respectively, which may contributed by irreversible phase transformation and SEI formation. The highly similar shapes indicate high Coulombic efficiency of Fe_2O_3-CNT-GNS hybrid materials.

The first charge/discharge profiles of four materials are shown in Figure 5-10(a) at a constant current density (74.4 $mA\cdot g^{-1}$, 0.1 C). In comparison, Fe_2O_3 nanoparticles (theoretic capacity [195-196, 203]: 1007 $mAh\cdot g^{-1}$) and bare GNS delivered reversible specific capacities of 1124 $mAh\cdot g^{-1}$and 435 $mAh\cdot g^{-1}$ with a Coulombic efficiencies of 71.5% and 28.5% in the first cycle, respectively. While Fe_2O_3-CNT-GNS-1 and Fe_2O_3-CNT-GNS-2 exhibited specific capacities of 885 $mAh\cdot g^{-1}$ and 984 $mAh\cdot g^{-1}$ in the first cycle, respectively. After 100 cycles, the specific capacity of the Fe_2O_3 electrode decreased to 112 $mAh\cdot g^{-1}$ (Figure 5-10(b)), which may be related to large volume change and the pulverization of materials during the lithiation process. However, Fe_2O_3-CNT-GNS hybrid materials demonstrated much improved cycling performance, owing to the open 3D architecture. The Fe_2O_3-CNT-GNS-2 sample maintained 812 $mAh\cdot g^{-1}$ after 100 cycles (Figure 5-10(b)). The corresponding morphologies of bare Fe_2O_3 and hybrid materials after cycling test are shown in Figure 5-11. As shown in Figure 5-11 (a) and (b), the surfaces of the electrode materials are covered by a SEI layer after cycling. TEM and HRTEM observations revealed that bare Fe_2O_3 particles were pulverised after cycling (Figure 5-11(c) and (d)). However, the Fe_2O_3-CNT-GNS-2 maintained the integrity. As shown in Figure 5-11 (e) and (f), Fe_2O_3 nanoring and CNT are clearly visible after 100 cycles. The relevant elemental mapping images and EDX spectra of Fe_2O_3-CNT-GNS hybrid materials after 100 cycles are shown in Figure 5-12(a-b).

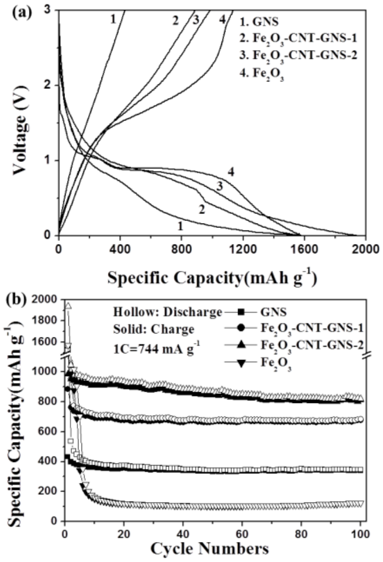

Figure 5- 10 The electrochemical performances of bare GNS, bare Fe_2O_3 nanoparticles, Fe_2O_3-CNT-GNS-1 and Fe_2O_3-CNT-GNS-2 electrodes: (a) Charge/discharge profiles of GNS, Fe_2O_3, Fe_2O_3-CNT-GNS-1 and Fe_2O_3-CNT-GNS-2 at a current density of 74.4 mA·g^{-1}, (b) Cycle performances of GNS, Fe_2O_3, Fe_2O_3-CNT-GNS-1 and Fe_2O_3-CNT-GNS-2 at a current density of 74.4 mA·g^{-1}.

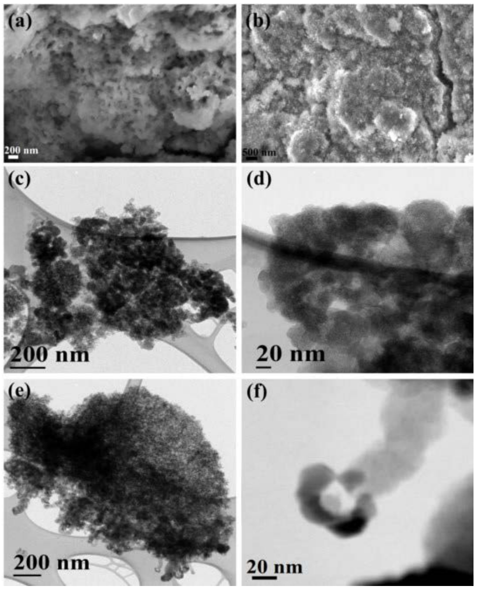

Figure 5- 11(a) SEM image of pure Fe_2O_3 after cycling test. (b) SEM image of Fe_2O_3-CNT-GNS-2 hybrid materials after cycling test. Low and high magnification TEM images showing structures of electrodes after cycling test. Pure Fe_2O_3 electrode after cycling test

are shown in images (c, d) and Fe_2O_3-CNT-GNS-2 hybrid materials after cycling test in (e, f). Images (d) and (f) are the magnified views of images (c) and (e), respectively.

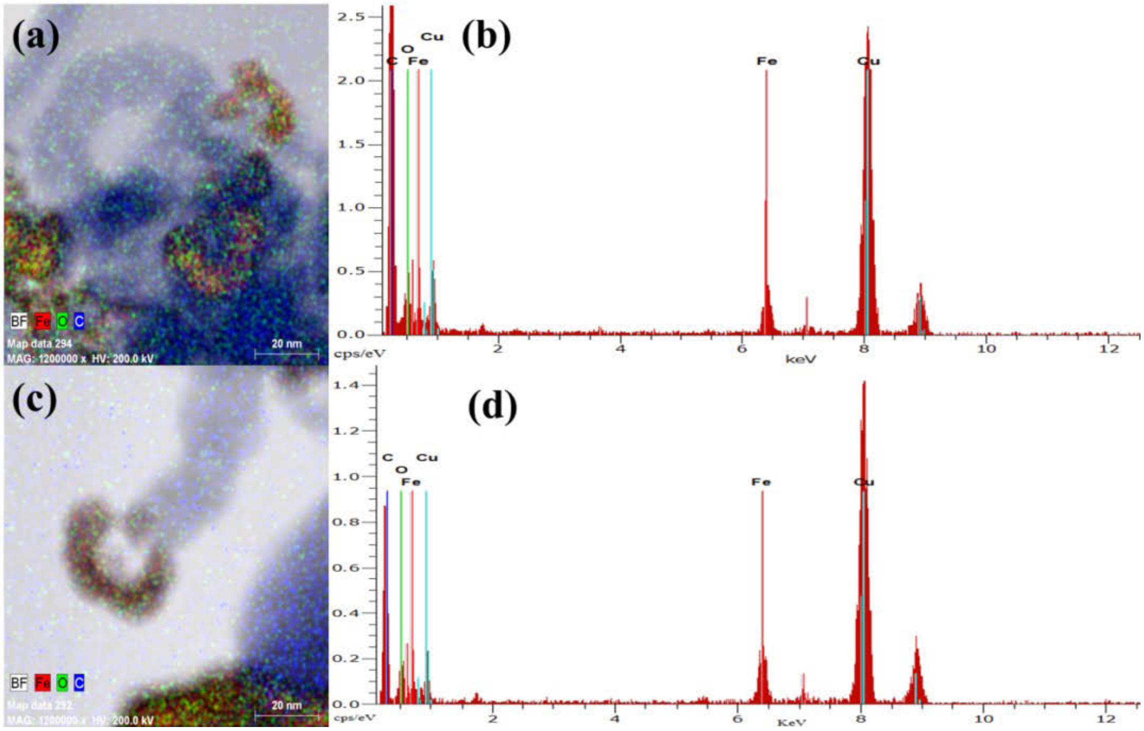

Figure 5- 12 The elemental mapping images of Fe_2O_3-CNT-GNS-1 and Fe_2O_3-CNT-GNS-2 hybrid materials after cycling test are shown in (a) and (c), respectively. The Energy Dispersive X-ray (EDX) spectra of the two hybrid material after cycling test are shown in image (b) and image (d), respectively.

The electrochemical performances of Fe_2O_3-CNT-GNS hybrid materials were also examined at higher current densities of 0.5 C, 1 C and 5 C, which are shown in Figure 5-13(a). The initial reversible specific capacity of Fe_2O_3-CNT-GNS-2 is 801 $mAh·g^{-1}$ at a current density of 372 $mA·g^{-1}$ (0.5 C), which is higher than that of Fe_2O_3-CNT-GNS-1 (787 $mAh·g^{-1}$). After 100 cycles, the specific capacity still remained 620 $mAh·g^{-1}$. When the current density was increased to 3720 $mA·g^{-1}$ (5 C), the Fe_2O_3-CNT-GNS-2 sample achieved a reversible capacity of 534 $mAh·g^{-1}$ and maintained 403 $mAh·g^{-1}$ after 100 cycles, with a retaining ratio of 75.5%. Furthermore, Fe_2O_3-CNT-GNS hybrid materials were also tested at various current densities (0.1 C, 0.5 C, 1 C and 5 C) and reversed back to lower current densities (Figure 5-13(b)). It should be noted that Fe_2O_3-CNT-GNS hybrid materials are tolerant to varied high current densities. When the current reverses back to a lower current, the specific capacities can almost recover to the original value. The electrochemical performances of Fe_2O_3-GNS hybrid materials are compared with other graphene based materials, which is shown in Table 5-1.

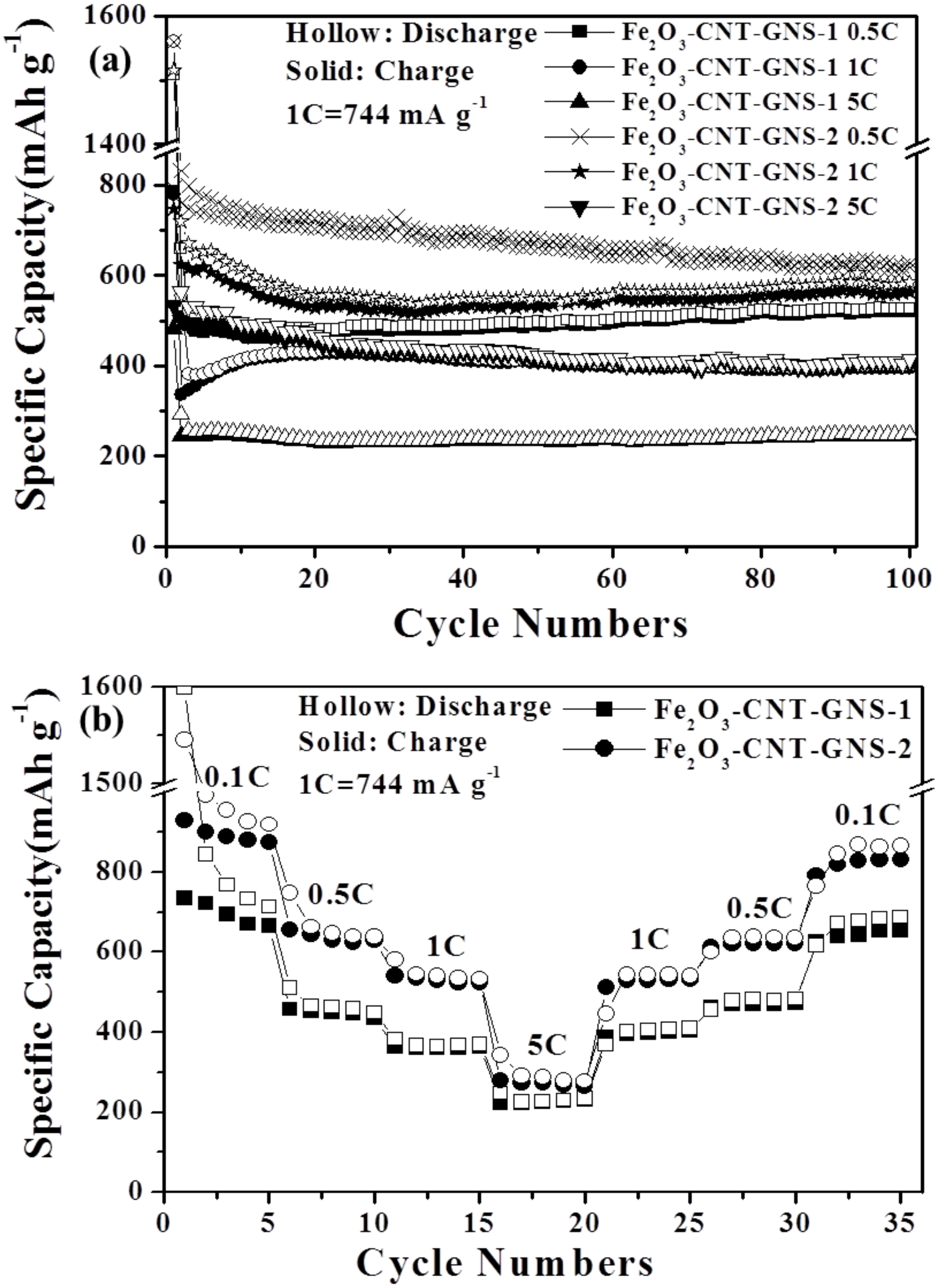

Figure 5- 13 The electrochemical performances at higher current densities (1 C= 744 mA·g^{-1}) of two hybrid materials: Cycling properties (a) and step-wise performances (b).

Table 5- 1 The comparison of electrochemical performances of different graphene basd materials.

Materials	Initial capacity (mAh/g)	Final capacity (mAh/g)	Retention ratio (mAh/g)	Rate capacity (mAh/g)
Fe_2O_3/GNS aerogel[204]	1045	995	95.2% (50 cycles)	601 (1 A/g)
Fe_2O_3/GNS[205]	711	668	94% (50 cycles)	660 (1.6 A/g)
Fe_2O_3/GNS[206]	960		81% (100 cycles)	435 (1 A/g)
The Thesis	984	812	82% (100 cycles)	659 (1 A/g)

The lithiation process in Fe_2O_3-CNT-GNS hybrid materials is described in Figure 5-14. Fe_2O_3 nanorings are anchored on the tips of CNTs, and carbon nanotubes are grown on the two sides of basal planes on GNS. Li^+ ions not only can react with Fe_2O_3 nanorings, but also can diffuse to the inside of CNTs through the open tips of CNTs. The cracks on the bamboo-like carbon nanotubes can further provide a direct path for Li^+ ions diffusion. In addition, the arc-like graphene layers contribute more active sites for Li ion storage. Furthermore, the outside of CNTs and two sides of GNS can also store Li^+ ions, which further increase the lithium storage capability. The 3D architecture based on CNTs and graphene networks could effectively buffer large volume changes during the lithium ion lithiation/delithiation and insertion/extraction process, and provide a highly conductive matrix for the diffusion of lithium ions and electron conduction [207-209].

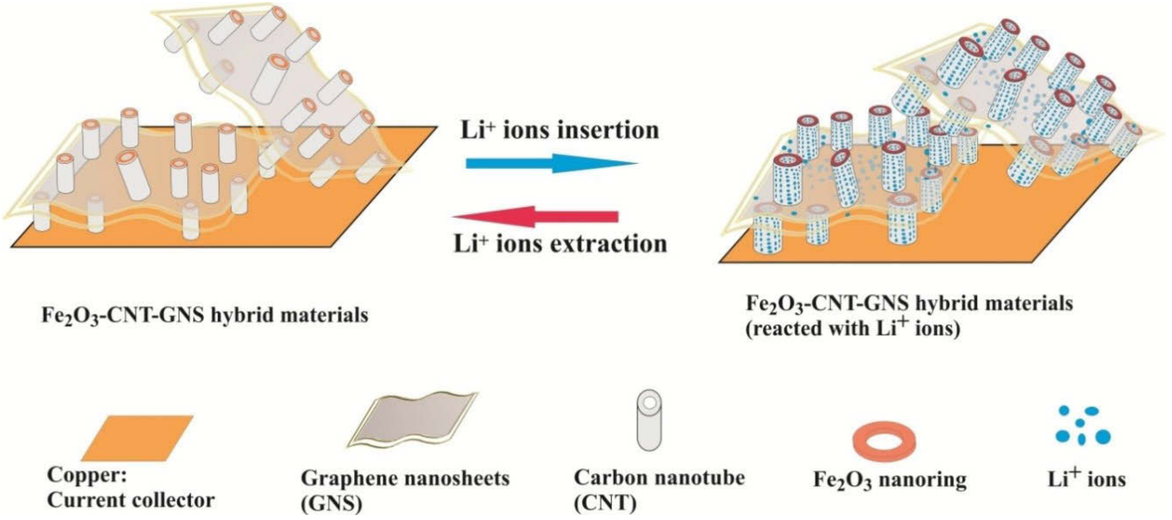

Figure 5- 14 Schematic processes of the Li^+ ions insertion and extraction in Fe_2O_3-CNT-GNS hybrid materials with an open 3D structure.

5.4 Conclusions

In summary, Fe_2O_3-CNT-GNS hybrid materials consisting of bamboo-like CNTs and Fe_2O_3 nanorings were successfully prepared by a chemical vapor deposition synthesis method. Fe_2O_3 nanorings play critical roles in forming bamboo-like carbon nanotubes. A modified “tip-growth” mechanism of carbon nanotubes and a unique lithiation process were proposed. When applied as anode materials in lithium ion batteries, the Fe_2O_3-CNT-GNS-2 hybrid materials exhibited a high specific capacity of 984 $mAh \cdot g^{-1}$ with a superior cycling stability and high rate capacity. This could be credited to the facile Li^+ ions diffusion through the open tips of CNTs and cracks on the outside walls of CNTs, and extra lithium storage sites provided by arc-like graphene layers inside CNTs. Flexible and highly conductive GNS and open 3D architecture also contribute to the superior electrochemical performance. The carbon-based hybrid materials with 3D structure could also be applied for lithium-air batteries, supercapacitors and fuel cells.

CHAPTER 6 LARGE-SCALE AND LOW-COST SYNTHESIS OF GRAPHENE AS ANODE FOR LITHIUM ION BATTERIES

6.1 Introduction

Since its discovery in 2004, graphene [147], a monolayer of carbon atoms with sp^2 bonds, has attracted intensive investigations world-wide. Many fascinating applications for graphene have been proposed, including electronics [146, 179, 210], super-strong composite materials, energy storage and conversion [211-213], molecular sensing and bio-medicine *etc*. [214-215]. Large-scale production of high quality graphene materials is critical to realize these applications. Graphene nanosheets have been prepared by micromechanical cleavage and chemical vapor deposition (CVD) growth on transition metal (Cu, Fe, Co, Ni) or noble metal (Ru, Pt) substrates [216-230]. Although gram-scale graphene materials have been produced through chemical methods such as modified Hummer method [94, 113-114, 231-232] and organic solvent dispersion method [233], these processes are labor intensive and involve in using toxic, corrosive or volatile chemicals. Longitudinal cutting of carbon nanotubes by plasma etching is also a good optional choice to achieve graphene with desired shape and size [234-237]. Among all previously reported techniques [217, 221, 238-241], CVD is regarded as a facile approach to prepare graphene in large quantities. Polycrystalline graphene films, four or six-lobe graphene flowers and hexagonally-shaped graphene grains have been prepared on Cu foils by several groups [219], [242-246]. However, it was found that the growth of graphene on Cu is self-limited. Monolayer or few-layer graphene and three-dimension graphene foam are also successfully deposited on nickel substrate (including Ni foam) [221, 247]. Driven by the “surface-catalysis-deposition” mechanism originated from the continuous connection of carbon fragments on the metal surface or the “dissolution-segregation-deposition” mechanism occurred through the segregation of absorbed carbon atoms at high temperature to metal surface and formation of graphene on cooling [226, 245, 248-249], maximum size of graphene grown on Cu, Co, Ni, Pt and Ru seldom exceeds the boundaries of the metal substrates [220-221, 242, 250-252]. Recently, electrochemical delamination has been reported to recycle metal substrates, demonstrating that copper foil can only be oxidized and consumed less than 40 nm during each growth-delamination-transfer cycle [253]. Repeated growth and bubbling transfer of graphene with millimeter-size using platinum as catalysts was reported by Cheng's group without any loss of Pt substrate [254]. The approaches capable to produce large quantity graphene must be developed to meet other demands of applications such as energy storage and conversion, molecular sensing and bio-medicine. Therefore, synthesis of high quality, large quantity and single crystalline graphene remains a considerable challenge.

With two times of theoretical capacity than that of graphite (372 mAh g^{-1}), fast carrier mobility and higher specific area, Graphene has been researched and applied as anode materials for a few years, illustrating both enhanced capacities and increased rate performances[86, 255]. Relevant graphene composites (Sn, Si, Ge, Co_3O_4, Fe_2O_3, NiO and MnO_2 *et al.*) also have substantially been investigated[49, 81, 94, 96, 106, 113, 116, 256-259], demonstrating improved specific capacities and cycliablities. Therefore, graphene and its composites are recognized as a promising material for the potential anode material in lithium ion batteries.

Inspired by the massive production of carbon nanotubes through the CVD method, we have developed an ambient pressure CVD (APCVD) process to produce graphene sheets on coral-like iron in gram-scale using a bottom-up strategy. The graphene growth is catalyzed by iron, which is similar to the production of carbon nanotubes. We proposed a new growth mechanism called "dissolution-deposition-growth". Differing from other transition metals, iron atoms arrange themselves into two stable crystal structures at different temperatures: the body-centered cubic structure (bcc structure, stable at 1394°C or above and 912°C or below, ferrite) and the face-centered cubic structure (fcc structure, stable between 912-1394°C, austenite) [195, 260]. Several factors including the concentration of carbon sources, growth time, morphologies and properties of substrates, pressure and cooling rate jointly affect the quality of graphene. Other research groups have demonstrated that graphene can be obtained by ambient pressure CVD or low pressure CVD method using Fe foils or films prepared by conventional magnetron sputtering method with varied thickness [227, 261-263], confirming that graphene with few layers can grow on Fe foils or films because the lattice constant of Fe (2.86Å) is closed to that of graphene (2.46Å) [227]. We found that the growth of graphene catalyzed by iron is not limited in the boundary of catalysts, leading to large-scale production. Herein, we report the large scale synthesis of graphene by the APCVD method using acetylene as carbon sources. The optimum temperature for the production of grapheme has been determined. The major advantages of the process are low cost (using acetylene and iron), high quality of the product (single crystalline) and scalable for large quantity production (1 gram graphene can be produced using 100 mg coral-like Fe catalysts).

6.2 Experimental

6.2.1 Preparation of catalysts

Fe_2O_3 nanoparticles were prepared by the chemical precipitation method. In a typical synthesis process, Iron nitrate nonahydrate (0.05 $mol\cdot L^{-1}$, 100 mL) was added into urea aqueous solution (1 $mol\cdot L^{-1}$, 100 mL) with magnetic stirring for 30 min. The as-obtained solution was kept at 102 ℃ under continuous magnetic stirring for 9 h in a 500 mL flask (equipped with a reflux condenser) in ambient atmosphere. Then the brownish red precipitation product was filtered and dried in a vacuum oven overnight at 95 ℃. The dry precursor was grounded into fine powders with an agate mortar and dispersed in ethanol with 1h ultrasonic treatment. After then, the suspension of Fe_2O_3 was dropped on silicon wafers. Finally, the Fe_2O_3-silicon wafers were dried overnight at 95 ℃.

6.2.2 Synthesis of graphene

In order to identify the optimum APCVD growth temperature and time, APCVD were carried out at 550 ℃, 650 ℃, 750 ℃, 825 ℃, 850 ℃, 875 ℃, 900 ℃ and 950 ℃, respectively, in a horizontal tube furnace. The furnace was heated at a rate of 5 $℃\cdot min^{-1}$ to the designated temperatures under flowing H_2/Ar (H_2: 5%, 400 sccm (standard cubic centimeter per minute)) and kept for 2h. Before cooling to room temperature, the C_2H_2/Ar gas (C_2H_2: 10%, 50 sccm) was introduced into the quartz tube. After the identification of the optimum temperature (850 ℃), APCVD was performed for different time durations: 5 min, 10 min, 30 min and 120 min at 850 ℃.

6.2.3 Materials characterisation

The as-prepared graphene products were characterised by X-ray diffraction (XRD, Rigaku D/max-2550V with Cu Kα radiation) operated at 40 KV and 30 mA. Raman spectra were measured using a Renishaw inVia Raman spectrometer system (Gloucestershire, UK) equipped with a Leica DMLB microscope (Wetzlar, Germany) and a 17mW at 633 nm renishaw helium neon laser with 50% power. Atomic force microscopy (AFM) measurements were performed on Dimension 3100 SPM with a tapping mode. The Brunauer–Emmett–Teller (BET) surface area was calculated using experimental points at a relative pressure of P/P^0= 0.05–0.25. The pore size distribution was derived from the desorption branch using the Barret–Joyner–Halenda (BJH) method. The morphologies and crystal structure of graphene sheets were analysed by a field emission scanning electron microscope (FE-SEM, JSM-6700F, 20kV) and transmission electron microscope/selected area electron diffraction (TEM/SAED, JEOL JEM-200CX and JEM-2010F) equipped with an energy-dispersive X-ray spectroscopy (EDX). A thermogravimetric analyser (TGA, SDT 2960) was applied to measure the weight percentage of graphene. X-ray photoemission spectroscopy (XPS) was measured by ESCALAB220i-XL (VG Scientific) system with a standard high vacuum at 2×10^{-9} mbar and a monocharomatic aluminium Kα source. Fourier Transform Infrared (FTIR) Spectra were obtained by Nicolet Magna 6700 FTIR spectrometer. Graphene sheets (1.5 g) were compressed into a round cylinder (at least 10 mm in height). The electrical conductivity was measured using a four-point probe method using a model 2000 6½-digit Keithley Multimeter.

6.2.4 Electrochemical measurements

The working electrodes were made from 80 wt% of active materials, 10 wt% of the conductive agent (acetylene black), and 10 wt% of the binder (polyvinylidene difluoride). The mixture was stirred by an adjustable high-speed electric agitator. The working electrodes were dried in a vacuum oven. CR2032 coin cells were assembled in an argon-filled glove box (Mbraun, Unilab, Germany), in which both the moisture and oxygen contents were controlled to be less than 0.1 ppm. Lithium foil was used as the counter electrode. The electrolyte (Zhangjiagang Guotai-Huarong New Chemical Materials Co., Ltd.) was 1M $LiPF_6$ in a 1:1 (weight ratio) mixture of ethylene carbonate and diethyl carbonate. Electrochemical measurements were performed using a LAND-CT2001C battery test system. The cells were discharged and charged galvanostatically in the fixed voltage range of 0.005-3.0 V with a current density of 74.4 $mA\cdot g^{-1}$ (0.1 C). Higher current rates (0.5 C, 1 C, 5 C and 10 C) were also used to test the electrochemical performance.

Cyclic voltammetry was measured on a CHI 660D electrochemical workstation at a scan rate of 0.5 $mV \cdot S^{-1}$.

6.3 Results and discussion

As described in the experimental section, large quantities of graphene have been synthesized at 850 °C by APCVD using a mixture gas of acetylene and argon. The growth of graphene sheets was catalyzed by coral-like iron particles. The as-grown graphene products can be easily harvested by dissolving iron catalysts in hot hydrochloric acid, then washing with copious de-ionized water and drying in a vacuum oven. An example of the as-synthesized products (about 1 gram) is shown Figure 6-1a and an application of a luminous light emitting diode powered by three cell batteries connected in series with as-prepared graphene as the anode material is also presented in Figure 6-1b, which can keep luminous for 5 days. The field emission scanning electron microscope (FESEM) image of coral-like iron catalysts covered by transparent graphene sheets can be easily observed in Figure 6-1c. Obviously, graphene sheets grow across the catalyst' boundaries and extend to blank and broad domains. The previous reported growth mechanisms both "surface-catalysis-deposition" and "dissolution-segregation-deposition" cannot well explain this phenomenon. Therefore, a new growth mechanism must be developed to explain the growth process. Figure 6-1d shows the SEM image of graphene sheets with a size of approximate 40 μm^2, which contains some winkles associated with the difference of the thermal expansion coefficient between graphene and Fe during cooling. In the first step of the synthesis, Fe_2O_3 nanoparticles (about 20 nm) were firstly prepared by a urea-assisted precipitation method. During deposition, Fe_2O_3 nanoparticles were reduced to Fe and form coral-like porous iron networks (as shown in Figure 6-2 a and b).

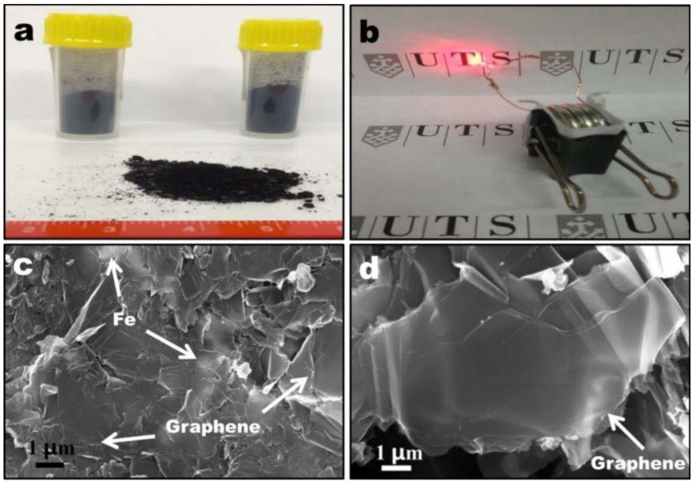

Figure 6- 1 (a) Example of graphene in large quantity (about 1 g) produced by CVD method using C_2H_2 as the carbon source and Fe as the catalyst. (b) A luminous light-emitting diode powered by three coincells cells connected in series with graphene electrode as the anode material. (c) FESEM images of the as-prepared graphene sheets with coral-like Fe particles. (d) Graphene sheets after the removal of iron catalysts.

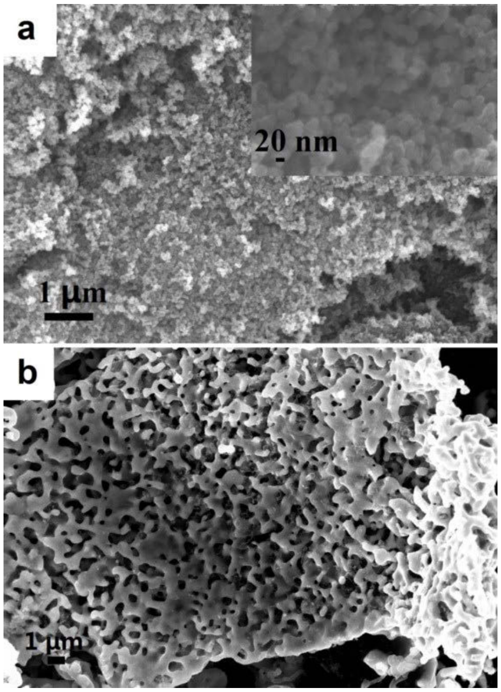

Figure 6- 2 Low and high magnifications of SEM images showing morphologies of Fe_2O_3 nanoparticles (a) obtained by urea-assistant precipitation method and the insert image represents the details of the precursor (~20 nm). (b) Coral-like Fe particles were formed when the precursor was reduced by H_2 at 850 ^{o}C for 2h.

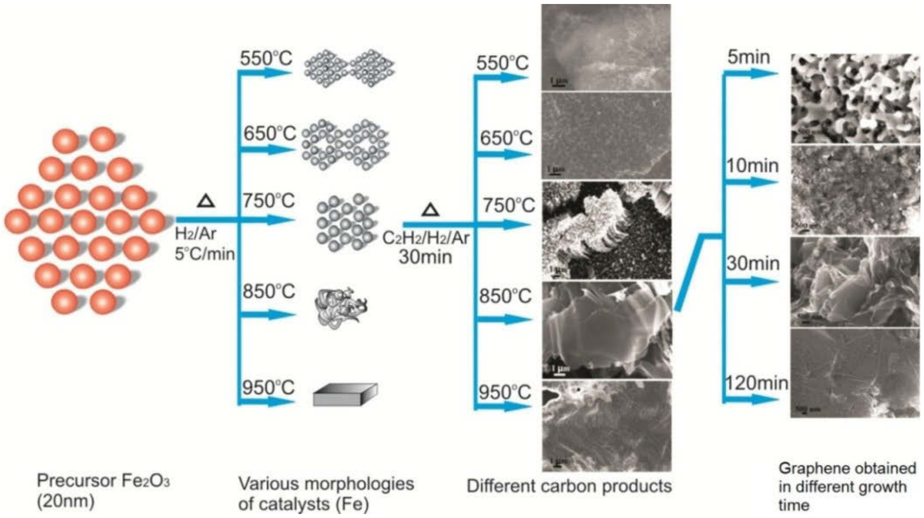

Figure 6- 3 The schematic diagram of synthesis graphene and other carbon materials (including carbon nanofibers, carbon nanotubes, vertically alligned carbon nanotubes and graphite) at different temperatures and different growth times.

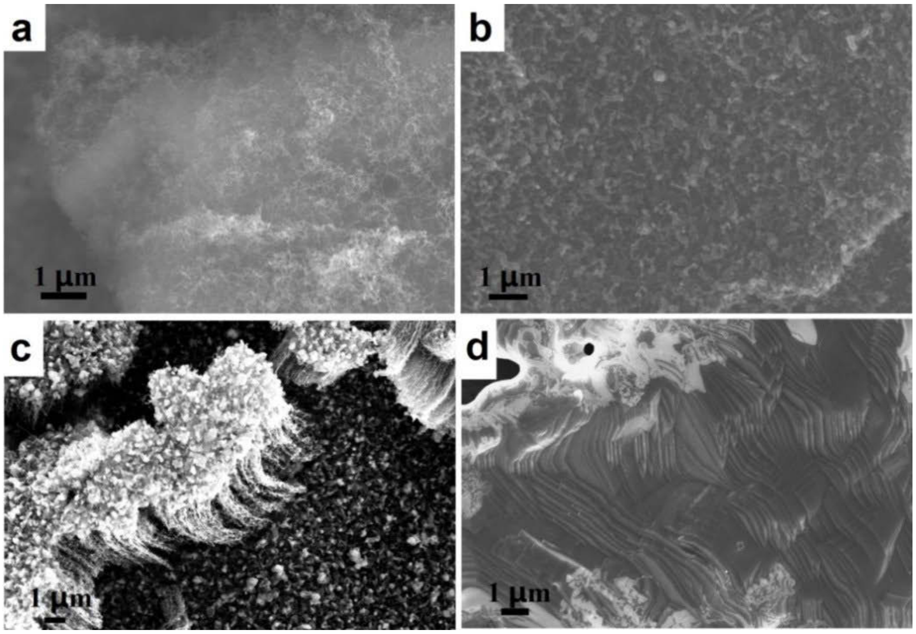

Figure 6- 4 Different products obtained by CVD at different temperatures. (a) Carbon nanofibers (550 ^{o}C). (b) Carbon nanotubes (650 ^{o}C). (c) Vertical carbon nanotubes (750 ^{o}C). (d) Graphene fragments (950 ^{o}C).

We explored the influences of temperature and growth time on the APCVD deposition products. Aiming to generate iron nanoparticles and complete the structure transformation of iron at the specific temperature, Fe_2O_3 nanoparticles were firstly reduced to Fe in H_2 for 2 h. As the volume of Fe_2O_3 is larger than that of Fe, the space of Fe nanoparticles occupied will shrink during the reduction process. When APCVD was carried out at 550 °C, carbon nanofibers (CNF) catalyzed by Fe nanoparticles with diameters less than 20 nm were obtained (Figure 6-3) [264], which could be ascribed to the "tip-growth" mechanism[265-267]. Fe particles were anchored on the tips of CNFs (Figure 6-4a and 6-5a-c). As the temperature was increased to 650 °C, carbon nanotubes were formed (Figure 6-3). With "tip-growth" mechanism, end-opened CNT can be observed in Figure 6-4b and 6-5d-f. When the temperature was set at 750 °C, vertically aligned carbon nanotubes were primarily formed, followed with "tip-growth" mechanism (Figure 6-4c and 6-6a-b). The agglomeration of iron nanoparticles could lead to the deposition of carbon layers following the "dissolution-deposition-growth" mechanism. Meanwhile, vertical "tip-growth" mechanism still played a role for growing carbon nanotubes [268]. Interestingly, when the APCVD was performed at 850 °C, porous coral-like iron structures with a smooth surface were formed, which could be ascribed to partial melted individual iron nanoparticles. The agglomeration of iron nanoparticles could absorb maximum 0.022% carbon at 850 °C [227]. The acetylene diffused and dissolved on the surface of Fe (body-centered-cubic structure), then decomposed to active carbon atoms and hydrogen atoms. Once the carbon concentration absorbed in the lattice of Fe reached the maximum value, active carbon atoms deposit along the outside of Fe particles, form hexagonal structure and gradually grow into graphene. With the assistance of high-energy hydrogen atoms and continuous supply of acetylene, large-size and gram-scale graphene sheets were produced (Figure 6-8), which is named as the "dissolution-deposition-growth" mechanism. TEM, High-resolution TEM (HRTEM) and SAED images in Figure 6-7a-d confirmed the proposed growth mechanism. However, when the reaction temperature was further increased to 950 °C, iron nanoparticles melted and formed a large size iron monolith with ladder-like surface structure (Figure 6-4d). Meanwhile, body-centered cubic structure of alpha iron was transferred into face-centered cubic structure, inducing a significantly decreased catalytic activity. Only a few carbon fragments were observed (Figure 6-4d). The X-ray diffraction (XRD) patterns show the phase changes of the catalysts at different APCVD conditions and different carbon products (Figure 6-9).

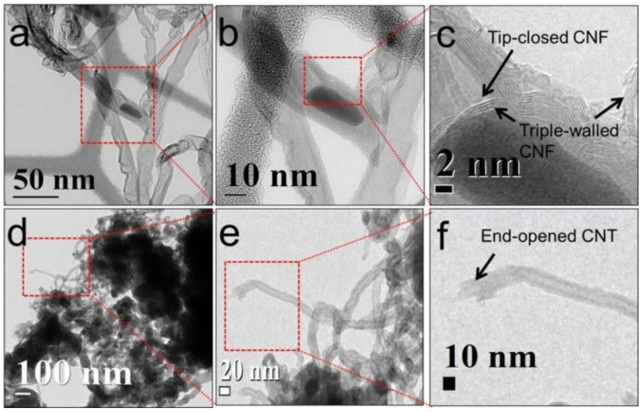

Figure 6- 5 High and low magnifications of TEM images (a-b) of CNF obtained at 550°C, followed with "tip-growth" mechanism. High and low magnifications of TEM images (c-d) of end-opened CNTs obtained at 650 °C, followed with "tip-growth" mechanism.

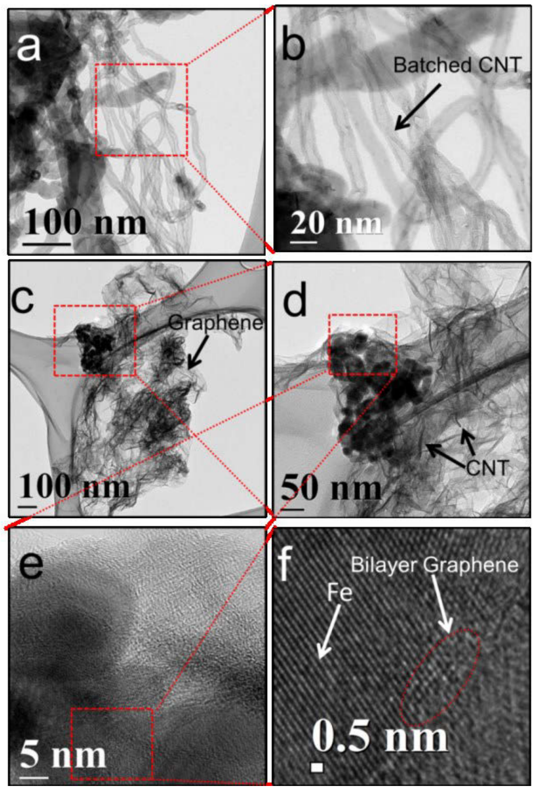

Figure 6- 6 High and low magnifications of TEM images (a-b) of vertical batched CNTs obtained at 750 °C, followed with "base-growth" mechanism. TEM and HRTEM images (c-f) of graphene sheets with few CNTs obtained at 825°C, followed with "dissolution-deposition-growth" mechanism, demonstrating that once the catalyst formed the coral-like shape, the carbon products are no longer forming an closed carbon cylinder shape, therefore, sheet-like carbon product is gained.

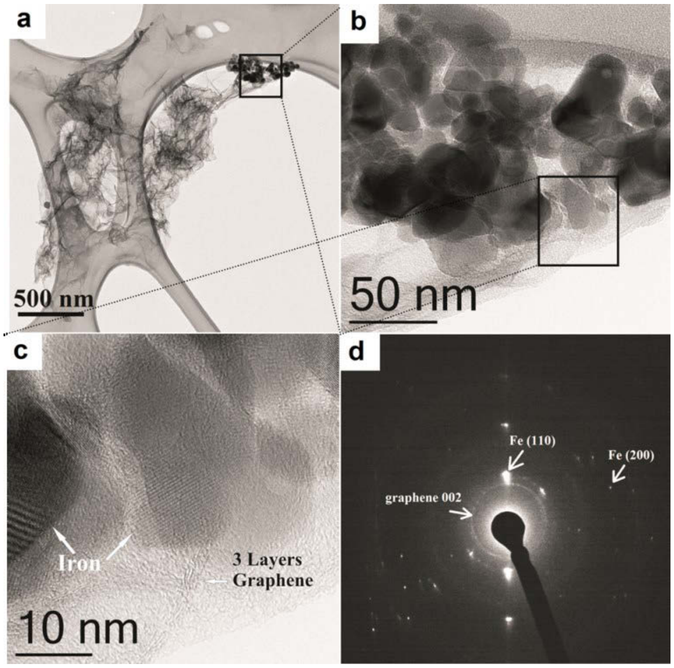

Figure 6- 7 TEM and HRTEM images (a-c) of graphene with coral-like Fe particles by CVD at 850 ^{o}C for 10 min. Image (b) is one part of image (a) where labeled by a black square. Image (c) represents the details of image (b) where labeled by a black square. The selected area electron diffraction (SAED) pattern (d) is taken from image (c) and the corresponding diffraction spots for each material have been labeled.

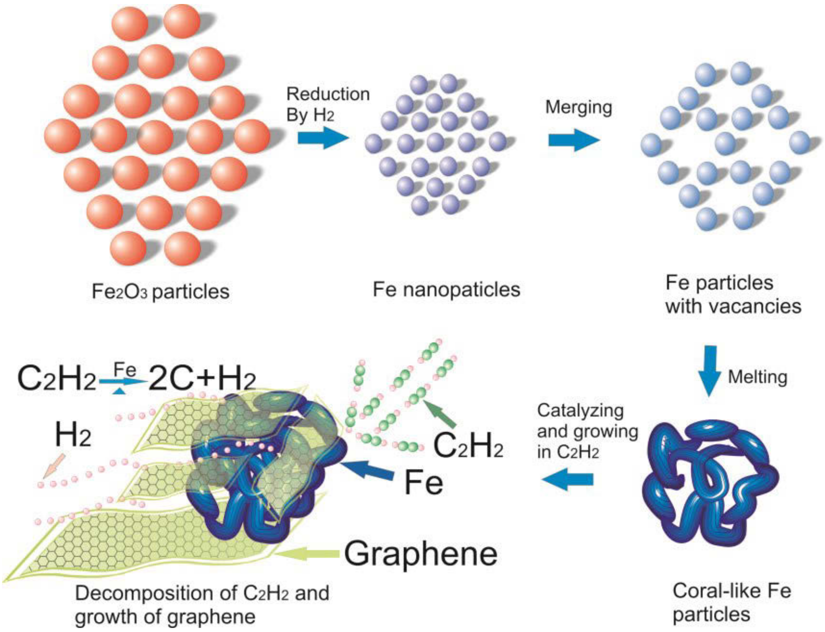

Figure 6- 8 Schematic illustration of the “dissolution-deposition-growth” mechanism. Fe_2O_3 nanoparticles (about 20 nm) were reduced by H_2 for 2h and shrank to Fe

nanoparticles. Affected by heat treatments, Fe particles are shrunk, merged and melton with the increasing of temperatures. The acetylene firstly diffuses on Fe surface (body-centered-cubic structure) and decomposes to active carbon atoms and hydrogen atoms. Once carbon concentration absorbed in the lattice of Fe reached the maximum value, active carbon atoms merge along outside of Fe particles, form hexagonal structure, and gradually grow into graphene sheets. With the assistance of high-energy hydrogen atoms and continuous supply of acetylene, large-size and gram-scale graphene sheets can be produced, which is called “dissolution-deposition-growth” mechanism.

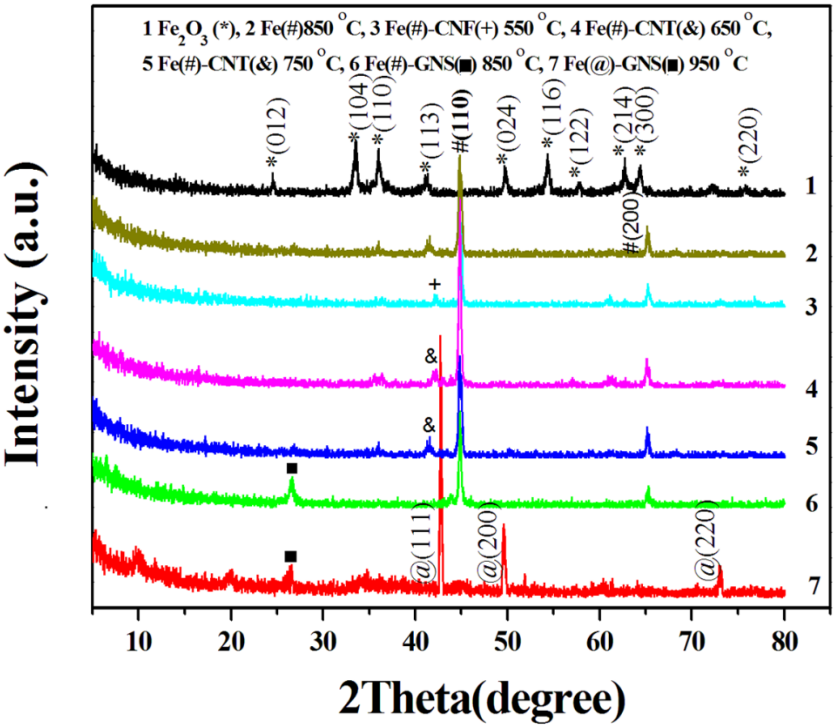

Figure 6- 9 X-Ray diffraction pattern of a series of samples: (1) Fe_2O_3 obtained by urea-assistant homogenous precipitation method. (2) Fe particles reduced by H_2 at 850 °C. (3) Fe-CNF (carbon nanofiber) hybrid materials obtained at 550 °C. (4) Fe-CNT hybrid materials obtained at 650 °C. (5) Vertically batched CNT and Fe hybrid materials obtained at 750 °C. (6) Graphene and coral-like Fe nanoparticles synthetized at 850 °C. (7) Multi-layer graphene sheets and molten Fe particles obtained at 950 °C. The Fe_2O_3 particles show the hematite state, which accords with JCPDS No. 33-0664 with space group at R-3c (167). The as-synthesised Fe nanoparticles at 850 °C agree well with Synthesis alpha iron (JCPDS No. 06-0696, with the space group at Im-2m (229)). And Fe nanoparticles at 950 °C

transfered to austenite which agrees well the JCPDS No. 52-0513, with the space group at Fm-3m (225). The followed samples with CNTs are show two kinds of peaks (CNTs and Fe), while the graphene and Fe hybrid materials reflect graphene and large size of Fe nanoparticles.

In order to further verify the optimum temperature for growing graphene, APCVD was also performed at 825 °C and 875 °C, respectively. We found that graphene sheets and small amount of carbon nanotubes were obtained at 825 °C and carbon coating phenomenon occurred at 875 °C (Figure 6-10a and 6-10b, repectively). Therefore, we have determined that 850 °C is the optimum temperature for the growth of graphene under the catalysis of coral-like iron nanoparticles. This temperature is much lower than that catalyzed by Cu [216, 218-219, 241, 246], Ni, Ru and Pt reported previously[223, 252, 269].

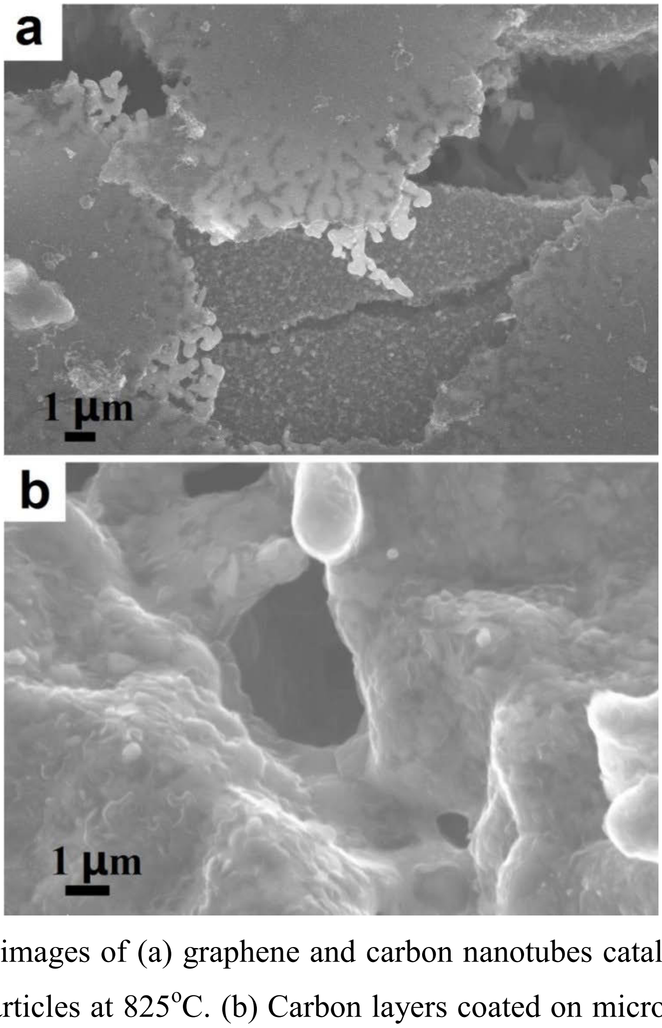

Figure 6- 10 SEM images of (a) graphene and carbon nanotubes catalyzed by polyporous and coral-like Fe particles at 825°C. (b) Carbon layers coated on micro-size Fe particles at 875 °C.

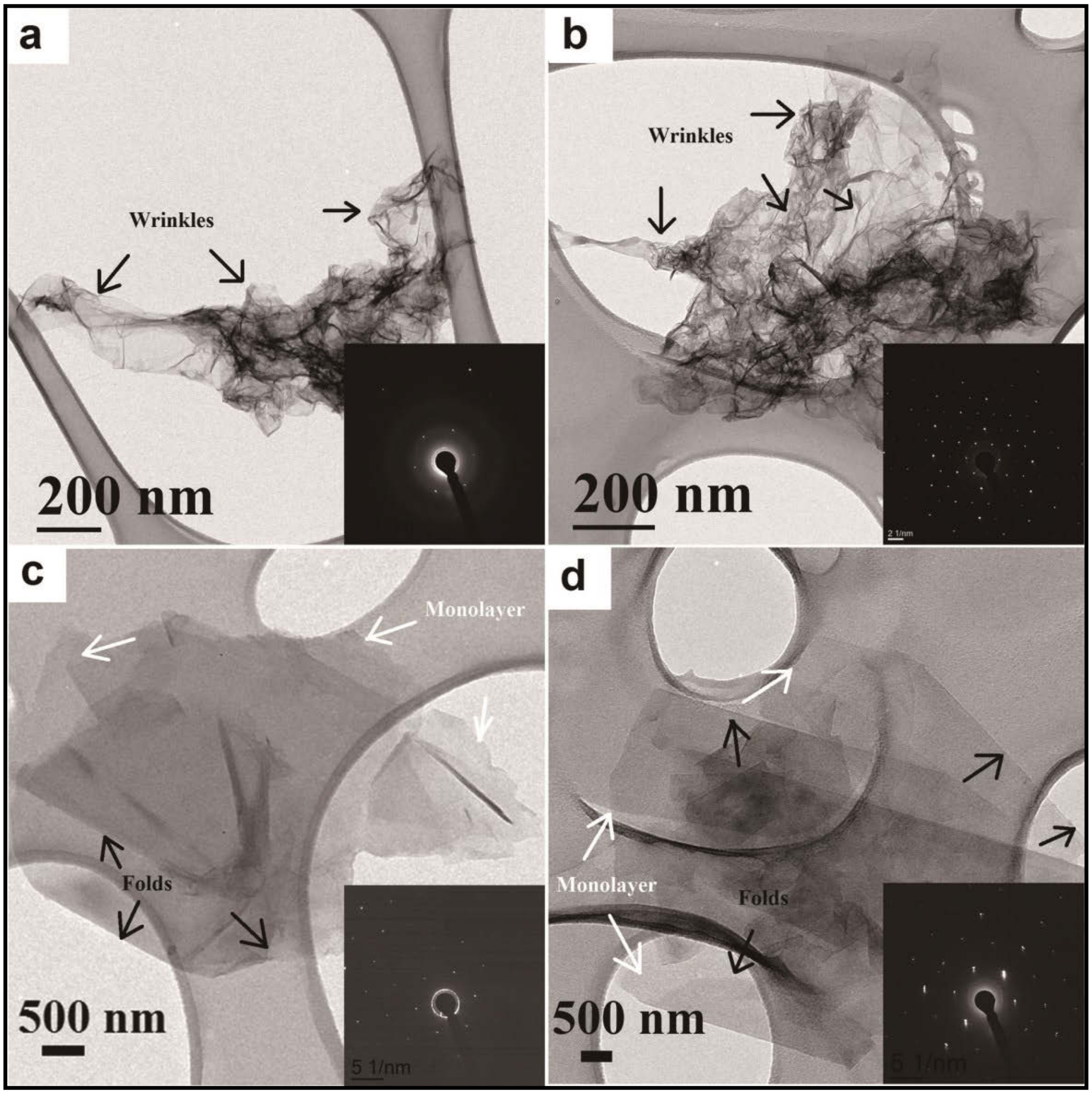

Figure 6- 11 TEM images of graphene sheets grown by APCVD at 850 ^{o}C with varied growth time. The inset images are the corresponding SAED patterns of graphene sheets. (a) Graphene with wrinkles obtained by APCVD growth for 5 min, pointed by black arrows. (b) Graphene with wrinkles obtained by APCVD growth for 10 min, pointed by black arrows. (c) Graphene with folds obtained by APCVD growth for 30 min, marked by black arrows. The monolayer graphene sheets are labeled by white arrows. (d) Graphene obtained by APCVD growth for 120 min. The folded graphene sheets are annotated by black arrows and monolayer graphene sheets are labeled by white arrows.

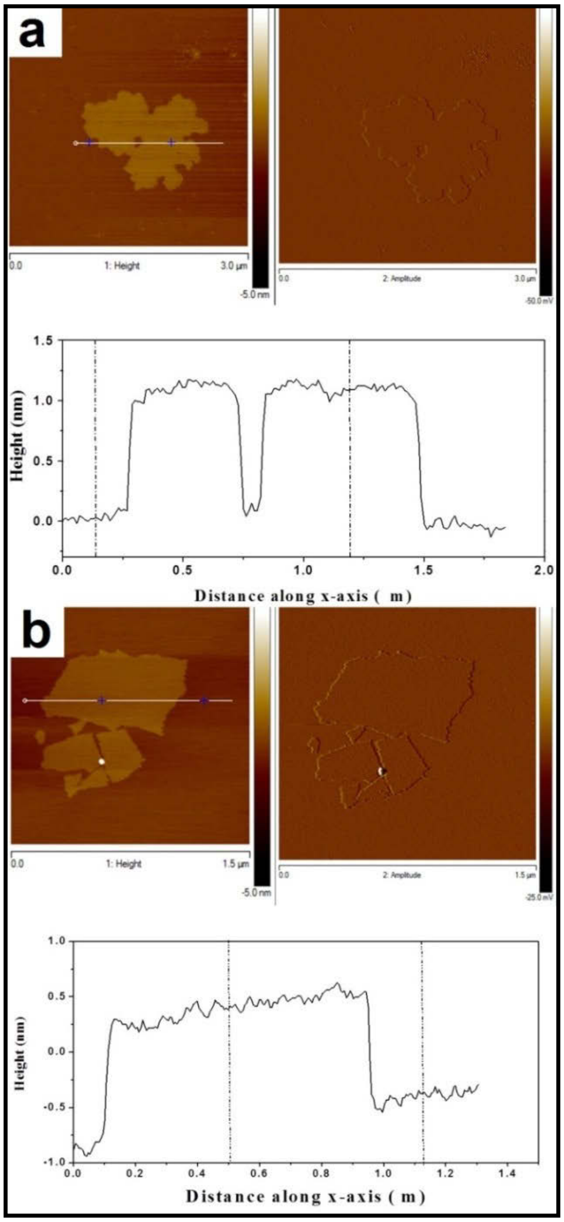

Figure 6- 12 AFM images of graphene sheets obtained by tapping mode. The topography, amplitude and height profile are included for each sample. The height profiles obtained from the topography images are marked by white line with Prussian blue cross. Mica discs were used as the substrate. (a) Porous graphene sheets obtained through APCVD growth for 5 min, (b) Crystalline graphene sheets obtained through APCVD deposition for 10 min.

After the identification of the optimum temperature, we investigated the influence of the APCVD reaction time on productivity, crystallinity and size of graphene sheets. Four batches of graphene were synthesized by APCVD at 850 °C for 5, 10, 30 and 120 minutes, respectively. Those graphene products were measured by the thermogravimetric analysis

(Figure 6-13a). Moreover, the percentage of graphene in composites were shown in Figure 6-13b, and a Boltzmann curve illustrated the relationship between weight percentage of graphene and growth time, showing growth speed was relatively fast in the first 30min, then witnessed a slowly increasing tendency. The products were characterized by FESEM, TEM and selected area electron diffraction (SAED) patterns (Figure 6-11) and atomic force microscopy (AFM) analysis (Figure 6-12). Figure 6-11a shows the TEM image of the graphene sheets obtained for 5 minutes, from which ripples and wrinkles marked by black arrows are clearly visible. One set of six-fold symmetric diffraction spots and two diffraction rings are observed. This indicates that the graphene sheets are single crystalline with some defects. AFM observation determined that the size of graphene sheets is about 2.5 μm^2 with a thickness of 0.9 nm, exhibiting the average size of graphene is approximate 2 μm^2 by statistics. It should be noted that this batch of graphene sheets has typical defects (as shown in Figure 6-12a). The defects of graphene sheets may be related to unsufficient supply of carbon source due to short growth time (5 min) and etching effect of hydrogen [252]. When the growth time is prolonged to 10 minutes, the size of graphene expands to ~ 3 μm^2 (Figure 6-11b) with a thickness of 0.7 nm. As show in the AFM image (Figure 6-12b), there is no obvious defects on graphene sheets, even though several larger cavities still exist. Figure 6-11c-d show monolayer graphene sheets with some folds, indicating the improvement of the quality.

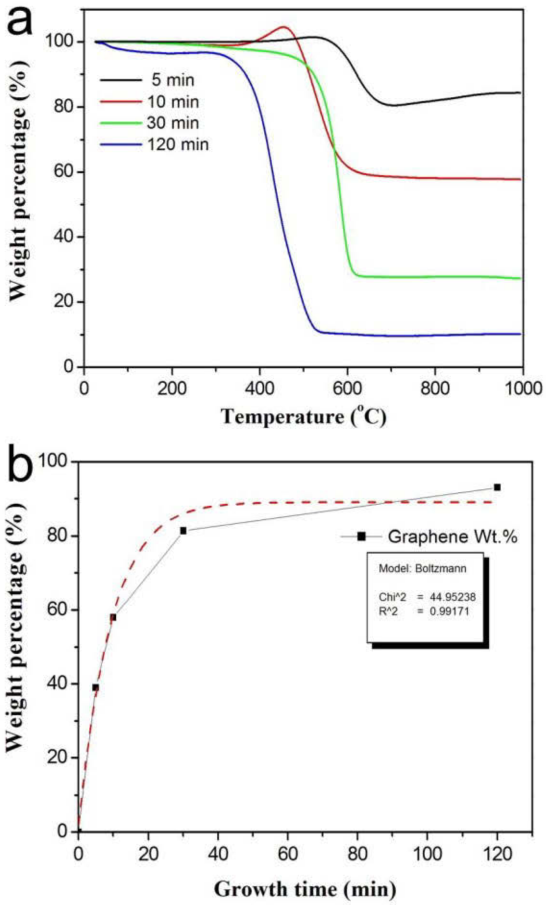

Figure 6- 13 (a) Thermal gravimetric analysis of graphene-Fe products obtained at 850^{o}C with different growth times (5, 10, 30 and 120 min, respectively). (b) The weight percentages of graphene in with different growth times and a Boltzmann curve is shown the possibility of growth speed.

The crystal structure of the as-synthesized graphene sheets was further analyzed by HRTEM, Figure 6-14a shows HRTEM images of monolayer, bi-layer, and triple-layer graphene sheets as well as their corresponding SAED patterns. The HRTEM observation is consistent with SAED identification. For monolayer graphene (Figure 6-14a), one set of six-fold symmetric diffraction spots is observed, which is consistant with previous reports[219, 242]. The bi-layer graphene presents two sets of six-fold symmetric diffraction spots with a rotation on stacking of 30^o between the two layers, and similar report also demonstrates the twisted angles with values between 0^o and 30^o. The triple-layer graphene sheets exhibit three sets of six-fold symmetric diffraction spots with a rotation of 3^o among those diffraction spots. Whereas, if there is no rotation among AB stacked graphene layers, only one set of six-fold symmetric diffraction spots can be detected. Figure 6-14b-e show HRTEM images of basal planes of graphene sheets produced in four different batches (5, 10, 30 and 120 min, respectively). Figure 6-14b exhibits a typical feature of amorphous carbon, indicating graphene has not been well crystallized within 5 min growth time, containing some defects. From Figure 6-14c, we can observe the co-existence of zigzag and arm-chair directions on the basal of graphene synthesized in 10 min. Previous studies claim that the zigzag edges are preferred in graphene grown on polycrystalline metal (Cu) substrate and arm-chair edges may be strongly influenced by CVD condition and electron beam exposure from the microscope[219, 270]. As illustrated in Figure 6-14d and e, well-crystalline lattices were achieved when the growth durations were extended to 30 min and 120 min, respectively.

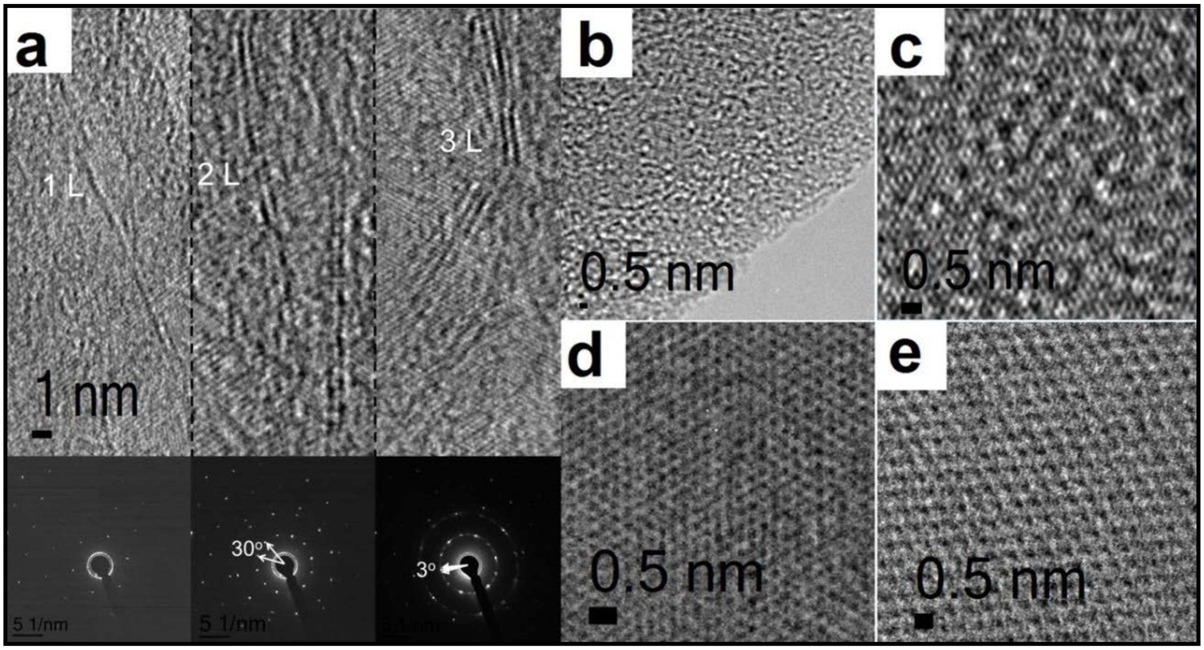

Figure 6- 14 HRTEM images of graphene sheets produced by APCVD at 850 ^{o}C in different growth times. (a) Graphene sheets with different number of layers and their corresponding SAED patterns. The hexagonal SAED pattern of bilayer graphene shows a rotation in stacking of 30^{o} between two layers and pattern of triple layers graphene exhibits a rotation in stacking of 3^{o}. (b-e) HRTEM images of fine structures of carbon atoms on the basal plane of graphene sheets produced by different APCVD deposition times (b: 5 min, c: 10 min, d: 30 min, e: 120 min), demonstrating improved crystallinity and quality of graphene sheets with the increase of growth time.

The physical and chemical properties of graphene sheets were also characterized by Raman spectra and XPS. Raman spectroscopy is a powerful tool to identify the number of graphene layers and detect amorphous structure [271]. According to the previous reports [161-162, 272], the intensity ratio of G and 2D bands (I_G/I_{2D}) increases with the number of graphene layers. When the value of I_G/I_{2D} is around than 0.5 and the full width at half maxima (FWHM) is less than 50 cm^{-1}, the graphene sheet can be confirmed to be monolayer. An optical microscope image, 40 μm in length, is presented in Figure 6-15a. The Raman spectra in Figure 6-15b were taken from the location A, B and C, marked in Figure 6-15a. The Raman spectrum taken from the location A has the lowest value of I_G/I_{2D} (<0.5), indicating monolayer graphene. The values of I_G/I_{2D} increase at the location B and C, illustrating bilayer and tri-layer graphene or the folded monolayer graphene sheet. Aiming to verify the state of graphene in a continuous area, Raman mapping spectroscopy was acquired from the rectangle part, showing the intensity ration of I_G/I_{2G} in Figure 6-15c (related to the thickness of graphene) and the profile of FWHM is shown in Figure 6-15d. The average FWHM is around 35.1 cm^{-1} (an average data statistic calculated from 85 Raman spectra), indicating less apparent defects and amorphous structure. Three-dimensional views of all Raman spectra and intensity of G and 2G bands are shown in Figure 6-15e-g, respectively, which can vividly demonstrate the distribution of graphene and intensities of G and 2D bands. Even though graphene varies among monolayer to triple-layer, the intensities of 2D band exhibited constant value, which might be those rotations of graphene sheets (Figure 6-14a) that largely reduced the interlayer coupling effect. AFM, HRTEM, SAED and Raman spectroscopy analysis clearly confirmed that monolayer to triple-layer graphene sheets have been obtained through the APCVD deposition catalyzed by iron.

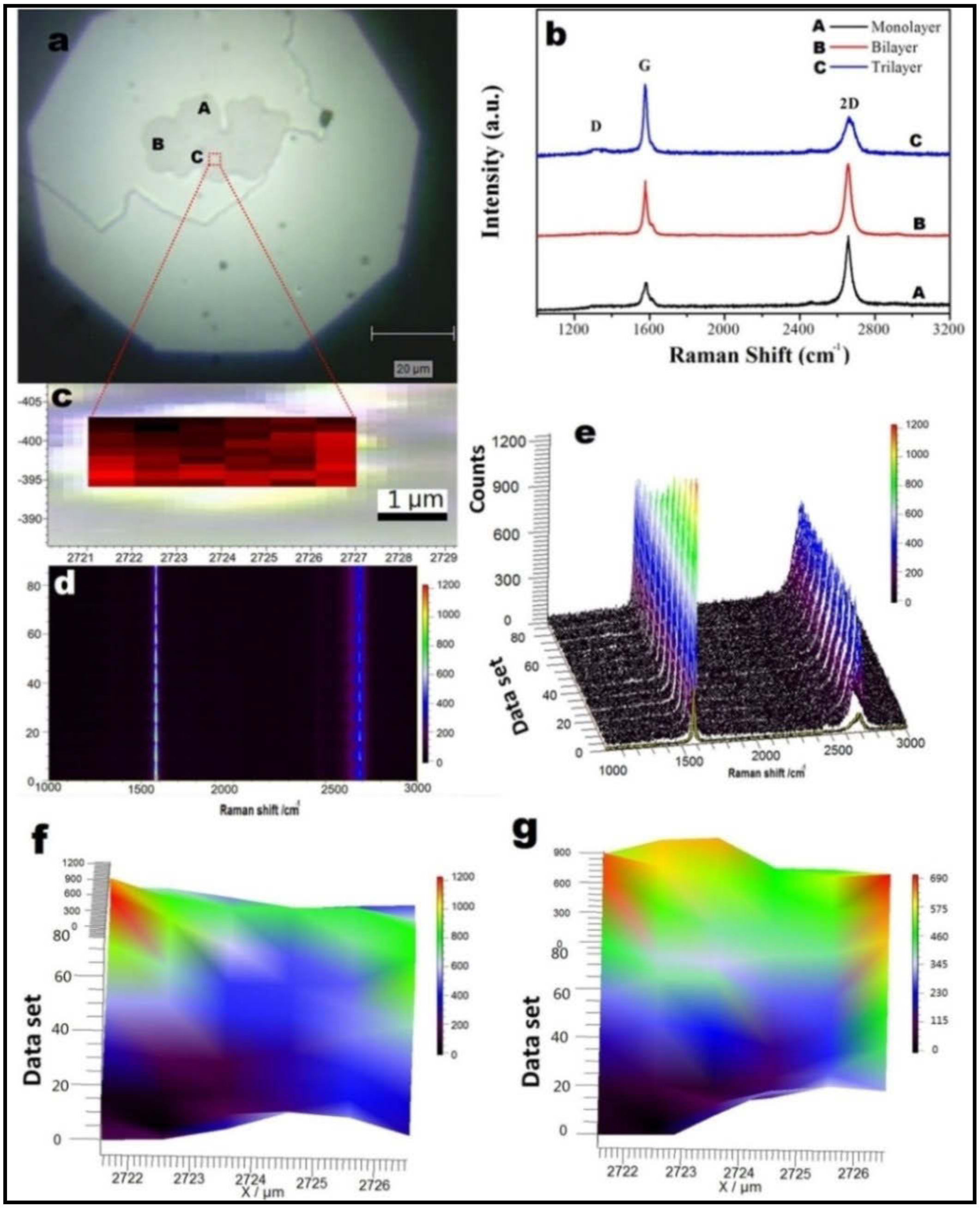

Figure 6- 15 (a) An optical microscope image of graphene taken by a Renishaw inVia Raman spectrometer. (b) Raman spectra of monolayer, bilayers and triple layers graphene sheets taken from the location A, B and C marked in (a). (c) An optical microscope image of Raman map of I_G/I_{2G} intensity ratio. (d) Top-view of Raman spectra acquired from the rectangle area in the image (c), showing average full width at half maxima (FWHM) of 35.1 cm^{-1}. (e-g) 3D-view of Raman spectra illustrated by full colour, intensity of G band and 2G bands, respectively.

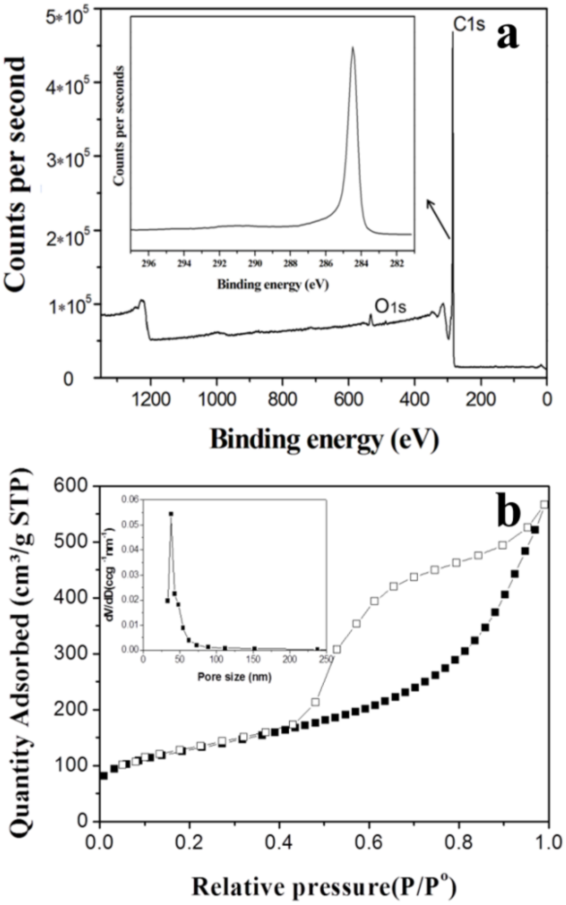

Figure 6- 16 X-ray photoelectron spectroscopy spectrum (a) of graphene obtained at 850 °C grown for 30 min. Insert: Peak comes from carbon atoms. The atomic concentration of carbon is more than 99.3%. Nitrogen adsorption/desorption analysis (b) of graphene obtained at 850 °C grown for 30 min. The insert in (b) is the pore size distribution of graphene.

XPS spectrum of the graphene sample synthesized by 30 min APCVD deposition is shown in Figure 6-16a, demonstrating a sharp C_{1s} peak at 284.2 eV. A small O_{1s} peak is related to the absorbed moisture. The elemental analysis by XPS determined that the graphene sample consists of 99.3% C, 0.51% O and 0.19% Cl (by atomic percentage). The trace Cl is the residual chlorine from dissolving iron catalyst by hydrochloride acid. XPS measurement further proved the high quality of the as-synthesised graphene [273]. This sample obtained in 30 min was also investigated by nitrogen adsorption and desorption isotherms (Figure 6-16b), showing a surface area of 449.2 $m^2 \cdot g^{-1}$.

We measured the electrical conductivity, electrochemical behavior and cycle performance of graphene sheets obtained at 850 ^{o}C for 30 min. Unlike chemically derived graphene sheets, the APCVD method can successfully avoid oxidization of graphene and produce pure graphene sheets, owing the protection effect of reducing gases. Compared with the electrical conductivities of previously reported chemically derived graphene sheets [221, 274], the as-prepared graphene shows a quite high value of ~9.02 S·cm^{-1}. The electrochemical reactivity of graphene sheets as anode materials in Li-ion cells was examined by cyclic voltammogram (as shown in Figure 6-17a). Figure 6-17b shows the discharge and charge profiles of graphene anode in the first cycle. Graphene sheets exhibited an initial rechargeable specific capacity of 887 mAh·g^{-1} at 0.1 C. The irreversible capacity is ascribed to the formation of solid electrolyte interphase. Nevertheless, the cycle performance becomes stable in the following cycles. After 200 cycles, graphene sheets still maintained a capacity of 730 mAh·g^{-1}. Even applied with step-wise current densities (0.1 C-10 C, 1 C=744 mA·g^{-1}, Figure 6-18a), the graphene electrode can sustain a good cycling performance and high Coulombic efficiency, demonstrating as-synthesized product can tolerate tests with large current densities. Furthermore, graphene sheets exhibited good cycling performances at high current rates (Figure 6-18b). In particular, the electrode delivered a lithium storage capacity of more than 560 mAh·g^{-1} at 1 C rate after 200 cycles, illustrating that the graphene electrode can tolerate high charge and discharge current densities. The electrochemical performances of graphene based materials are compared with other graphene based materials, which is shown in Table 6-1.

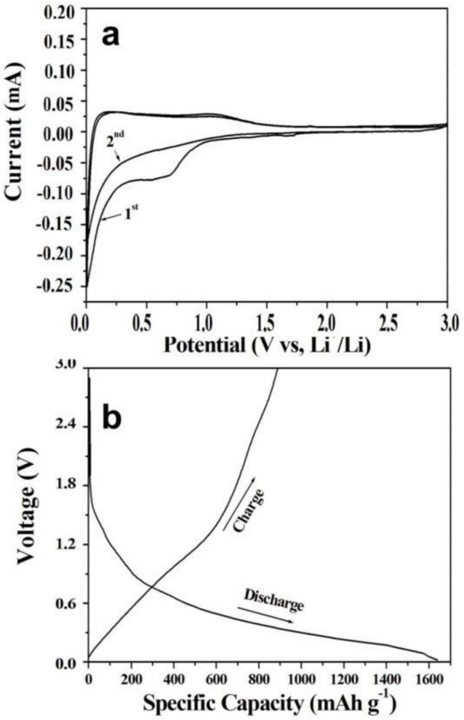

Figure 6- 17 (a) Cyclic voltammogram profiles of graphene obtained at 850 °C grown for 30 min in the first two cycles with a scan rate of 0.5 mV·S^{-1}. (b) Charge/discharge profiles of graphene at a current density of 74.4 mA·g^{-1}.

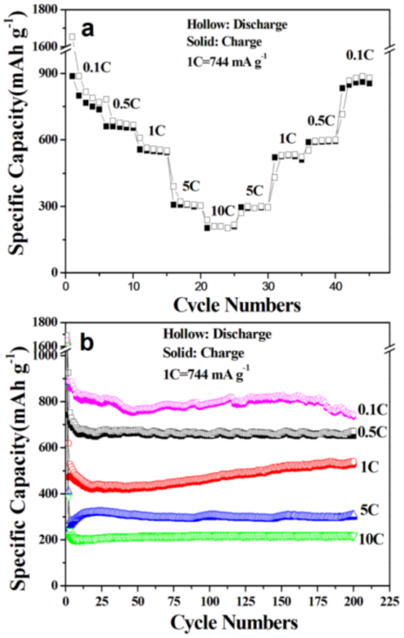

Figure 6- 18 The electrochemical performances of graphene sheets. (a) Electrochemical performances of GNS at step-wise current densities. (b) Cycle performances of graphene sheets at different current rates (0.1 C, 0.5 C, 1 C, 5 C and 10 C, 1 C=744 mA·g^{-1}).

Table 6- 1 The electrochemical performance comparison of graphene based materials

Materials	Initial capacity (mAh/g)	Final capacity (mAh/g)	Retention ratio (mAh/g)	Rate capacity (mAh/g)
CNF/G[165]	667	606	91% (30 cycles)	189 (6 mA/cm^2)
GNS[166]	672	502	74.7% (30 cycles)	554 (1 mA/cm^2)
N-doped GNS[167]	1043	872	83.6% (30 cycles)	493 (0.5 A/g)

6.4 Conclusions

Monolayer to triple-layer graphene sheets have been successfully prepared by APCVD deposition using acetylene gas as the carbon source and coral-like iron as catalyst. The process can be scaled up for large quantity production at a low cost. The optimum CVD temperature has been identified to be 850 °C, which is much lower than other methods with other metals. TEM, AFM, Raman spectroscopy and XPS characterizations show the single crystalline and high quality nature of the as-prepared graphene produced by the bottom-up APCVD approach. A new horizontal "dissolution-deposition-growth" mechanism is proposed and verified by TEM and HRTEM analyses. When applied as anode materials in lithium ion batteries, graphene sheets exhibit high initial rechargeable capacity and stable multi-current rate cycling performance. Large scale production of graphene could pave the way for a wide range of applications of graphene materials.

CHAPTER 7 HIERACHICAL 3D MESOPOROUS SILICON@GRAPHENE NANOARCHITECTURE FOR LITHIUM ION BATTERIES

7.1 Introduction

Currently, lithium ion batteries are the dominant power sources for portable electronic devices, such as notebook and tablet computers, mobile phones and camcorders. Lithium ion batteries are also becoming the choice of power for vehicle electrification, including electric vehicles and hybrid electric vehicles. Substantial efforts have been devoted to improving the performance of lithium ion batteries with high energy density, long cycle life and high rate performance[8, 185, 275-278]. Various carbonaceous materials are used as anode materials in commercial lithium ion batteries with relatively low specific capacity (~372 mAh/g) [169]. Many anode materials with high capacities have been investigated [116, 279-280]. Among them, silicon has been recognized as the most promising and appealing anode material for lithium ion batteries, owing to its high theoretical capacity of 4200 mAh/g (more than 11 times over graphite) [281]. However, extremely large volume variations (up to 400%) during lithium driven alloying and de-alloying induce pulverization of Si electrodes, leading to significant capacity loss on cycling. The approaches to overcome this problem include zero-dimensional Si hollow spheres with low diffusion-induced stress[185, 282-283], one-dimensional Si nanowires to prohibit pulverization[8, 284], core-shell nanostructures using a carbon layer to confine volume expansion [285-286], Si@void@C Yolk-shell structure to maintain superior cycling performance [10], decreasing the size of Si particles [287-288], applying new binder (alginate [289], polyacrylic acid [290-291] and carboxy-methyl cellulose [292-293]) to enhance the strength, and adding conductive additives (Cu [294], Ag [295-296], C [297]) to increase electric conductivity. Furthermore, other Si-C nanocomposites have also been reported such as CNT-Si thin films [286, 298-299], 3D C-Si-C trilayer nanomembranes [300], 3D Si-ATO-Si freestanding electrode [103], nanosize Si loaded on hierarchical structures [301-302], and Si-graphene paper [303-304]. Maier and coworkers [305] reported a Si@SiOx/C composite with a typical core/shell structure, which shows remarkably improved lithium storage capacity (1100 mAh/g at a current density of 150 mA/g). Cui and coworkers [278] prepared Si-base frameworks containing conducting polymer hydrogels, which delivering a long cycle life (5,000 cycles, 550 mAh/g) and high capacity retention (over 90%) at a current density of 6 A/g. Guo and coworkers [288] achieved Si/graphene film using a spin-coating technique, demonstrating a superior rate capability of 648 mAh/g at 10 A/g and a long cycle life (200 cycles) with 74% capacity retention.

In general, three strategies can be applied to achieve high performance Si electrodes for reversible lithium storage. These include: (i) decrease the size of Si particles to shorten lithium ion diffusion distance and increase specific surface areas, (ii) enhance mechanical strength and electrical conductivity by embedding Si nanoparticles in graphene frameworks, (iii) cushion volume expansion through carbon coating and formation of mesoporous nanostructure. Herein, we report a thermal bubble ejection assisted chemical-vapour-deposition (CVD) and magnesiothermic reduction method for the synthesis of hierarchical 3D mesoporous carbon-coated Si@graphene foam (C@Si@GF) nanoarchitectures. When applied as anode materials for lithium storage in lithium ion batteries, C@Si@GF nanocomposites exhibited superior electrochemical performance including a high lithium storage capacity of 1200 mAh/g at the current density of 1 A/g, an excellent high rate capability and an outstanding cyclability.

7.2 Experimental

7.2.1 Preparation of graphene foam

Graphene oxide (GO) prepared by a modified Hummers method was firstly dissolved in de-ionized water (2 $\mathrm{mgmL^{-1}}$) by sonicating for 2 h.[94, 306] GO (20 mL, 2 $\mathrm{mgmL^{-1}}$) was mixed with octadecylamine (ODA, 40 mg, dissolved in 20 mL ethanol) and refluxed at 90 ℃ for 15h to form GO-ODA solution.[307] Polyurethane (PU) foam was cut into a cuboid (4*2*2) and immersed in GO-ODA solution. The precursor was treated by microwave synthesizer at 180 ℃ for 30 min, washed with de-ionized water several times and dried at 60 ℃ overnight in a vacuum oven. The GF-ODA-PU foam was then placed in a tube furnace and heated to 400 ℃ for 3h at 1 $\mathrm{°Cmin^{-1}}$ in Argon to remove PU foam and obtain GF.

7.2.2 Preparation of C@Si@GF nanocomposites

TEOS was preheated to 95 ℃ and carried by H_2/Ar gas through GF to load SiO_2 nanoparticles in the quartz tube at 700 ℃ with different growth durations (1h, 2h, 3h, 4h and 5h). The obtained materials were labelled as the sample I, II, III, Iv and V, respectively. After cooling to room temperature, SiO_2@GF was taken out and sealed with magnesium (1:0.8 in weight ratio) using two porcelain boats in a glove-box. Then the boats were transferred to a tube furnace and heated to 700 ℃ protected by H_2/Ar gases for 2h. Before cooling to RT, C_2H_2/Ar (10%) was introduced to the quartz tube for carbon coating. The products were washed with HCl (1 M, 20 mL for 30 min) and HF (0.5%, 10 mL for 30 min) to remove the by-product MgO and other impurities.

7.2.3 Materials characterization

The as-prepared C@Si@GF nanocomposites were characterized by X-ray diffraction (Rigaku D/max-2550V with Cu Kα radiation) operated at 40 KV and 30 mA. Raman spectra were measured by a Renishaw inVia Raman spectrometer system (Gloucestershire, UK) equipped with a Leica DMLB microscope (Wetzlar, Germany) and a 17mW at 633 nm Renishaw helium neon laser with 50% power. AFM measurements were performed on Dimension 3100 SPM with a tapping mode. The Brunauer–Emmett–Teller surface area was calculated using experimental points at a relative pressure of $P/P^0 = 0.05–0.25$. The pore size distribution was derived from the desorption branch using the Barrett–Joyner–Halenda method. A thermogravimetric analyzer (TGA, SDT 2960) was used to measure the weight percentage of Si from RT to 1000 ℃ in air. The morphologies and crystal structure of materials were analyzed by a field emission scanning electron microscope (JSM-6700F, 20kV) and transmission electron microscope/selected area electron diffraction (TEM/SAED, JEOL JEM-200CX and JEM-2010F) equipped with an energy-dispersive X-ray spectroscopy (EDX).

7.2.4 Electrochemical measurements

The working electrodes were made from 80 wt.% of active materials, 10 wt.% of the conductive agent (acetylene black), and 10 wt.% of the binder (Alginic acid sodium salt extracted from brown algae). The mixture was stirred by an adjustable high-speed electric agitator. The working electrodes were dried in a vacuum oven. CR2032 coin cells were assembled in an argon-filled glove box (Mbraun, Unilab, Germany), in which both the moisture and oxygen contents were controlled to be less than 0.1 ppm. Lithium foil was used as the counter electrode. The electrolyte was 1M $LiPF_6$ in a mixture of ethylene carbonate and diethyl carbonate. Electrochemical measurements were performed using a LAND-CT2001C battery test system. The cells were discharged and charged galvanostatically in the fixed voltage range of 0.005–2.0 V at current densities of 100 mA/g, 500 mA/g, 1 A/g, 5 A/g and 10 A/g, respectively. Cyclic voltammetry was measured on a CHI 660D electrochemical workstation at a scan rate of 0.1 $mV\cdot S^{-1}$.

7.3 Results and discussion

Graphene foam (GF) has been synthesized by either chemical vapor deposition or freeze-drying method. It has been reported that GF has an extremely light weight (0.16 mg cm^{-3}), high electrical conductivity, high specific surface area and strong mechanical strength [19, 81, 113, 221, 308-317], which should be an ideal matrix for loading Si nanoparticles. Scheme 1 shows a schematic illustration of the synthesis process. In the first step, graphene foam with 3D nanostructure was synthesized by a template-assisted microwave digestion method. The pre-treated graphene oxide-octadecylamine (GO-ODA) solution with polyurethane (PU) foam was heated and reduced by single-mode microwave synthesizer at 180 ℃ under the pressure of 8.2 atm for 30 min, which is presented in electronic supplementary material (ESM) as Table S1. The reduced GF-ODA sheets with wrinkles and cavities tightly wrapped the skeleton of PU foam, inducing transparent aqueous solution (Fig. S1 and S2, ESM). Graphene foam was obtained by pyrolysis at 400 ℃ for 3h, during which ODA surfactants were removed and the thickness of GF was ~0.7 nm, measured by atomic force microscopy (Fig. S3, ESM). In the second step, mixed gases (H_2/Ar, 5%) flew through a preheated vessel filled with Tetraethyl orthosilicate (TEOS, 95 ℃, about 100 Torr of vapor pressure) by thermal bubble ejection method and went through a hot reaction zone (700 ℃) in the tube furnace. TEOS molecules were pyrolyzed and generated silica nanospheres. The pyrolysis process can be described as:

$$Si(OC_2H_5)_4 \rightarrow SiO_2 + 2(C_2H_5)_2O$$

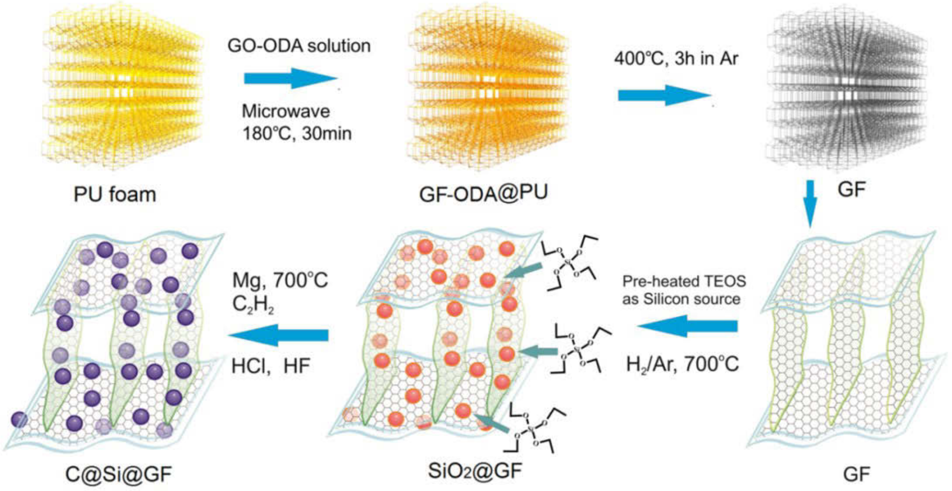

Scheme 7- 1 The schematic illustration of the synthesis process for mesoporous C@Si@graphene foam nanoarchitectures.

When mixed gases carrying TEOS vapors flew through porous GF, silica nanoparticles were homogenously deposited on the two sides of graphene sheets, forming SiO_2@GF nanocomposites (Fig. S1(e) and Scheme S1 in ESM). After that, SiO_2@GF nanocomposites were reduced to Si@GF nanocomposites by the magnesiothermic reduction method [318]. Commercial Si powders, relevant intermediate products and hierarchical 3D mesoporous C@Si@graphene nanocomposites were characterized by X-ray diffraction (Fig. S4, ESM). In the third step, Si@graphene nanocomposites were coated with carbon nanolayers to achieve hierarchical 3D mesoporous C@Si@graphene nanocomposites.

The representative field emission scanning electron microscope (FESEM) and transmission electron microscope (TEM) images of C@Si@GF nanocomposites are presented in Figure 1. As shown in Fig. 1(a), spherical Si nanoparticles (approximate 300 nm) are homogeneously distributed on the surface of graphene sheets. The inset in Fig. 1a further illustrates Si nanoparticles anchored on both sides of graphene sheets. Figure 1(b) shows a low magnification TEM image of C@Si@GF nanocomposites, from which the porous nature of Si nanoparticles can be easily identified.

A high magnification TEM image is shown in Fig. 1(c), which consists of small Si nanocrystals with sizes of about 15 nm. The nanopores originate from the volume shrinkage during the conversion of SiO_2 to Si, which has been confirmed by the dramatic increase of surface areas from 59.8 m^2g^{-1} (SiO_2@GF) to 243.2 m^2g^{-1} (C@Si@GF) (Fig. S5 in the ESM). The pore size distribution of SiO_2@GF, obtained from the BJH method, is shown as the inset in Fig. S5(a), which exhibits a mean pore size of 4.5 nm. On contrary, the mean pore size increases to 9.87 nm for C@Si@GF nanocomposites (inset in Fig. S5(b)). The mesoporous structures provide extra voids for Si nanospheres to expand during lithiation, and increase the specific area of C@Si@GF nanocomposites.

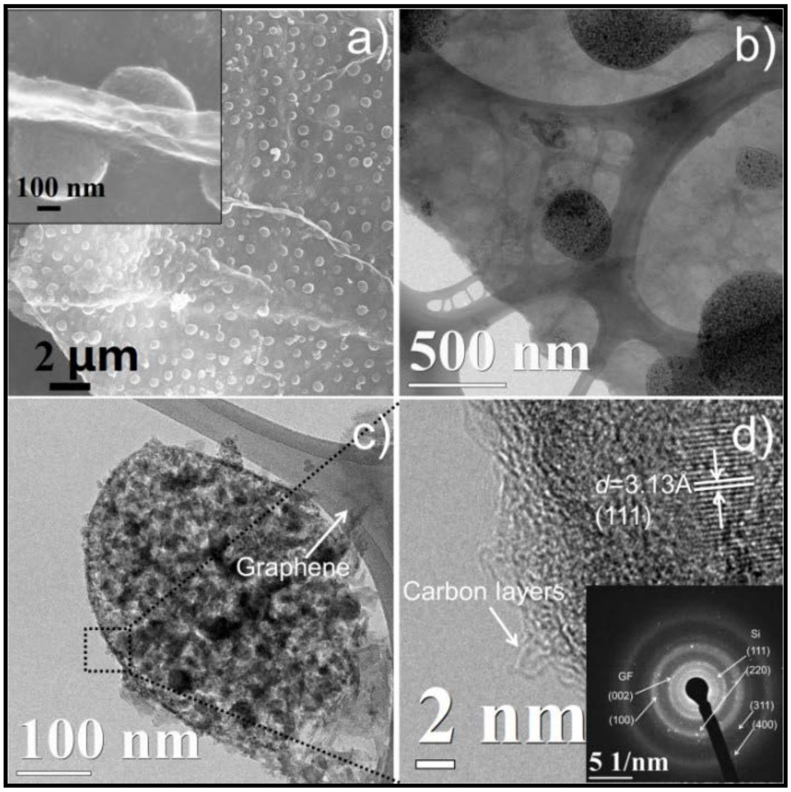

Figure 7- 1 FESEM and TEM characterisation of C@Si@GF nanocomposites prepared by CVD deposition for 5 h (the sample V). (a) FESEM image of C@Si@GF (Insert. Si spheres anchored on the two sides of graphene). (b) TEM image of Si spheres with mesoporous structure. (c) Si particles with approximate size of 15 nm wrapped by carbon layers and anchored on graphene sheets. (d) HRTEM image and SAED pattern demonstrating Si nanoparticles are covered by thin carbon layers.

The lattice resolved HRTEM image of Si nanocrystals is shown in Figure 1(d). The interplanar distance of the lattice is measured to be 0.313 nm, corresponding to the (111) crystal planes of Si. It should be noted that thin carbon layers have been coated on Si nanocrystals with a thickness of about 1–2 nm, which can cushion the expansion of Si nanospheres during lithiation/de-lithiation and confine the maximum expansion volume. The diffraction rings in the selected area electron diffraction (SAED, insert in Fig. 1(d)) can be fully indexed to Si phase and graphene, which coincides with XRD patterns.

Moreover, carbon layers coated on Si nanospheres can enhance the electrical conductivity of Si spheres. Tarascon and coworkers [319] have previously reported that compressive stress is induced by carbon coating effect and demonstrated that the carbon layer derived from poly(vinyl chloride) and compressive pressure render electrode particles to maintain in good electrical contact during cycling, and thus limit the pulverization of the electrode. As shown in Fig. 2(b), the commercial Si powders show a Raman peak at 515 cm^{-1}. However, C@Si@GF nanocomposites present a lower intensity and blue shift of the band at 505 cm^{-1}, which might be from the transverse opitcal mode. A similar phenomenon was previously reported [305] and ascribed to a phonon confinement effect, indicating small size of Si and thin carbon layers on Si nanospheres.

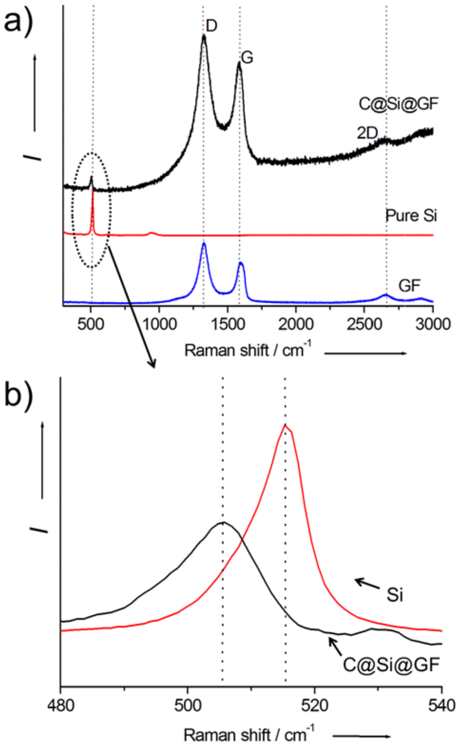

Figure 7- 2 (a) Raman spectra of GF, Si and C@Si@GF materials respectively. b) Magnified view of peaks marked in the image (a), demonstrating blue shift of C@Si@GF band (I = intensity).

To investigate the presence of graphene and mesoporous Si nanospheres, energy-dispersive X-ray spectroscopy (EDS) mapping were performed over a random area of C@Si@GF nanocomposites (Figure S6(a) in the ESM). Graphene layers (Fig. S6(b), ESM) in green and mesoporous Si nanospheres (Fig. S6(c), ESM) in red were detected, validating our structural design and demonstrating that mesoporous Si nanospheres were distributed on graphene sheets and obvious voids appeared in Si nanospheres. The content of Si in nanocomposites was determined to be 56 wt % for the sample obtained by CVD deposition for 5 h (thermal gravimetric analysis, TGA, Fig. S7a, ESM). The co-relationships between load ratio, growth time and morphology were analyzed by thermogravimetric analysis (Fig. S7b, ESM) and FESEM observations (Fig. S8, ESM).

The electrochemical properties of the as-prepared mesoporous C@Si@GF nanocomposites were evaluated by cyclic voltammetry (CV) and galvanostatic charge/discharge testing. Figure S9(a) and (b) in the ESM show the CV curves of bare Si and C@Si@GF electrodes, respectively. In Fig. S9(a), the irreversible cathodic peak at 0.75 V is associated with the formation of the solid electrolyte interphase (SEI) layer, and two anodic peaks at 0.31 V and 0.45 V correspond to the de-lithiation of Li^+ from Li_xSi, which is similar to the previous report [289]. The C@Si@GF electrode only displays one anodic peak at 0.448 V. As indicated by Kovalenko *et al.* [289], the anodic peak at 0.3 V is related to the surface property of bare Si, which vanishes when Si particles are combined with carbon. This is also indirectly verified that Si nanospheres are coated with carbon layers in C@Si@GF nanocomposites.

Figure 4(a) shows the charge/discharge profiles of bare Si and C@Si@GF nanocomposite electrodes at the current density of 100 mA/g in the first cycle. The C@Si@GF nanocomposite electrode delivered a reversible initial capacity of 1480 mAh/g with a Coulombic efficiency of 66% in the first cycle. (Based on the content and theoretical capacity of carbon, the maximum capacity of 163.68 mAh/g may be contributed by carbon). The bare Si electrode showed a reversible capacity of 1610 mAh/g with a much lower Coulombic efficiency of 48% in the initial cycle. The irreversible capacity should be ascribed to the formation of the SEI layer on the surface of the electrode. From the second cycle, the C@Si@GF electrode exhibited a stable cycling performance with capacity retention of 89.1% after 200 cycles (Fig. 4(b)). On contrary, the specific capacity of bare Si electrode quickly decreased to 25.8 mAh/g at 20th cycle, exhibiting a very poor cyclability with the capacity retention of 1.6% after 200 cycles, which is related to large volume expansions of Si electrodes during lithiation and repeat growth of SEI layers on Si electrodes by exposure to fresh electrolytes, resulting in pulverization of Si electrodes. As show in Figure S8 (ESM), the size and weight percentage of Si nanoparticles in C@Si@GF nanocomposites increase with extending the CVD deposition time. We also tested the electrochemical performances of C@Si@GF nanocomposites obtained by different deposition times (1h, 2 h, 3h and 4h). All C@Si@GF electrodes exhibited excellent cycling performances (Figure S10).

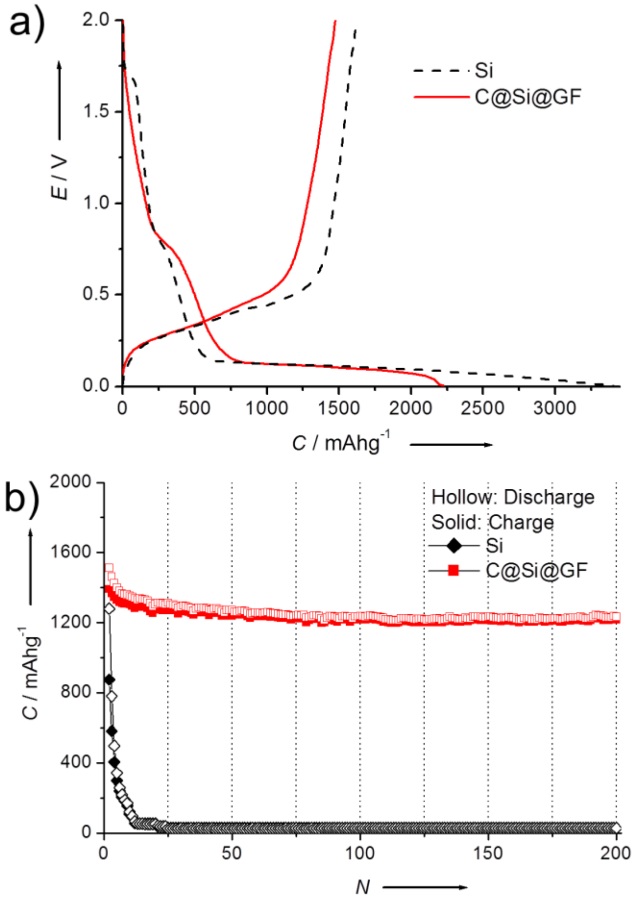

Figure 7- 3 Electrochemical performance of the C@Si@GF composite electrode (sample V): (a–b) Galvanostatic charge-discharge profiles and cycling performances of Si and C@Si@GF nanocomposites with cut-voltage between 5 mV and 2V respectively (C = Specific capacity, N = Cycle number).

The as-synthesized C@Si@GF electrodes were further tested at various step-wise current densities. The cells were subjected to charge/discharge cycling from 100 mA/g to 10 A/g and then reversed twice to 100 mA/g (Fig. 4(a)). The C@Si@GF electrode was quite tolerant to high rate cycling. When the current densities were reversed to lower values, the electrode recovered high capacities, which indicated that the integrity of the electrode was maintained. In order to test the long-term cycling performance at high current densities, the C@Si@GF electrodes (Fig. 4(b)) were cycled 500 mA/g, 1 A/g, 5 A/g and 10 A/g for 200 cycles, respectively. Mesoporous C@Si@GF nanocomposites demonstrated superior performance on long term cycling. The electrodes delivered specific capacities of 1104 mAh/g and 969 mAh/g at 500 mA/g and 1 A/g after 200 cycles, respectively. Even at the current rate of 10 A/g, the electrode still achieved a capacity of 659 mAh/g after 200 cycles, illustrating the high power density of mesoporous C@Si@GF nanocomposites. This outstanding electrochemical performance could be ascribed to the unique nano-architecture. As observed by FESEM and TEM analyses, the nanocomposites consist of a hierarchical structure. Mesoporous Si nanospheres are coated with carbon layers and embedded in porous graphene foam networks, which provides sufficient spaces to cushion the volume change of Si during lithiation and de-lithiation processes. Moreover, Si nanospheres were also coated with a nanolayer of carbon, which enhances electronic conductivity for semi-insulating Si nanoparticles. The hierarchical nanostructures not only contribute to high lithium storage capacity, but can also result in excellent high rate performance and long cycle life. The electrochemical performances of Si@GF nanocomposites are compared with other Si/GNS based materials, which is shown in Table 7-1.

The Si@GF nanocomposite without carbon coating (Figure S11a and b) presents a stable cycling performance only in the first 102 cycles and then quickly decreases to a relative low capacity (560 mAh/g). This verified that the coated carbon layers play an important role in confining large volume expansion and maintaining good electric contact of electrode for the enhancement of cycling performance.

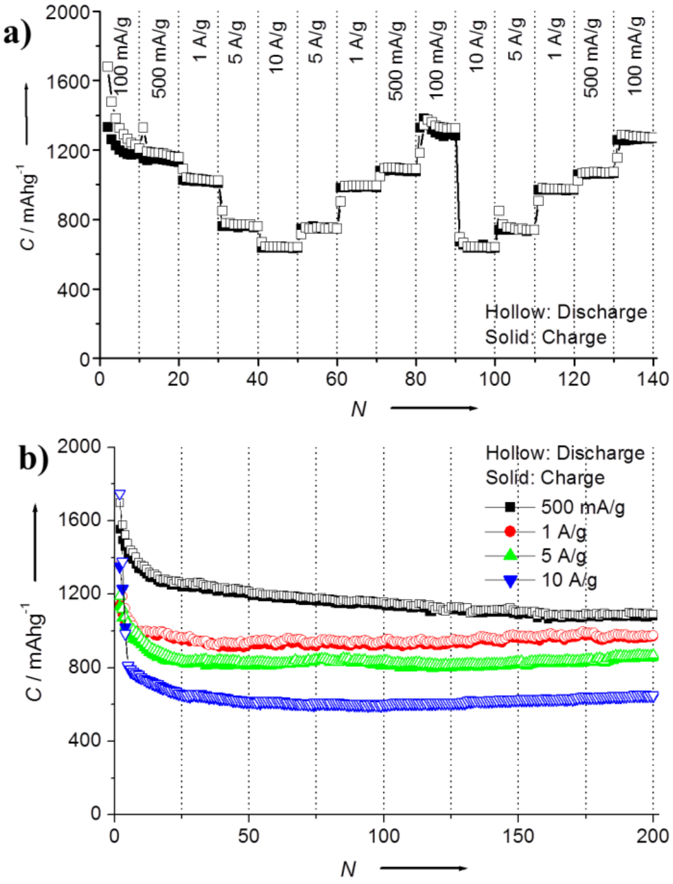

Figure 7- 4 (a) Step-wise rate performance of C@Si@GF composites (sample V) at different current densities. (b) Cycling performances at high current densities.

Table 7- 1 The electrochemical performances of Si/GNS hybrid materials are compared.

Materials	Initial capacity (mAh/g)	Final capacity (mAh/g)	Retention ratio (mAh/g)	Rate capacity (mAh/g)
Si/GNS[320]	2035	1386	68% (30 cycles)	---
Si/GNS[321]	938	370	39% (100 cycles)	519 (0.4 A/g)
Si/GNS[322]	1000	760	76% (100 cycles)	800 (4 A/g)
The Thesis	1480	1317	89% (200 cycles)	798 (5 A/g)

The electrochemical impedance spectra of commercial Si and C@Si@GF electrodes in Figure 5 further demonstrate the inner electrochemical resistances and interfacial properties (both before and after 200 cycles). The corresponding equivalent circuit is presented in Fig. 5b. All cells display Nyquist plots (Fig. 5a), which consist of a deprepressed semicircle in high frequency and a straight line in low frequency domain. The relative smaller radius of the semicircle for C@Si@GF nanocomposites, represents a lower electrochemical reaction resistance in the electrode, indicating higher electric conductivity than that of bare Si electrode. Even cycled for 200 times, the electrochemical resistance of C@Si@GF electrode was still much lower than the bare of Si electrode.

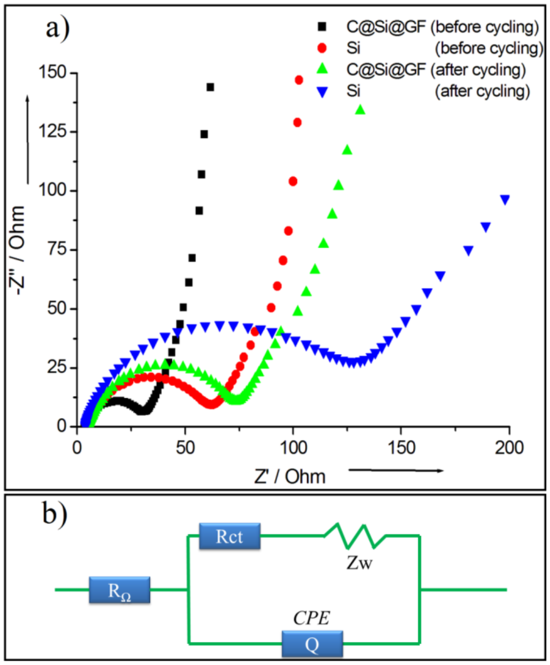

Figure 7- 5 (a) The a.c. impedance spectra of commercial silicon and C@Si@GF electrodes. Each cell was tested before and after cycling, respectively. (b) The corresponding equivalent circuit (R_Ω: Ohm resistance; Rct: Charge transfer resistance; Zw: Warburg diffusion process; CPE: constant-phase element).

Post-mortem analyses were performed on the bare Si and mesoporous C@Si@GF electrodes after 200 cycles. Compared with original morphologies of commercial Si particles (Figure S12 in the ESM), Figure 6(a) revealed that many cracks were formed on the surface of the bare Si electrode, which should be the major reason for the poor cyclability. On contrary, the C@Si@GF nanocomposite electrode preserved well connected nanostructure and integrity, in which Si nanoparticles uniformly distributed on porous graphene networks without any cracks even after long-term cycles (Fig. 6(b)). The HRTEM image and fast Fourier transform (FFT) pattern further confirmed the crystalline nature of Si nanoparticles after cycling (the insets in Fig. 6(c-d)). Therefore, the *ex-situ* FESEM and TEM observations clearly verified that the mesoporous hierarchical nano-architecture can efficiently maintain the structural integrity of the electrode and significantly reduce the capacity fading on charge/discharge cycling.

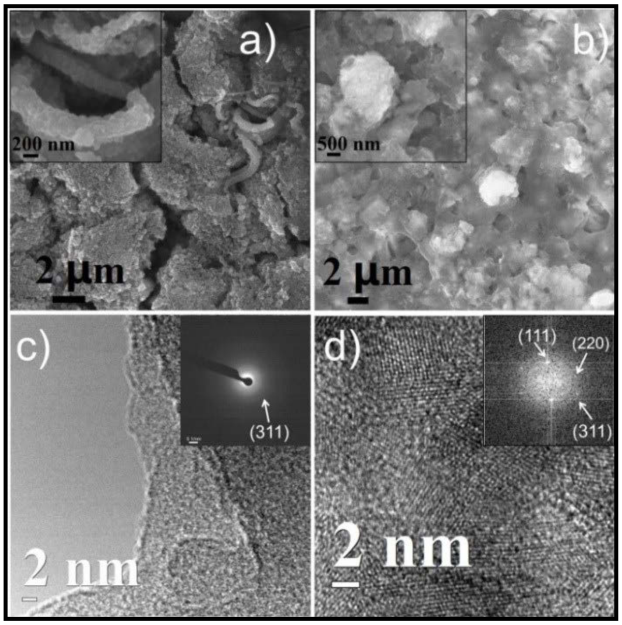

Figure 7- 6 (a–b) SEM images of morphologies of Si and C@Si@GF electrodes after 200 cycles (insert images presenting the details), respectively. c-d) HRTEM images of bare Si and C@Si@GF electrodes after 200 cycles (insert: SAED pattern of Si and FFT pattern of C@Si@GF, respectively).

7.4 Conclusions

In conclusion, mesoporous C@Si@GF nanoarchitectures were successfully synthesized by a thermal bubble ejection assisted chemical-vapor-deposition and magnesiothermic reduction method. Mesoporous Si nanospheres were coated with a nanolayer carbon and embedded in graphene foam, which provides sufficient voids to cushion the large volume changes of Si during lithiation and de-lithiation processes and enhance electronic conductivity for semi-insulating Si nanoparticles. When applied as anode materials for lithium storage in lithium ion batteries, C@Si@GF nanocomposites exhibited superior electrochemical performances, including a high lithium storage capacity of 1200 mAh/g at current density of 1 A/g, excellent tolerances to high current densities and an outstanding cyclability. The as-developed approach could also be extended to synthesize other 3D materials.

CHAPTER 8 MICROWAVE-ASSISTED SYNTHESIS OF Co_3O_4 NANOFLAKES FOR LITHIUM ION BATTERIES

8.1 Introduction

Energy storages have been substantially researched and applied in recent decades, including traditional rechargeable batteries (lead-acid batteries, nickel-cadmium batteries and nickel-metal hydride batteries) and lithium-ion batteries.[1-2, 271, 280] Due to toxic materials, self-discharge and memory effect of traditional batteries, lithium ion batteries are regarded as the most promising energy storage devices. For commercial lithium ion batteries, graphite with a theoretical capacity of 372 mAh/g cannot meet the current requirements of high capacity, long cycling life and excellent tolerance of fast charge/discharge.[265, 323-324] Recently, many efforts have been devoted to developing good electrochemical performances of anode materials, including carbon based materials, Si, Sn and various transition metal oxides.[76, 81, 90, 94, 185, 258, 309, 325-329] Among those transition metal oxides, Co_3O_4 has been recognised as one of the promising materials because of its high theoretical capacity of 890 mAh/g and multiple usages.[113, 330-331] However, Co_3O_4 is also plagued by low rechargeable capacity and fast capacity decay due to the large volume expansion during charging. It should be noted that morphology and nanostructure have large influences on the electrochemical performances. It is demonstrated that crystal plane structures of Co_3O_4 have a critical impact on the lithium ion storage and cycling performances, showing that (110) plane of Co_3O_4 is ideal for lithium ion batteries, compared with other facets. Liu *et al* has reported unusual single-crystal Co_3O_4 nanocages with highly reactive {110} facets via hydrothermal method, followed with the treatment of H_2O_2, demonstrating a high reversible capacity of 864 mAh/g at 0.2 C over 50 cycles.[332] Many reports also illustrate that Co_3O_4 with different morphologies including nanotubes, nanorods, nanoneedles, nanowires, platelets and mesoporous structures have enhanced capacities and better cycle life than bulk materials.[333-338]

Water splitting is an efficient way to generate hydrogen in high purity, but it needs stable and effective catalysts to drive water oxidation into molecular oxygen.[330, 339-341] The corresponding oxygen evolution reaction (OER) plays the critical role on the process of water splitting. Despite substantial efforts have been devoted to developing the effective catalysts for OER, it remains a great challenge without using noble metal catalysts. Although the oxides of Ruthenium, Iridium and other rare earth metals in high oxidation states were tested to be effective catalysts for OER, the high price of those metal oxides make them impossible for practical large-scale applications. Cobalt oxides and other transition metal oxides with different morphologies are also active for oxygen evolution reaction in alkaline solution.[342-343] Esswein *et al.* discovered that the sizes of Co_3O_4 had different catalysis abilities on OER, illustrating that the current density of 10 mA/cm^2 of cubic nanoparticles with an average diameter of 5.9 nm was achieved at overpotential of 328 mV.[344] Wu *et al.* reported that Co_3O_4 nanocrystal anchored on single-walled carbon nanotube, synthesized via a self-assembly approach, exhibited much enhanced catalytic activity and excellent stability under both neutral and alkaline solutions.[345]

Herein, we report mesoporous Co_3O_4 nanoflakes with an interconnected architecture synthesized by a microwave-assisted hydrothermal and low-temperature conversion method, which exhibits excellent electrochemical performances as anode materials in lithium ion batteries and as catalyst in OER under alkaline solutions. FESEM and TEM analyses show the unique interconnected and mesoporous structure. When employed as anode materials for lithium ion batteries, mesoporous Co_3O_4 nanoflakes delivered a high specific capacity of 883 mAh/g at 0.1 C current rate and stable cycling performances. The mesoporous Co_3O_4 nanoflakes also show both OER active property and good catalytic stability, even cycled 1000 times. This could be attributed to both the stability of the unique mesoporous structure and exposed highly reactive energy facets on the edges

8.2 Experimental

8.2.1 Preparation of mesoporous Co_3O_4 with microwave-assited method

In a typical synthesis, ethylene glycol (20 mL), Hexamethylenetetramine aqueous solution (8 mL, 0.06M), Ammonium carbonate aqueous solution (8 mL, 0.06M) and Cobalt(II) carbonate aqueous solution (10 mL, 0.08M) were mixed under vigorous stirring to obtain a homogeneous purple solution. Once the precursor was transferred to a glass vessel with a volume of 23 mL, a thermal treatment was performed in a single-mode microwave synthesizer (NOVA II microwave synthesizer with magnetron stirring and monitoring the real pressure in the vessel) at 180 ℃ for 10 min. After cooling to room temperature, the sample deposited at the bottom was collected and washed by filtration apparatus with copious de-ionized water (D.I. water) and ethanol. The as-synthesized sample was dried in a vacuum oven at 80 ℃ overnight to remove the absorbed water for the subsequent characterizations. Then, the dried precursor was annealed at 250 ℃ for 3h with a temperature ramp rate of 2 ℃/min.

8.2.2 Materials characterization

The as-prepared mesoporous Co_3O_4 with interconnected structure was characterized by X-ray diffraction (Rigaku D/max-2550V with Cu Kα radiation) operated at 40 KV and 30 mA. Raman spectra were measured by a Renishaw inVia Raman spectrometer system (Gloucestershire, UK) equipped with a Leica DMLB microscope (Wetzlar, Germany) and a 17 mW at 633 nm Renishaw helium neon laser with 50% power. Nitrogen adsorption-desorption measurements were conducted on 3 Flex surface characterization analyzer to determined the Brunauer–Emmett–Teller (BET) specific surface areas using a Quadrasorb SI analyzer at 77 K. The BET surface area was calculated using experimental points at a relative pressure of P/P_0=0.05–0.25. The pore size distribution was derived from the desorption branch using the Barret–Joyner–Halenda (BJH) method.The morphologies and crystal structure of materials were analyzed by field emission scanning electron microscope (JSM-6700F, 20kV), and transmission electron microscope (TEM, JEOL JEM-200CX and JEM-2010F)

8.2.3 Electrochemical measurements

The working electrodes were made from 80 wt.% of active materials, 10 wt.% of the conductive agent (acetylene black), and 10 wt.% of the binder (polyvinylidene difluoride). The mixture was stirred with an adjustable high-speed electric agitator. The working electrodes were dried in a vacuum oven. CR2032 coin cells were assembled in an argon-filled glove box (Mbraun, Unilab, Germany), in which both the moisture and oxygen contents were controlled to be less than 0.1 ppm. Lithium foil was used as the counter electrode. The electrolyte was 1M $LiPF_6$ which dissolved in a 1:1 (weight ratio) mixture of ethylene carbonate and diethyl carbonate. Electrochemical measurements were performed using a LAND-CT2001C battery test system. The cells were discharged and charged galvanostatically in the fixed voltage range of 0.01-3 V with a current density of 89 mA/g (0.1 C). Higher current rates (0.5 C, 1 C, 5 C and 10 C) were also applied to test the electrochemical performances. After 300 cycles, the electrode materials were taken out from those coin cells in glove box, washed by ethylene carbonate to remove contained electrolyte. The cycled electrode materials were analyzed by SEM.

Electrocatalytic activity was carried out on a CH instrument Model 600E electrochemical workstation with a three-electrode glass cell in 1 M, 0.1 M KOH. Glass carbon (GC) with the sample used as the working electrode while the platinum wire and the Ag/AgCl as the counter and the reference electrode. The working electrode was prepared as follows: 4 mg of the Co_3O_4 dispersed in 1 mL of 1:1 v/v water/isopropanol, and then 80 μL 5 wt % Nafion was added into the solution. The mixture was sonicated for more than 30 min to obtain a homogeneous ink. Then, 10 μL of the catalyst ink was loaded onto the GC electrode of 5 mm in diameter. Linear sweep voltammetry (LSV) was conducted with a scan rate of 5 mV/s.

8.3 Results and discussions

The mesoporous Co_3O_4 nanoflakes with interconnected architecture were synthesized by a microwave-assisted hydrothermal and low-temperature conversion method. This approach has been widely applied to the preparation of various nanomaterials and even industrial productions because of its advantages, such as less time-consuming, simple operation and energy efficiency. A schematic diagram of the synthesis procedure is presented in Figure 8-1. With the assistance of microwave energy and high pressure (~4 atm), layered intermediate cobalt carbonate hydroxide hydrates ($Co(CO_3)_{0.5}(OH)_{0.11}H_2O$) with interconnected architectures are formed, assisted by the bihydroxyl functional group from ethylene glycol. After treatment at 250 ℃ in air, layered $Co(CO_3)_{0.5}(OH)_{0.11}H_2O$ releases carbon dioxide and moisture. After then, mesoporous Co_3O_4 nanoflakes with interconnected architecture are obtained.

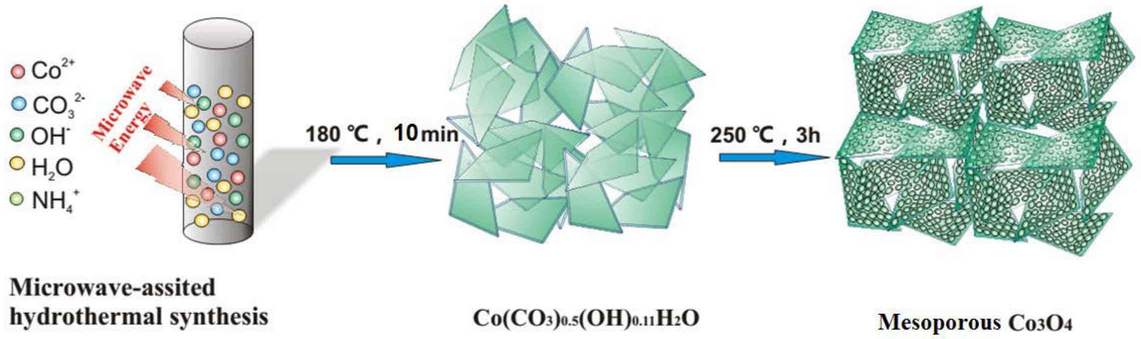

Figure 8- 1 Schematic illustration of microwave-assisted hydrothermal synthesis of mesoporous Co_3O_4 nanoflakes.

The as-synthesised materials were characterized by X-ray diffraction (XRD), and shown in Figure 8-2a. The intermediate is indexed to be cobalt carbonate hydroxide hydrates ($Co(CO_3)_{0.5}(OH)_{0.11}H_2O$) (JCPDS: 48-0083, a=8.792) and the final product is confirmed to be Co_3O_4 with typical characteristic peaks of (020), (311), (400), (511) and (440).[346] The positions and intensities of diffraction peaks match well with the standard JCPDS card (42-1467 with a space group of Fd3m (227), a=8.084). Figure 8-2b shows the Raman spectrum of mesoporous Co_3O_4 nanoflakes. The peaks of Raman shift at 194, 518 and 617 cm^{-1} can be assigned to the F_{2g} mode of Co_3O_4, and the peaks at 475 and 682 cm^{-1} are ascribed to the E_g and A_{1g} modes of Co_3O_4, respectively. Values of Raman shift are slightly different from the previous reports,[347] which is probably owing to different sizes and morphologies of Co_3O_4 nanoflakes. The surface areas of mesoporous Co_3O_4 nanoflakes were investigated by nitrogen adsorption and desorption isotherms, as shown in Figure 8-2c. The mesoporous Co_3O_4 nanoflakes have a relatively high specific surface area of 139.8 m^2/g with a hysteresis feature, which is much larger than that of the $Co(CO_3)_{0.5}(OH)_{0.11}H_2O$ nanohydrates (19 m^2/g). It indicates that many voids are formed on the planes of the Co_3O_4 nanoflakes during the heat treatment process. The total pore volume of the mesoporous Co_3O_4 nanoflakes was determined to be 0.346 cm^3/g, and the average pore size (insert image in Figure 8-2c) was approximately 11.5 nm, based on the Barrett-Joyner-Halenda method. This mesoporous and interconnected nanostructure not only can provide many reactive sites for lithium storage and enhance the electrolyte diffusion for lithium ions transport, but also offer active planes for the OER activities.

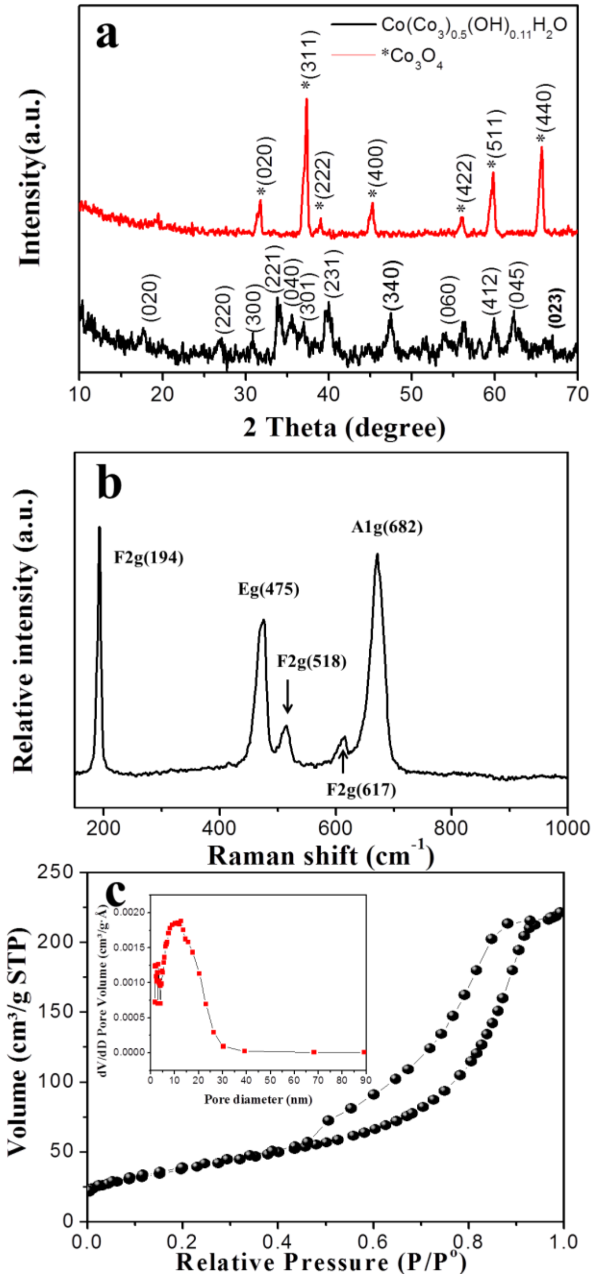

Figure 8- 2 (a) X-ray diffraction pattern of intermediate $Co(CO_3)_{0.5}(OH)_{0.11}H_2O$ and Co_3O_4. (b) Raman spectrum of Co_3O_4. (c) Nitrogen adsorption and desorption isotherms of mesoporous Co_3O_4 nanoflakes with insert plot of pore size distribution.

Figure 8-3 shows the field-emission scanning electron microscopy (FESEM) images of the intermediate ($Co(CO_3)_{0.5}(OH)_{0.11}H_2O$) and mesoporous Co_3O_4 nanoflakes. It can be observed from Figure 8-3a and 8-3b that the cobalt carbonate hydroxide hydrates arrange themselves into a thin plate structure with a thickness of ~20 nm, which is probably ascribed to the assistance of ethylene glycol. Double-headed hydroxyl groups in ethylene glycol molecules can intercalate into neighbouring layers and act as soft templates to assist the formation of interconnected layered architecture. Previous reports also mentioned ethylene glycol molecules act as molecular pillars to separate and stabilize layered intermediate via hydrogen bonding action, resulting in the formation of layered structures.[24, 25] This morphology is similar to layered double-metal hydroxides (LDH), which contains anion of carbonate or hydroxyl groups. Meanwhile, the strong microwave absorption of ethylene glycol molecules results in severe stretching vibrations, leading to partially disordered layered planes and forming an interconnected, three-dimensional architecture. Those anions of carbonate, hydroxyl or other groups on the interconnected structure are thermal sensitive, which tends to emit gases including carbon dioxide, moisture and ammonium molecules under subsequent thermal treatment. Mesoporous architecture can be generated upon the remaining metal oxides, which is a general strategy to achieving mesoporous structures originating from LDH compounds. Single-layered nanomesh, nanoparticles, nanoplates and nanobelts have also been successfully obtained by means of the unique physical and chemical instability of LDH compounds.[348]

Inspired by this strategy, the intermediate $Co(CO_3)_{0.5}(OH)_{0.11}H_2O$ was slowly heated in air at 250 ℃ for 3h. The release of carbon dioxide, ethylene glycol and moisture from layered planes upon the precursor’s thermal decomposition leaves copious amounts of mesoporous voids,[346] which have been verified by the BET measurement in Figure 8-2c and FE-SEM images in Figure 8-3c-d. Meanwhile, the unique interconnected architecture of the intermediate is also completely maintained, which is demonstrated by the typical low and high magnification of FESEM in Figure 3c-d. The FESEM images clearly show the uniformity, interconnected property and regularity of mesoporous Co_3O_4 nanoflakes. It should be noted that the overall size of interconnected mesoporous Co_3O_4 nanoflakes is more than 30 μm, indicating that more than hundreds of square meters are obtained by this effective microwave-assisted and thermal decomposition method. Interestingly, the planes of mesoporous Co_3O_4 nanoflakes connect themselves by a continuously end-to-end manner, which substantially increases the mechanical strength and overall stability. Several mesoporous Co_3O_4 nanoflakes with a thickness of around 15 nm enclose extra voids. The average voids are approximately 11.5 nm, providing enough space for the subsequent volume expansion when applied as anode materials for lithium ion batteries and extra space for oxygen evolution reaction.

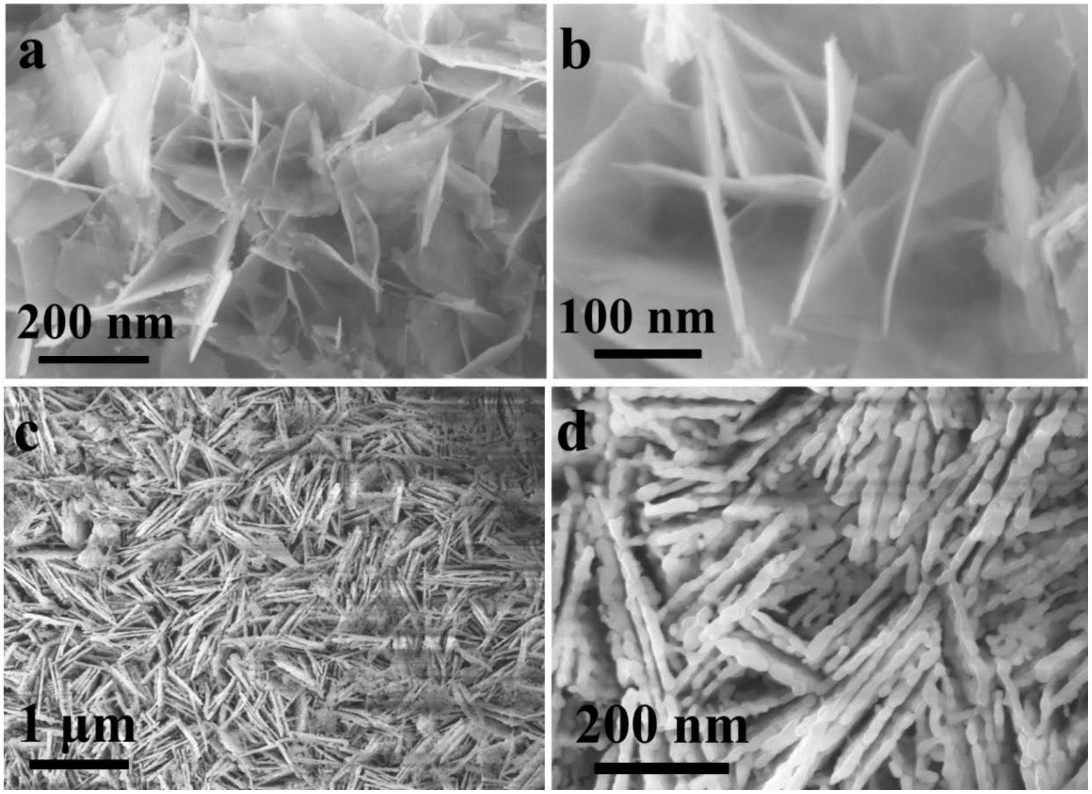

Figure 8- 3 Low and high magnification of field-emission scanning electron microscopy (FESEM) images of $Co(OH)_2$ (a and b). Low and high magnification FESEM images of Co_3O_4 with mesoporous structure (c and d).

The mesoporous architecture and crystal structure of interconnected Co_3O_4 nanoflakes were further characterized by transmission electron microscopy (TEM) and high resolution TEM (HR-TEM). From Figure 8-4a-b, it is observed that the planes of Co_3O_4 nanoflakes consist of many mesopores. The insert image in Figure 8-4b is shown the enlarged view of mesoporous Co_3O_4 nanoflakes. As observed from Figure 8-4c, lattice distance agrees well with the {220} facet of the face-centred-crystal Co_3O_4 and its corresponding lattice profile. The other insert image in Figure 8-4c exhibits a structure stimulation of the (220) plane in the same direction, demonstrating the arrangement of cobalt and oxygen atoms. The corresponding fast Fourier transform (FFT) pattern is shown in Figure 8-4d.

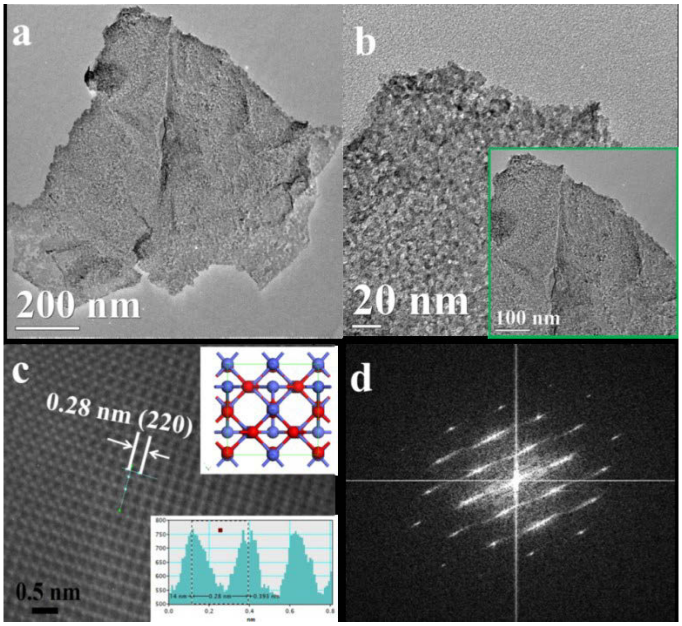

Figure 8- 4 . (a) Low magnification TEM image and (b) high resolution TEM (HR-TEM) image of mesoporous Co_3O_4 nanoflakes with an enlarged view. (c) HR-TEM image and the corresponding lattice profile of (220) plane and its corresponding simulation scheme, respectively. (d) The relevant fast Fourier transform (FFT) pattern.

The electrochemical performances of mesoporous Co_3O_4 nanoflakes electrodes with the interconnected architecture were evaluated using CR2032 coin cells by galvanostatic charge-discharge. The charge/discharge profiles of the mesoporous Co_3O_4 nanoflakes in the 1st, 100th and 300th cycle are shown in Figure 8-5a at a constant current density (89 $mA{\cdot}g^{-1}$, 0.1 C). The electrochemical process of Co_3O_4 with lithium ions is based on the conversion reaction mechanism.[349] The corresponding lithium storage mechanism of Co_3O_4 is indicated by the following equation:

$$Co_3O_4 + 8Li^{+} + 8e \leftrightarrow 3Co + 4Li_2O$$

The cyclic voltammetry (CV) of mesoporous Co_3O_4 nanoflakes at the scan rate of 0.5 mV/s is presented in the Figure 8-5. Two cathodic peaks (1.12 V and 0.86 V) are observed in the first cycle, which are related to the formation of SEI layer and the multi-step lithiation processes. One main anodic peak at 2.1 V is ascribed to the oxidation of Co. In the following cycle, only one main cathodic peak at 1.12 V is left, which is attributed to the reduction of Co_3O_4. The anodic peak at around 2.1 V is only slightly shifted.

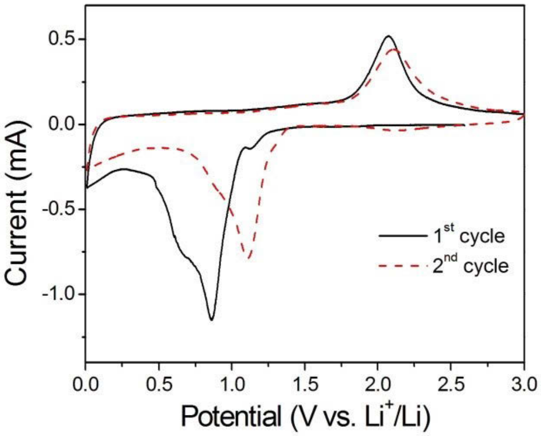

Figure 8- 5 The cyclic voltammetry of mesoporous Co_3O_4 nanoflakes at the scan rate of 0.5 mV/s.

The charge-discharge curves exhibit typical characteristic electrochemical behaviours of Co_3O_4 nanoflakes electrodes. In the first cycle, the mesoporous Co_3O_4 nanoflakes electrode delivered a discharge capacity of 1192 mAh/g, which is higher than the theoretical specific capacity (890 mAh/g).[113, 350] The extra capacity is probably attributed to the formation of the solid electrolyte interphase (SEI) layer and contribution from nanocavities. The initial reversible capacity is 883 mAh/g with a Coulombic efficiency of 74% and the lithiation/delithiation processes are coincided to the CV curves in Figure 8-5. The following specific capacities, such as 100th and 300th, exhibit no obvious capacity degradation. The cycling performance, together with the corresponding Coulombic efficiency as insert image in Figure 8-5b, exhibits a stable and long cycling life. After 300 cycles, the reversible capacity still maintains at around 806 mAh/g with a capacity decay ratio about 0.1 % per cycle. This result demonstrates that the mesoporous Co_3O_4 nanoflakes with interconnected architecture can sustain long cycling life testing. The corresponding electrochemical impedance spectra were also measured before and after the 100th and 300th cycles in Figure 8-6, which reveals the changes of electrochemical resistances. All three stages present Nyquist plots, which consist of a depressed semicircle in high frequency region and an oblique line in medium frequency region. A small semicircle in the high frequency region of fresh cell indicates a lower electrochemical reaction resistance, and the relative larger semicircles after the 100th and 300th times illustrate that after long cycles, the electrochemical resistances only slightly increased, which might account for the high reversible capacity of mesoporous Co_3O_4 nanoflakes.

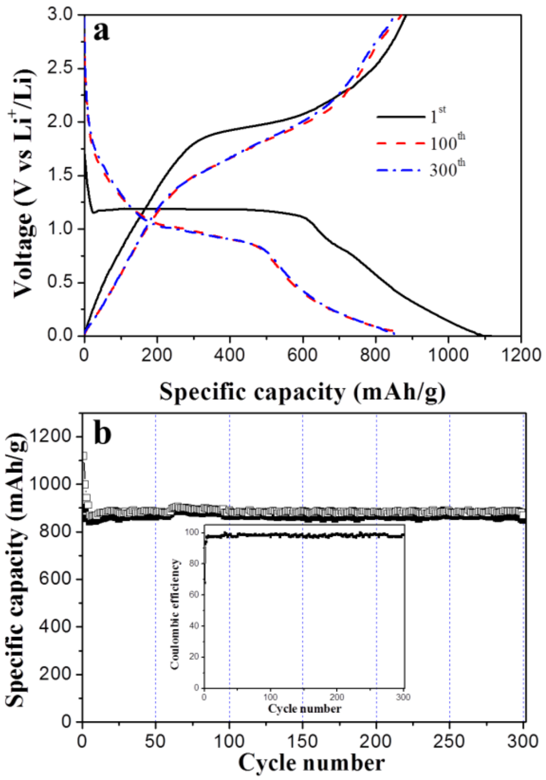

Figure 8- 6 The electrochemical performance of mesoporous Co_3O_4 nanoflakes electrode. (a) Galvanostatic charge/discharge profiles cycled at 1st, 100th and 300th between 0.01 and 3 V (vs Li^+/Li) at a current density of 89 mA/g (0.1 C). (b) Cycling performance of mesoporous Co_3O_4 nanoflakes electrode and its Coulombic efficiency at 0.1 C as insert image.

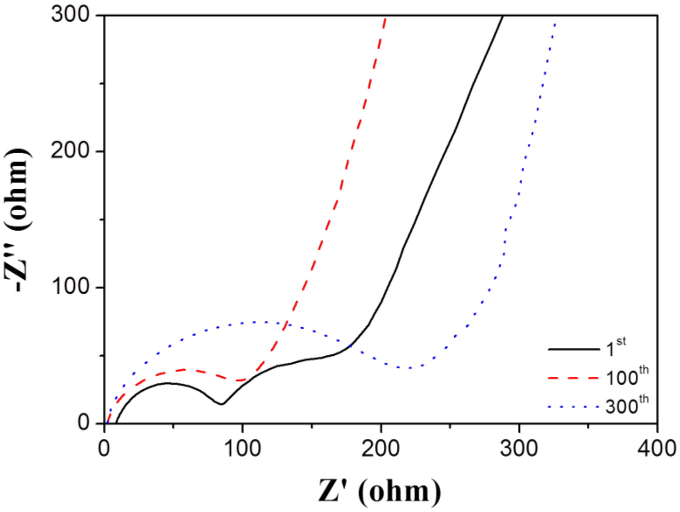

Figure 8- 7 The impedance spectra of mesoporous Co_3O_4 nanoflakes obtained before test and after 100th cycle and 300th cycle.

Mesoporous Co_3O_4 nanoflakes electrodes were also measured at step-wise current densities: from 0.1 C, 0.5 C, 1 C, 5 C to 10 C, and then reverse to low current rate. The relevant electrochemical performance is presented in Figure 8-7a. As can be observed, the capacity of mesoporous Co_3O_4 nanoflakes electrode shows a considerable stability even the current rates step-wised increased. Note that when the current rate reverse back to low current rate, the capacity of mesoporous Co_3O_4 nanoflakes electrode nearly fully recovers to the initial value, illustrating that the particular interconnected mesoporous Co_3O_4 nanoflakes electrode can tolerant to the sudden changes of current rates. The charge/discharge profiles and cycling performances of mesoporous Co_3O_4 nanoflakes electrodes at high current rates of 0.5 C, 1 C, 5 C and 10 C were shown in Figure 8-7b and 8-7c, respectively. After 300 cycles, the reversible specific capacity of mesoporous Co_3O_4 nanoflakes electrode at 0.5 C (445 mA/g) maintained 686 $mAh \cdot g^{-1}$ even though capacity decay occurred at first 60 cycles. Specific capacity of 548 mAh/g was observed for 1 C (890 mA/g), 380 mAh/g for 5 C (4450 mA/g) and 285 mAh/g for 10 C (8900 mA/g). It should be noted that both the capacities and cycling performances are apparently better than those of commercial anode materials (such as graphite and mesocarbon microbeads). Aiming to investigate the reason of as-presented electrochemical performance, post-mortem analysis was conducted on the cycled electrode by means of *ex-situ* FE-SEM images. Figure 8-8a and b exhibit the low and high magnification FE-SEM images of mesoporous Co_3O_4 nanoflakes electrode after 300 cycles at 10 C. Even though the cycled electrode is covered by SEI layer, the unique interconnected architecture of mesoporous Co_3O_4 nanoflakes electrode can still be identified, which means the particular structure has been well maintained after long-term charge/discharge cycling and verifies the robust properties of mesoporous Co_3O_4 nanoflakes electrode. Moreover, the regular arrangement of electrode is also benefited to the distribution of electrolyte and transport of lithium ions, which is might ascribed to good tolerance ability of mesoporous Co_3O_4 with interconnected architecture to high current densities and remarkable cyclibility. The electrochemical performances of mesoporous Co_3O_4 nanoflakes are compared with other Co_3O_4 materials, which are shown in Table 8-1.

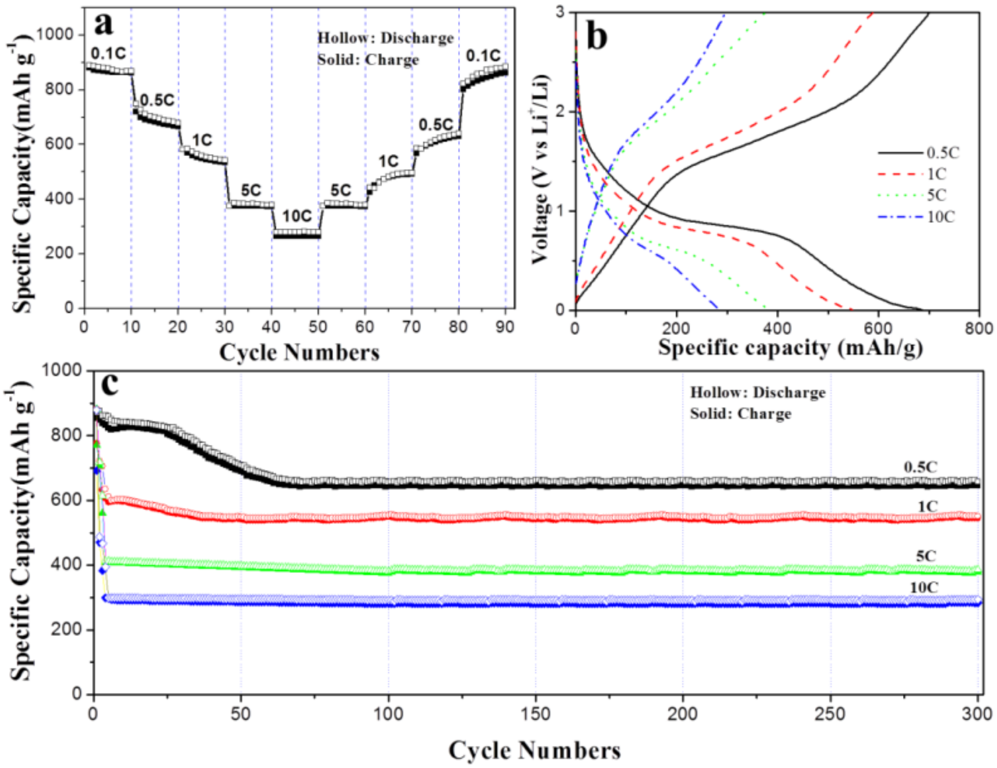

Figure 8- 8 (a) Step-wise rate performance at different current densities. (b) The galvanostatic charge/discharge profiles of mesoporous Co_3O_4 nanoflakes electrodes at 0.5 C, 1 C, 5 C and 10 C at 300th cycle. (c) Cycling performance of mesoporous Co_3O_4 nanoflakes electrodes at higher current densities.

Table 8- 1 The electrochemical performances of mesoporous Co_3O_4 nanoflakes hybrid materials are compared with other Co_3O_4 materials

Materials	Initial capacity (mAh/g)	Final capacity (mAh/g)	Retention ratio (mAh/g)	Rate capacity (mAh/g)
Macroporous Co_3O_4 Platelets[350]	933(0.1 C)	900	96% (30 cycles)	852 (1 C)
Co_3O_4[351]	817(0.1 C)	200	24% (30 cycles)	400 (0.15 A/g)
Mesoporous Co_3O_4 [352]	1089(0.05 A/g)	1089	75%(80 cycles)	590 (0.8 A/g)
Mesoporous Co_3O_4 nanoflakes in the Thesis	833 (0.1 C)	806	96.7%(300 cycles)	548 (1 C)

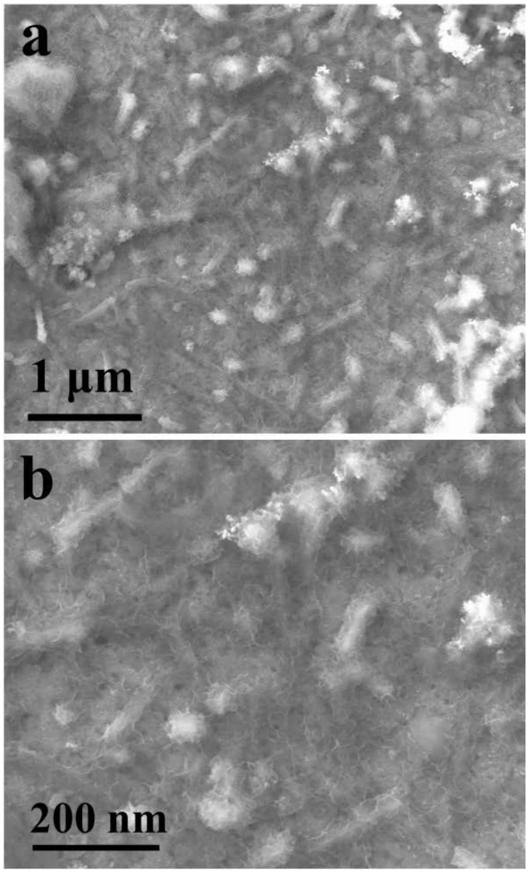

Figure 8- 9 Low and high magnification of mesoporous Co_3O_4 electrode after 300 cycles.

Cobalt oxides and other transition metal oxides with different morphologies have demonstrated to be active for oxygen evolution in alkaline solution.[331, 353-360] Mesoporous Co_3O_4 with the interconnected architecture and highly reactive surface is rarely studied. In order to explore other potential applications for mesoporous Co_3O_4 nanoflakes, it is also evaluated as catalysts for oxygen evolution reaction (OER). The performance of mesoporous Co_3O_4 towards water oxidation is measured in a standard three-electrode system in the 1 M and 0.1 M KOH solution, and the working electrode was continuously rotating at 1600 rpm to remove the generated oxygen bubbles. The anode measured potentials *vs.* Ag/AgCl was converted to the normal hydrogen electrode (NHE) according to Nernst equation $E_{NHE} = E_{Ag/AgCl} + 0.059\times pH + 0.2224$. In 0.1M KOH, the anodic current, as shown in Figure 8-7a, showed an onset potential towards OER of 0.529 V (vs. Ag/AgCl) and afforded a current density of 10 mA/cm^2 at a small overpotential of 0.483 V. Along with increasing the concentration of KOH to 1 M, the Co_3O_4 displayed a higher performance towards the OER with a much smaller overpotential of 401 mV to obtain a current density of 10 mA/cm^2. This outcome is comparable to the best performance of the previously reported about Co_3O_4 towards the OER at the same condition.[345]

In order to further demonstrate the high activity of the Co_3O_4 nanoflakes. Tafel plot was obtained from the equation η= blog(j/j_0).[357, 361] As shown in Figure 8-7b, mesoporous Co_3O_4 nanoflakes exhibited a Tafel slope of b = 48 mV/decade in 1 M KOH and b = 56 mV/decade in 0.1 M KOH. This value is smaller than those of both Co_3O_4/CNT and Co_3O_4/Graphene,[23, 36] which implies that the synthesized mesoporous Co_3O_4 nanoflakes is an efficient catalyst to the OER.

The long-time stability of the electrode is also important for practical applications. The stability of Co_3O_4 nanoflakes was assessed for 1000 cycles (as shown in Figure 8-7c). The Co_3O_4 nanoflakes exhibit a good catalytic stability during OER and no obvious decay of the activity was observed after 1000 cycles. This could be attributed to the stability of the unique mesoporous and interconnected structure. In order to probe the stability of mesoporous Co_3O_4, post-mortem analysis was performed on the electrode after 1000 cycles via *ex-situ* FE-SEM images. It should be noted that even though the mesoporous Co_3O_4 material has experienced 1000 cycles, the mesoporous structure and interconnected particular feature are still well maintained, which provides solid evidence to the robust structure stability and superior electrochemical catalysis on oxygen evolution reaction. The results indicate that the mesoporous Co_3O_4 material with highly reactive facets and unique architecuture can resist the strong causticity of alkaline conditions and microforces generated from oxygen bubbles.

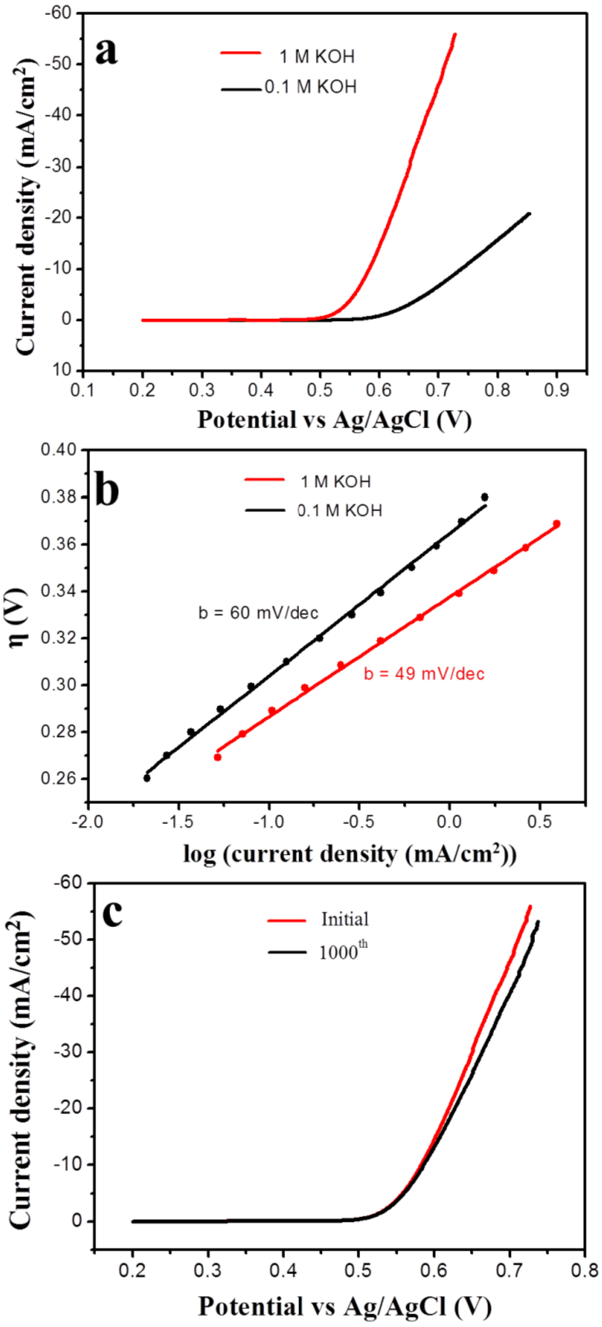

Figure 8- 10 (a) The electrochemical performance on oxygen elvolution reation of mesoporous Co_3O_4 swept from 200 to 900 mV vs Ag/AgCl at 1mV/s in 0.1 M (black) and 1 M (red) KOH aqeous solution. (b) Tefel plot (overpotential versus log current) derived from (a). (c) OER polarization curves for mesoporous Co_3O_4 nanoflakes electrode in the 1st and 1000th cycle of accelerated stability test.

8.4 Conclusions

We have sucessfully synthesized mesoporous Co_3O_4 with interconnected achitechture by means of a microwave-assisted hydrothermal and low-temperature conversion method, which exhibits excellent electrochemcial performances as anode materials in lithium ion batteries and as catalyst in oxygen evolution reaction under alkaline solutions. FESEM and TEM images show the unique interconnected and mesoporous structure. When employed as anode materials for lithium ion batteries, mesoporous Co_3O_4 delivered high specific capacity of 883 mAh/g at 0.1 C current rate and stable cycling performances even at higher current rates. Post-mortern analysis of ex-situ FESEM images reveal that the particular structure has been well maintained after long-term charge/discharge cycling and verifies the robust properties of mesoporous Co_3O_4 nanoflakes electrode. The mesoporous Co_3O_4 material also exhibits OER active property, showing an onset potential towards OER is 0.529 V (vs. Ag/AgCl) in alkaline solution and smaller Tafel slopes of b = 49 mV/decade in 1 M KOH and b = 60 mV/decade in 0.1 M KOH. That implys that the synthesized mesoporous Co_3O_4 is an efficient catalyst to the OER. Meanwhile, the mesoporous Co_3O_4 exhibits a good catalytic stability during OER even cycled 1000 times, which was attributed to the stability of unique mesoporous, interconnected structure and exposed reactive edges.

CHAPTER 9 3D HYPERBRANCHED CARBON NANORODS ENCAPSULATED SULFUR COMPOSITES FOR LITHIUM SULFUR BATTERIES

9.1 Introduction

Lithium-sulfur (Li-S) batteries are regarded as a promising rechargeable battery system due to the low cost, natural abundance of sulfur (almost 3% of the Earth's mass) and environmentally friendly. The redox reaction of a lithium-sulfur battery can be described as:

$$S_8 + 16Li \leftrightarrow 8Li_2S \qquad (1)$$

The reaction occurs at around 2.1 V with respect to Li^+/Li. However, Li-S batteries suffer several drawbacks, including the intrinsic low electrical conductivity of sulfur, dissolution of polysulfides in electrolytes, shuttling effects and volume expansion/contraction of sulfur during cycling. These lead to fast capacity loss and low Coulombic efficiency. There are three main techniques that can significantly confine sulfur and address those aforementioned problems: (i) encapsulate sulfur into various carbon matrices,[45] (ii) strengthen sulfur's chemical bonds with metal oxide additives, (iii) wrap sulfur with conducting polymers. In the last decade, substantial efforts have been devoted toward alleviating these drawbacks and enhancing cycling performances. This has been through melting or infiltrating sulfur at 155 ℃ into various carbon matrices such as mesoporous carbon materials, hollow or double-shelled hollow carbon spheres, aligned carbon nanotubes or carbon nanofibers and graphene based composites.[27, 29-31, 37, 42-43, 50, 52, 59, 362-363] Metal oxide additives, such as yolk-shell TiO_2 spheres, mesoporous silica and metal-organic frameworks, can effectively strengthen the interactions with sulfur and significantly reduce the shuttling effect.[60-61, 326] Conducting polymers or amphiphilic polymers (poly (3,4-ethylenedioxythiophene) PEDOT,[56] Polypyrrole-polyethylene glycol (PPY-PEG) and polyvinylpyrrolidone (PVP)) form a strong membrane,[28, 47, 364-365] which can resist large volume expansion during discharge and avoid sulfur from direct contact with electrolytes, and therefore, prevent the dissolution of polysulfides.

Besides investigations into carbon matrix and polymer functionalization, sulfur source (assembling to a S_8 ring) plays a major role in the redox reactions in Li-S batteries. Commercial sulfur was chosen as the sulfur source in most previous reports, and it was directly mixed with carbon matrix or dissolved into different solvents, [29, 116, 363, 366] such as toluene,[30] carbon disulfide,[56, 367] and dimethyl sulfoxide,[39] then heated to 155 ℃ to obtain homogenous nanocomposites. Cui and co-workers exploited a novel sulfur source via an *in situ* precipitation method.[365] Colloidal monodisperse PVP-encapsulated sulfur spheres were obtained through a simple reaction between sodium thiosulfate and hydrochloric acid at room temperature. Another sulfur source, lithium polysulfidophosphates, was discovered by Liang and co-workers.[368] This sulfur rich compound has a high ionic conductivity of 3.0×10^{-5} S/cm at 25 °C (eight orders of magnitude higher than that of Li_2S) and delivered an excellent cycling performance.

Recently, Nazar and co-workers demonstrated that PEG-functionalized CMK-3 trapped highly polar polysulfides and achieved 1320 mAh/g in the initial cycle and 1100 mAh/g at the 20th cycle.[362] It was reported that the PVP-modified carbon nanofibers with strong interactions between non-polar carbon and polar Li_xS clusters delivered a high specific capacity of 1180 mAh/g at 0.2 C current density and maintained 80% of the initial capacity at the 300th cycle.[53] Moon and co-workers encapsulated sulfur into thin-walled carbon nanowires which were obtained with the assistant of anodic aluminium oxide (AAO) template, demonstrating high-rate electrochemical behaviors.[51] However, the noble metal (platinum) and expensive template (AAO) are involved in the synthesis process, which makes it hard to scale up.

Herein, we report the synthesis of hyperbranched hollow carbon nanorod encapsulated sulfur (CNR-S) as the cathode materials for lithium-sulfur batteries. Considering the advantage of the *in situ* synthesis technique, we chose sodium thiosulfate as the sulfur source and applied a relatively moderate acid as the precipitation agent to minimize sulfur size and break the puckered ring of sulfur, which can facilitate sulfur nanoparticles to transfer inside carbon nanorods via capillary forces during a heat treatment. The as-prepared composite sulfur cathodes delivered a high specific capacity of 1378 mAh/g at 0.1 C current rate. The materials also exhibited a superior high rate performance and extended cyclability. Post-mortem analyses verified the preservation of the integrity of the hyperbranched carbon nanorods-encapsulated sulphur electrode after long-term high rate cycling.

9.2 Experimental

9.2.1 Preparation of hyperbranched MgO with maze-like structure

The hyperbranched MgO with maze-like structure (Figure 9-1) was prepared via bubble-ejected assisted chemical vapor transport and condensation method, and the schematic reaction apparatus was presented in Figure 9-2. The apparatus was equipped with two supplying gases (H_2/Ar (H_2, 5%) and C_2H_2/Ar (C_2H_2, 5%)), which were used for different purposes.[369] After the two ceramic crucibles were filled by Mg vapor at 900 ^{o}C, preheated moisture was carried into the quartz tube by gas bubbles, which were carried by Ar gas (100 sccm, 600 ppm moisture).[370] The reaction can be described as:

$$\text{Mg (vapor)} + H_2O \text{ (gas)} = \text{MgO (solid)} + H_2 \text{ (gas)} \quad (2)$$

The typical synthesis procedure can be described as follows: 1 gram magnesium was sealed by two ceramic crucibles in a glove box, then covered by polymer membrane to avoid magnesium contacting with air. After removed the polymer cover, the precursor was quickly transferred into a horizontal furnace which was pumped to high vacuum, and then filled with H_2/Ar mixed gases (5% H_2, 100 sccm) and heated to 900 ℃ with a heat rate of 5℃/min, maintained at 900 ℃ for 10 mins. Preheated water vapor carried by Ar gas (100 sccm) was then introduced into the reaction apparatus. The whole reaction was kept for 130 mins (10 mins for the diffusion of Mg vapor). The carrying gas was subsequently switched off and the furnace was allowed to cool to room temperature in H_2/Ar mixed gases.

9.2.2 Preparation of hyperbranched hollow carbon nanorods with maze-like hierarchical structure

The as-prepared hyperbranched MgO obtained in 130 min was placed into a horizontal furnace and heated to 750 ℃ with a heat rate of 5 ℃/min in Ar (100 sccm), followed by the introduction of acetylene/Ar mixed gases (5% C_2H_2, 50 sccm) and kept for 30 min. The furnace was then cooled to room temperature in Ar. The as-obtained product was washed with HCl (1 M, 200 mL for 10 h) to remove the template MgO and other impurities, washed with copious de-ionized water and dried overnight in a vacuum oven at 80 ℃.

9.2.3 Preparation of hyperbranched carbon nanorods/sulfur composites

50 mg as-synthesized hollow carbon nanorods were transferred into a sodium thiosulfate solution (6.25 mM, 90 mL de-ionized water and 10 mL ethanol), stirring intensely for 30 mins, Acetic acid (1M, 15 mL) solution was, drop-by-drop, added to the dark suspension and continually stirred for 30 mins. After that, 10 mg polyvinylpyrrolidone (PVP) was added and stirring maintained for 3 hrs. The suspension was then treated by pulsed sonication for 30 mins (5s on and 5s off) in an ice bath using a Branson S-450D sonifier with a horn of 13 mm in diameter (40% amplitude). After that, the suspension was washed with de-ionized water and dried overnight in a vacuum oven at 80 ℃. Finally, the composites were quickly placed into a preheated horizontal furnace (155 ℃) with a flow of Ar (100 sccm) gas for 12 hour, and then cooled to room temperature.

9.2.4 Materials characterization

The as-prepared hyperbranched carbon nanorods-sulfur composites were characterized by X-ray diffraction (Rigaku D/max-2550V with Cu Kα radiation) operated at 40 KV and 30 mA. Raman spectra were measured by a Renishaw inVia Raman spectrometer system (Gloucestershire, UK) equipped with a Leica DMLB microscope (Wetzlar, Germany) and a 17 mW at 633 nm Renishaw helium neon laser with 50% power. A thermogravimetric analyzer (TGA, SDT 2960) was used to measure the weight percentage of S from RT to 825 ℃ in air. The morphologies and crystal structure of materials were analyzed by field emission scanning electron microscope (JSM-6700F, 20kV), Zeiss EVO MA 15 scanning electron microscope and transmission electron microscope/selected area electron diffraction (TEM/SAED, JEOL JEM-200CX and JEM-2010F) equipped with an energy-dispersive X-ray spectroscopy (EDX).

9.2.5 Electrochemical measurements

The working electrodes were made from 80 wt.% of active materials, 10 wt.% of the conductive agent (acetylene black), and 10 wt.% of the binder (alginic acid sodium salt extracted from brown algae). The mixture was stirred by an adjustable high-speed electric agitator. The working electrodes were dried in a vacuum oven. CR2032 coin cells were assembled in an argon-filled glove box (Mbraun, Unilab, Germany), in which both the moisture and oxygen contents were controlled to be less than 0.1 ppm. Lithium foil was used as the counter electrode. The electrolyte was 1 M lithium bis-(trifluoromethanesulfonyl) imide (LiTFSI) and 1 wt.% lithium nitrate ($LiNO_3$) in 1,3-dioxolane and 1,2-dimethoxy-ethane (volume ratio 1:1). Electrochemical measurements were performed using a LAND-CT2001C battery test system. The cells were discharged and charged galvanostatically in the fixed voltage range of 1.7–2.6 V with a current density of 167.3 mA/g (0.1 C). Higher current rates (0.5 C, 1 C, 5 C and 10 C) were also applied to test the electrochemical performances.

9.3 Results and discussions

Hyperbranched nanowires/trees/rods of SiO_2,[371] PbS,[372] ZnO[373-374] and MgO[375-377] have been synthesized by a chemical vapor transport and condensation method and applied for electronic devices and sensors. However, hyperbranched nanostructures are seldom exploited for energy storage applications. We intend to synthesize hyperbranched hollow carbon nanorods as a matrix for sulfur cathodes using MgO nanorods as templates. Figure 9-1 shows a schematic illustration of the synthesis process. In the first step, hyperbranched MgO nanorods with a 3D nanomaze architecture were prepared by a CVTC approach (Figure 9-1a and Figure 9-2). In the second step, carbon coating was performed to coat a carbon nanolayer on the surface of MgO nanorods (Figure 9-1b). Then, hollow carbon nanorods were obtained by etching MgO templates, during which the carbon nanorods inherited the hyperbranched nanorod-like 3D architecture (Figure 9-1c). In the final step, sulfur was encapsulated into hyperbranched hollow carbon nanorods and functionalized with PVP polymers by an *in situ* precipitation and ultrasonic treatment method using sodium thiosulfate as the sulfur source. After that, a heat treatment was performed with flowing argon gas to remove sulfur adsorbed on the outer surfaces of the carbon nanorods (Figure 9-1d).

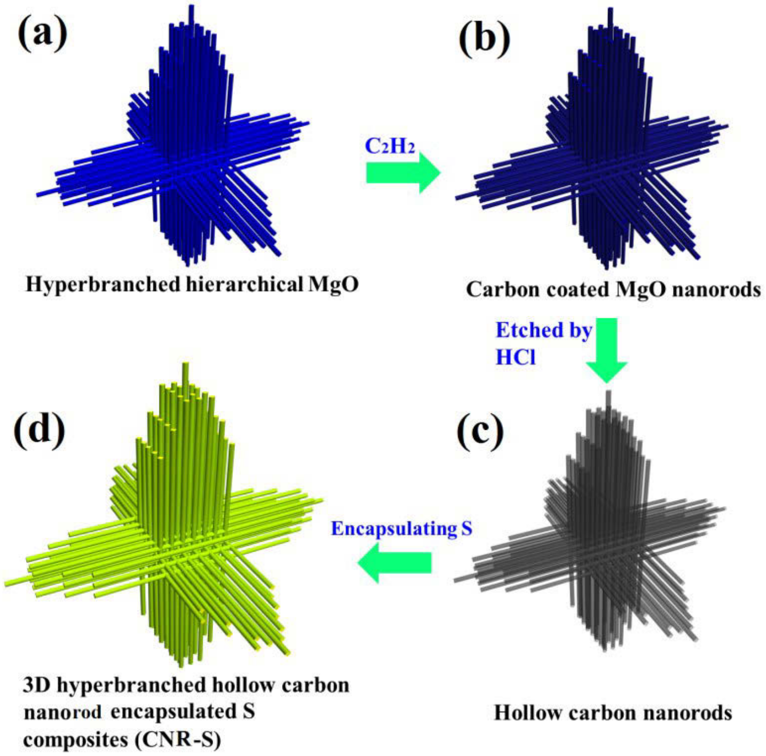

Figure 9- 1 The schematic illustration for the synthesis route of 3D hyperbranched hollow carbon nanorod-sulfur (CNR-S) nanocomposites. (a) Hyperbranched MgO nanorods template. (b) Carbon coated MgO nanorods. (c) Hollow carbon nanorods with a new maze-like architecture. (d) Carbon nanorod encapsulated sulfur nanocomposites.

Just like other hyperbranched materials, MgO clusters also follow the noted vapor-solid (VS) mechanism via a chemical vapour transport and condensation method. More specifically, the growth directions are perpendicular to high surface energy trunks or sub-branches, and their cross-sections always have well-defined squares or rectangles (Figure 9-3a-h and Figure 9-4a), which is also reflected on the SAED pattern (Figure 9-4b). The side surfaces are enclosed by certain low-index crystallographic planes with low energy {100} facets to minimize the surface energy, subsequently exposed Mg vapor reacts with moisture and generates fresh MgO seeds, which are transported by carrying gases and migrated to an orthogonal direction. Therefore, hyperbranched MgO nanorods are grown according to the principle of growth kinetics and minimizing surface energy. Branch trunks are perpendicular to the main trunks and form a maze-like architecture. Each trunk has a length of about 10–60 μm and a rectangular cross-section with a side width range of about 100-300 nm.

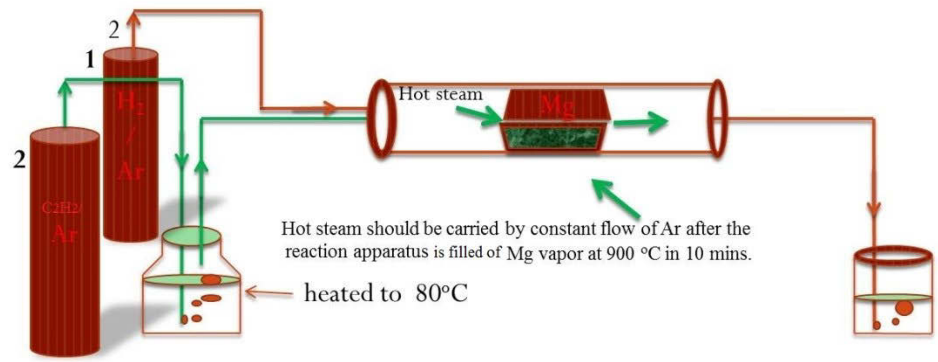

Figure 9- 2 Schematic image of reaction apparatus where a small gap was left between the two ceramic crucibles as a path for preheated steam (H_2/Ar mixed gas used for expelling oxygen in the tube. Hot steam should be carried by constant flow of Ar gas after the reaction apparatus full of Mg vapor at 900 ^{o}C in 10 mins).

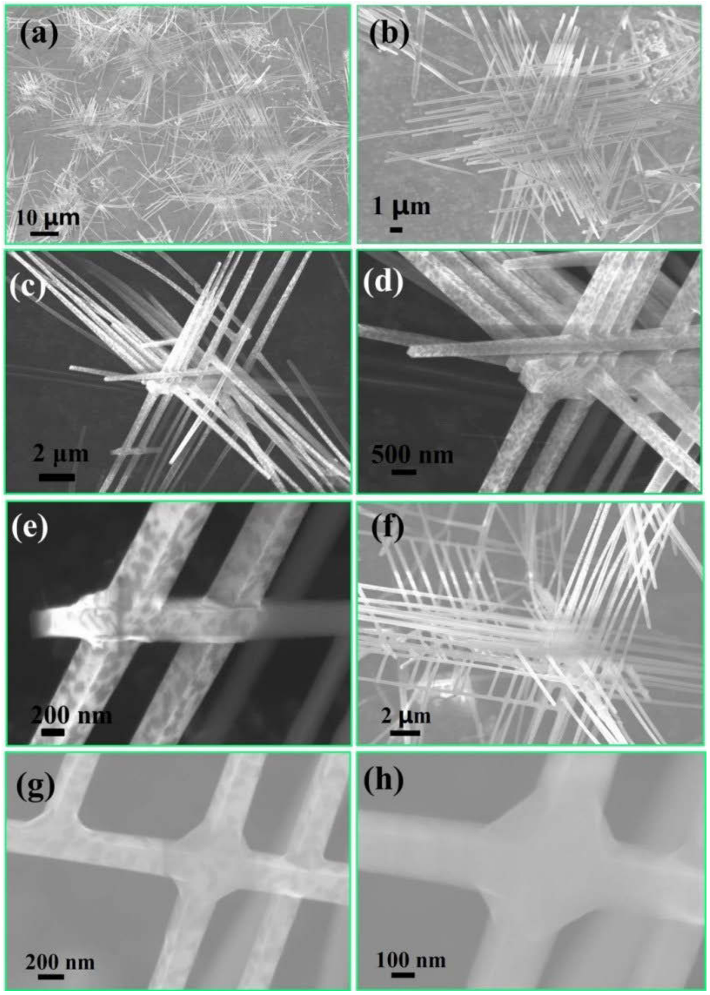

Figure 9- 3 Low and high magnified SEM images of hyperbranched MgO templates, illustrating the multiple branches are perpendicular to the main trunks.

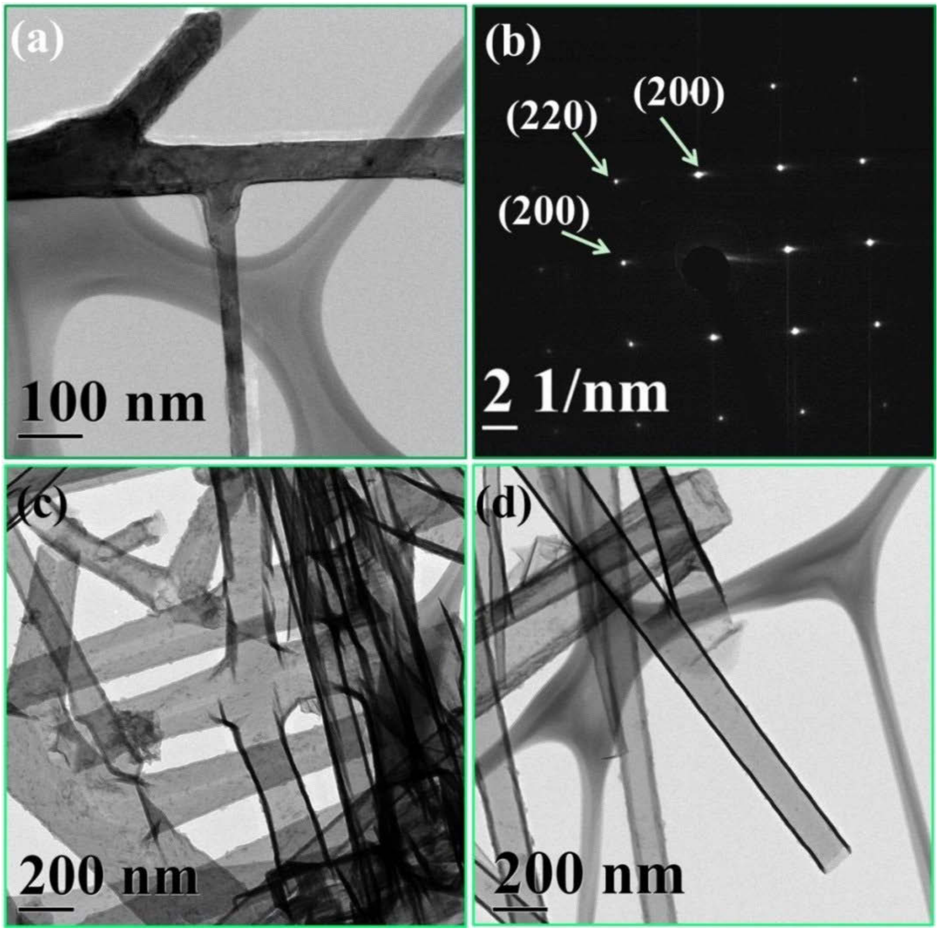

Figure 9- 4 TEM image of MgO template (a) and selected area electron diffraction (SAED) pattern (b). TEM images of hollow carbon nanorods with hyperbranched and open-ended structure (c-d).

X-ray diffraction and Raman spectroscopy measurements were employed to analyze the products obtained in each step (Figure 9-5a and b). X-ray diffraction patterns in Figure 9-5a examine samples obtained in each stage (the peaks of MgO are indexed to JCPDS No. 65-0476 with a face-centered cubic structure). The CNR-S composites present similar peak position to pure S (JCPDS No. 42-1278) with an F*ddd* orthorhombic structure, indicate sulfur trapped in carbon nanorods is highly crystal. Raman spectroscopy measurements were employed to analyze pure S, carbon nanorods and CNR-S composite (Figure 9-5b). The intensity ratio I_D/I_G of approximate 1 revealed that hollow carbon nanorods are partially graphitized, which can enhance the conductivity of insulated S in nature. Additionally, the characteristic peak of S at 490 cm^{-1} related to the A_1 symmetry modebetween sulfur bonds also appeared in the spectrum of CNR-S composite with relative low intensity,[1-3] verifying the crystalline feature of S is well maintained in the CNR-S composite.

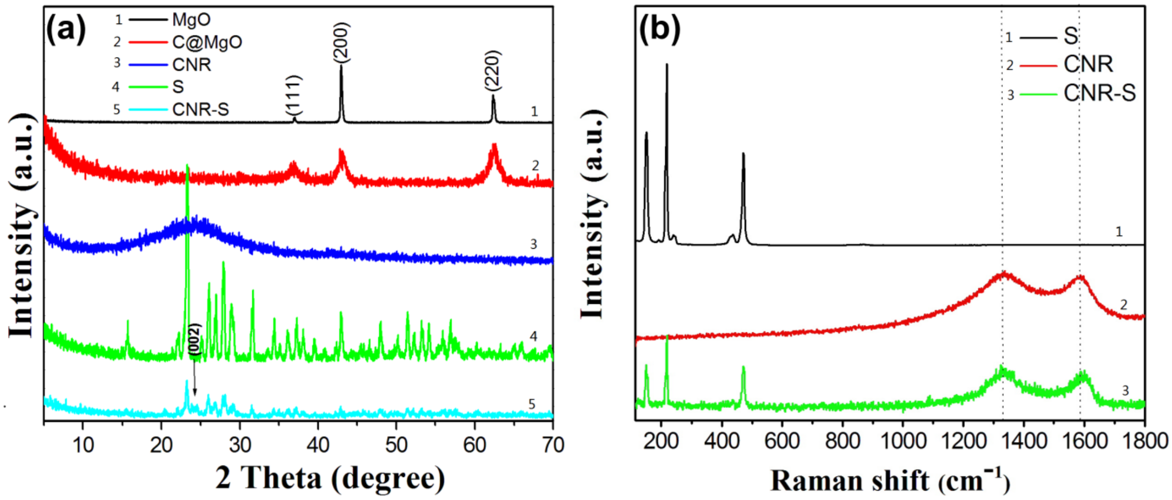

Figure 9- 5 (a) The XRD patterns of hyperbranched MgO, C@MgO, hyperbranched carbon nanorods, pure sulfur and CNR-S composites, respectively. (b)Raman spectra of sulfur, carbon nanorod and CNR-S composites.

Figure 9-6 (a) and (b) show the low and high magnification FESEM images of hyperbranched MgO nanorods, which demonstrate a hierarchical 3D nanostructure. Branch trunks are perpendicular to the main trunks and form a maze-like architecture. Each trunk has a length of about 10–60 µm and a rectangular cross-section with a side length of about 100-300 nm. Coating carbon layers on hyperbranched MgO nanorods to duplicate the hierarchical architecture can be easily realized by the CVD method.[81, 265, 378-380] Figure 9-6(c) shows the FESEM image of carbon-coated MgO nanorods, from which it can be seen that hyperbranched and maze-like architectures have been preserved. The elemental mapping image (TEM) further confirmed the core-shell structure with the thickness of coated carbon layer of about 10 nm (Figure 9-6(d)). MgO nanorods templates were etched by diluted HCl solution to obtain hollow carbon nanorods.

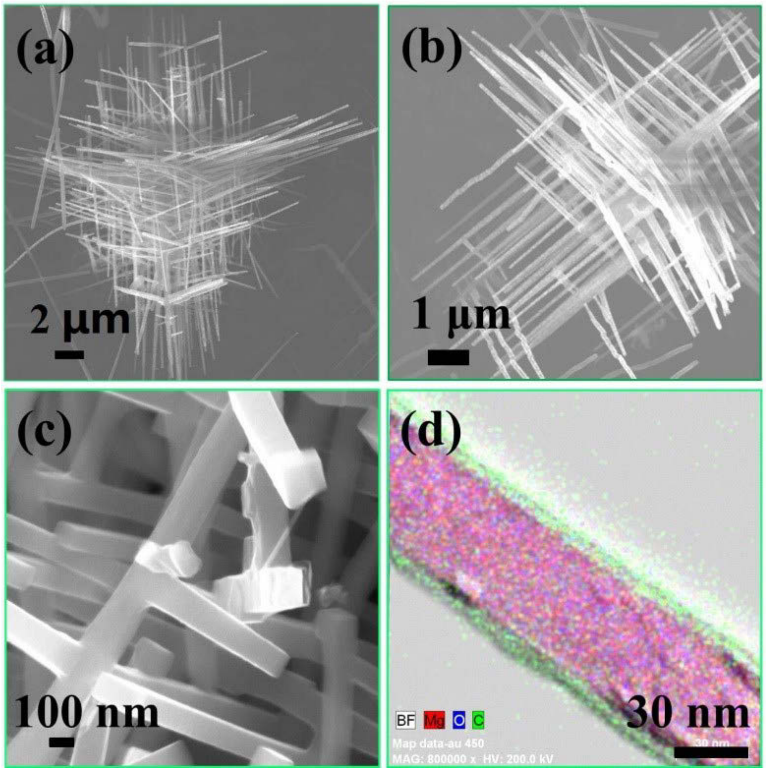

Figure 9- 6 The morphologies of hyperbranched hierarchical MgO and C@MgO nanocomposites. (a and b) FESEM images of hyperbranched hierarchical MgO. (c) FESEM image of C@MgO composites. (d) TEM elemental mapping image of one C@MgO nanorod.

The morphology and structure of hollow carbon nanorods were characterized by FESEM and TEM. As shown in Figure 9-7(a), the carbon nanorods inherited the hyperbranched and maze-like architecture, indicating the successful duplication of the template. The insert image in Figure 9-7(a) represents an open-ended carbon nanorod with a right angle. The hollow structure was verified by TEM observation (as shown in Figure 9-7(b) and (c)). Figure 9-7(c) shows a high resolution TEM image of a branch of carbon nanorod and the corresponding thickness profile,[271] from which the thickness of the wall can be determined to be about 10.1 nm. The ends of the hollow carbon nanorods are open, which is important for loading sulfur and reacting with Li ions when applied as cathodes in Li-S batteries. The TEM image on the right in Figure 9-7(c) illustrates the hollow feature of the junction between two jointed carbon nanorods. This unique interconnected hollow structure can effectively encapsulate sulfur and confine the diffusion of polysulfides.

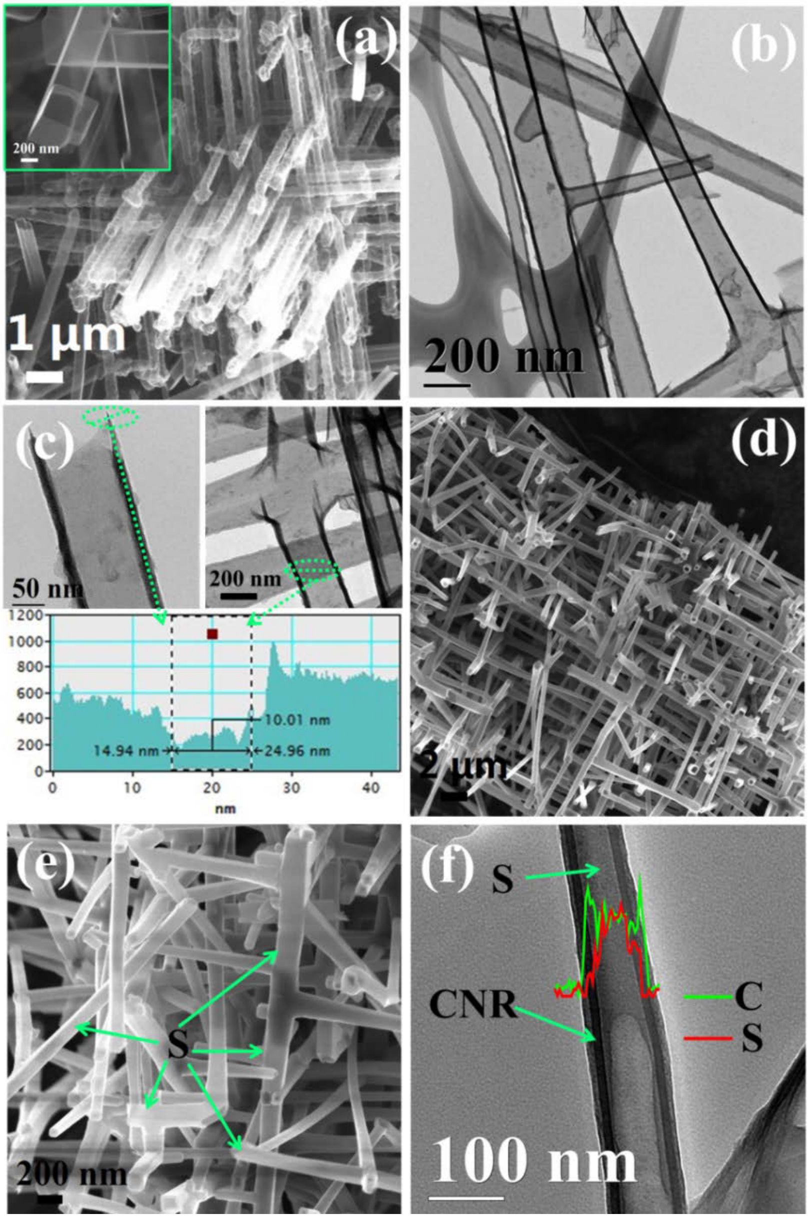

Figure 9- 7 The hollow CNR and CNR-S nanocomposites. (a) FESEM images of hollow carbon nanorods, insert image represents a typical open-ended carbon nanorod. (b and c) Low and high magnified TEM images of hollow carbon nanorods, insert image and profile in (c) showing the interconnected junction structure and thickness of carbon nanorod. (d) FESEM image of CNR-S with a hyperbranched architechture. (e) FESEM image of CNR-S nanocomposites (S is pointed with green arrows). (f) TEM image of CNR-S nanocomposites with insert elemental line scan of carbon and sulfur (C and S are indicated by green and red arrows, respectively).

Sulfur loading into hollow hyperbranched carbon nanorods was carried out using a modified *in situ* precipitation method. This approach has been previously reported for the preparation of hollow PVP-S spheres and yolk-shelled S-TiO_2 nanostructures,[326, 365] in which amphiphilic PVP polymers wrapped hydrophobic S nanoparticles and served as soft templates for self-assembling hollow PVP-S spheres with diameters of 400–500 nm. However, it is difficult to encapsulate such large PVP-S spheres into hollow carbon nanorods with high length/radius aspect ratios. We employed acetic acid as the reactant and strong ultrasonic agitation to generate small sulfur particles to avoid the formation of large PVP-S spheres. The reaction of sulfur formation can be described as:

$$Na_2S_2O_3 + 2CH_3COOH \rightarrow S\downarrow + SO_2\uparrow + 2CH_3COONa + H_2O \qquad (3)$$

The sulfur-loaded hyperbranched carbon nanorods were heated at 155 ℃ for 12h in Ar, followed by FESEM and TEM observation. It was found that sulfur had been completely encapsulated within the hyperbranched hollow carbon nanorods (FESEM in Figure 9-7(d) and (e)). Sulfur was pointed with green arrows. TEM analysis revealed a hierarchical structure of carbon nanorods-S, in which sulfur was wrapped by PVP polymers and trapped in hollow carbon nanorods. The surfaces of the carbon nanorods were also coated with a thin layer of PVP polymers (as shown in Figure 9-7f). The presences of carbon (green line) and sulfur (red line) were confirmed by elemental line scan in Figure 9-7(f), which clearly verified that sulfur was loaded into hollow carbon nanorods.

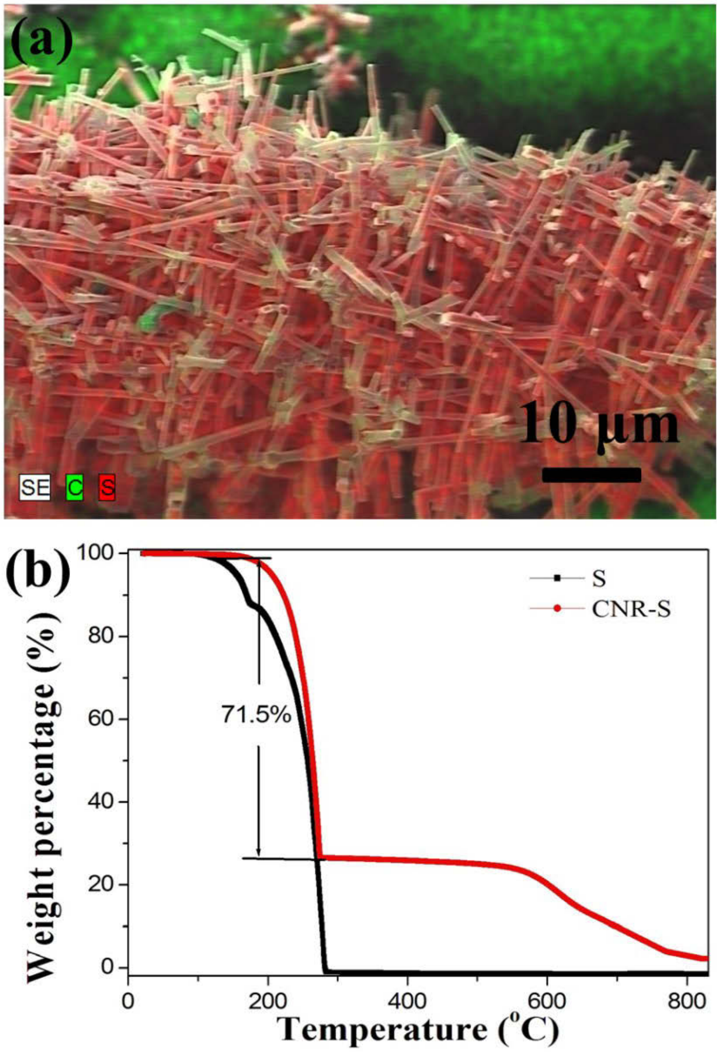

Figure 9- 8 (a) SEM elemental mapping image of CNR-S composites. (b) Thermal gravimetric analysis of commercial sulfur and CNR-S composites between 25 and 825 °C.

Furthermore, SEM elemental mapping image in Figure 9-8a clearly exhibites that sulfur (in red) is encapsulated into hyperbranched hollow carbon nanorods (in green) and sulfur neither aggregates into large agglomerates nor appears outside of carbon nanorods, which can effectively avoid the direct contact between sulfur and electrolyte, further effectually reduce the dissolution of polysulfides. The content of sulfur in the composites was determined to be 71.5 wt.% by thermal gravimetric analysis (TGA, Figure 9-8b). It should be noted that sulfur in the PVP-wrapped CNR-S composites starts to evaporate at 220 ℃, which is higher than that of pure sulfur (180 ℃). This indicates an enhanced thermal stability of the as-prepared sulfur composite materials.

The electrochemical performances of hyperbranched CNR-S nanocomposites were evaluated by galvanostatic charge/discharge cycling. It should be noted that all the capacities in this paper are calculated on the actual mass of sulfur and each electrode is around 1.25 mg. Therefore, the mass of sulfur in each electrode is approximate 0.71 mg and the weight ratio of S:CNR:PVP is 1:0.35:0.07. Typical charge/discharge profiles are shown in Figure 9-9a (0.1 C, 1 C= 1673 mA/g) within a voltage window of 1.7-2.6 V. The electrode delivered an initial discharge specific capacity (lithiation) of 1378 mAh/g with two discharge plateaus. The two plateaus correspond to the formation of long-chain polysulfides (Li_2S_x, $4 \leq x \leq 8$) at around 2.3 V and short-chain L_2S_2 and Li_2S near 2.1 V, respectively. The charge capacity (delithiation) of CNR-S reached to 1630 mAh/g. After 275 cycles, the electrode in Figure 9-9b still presented a discharge capacity of 1169 mAh/g with a capacity retention ratio of 84.8%. When the current density was increased to 1 C, the electrode in Figure 9-10a exhibited a discharge capacity of 990 mAh/g and charge capacity of 995 mAh/g. After 500 cycles, the electrode still maintained at 934.5 mah/g with a capacity retention of 94.4%, indicating a substantial depression of shuttling effect. However, for pure sulfur electrode, the initial charge capacity (1195 mAh/g) in Figure 9-10b is much higher than that of discharge capacity (392 mAh/g), implying the existence of shuttle effect. Without the confinement of carbon matrix or conducting polymers, the charge/discharge capacities of pure sulfur electrode quickly declined to ~25 mAh/g. Figure 9-10c shows the cycling performance and Coulombic efficiency of the CNR-S composite and pure sulfur electrode over long-term cycles, respectively. The capacity stability and Coulombic efficiency of pure sulfur are significantly lower than that of CNR-S electrode. The CNR-S electrode retained 94.4% of the initial capacity after 500 cycles at 1 C, while the capacity retention ratio of pure sulfur was only ~2%. Compared with pure sulfur electrode and the previous reports,[27, 46, 363] the enhanced electrochemical performances of CNR-S composite indicated that the dissolution of polysulfides and the shuttling effect had been distinctly suppressed.

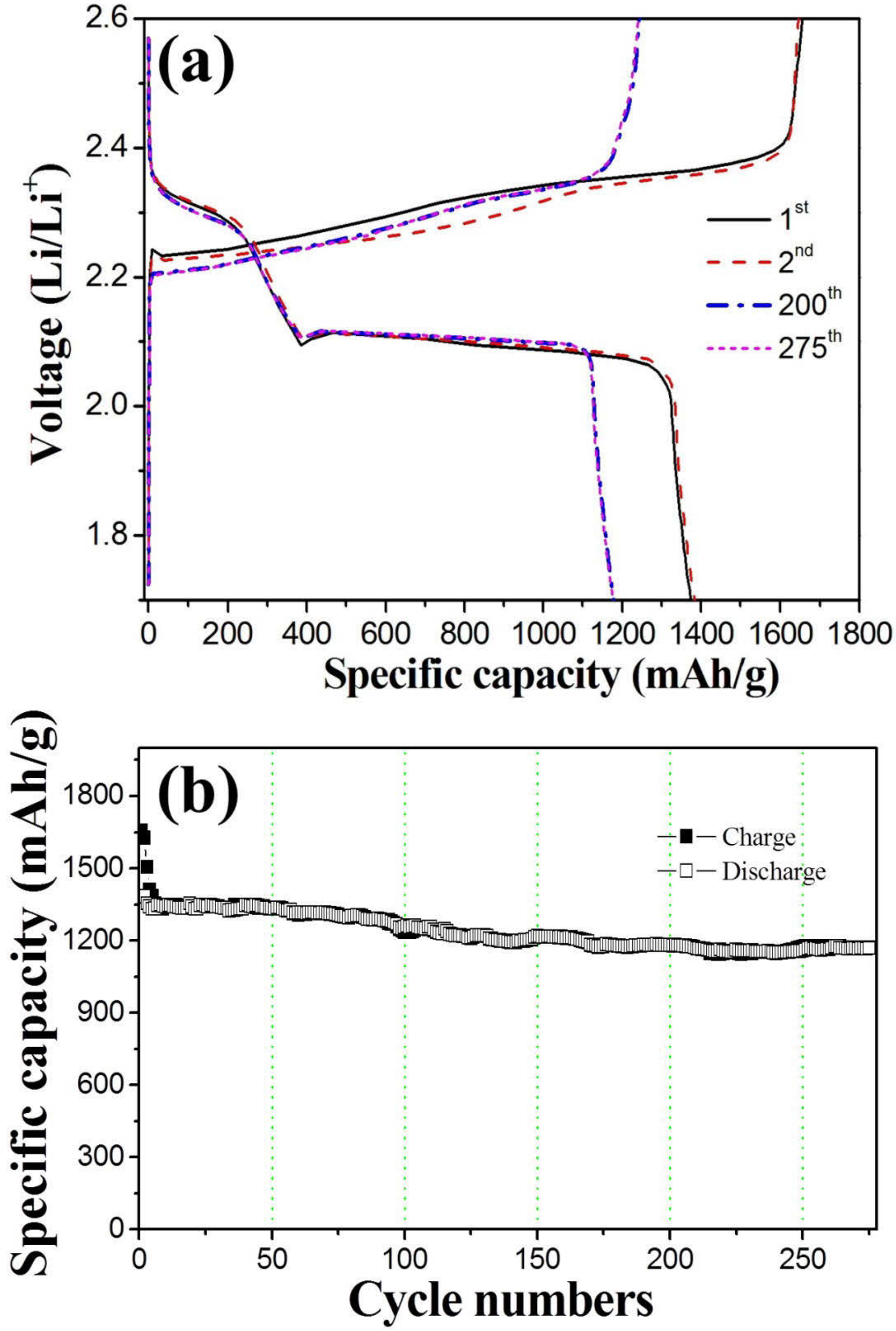

Figure 9- 9 Electrochemical performance of CNR-S electrodes. (a) Typical charge-discharge profiles of CNR-S nanocomposites at 1st, 2nd, 200th and 275th cycles at 0.1 C. (b) Cycling performance of CNR-S nanocomposites at 0.1 C with testing voltages between 1.7 V and 2.6V.

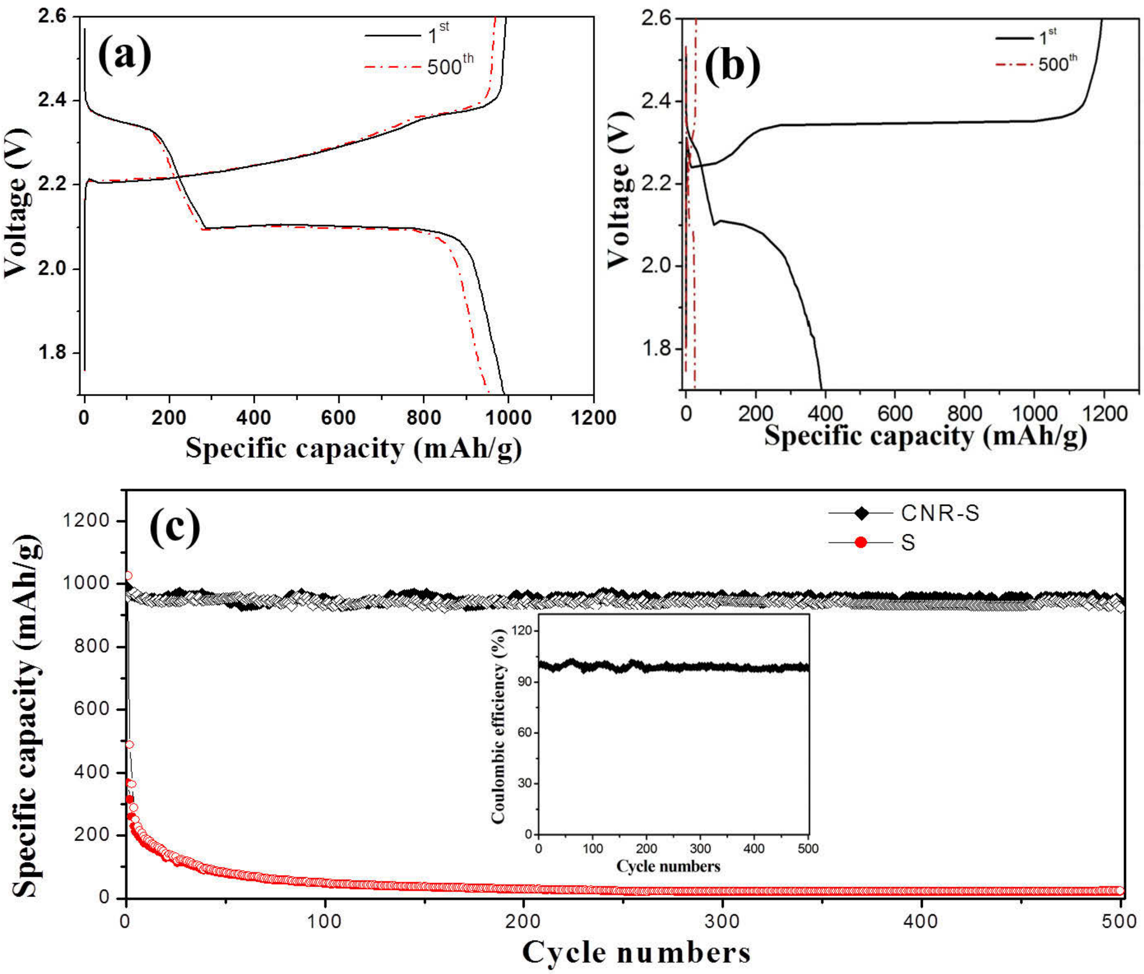

Figure 9- 10 Electrochemical performance of CNR-S electrodes. (a) Typical charge/discharge profiles of CNR-S nanocomposites at the 1st and 500th cycles at 1 C (1 C = 1673 mA/g). (b) The charge/discharge profiles of pure S at 1st and 500th cycle at 1 C. (c) Cycling performances of CNR-S nanocomposites and pure S at 1 C with testing voltages between 1.7 V and 2.6V. Insert image: Coulombic efficiency of CNR-S nanocomposites.

We also cycled the CNR-S electrodes at different current rates (Figure 9-11a) and the discharge/charge profiles are presented in Figure 9-11b. Figure 9-11a shows the results of a CNR-S composite electrode cycled at step-wise current rates. During the charge/discharge process, the electrode was cycled from low current rates to high current rates and then reversed back to low rates. It should be noted that when the current rates reversed back to lower rates, the electrode recovered its high capacities. The corresponding charge/discharge profiles in different current densities are presented in Figure 6b, demonstrating larger voltage platinum gaps along with higher current densities. The CNR-S electrodes exhibited an initial capacity of 1255 mAh/g at 0.5 C in Figure 9-11c rate with 91.4% capacity retention ratio after 500 cycles. When increased the current rates to 5 C and 10 C, the CNR-S electrodes achieved capacities of 861 mAh/g and 663 mAh/g in the initial cycle, respectively. Furthermore, the electrodes also demonstrated superior cycling performances with the capacity retention ratio of 95.5% and 85.6% after 500 cycles at current rates of 5 C and 10 C, respectively. This result manifests that the CNR-S composites can tolerate a varied high current charge/discharge. The superior electrochemical performances could be ascribed to the hyperbranched hollow carbon nanorod and the PVP-functionalized hierarchical nanomaze-like architecture. The hyperbranched hollow carbon nanorod, high aspect ratio and multiple cross junctions can effectively hinder the dissolution of polysulfides. Furthermore, the 3D hierarchical hollow structure can allow sulfur to expand along the carbon nanorods upon lithiation, which is critical in maintaining the stability of the electrode at high current rates. The PVP polymer coating also plays a supportive role in stabilizing the cycling performance, which has been confirmed by previous reports.[53, 56, 365] Sulfur encapsulated in the 3D hierarchical hollow carbon nanorods does not directly contact with the electrolyte, which can prevent the dissolution of polysulfides and minimize the shuttling effect. On the other hand, Li ions can facilely diffuse through carbon layers and react with sulfur. Moreover, hyperbranched carbon nanorods with interconnected nanostructures can provide electrochemically conductive networks for insulating sulfur. Therefore, these effects jointly contribute to the high capacity, excellent rate ability and superior cycling performance of CNR-S composites as cathode materials in Li-S batteries. The electrochemical performances of CNR-S materials are compared with other carbon-sulfur based materials, which are shown in Table 9-1.

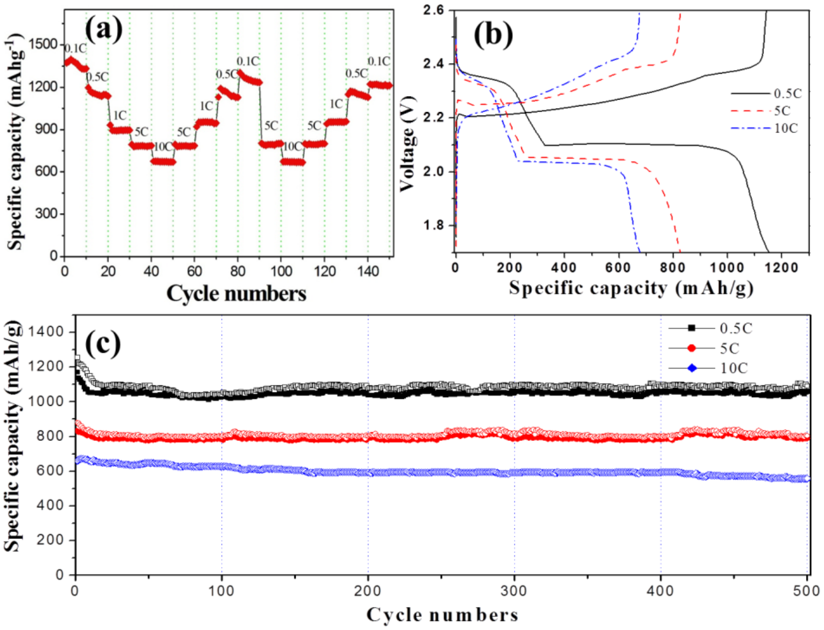

Figure 9- 11 (a) Cycling performance of CNR-S nanocomposites at step-wise rates. (b) Typical charge/discharge profiles of CNR-S electrodes at 0.5 C, 5 C and 10 C in the first cycle, respectively. (C) Cycle lifes of CNR-S nanocomposites at higher current densities (0.5 C, 5 C and 10 C).

Table 9- 1 The electrochemical performances of CNR-S materials are compared with other carbon-sulfur based materials

Sulfur cathode Ref.	Sulfur percentage	Rate capacity based on sulfur mass (mAh/g)	Rate capacity at 0.1 C based on entire electrode mass (mAh/g)	Cycle life	Remained capacity at 0.1 C based on sulfur mass (mAh/g)	Remained capacity at 0.1 C based on entire electrode mass (mAh/g)
Double hollow carbon spheres-S[42]	64%	1020(0.1 C)	653(0.1 C)	100	690(0.1 C)	441(0.1 C)
Highly ordered carbon fibers-S[30]	75%	1100(0.2 C)	825(0.2 C)	150	730(0.2 C)	547(0.2 C)
Porous graphene[363]	66%	1068(0.5 C)	704(0.5 C)	35	653(0.5 C)	430(0.5 C)
The CNR-S cathode in the Thesis	71.5%	1378(0.1 C)	985(0.1 C)	275	1169(0.1 C)	835(0.1C)

Aiming to examine the integrity of the CNR-S electrodes after long-term cycling, post-mortem SEM analysis was performed on the cycled electrodes. Figure 9-12a shows the FESEM image of the CNR-S composite electrode after 500 cycles. The nanorod shape and interconnected nanorod architecture have been well maintained even after long-term charge/discharge cycling, verifying the robust properties of CNR-S composites. The inset schematic in Figure 9-12a illustrates that this interconnected architecture can effectively resist the stress from volume expansion upon lithiation, allowing the volume expands along the radial direction. The distribution of sulfur in carbon nanorods after long time cycles is examined and presented in Figure 9-13a-d. Most of sulfur is still confined in the hollow carbon nanorods and carbon nanorod's skeleton can be distinguished according to the shape of sulfur element. The related EDX spectrum is presented in Figure 9-13e. Additionally, electrochemical impedance spectroscopies were also measured before and after 500 cycles in Figure 9-12b. Both of them present Nyquist plots which were consisted by a depressed semicircle in high frequency region and an oblique line in medium frequency region. The small semicircle of electrode before cycle indicates a lower electrochemical reaction resistance and the relative larger semicircle after cycles confirms that after long cycles, the electrochemical resistance is only slightly increased, which might one of reasons for stable and long cycle life of CNR-S electrodes even at higher current densities.

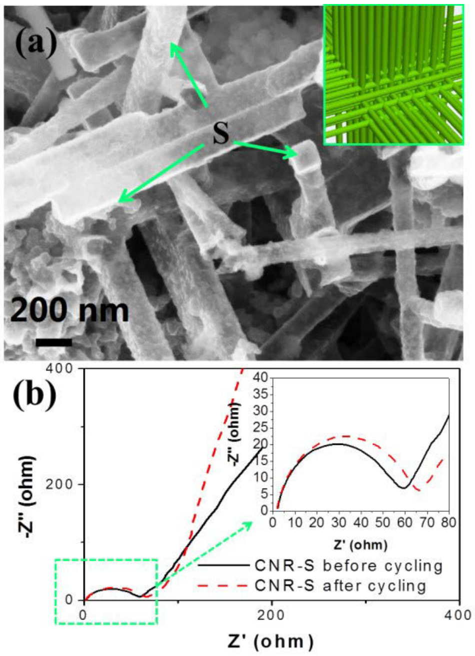

Figure 9- 12 (a) SEM image of CNR-S nanocomposite after 500 cycles with insert image of the schematic illustration of nanorod structure (S was indicated by green arrows). (b) Electrochemical impedance spectra of CNR-S composites before and after 500 cycles. Insert image shows the details.

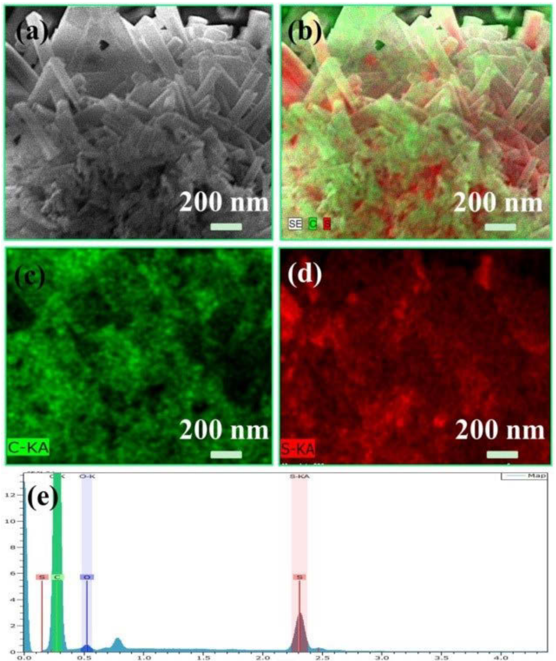

Figure 9- 13 (a-d) Elemental mapping image of CNR-S nanocomposites after 500 cycles, demonstrating a well-maintained state of the electrode. (e) The corresponding EDX spectrum of CNR-S nanocomposites after 500 cycles.

9.4 Conclusions

In conclusion, we have successfully designed and synthesized graphitic hyperbranched hollow carbon nanorod encapsulated sulfur composites as the cathode materials for lithium sulfur batteries. FESEM and TEM characterization confirmed the hierarchical 3D nanomaze-like architecture, in which sulfur was confined inside hollow and interconnected carbon nanorods. When applied as cathodes in lithium-sulfur batteries, CNR-S composites delivered a high specific capacity of 1378 mAh/g at 0.1 C current rate and a stable cycling performance. The CNR-S composites also demonstrated high capacities of 990 mAh/g, 861 mAh/g and 663 mAh/g at 1 C, 5 C and 10 C with capacity retentions of 94.4%, 95.5% and 85.5% after 500 cycles, respectively. Post-mortem FESEM analysis illustrates that the integrity of the CNR-S composite electrode has been well preserved after long-term cycling. The superior electrochemical performances of CNR-S composites should be ascribed to the unique graphitic hyperbranched hollow carbon nanorods architecture, which can effectively suppress the dissolution of sulfur during charge/discharge cycling. The approach and strategy developed in this paper could also be applied to other battery systems, such as lithium-air batteries and sodium-ion batteries.

CHAPTER 10 MULTI-SHELLED HOLLOW CARBON NANOSPHERES FOR LITHIUM-SULFUR BATTERIES

10.1 Introduction

Energy storage devices with merits of high energy density, long cycle life, low cost and safety are in high demand. Substantial efforts have been devoted to develop various energy storage systems, including traditional secondary batteries, lithium-ion, lithium-oxygen and lithium-sulfur (Li-S) batteries, for both portable electronic devices and electric vehicles or plug-in hybrid electric vehicles.[10, 81, 94, 116, 168, 170, 369, 381-382] Among them, Li-S batteries are regarded as a promising system with many advantages, such as low cost, natural abundance of sulfur (around 3% of earth mass), environmental friendliness and high theoretical capacity (1673 mAh/g, energy density of ~2600 Wh/kg).[21, 35, 54, 170, 383] Previous reports on sulfur loading in cathodes are mostly around 70%, which is confined by volume expansion (~80%, charge) and limited inner voids. Most importantly, recent report by Abruña group showed that the volumetric energy density of Li-S cells with a sulfur loading more than 70 wt. % exceeded that of lithium ion cells.[384] In order to achieve high energy density, high percentage of sulfur loading carriers with sufficient inner spaces and good conductivity are required to develop high performance Li-S batteries. In the discharge process of a Li-S battery, there are two main reaction stages, and each stage includes several reactions relating to the transformation of cyclo-octasulfur (S_8) to soluble long-chain lithium polysulfides at the first plateau (2.15-2.4 V), and further decompose to insoluble lithium sulfide (Li_2S) or lithium persulfide (Li_2S_2) at the second plateau (2.0-2.1 V). The subsequent charging process is mainly dominated by the slow kinetic reaction of oxidizing lithium sulfides to lithium polysulfides, and then rapid reversing to cyclo-octasulfur.[26, 28, 385] Two broad oxidation peaks were commonly observed in previous reports.[26, 28, 46]

Multi-shelled carbon and metal oxides nanospheres with high surface area, high electron mobility and robust physical architecture have been extensively applied in lithium ion batteries and photovoltaic cells, exhibiting superior electrochemical and catalytic performances.[386-393] Similarly, multi-shelled hollow carbon nanospheres (MHC) with high specific surface area and large total pore volume could be an ideal carrier for sulfur immobilization.[394] Voids between carbon layers can provide a huge space to accommodate sulfur and tolerate the volume change during charge/discharge processes;[395-400] While the multi-shelled hollow carbon skeletons can enhance the electrode conductivity and prevent sulfur loss. Compared with mono-shelled and double-shelled carbon nanospheres,[42] the multi-shelled spherical structure may offer extra protection to sulfur, because multiple carbon shells can provide alternating barriers to restrain the dissolution of polysulfides.

Herein, we report the synthesis of multi-shelled hollow carbon nanospheres encapsulated sulfur (MHCS) composites as sulfur-rich cathode materials for high performance Li-S batteries. MHC with a high specific surface area of 1050 m^2/g was prepared by an aqueous emulsion approach. Through an *in-situ* sulfur impregnation, MHCS composites with the highest sulfur loading of 86 wt. % were achieved. When applied as cathodes in lithium sulfur batteries, the composites delivered a high specific capacity of 1350 mAh/g at the current density of 0.1 C (167.3 mA/g). The composites also exhibited significantly enhanced cycling stability and high rate capabilities.

10.2 Experimental

10.2.1 Preparation of resol precursors.

The resol precursor with a low molecular weight (Mw < 500) was made using a typical approach reported by Zhao's group.[394] In a typical procedure, 4 g of phenol and 0.63 g of 20 wt.% NaOH aqueous solution were mixed under stirring at 40 ~ 43 °C in a flask for 10 min. Then, formalin (7 g, 37 wt.% formaldehyde) was added dropwise below 50 °C, and the reaction mixture was further stirred at 70 °C for 1h. After the mixture cooled to room temperature, the pH value was adjusted to neutral (around 7.0) by means of HCl solution. Then, water was evaporated in a vacuum oven at 50 °C overnight. Finally, the precursor was redissolved in ethanol before further use.

10.2.2 Synthesis of multi-shelled hollow carbon nanospheres.

Multi-shelled hollow mesoporous polymer–silica precursors and carbon nanospheres were prepared by the multi-constituent co-assembly method, assisted with Pluronic F127 (Mw=12600, poly(ethylene oxide)-*b*-poly(propylene oxide)-*b*-poly(ethylene oxide) (PEO-PPO-PEO), purchased from Sigma Aldrich) in an aqueous solution. The typical synthetic procedure can be described as follows: 0.5 g of Pluronic F127 was dissolved in a resol enthanolic solution (3.2 g) containing 4.0 mmol of phenol and 8.0 mmol of formaldehyde. Then, 3.75 g of ethanol mixed with 1.0 g of TMB was added to the aforementioned solution with strong stirring until forming a clear solution (marked as solution-1). Meanwhile, 1.2 g of Tetraethylorthosilicate (TEOS) was hydrolyzed in an aqueous solution of HCl (75 mL, 1M) at 40 °C for half an hour. Solution-1 was then added dropwise under continuous stirring, forming a lactic solution in a few seconds. After stirring for 12 h, the solution was transferred into an autoclave and maintained at 90 °C for 24 h. Then, lactic precipitates were obtained by filtration with copious water, and dried in air. After that, the precursors were calcined at 350 °C for 2h then 900 °C for 3h, with a heating rate of 1 °C/min for 3 h under N_2, named as MHC-SiO_2. 200 mg of calcined MHC-SiO_2 was treated with 50 mL of 2M NaOH solution, with stirring overnight, and then the multi-shelled hollow carbon nanospheres were obtained by filtration with copious de-ionized water and ethanol, and then dried at room temperature.

10.2.3 Preparation of multi-shelled hollow carbon nanosphere-sulfur composites:

50 mg as-synthesized hollow multi-shelled hollow carbon nanospheres were transferred in a mixed solution of sodium thiosulfate solution (3.2 mmol, 0.403 g dissolved into 50 mL de-ionized water and 10 mL ethanol) and sodium sulfide (6.4 mmol, 0.499 g) with strong stirring for 30 min. Hydrochloric acid (1M, 20 mL) solution was dropwise added to the dark suspension and stirred for 30 min. After this, 10 mg polyvinyl pyrrolidone (PVP) was added and maintained stirrings for 3 h. The suspension was then treated by pulsed sonication for 30 min (5s on and 5s off) in an ice bath using a Branson S-450D sonifier with a horn of 13 mm in diameter (40% amplitude). After that, the suspension was washed with de-ionized water and dried overnight in a vacuum oven at 80 ℃. Finally, the composites were quickly placed in a preheated horizontal furnace (155 ℃) with a flow of Ar (200 sccm) gas for 12 hrs, and then cooled to room temperature.

10.2.4 Structural and phase characterization.

The as-prepared hyperbranched carbon nanorods/sulfur composites were characterized by X-ray diffraction (Rigaku D/max-2550 V with Cu Kα radiation) operated at 40 KV and 30 mA. Raman spectra were measured by a Renishaw inVia Raman spectrometer system (Gloucestershire, UK) equipped with a Leica DMLB microscope (Wetzlar, Germany) and a 17 mW at 633 nm Renishaw helium neon laser with 50% power. A thermogravimetric analyzer (TGA, SDT 2960) was used to measure the weight percentage of Si from RT to 800 ℃ in air. The morphologies and crystal structure of materials were analyzed by a field emission scanning electron microscope (JSM-6700F, 20 kV) and transmission electron microscope (TEM, JEOL JEM-2010F) equipped with an energy-dispersive X-ray spectroscopy (EDX).

10.2.5 Electrochemical measurements.

The working electrodes were made from 80 wt.% of active materials, 10 wt.% of the conductive agent (acetylene black), and 10 wt.% of the binder (Alginic acid sodium salt extracted from brown algae). The mixture was stirred by an adjustable high-speed electric agitator. The working electrodes were dried in a vacuum oven. CR2032 coin cells were assembled in an argon-filled glove box (Mbraun, Unilab, Germany), in which both the moisture and oxygen contents were controlled to be less than 0.1 ppm. Lithium foil was used as the counter electrode. The electrolyte was 1 M lithium bis (trifluoromethanesulfonyl)imide (LiTFSI) and 1 wt.% lithium nitrate ($LiNO_3$) in 1,3-dioxolane and 1,2-dimethoxy-ethane (volume ratio 1:1). Electrochemical measurements were performed using a LAND-CT2001C battery test system. The cells were discharged and charged galvanostatically in the fixed voltage range of 1.7–2.6 V, with a current density of 167.3 $mA \cdot g^{-1}$ (0.1 C). Higher current rates (0.5 C, 1 C and 5 C) were also used to test the electrochemical performances. Cyclic voltammogram was measured on a CHI 660E electrochemical workstation, at a scan rate of 0.1 $mV \cdot S^{-1}$.

10.3 Results and discussion

The schematic illustration of the synthesis procedure is presented in Figure 10-1. Multi-shelled hollow carbon nanospheres were synthesised by an aqueous emulsion approach, during which 1, 3, 5-trimethylbenzene (TMB) served as an organic co-solvent, and silica and Pluronic F127 served as co-templates.[61] After heat treatment at high temperature in an inert atmosphere and the subsequent removal of silica, multi-shelled hollow carbon nanospheres were obtained.

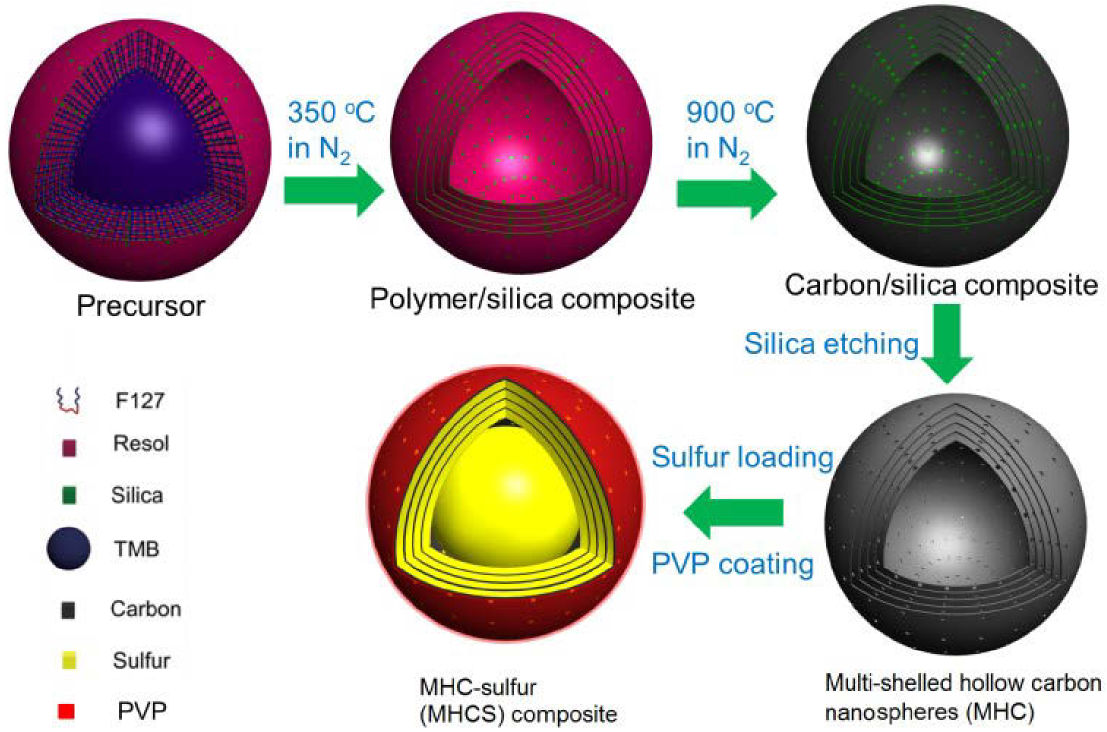

Figure 10- 1 Schematic illustration of the synthesis of MHCS composites.

Figures 10-2a and 2b show the low and high magnification field emission scanning electron microscopy (FESEM) images of multi-shelled hollow carbon nanospheres. Homogenous multi-shelled hollow carbon nanospheres with a diameter of approximately 150 nm are presented. Figure 10-2c exhibits the transmission electron microscopy (TEM) image of multi-shelled hollow carbon nanospheres. The multi-shelled hollow structure of MHC with a shell thickness of 20 nm is shown in Figure 10-2d. A six layer-lamellar structure can be clearly identified. The interlayer distance is approximate 3 nm, which provides large inner spaces to accommodate guest components. Additionally, many tiny pillars can be distinguished in interlayer spaces. Nitrogen adsorption-desorption results presented in Figure 10-3 exhibit the changes of structural features of products obtained at each stage. Before removal of the silica template, the interlayer spaces and inner voids are partially occupied. Once the silica template is etched by a strong base aqueous solution, the surface area of multi-shelled hollow carbon nanospheres dramatically increases. The Brunauer-Emmett-Teller (BET) surface areas calculated from Figures 10-3a_1 and 10-3b_1, rapidly increase from 226 m^2/g to 1050 m^2/g, verifying that vast mesoporous voids are released. The corresponding pore size distributions in Figures 10-3a_2 and 10-3b_2 also provide additional evidence to demonstrate the changes. Before etching, the average pore size appears at around 8 nm, which is associated with the pyrolysis of triblock copolymers (F127). Subsequently, after the high temperature treatment and removal of silica, two more peaks of pore sizes appear at around 4.5 nm and 50 nm, respectively. This indicates that the additional spaces previously occupied by silica are released and some mesopores are probably formed during the etching process.[44] Estimated from the isotherms in Figure 10-3b_2, MHC material has a high total pore volume of 0.75 cm^3/g.

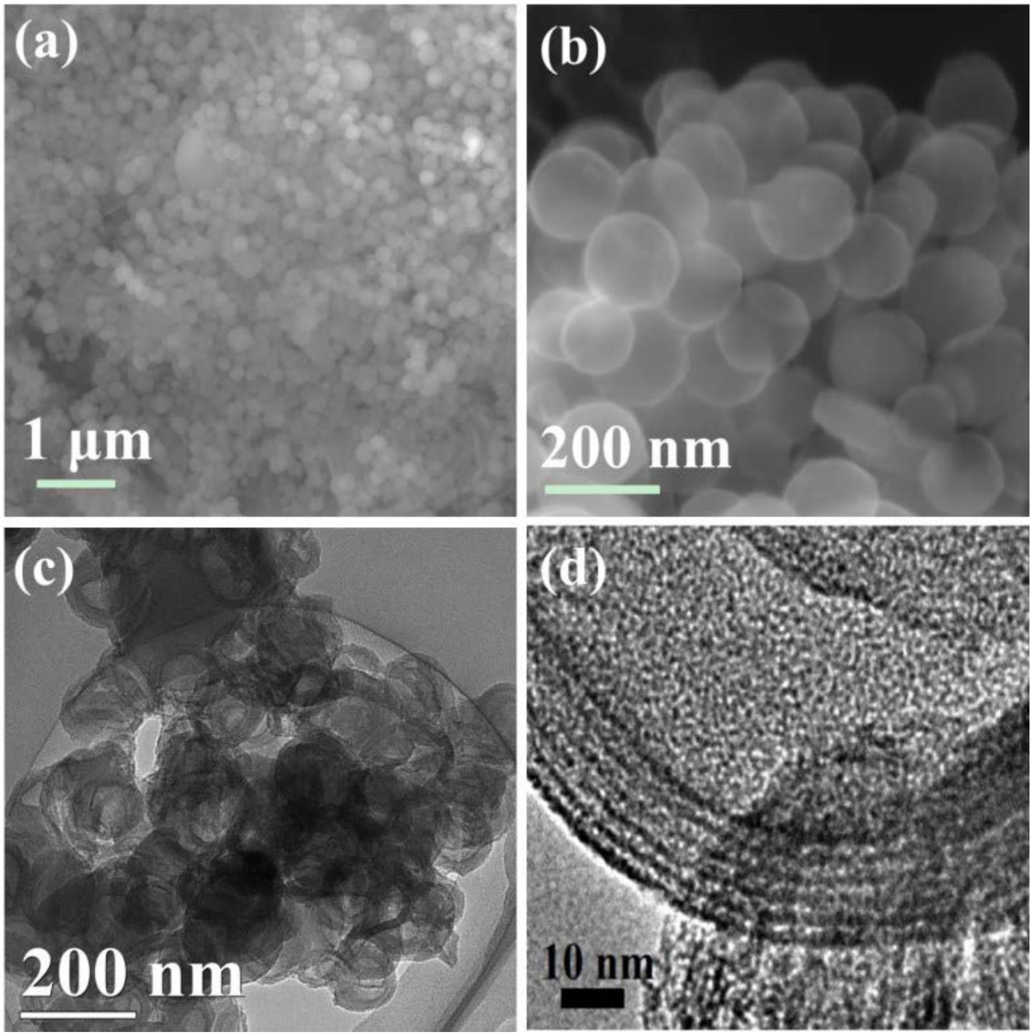

Figure 10- 2 Morphology observation and structural characterization of MHC. (a-b) Low and high magnification FESEM images of MHC. (c) TEM image of MHC. (d) HRTEM image of MHC.

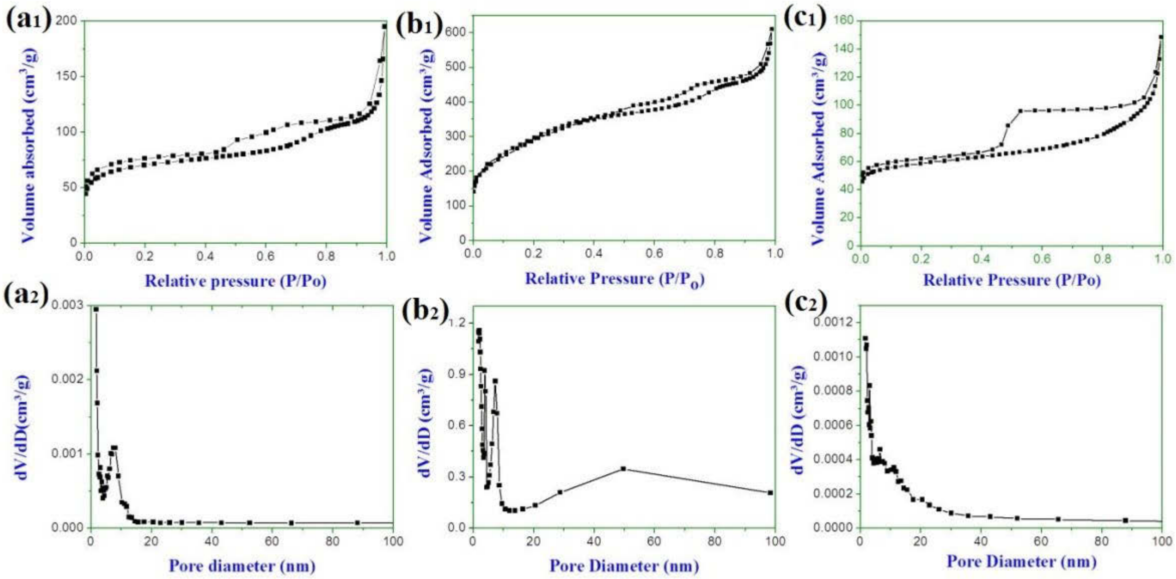

Figure 10- 3 Specific surface areas and pore size distributions of multi-shelled hollow carbon nanospheres-SiO_2, multi-shelled hollow carbon nanospheres, and multi-shelled hollow carbon nanospheres-sulfur composites. (a_1 and a_2) Specific surface area and pore size distribution of multi-shelled hollow carbon nanospheres-SiO_2. (b_1 and b_2) Specific surface area and pore size distribution of multi-shelled hollow nanocarbon spheres. (c_1 and c_2) Specific surface area and pore size distribution of multi-shelled hollow carbon nanospheres-sulfur composite.

The impregnation of sulfur was performed by an *in-situ* approach and then coated by polyvinyl pyrrolidone (PVP). Sulfur impregnation proceeded *via* a disproportionate reaction, which can be described in a chemical equation as:

$$2Na_2S + Na_2SO_3 + 6HCl \rightarrow 3S\downarrow + 6NaCl + 3H_2O \qquad (1)$$

After further heat treatment, sulfur was absorbed into the mesopores and stored in the interlayer spaces and hollow carbon cavities *via* the strong capillary forces. MHCS composites with uniform sizes and homogeneous spherical morphology are shown in Figure 104a. For comparison, the morphology of pure sulfur is displaying a micro-sized irregular granular structural feature. A high magnification view of MHCS composites is presented in Figure 10-4b. Compared with the semi-transparent pristine MHC (Figure 10-2a), MHCS composites exhibit a much deeper contrast, suggesting a successful S encapsulation. The insert image in Figure 10-4b shows the relatively dense nature of the sample, implying the existence of sulfur. No obvious sulfur aggregates can be found in either Figure 10-4a or 10-4b, which indicates a very homogeneous impregnation of sulfur. The TEM image of MHCS composites is shown in Figure 10-4c, and the insert image in Figure 10-4c also exhibits a darker contrast than the pure carbon nanospheres (Figure 10-2b), indicating a good sulfur loading. Yet, the spherical morphology is still maintained. The elemental mapping image in Figure 10-4d further reveals the distribution of sulfur (red) and carbon (green) elements in MHCS composites. Apparently, sulfur is distributed in carbon interlayer voids and hollow carbon cavities. The insert images in Figure 10-4d are the corresponding elemental mapping in TEM. It is worth to note that sulfur (red) with a tiny size of around 5 nm is distributed into the inter-shelled carbon nanostructure (green). Sulfur is preferred to accommodate in the inter-shelled space other than the large hollow chamber through the strong attraction forces between sulfur and multilayered lamellar carbon structure. Pure sulfur rarely can be observed outside of multi-shelled hollow carbon nanospheres. To further confirm the homogeneous sulfur impregnation. It should be noted that those multi-shelled hollow carbon nanospheres are completely filled by sulfur, but some of them have only their interlayer voids filled, implying that the encapsulation process is started from voids on the shell, then diffused inward, layer by layer, finally reaching hollow centers. Nitrogen adsorption-desorption results also reveal the internal structure change after sulfur impregnation. Both the specific surface area and the amount of mesopores are substantially decreased. Sulfur is homogenously distributed in the carbon nanospheres and occupies the mesopores, which reduces the surface area to 182 m^2/g, as shown in Figure 10-3c_1. Pore volume also decrease from 0.75 cm^3/g of MHC to 0.16 cm^3/g of MHCS composites. There is no apparent peak in the pore size distribution plot in Figure 10-3c_2, implying that the mesopores are completely occupied by sulfur.

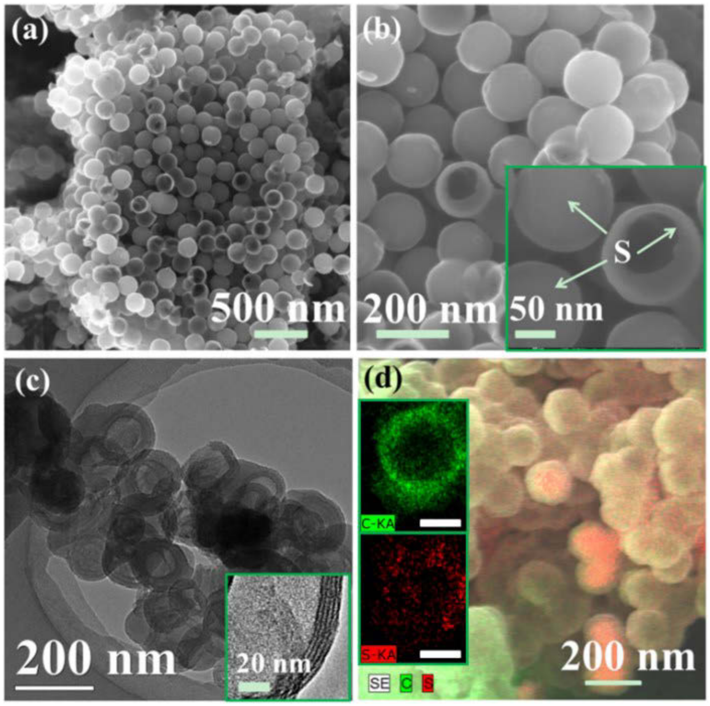

Figure 10- 4 (a) Low magnification FESEM image of MHCS composites. (b) High magnification FESEM image of MHCS composites with an insert image of an enlarged view. (c) TEM image of MHCS composites. The inset is a HRTEM image of MHCS composites. (d) Elemental mapping SEM images of sulfur (red) and carbon (green) in MHCS composites. The insets are TEM elemental mapping of carbon (green) and sulfur (red) the scale bar is 100 nm.

MHC, pure S and MHCS were characterized by X-ray diffraction (XRD) to reveal the crystalline nature of the samples (as shown in Figure 10-5a). The observation of the (002) peak in the pattern of MHC implies carbon nanospheres are partially graphitized during the high temperature calcination. The XRD pattern of MHCS composites can be distinguished as the characteristic peaks of crystalline sulfur, which agrees well with those peaks of pure sulfur (indexed to JCPDS NO. 42-1278). The Raman spectrum intensity ratio of I_D/I_G for multi-shelled hollow carbon nanospheres equals the 1.43 in Figure 10-5b, further proving the partial graphitization of carbon at high temperature, which should benefit for the enhancement of the electrical conductivity. Compared with the Raman spectrum of pure sulfur, the intensities of peaks at 205 and 485 cm^{-1} of MHCS composites substantially decrease, implying that the signal of sulfur is occulted by multi-shelled hollow carbon nanospheres, and that less sulfur can be detected on the outside of MHC.

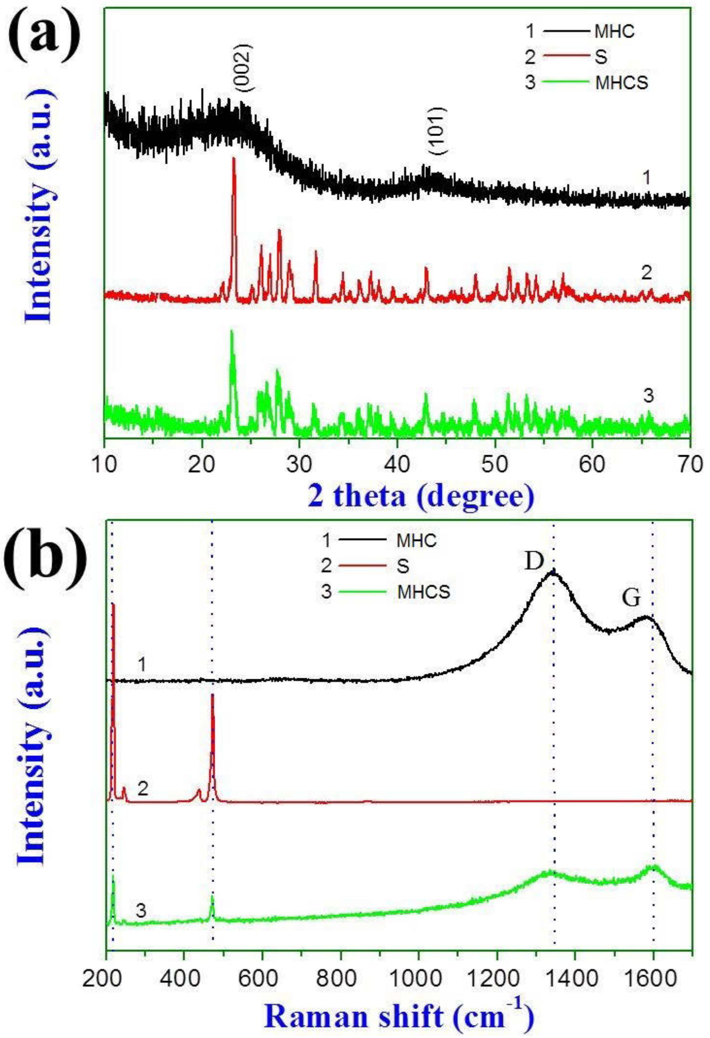

Figure 10- 5 Phase characterization of MHCS composites. XRD patterns of pure sulfur, MHC and MHCS composites. (b) Raman spectra of MHC, pure sulfur and MHCS composites.

The loading amount of sulfur in those multi-shelled hollow carbon nanospheres has been determined to be 86 wt. % by thermal gravimetric analysis (TGA) in Figure 10-6, which is the highest sulfur content to our best knowledge. It is worth noting that the evaporating temperature of sulfur accommodated in MHC is around 250 ℃, which is higher than that of pure sulfur (180 ℃). This might be ascribed to a strong affinity between sulfur and multi-shelled hollow carbon nanospheres, demonstrating enhanced thermal stability of MHCS composites. The corresponding differential scanning calorimetry (DSC) plot of MHCS composites is also presented in Figure 10-6. The first peak positioned at around 250 ℃ is ascribed to the evaporation of sulfur stored in the carbon interlayers, and the second peak at

320 ℃ might be related to sulfur absorbed in the carbon inner cores. This retardation phenomenon demonstrates the strong physical confinement of multi-shelled hollow carbon nanospheres for sulfur. The peak at 600 ℃ is related to the pyrolysis of MHC.

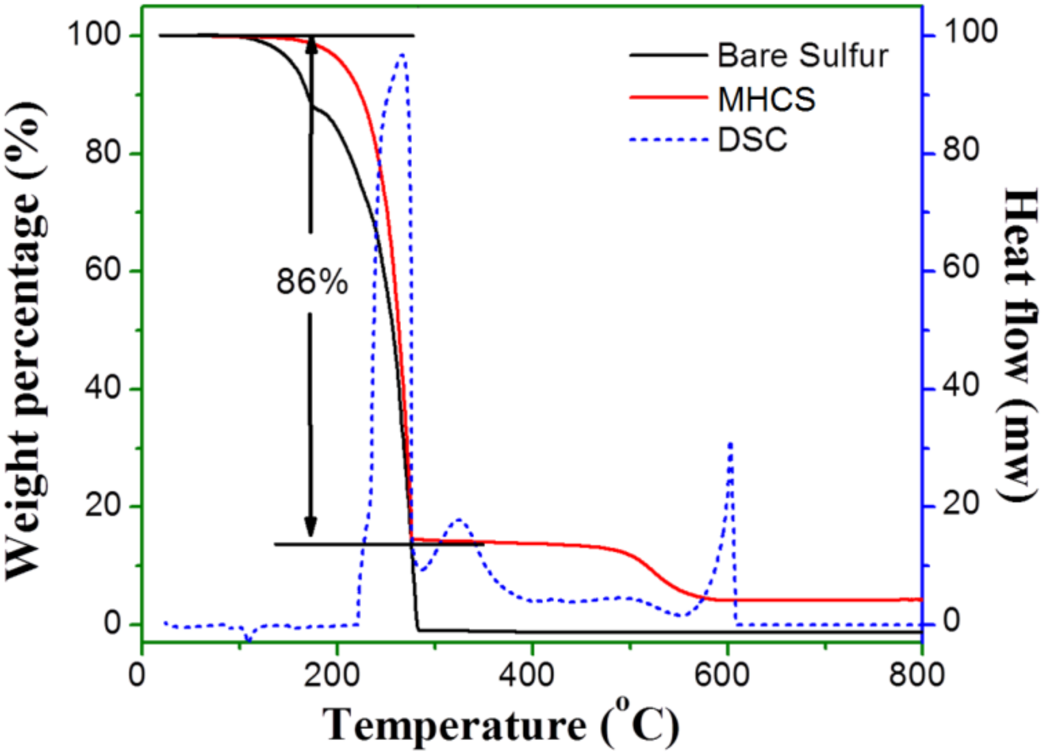

Figure 10- 6 Thermogravimetric analysis of pure sulfur and MHCS composites (The dashed line is the corresponding differential scanning calorimetry of MHCS composites).

The electrochemical performances of MHCS composite were systematically measured by cyclic voltammogram (CV), galvanostatic charge/discharge cycling tests and electrochemical impedance spectroscopy (EIS). The CV curves illustrate the typical electrochemical reaction behaviors between Li^+ ions and sulfur in the multi-shelled hollow carbon nanosphere-sulfur composite in Figure 10-7a. Two broad reduction peaks centered at 2.28 V and 2.05 V were observed, corresponding to the two main stages of reduction reactions.[48, 49, 51-53] The first peak is ascribed to the transformation of cyclo-octasulfur to soluble long chain lithium polysulfides, related to a fast kinetic reaction; While the other one originates from further decomposition of those polysulfides to insoluble Li_2S_2/Li_2S, corresponding to the slow kinetics.[398] One main peak associated with slow oxidation kinetics from lithium sulfides to lithium polysulfides and cyclo-octasulfur dominates the subsequent electrochemical reaction. The corresponding electrochemical reaction equation can be described as:

$$S_8 + 16Li \leftrightarrow 8Li_2S \qquad (2)$$

Apparently, little peak changes demonstrate the good reversibility and successful suppression of shuttle effect in the sulfur nanocomposites. Furthermore, the perfect flat anodic base lines suggest that the shuttle effect at cathode has been almost eradicated.

Typical charge/discharge profiles in the first and 200th cycle recorded at the current density of 0.1 C (167.3 mA/g) are presented in Figure 10-7b, in the voltage range of 1.7-2.6 V. A high initial discharge specific capacity of the MHCS electrode delivered 1350 mAh/g. Table 1 lists the comparisons of sulfur loading and electrochemical performances of different carbon-sulfur composite electrodes. Two main characteristic plateaus corresponding to the formation of long-chain polysulfides at around 2.28 V and short-chain Li_2S_2/Li_2S centered at 2.1V are observed, which agrees well with the electrochemical behaviors in CV curves. After 200 cycles, a reversible capacity of 1250 mAh/g (1075 mAh/g based on the entire electrode mass) is well maintained with a capacity retention ratio of 92%, demonstrating an excellent cycling stability. However, without the confinement of multi-shelled hollow carbon nanospheres, the pure sulfur electrode is plagued by an insulation nature and the severe shuttle effect of lithium polysulfides. It exhibits a charge capacity of 1203 mAh/g with a reversible capacity of 801 mAh/g and a low Coulombic efficiency of 33.4% in the 1st cycle (as shown in Figure 10-8a). The cycling performances of the MHCS electrode and the pure sulfur electrode are shown in Figure 10-7c, with insert plots of the corresponding Coulombic efficiencies. A significantly improved long-term stability of the MHCS electrode has been achieved, implying the excellent sulfur confining effect of multi-shelled hollow carbon nanospheres.

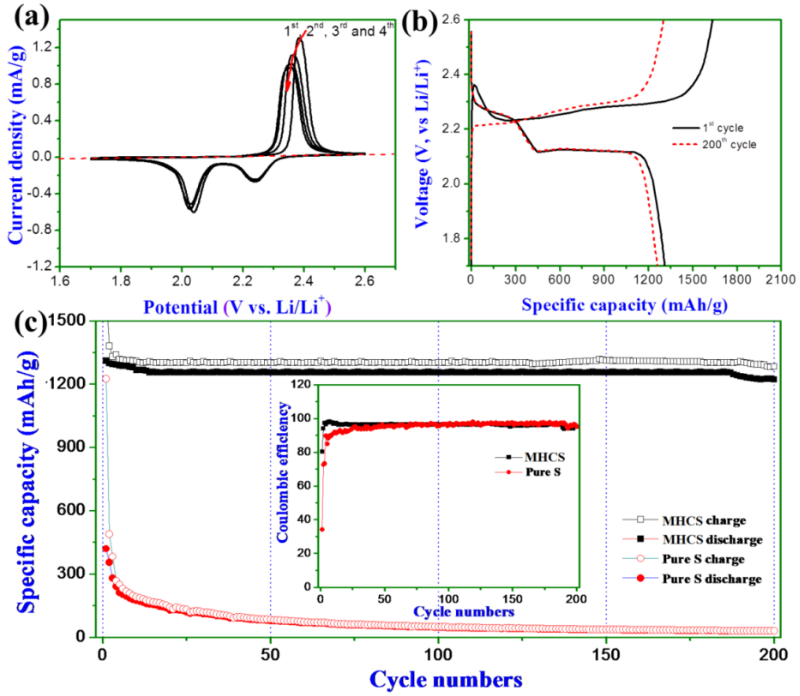

Figure 10- 7 Electrochemical performances of pure sulfur and MHCS. (a) Cyclic voltammogram of MHCS composite at a scan rate of 0.1 mV/s. (b) The charge/discharge profiles of MHCS composites in the 1st and 200th cycles. (c) The cycling performances of pure sulfur and MHCS composites. The insert shows the corresponding Coulombic efficiency of the two materials.

Table 10- 1 The comparisons of sulfur loading and electrochemical performances of different carbon-sulfur composite electrodes

Sulfur cathode Ref.	Sulfur percentage	Rate capacity based on sulfur mass (mAh/g)	Rate capacity at 0.1 C based on entire electrode mass (mAh/g)	Cycle life	Remained capacity at 0.1 C based on sulfur mass (mAh/g)	Remained capacity at 0.1 C based on entire electrode mass (mAh/g)
This paper: Multi-shelled hollow carbon nanosphere-S	86%	1350(0.1 C) 1003(1 C)	1161(0.1 C) 862(1 C)	200	1250(0.1 C) 846(1 C)	1075(0.1 C) 727(1 C)
Ordered mesoporous carbon particales-S[401]	50%	1200(1 C)	600(1 C)	100	730(1 C)	365(1 C)
Dual coaxial carbon nanocable-S[402]	53.9%	800(1 C)	431(1 C)	100	527(1 C)	284(1 C)

Aiming to examine the cycling performances of MHCS electrodes at high current densities, the electrodes were cycled at several current rates (0.5 C, 1 C and 5 C), and the results are shown in Figure 10-9. Figure 10-9a shows the cycling performances under the step-wise current rate tests, exhibiting the stable cyclability at high current rates, and the complete capacity recovery (back to 0.1 C). The associated charge/discharge profiles at different current rates are shown in Figure 10-8b. Discharge plateaus become shortened and lower when the current densities are increased, which can be ascribed to the very fast lithium ions diffusion.

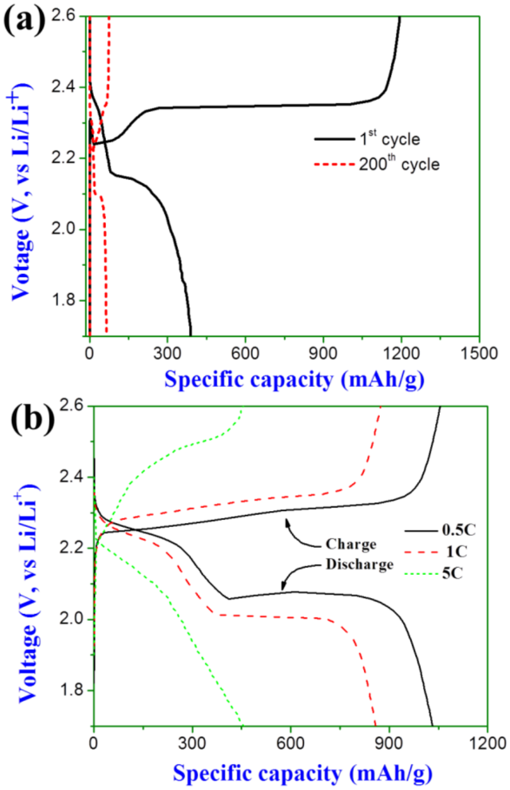

Figure 10- 8 (a) The charge/discharge profiles of pure sulfur at the 1st and 200th cycles (b) The charge/discharge profiles of MHCS composites at different current rates at the 200th cycle.

Long-term cycling performances of MHCS cathodes at different current rates are presented in Figure 10-9b. The MHCS electrode exhibits an initial specific capacity of 1057 mAh/g at 0.5 C (909 mAh/g based on entire electrode mass), with a capacity retention ratio of 94% after 200 cycles. The electrode delivered 1003 mAh/g (862 mAh/g based on entire electrode mass) and 541 mAh/g (465 mAh/g based on entire electrode mass) at 1 C and 5 C in the initial cycle, respectively. After 200 cycles, specific capacities of MHCS composites still maintain at 846 mAh/g and 452 mAh/g, with capacity retention ratios of 84% and 83.5%, respectively.

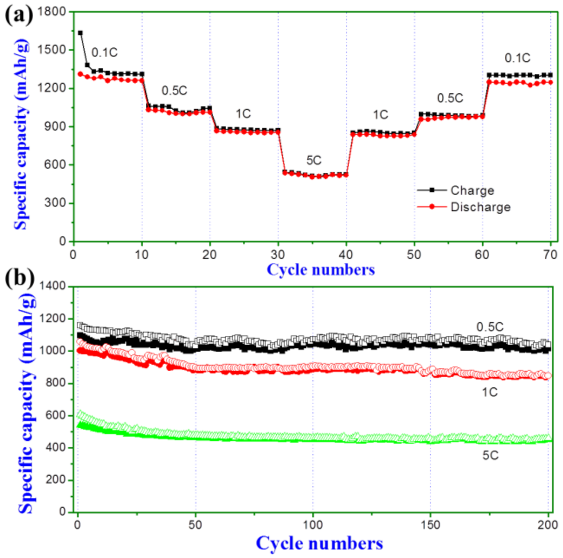

Figure 10- 9 Electrochemical performances of MHCS composites at different current densities. (a) Step-wise cycling performance of MHCS composites. (b) The cycling performances of MHCS electrodes at different current rates.

To further exploit the integrity of the MHCS electrode and electrochemical impedance changes before and after 200 cycles, *ex-situ* SEM analysis, elemental mapping and EIS measurement were performed on the cycled electrodes. The elemental mapping image of the MHCS electrode after cycling is shown in Figure 10-10a. Sulfur is still confined in the interlayer spaces of multi-shelled hollow carbon nanospheres, and no sulfur can be observed on the outside of the multi-shelled hollow carbon nanospheres, indicating that the unique carbon architecture can effectively prevent the loss of sulfur and suppress the shuttle effect. Figure 10-10b and 10-10c clearly distinguish the distribution of sulfur and carbon. The EDX spectrum in Figure 10-10d shows the elemental information. Even after long time cycling, the robust multi-shelled hollow carbon nanosphere-sulfur composites can maintain their structure and integrity. The electrochemical impedance spectra are presented in Figure 10-11. The impedance spectra, consisting of a depressed semicircle in the high frequency area and an oblique line in the medium frequency region, reflect the changes of impedances of the electrode before and after 200 cycles. Obviously, there are little changes of the radius of two semicircles in the high frequency region, illustrating that the electrochemical impedances do not increase dramatically. This further demonstrates the robust properties and superior conductivity of multi-shelled hollow carbon nanospheres, and the stable cycling characteristics of multi-shelled hollow carbon nanosphere-sulfur composites.

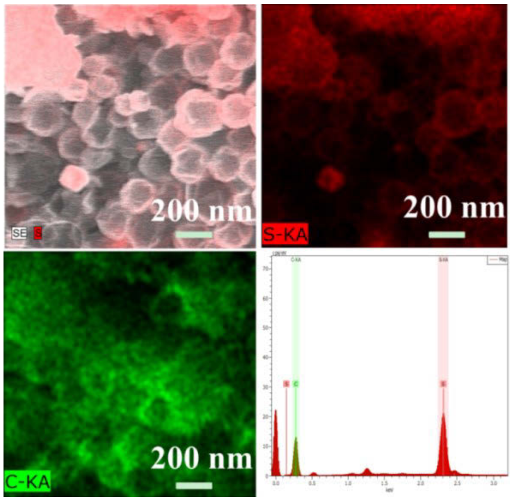

Figure 10- 10 Elemental distribution and energy dispersive X-ray spectrum of MHCS electrode after cycling. (a-c) Elemental distributions of sulfur and carbon in MHCS electrode after cycling. (d) Energy dispersive X-ray spectrum of MHCS electrode after cycling.

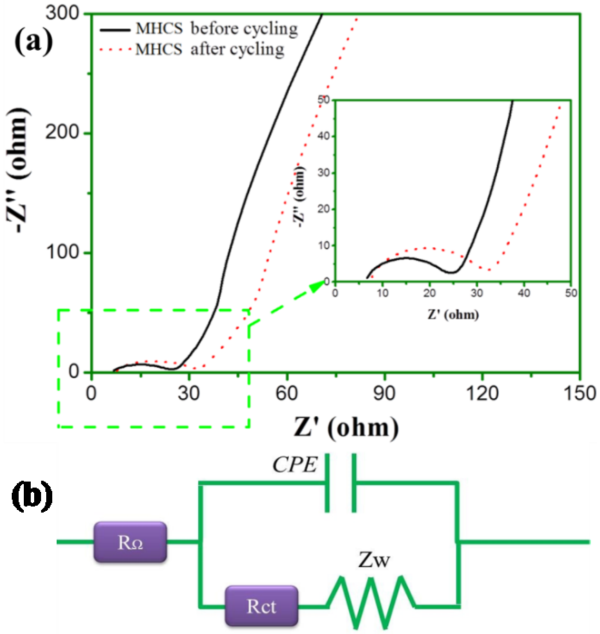

Figure 10- 11 (a) Electrochemical impedance spectra of MHCS electrode before and after cycling. (b) The corresponding equivalent circuit (R_Ω: Ohm resistance; Rct: Charge transfer resistance; Zw: Warburg diffusion process; CPE: constant-phase element).

Based on the aforementioned analysis, the enhanced electrochemical performances of sulfur-rich MHCS composites can be ascribed to the rationally designed dual sulfur confining approach. The physical confinement of multi-shelled hollow carbon nanospheres and the chemical bonding force of the PVP polymer layer jointly restrain the sulfur loss during discharge/charge processes. Furthermore, the heat treatment of carbon nanospheres at high temperature can effectively enhance the conductivity of electrodes. The large inner voids and spaces in multiple carbon shells provide sufficient spaces to buffer the volume changes during charge/discharge. The high sulfur content in the composite electrodes can enhance both gravimetric and volumetric energy density. The electrolyte additive of $LiNO_3$ also assists in suppressing the shuttle effect originated from lithium polysulfide ions during both charge and discharge processes. TEM and elemental mapping confirmed that sulfur was fully encapsulated into intershell spaces and inner cores of multi-shelled hollow carbon nanospheres, which maintained the unique structure even after 200 cycles and exhibited the enhanced electrochemical performances.

10.4 Conclusions

In summary, the sulfur-rich (86 wt. %) MHCS composites were successfully synthesised by an aqueous emulsion approach and *in-situ* impregnation method. Multi-shelled hollow carbon nanospheres and PVP polymers were employed as a dual sulfur confining strategy. When applied as cathodes in lithium sulfur batteries, multi-shelled hollow carbon nanosphere-sulfur composites delivered a high specific capacity of 1350 mAh/g, and excellent cycling stability at the current density of 0.1 C. Reversible curves from cyclic voltammogram curves validate successful suppression of shuttle effect. The electrode delivered 1003 mAh/g and 541 mAh/g at 1 C and 5 C in the initial cycle, respectively. After 200 cycles, specific capacities of the MHCS composites at 1 C and 5 C still maintained 846 mAh/g and 452 mAh/g with capacity retention ratios of 84% and 83.5%, respectively, which demonstrates enhanced cyclability and good capacity retentions.

CHAPTER 11 MESOPOROUS RUBIK'S CARBON NANOCUBES AS SULFUR CARRIES FOR LITHIUM SULFUR BATTERIES

11.1 Introduction

Requirements for energy storage with high energy density and power density have been a worldwide imperative owing to ever-increasing energy consumption and environmental pollution.[81, 116, 168, 185, 369] Lithium-sulfur (Li-S) batteries are regarded as one of the most promising energy storage system, having exceptional advantages such as high theoretical capacity (1673 mA/g), high power density (~2600 W·h/kg), natural abundance, low cost and being environmentally friendly.[22-23, 26, 60, 69, 363, 397] However, Li-S batteries with bare sulfur cathodes are plagued by many drawbacks, including fast capacity degradation, low Coulombic efficiency and poor rate capability, which are associated with the insulating nature of sulfur, dissolution of lithium polysulfides (causing shuttle effect) and large volume changes during cycling. Considerable efforts have been devoted to improving electrochemical performances of Li-S batteries.[170, 403-405] There are four main strategies: (i) adding conductive additives (carbon black) to enhance the cathode conductivity;[45, 406] (ii) using ordered or flexible carbon based materials (carbon nanosphere, [42, 407] carbon nanotube/fiber,[30, 53] tunnel carbon materials[362, 408] and graphene based materials[47-48, 59, 409]); (iii) strengthening chemical bonding with lithium polysulfides with conductive polymers (poly (3,4-ethylenedioxythiophene) (PEDOT), polypyrrole and polyaniline),[58, 410-412] other chemicals (ployvinylpyrrolidone, polyethylene glycol, cetyltrimethyl ammonium bromide) [41, 53, 59, 364, 366] and metal oxides (SiO_2 and TiO_2);[61, 326] (iv) modifying electrolyte (addition of $LiNO_3$) or new types of separators (coating graphene, carbon paper or graphite on separators),[45, 48, 406, 413, 414]. The ideal cathode host for Li-S batteries should have the following characteristics: (i) highly porous materials with interconnected architecture to encapsulate sufficient sulfur and confine sulfur into individual small pores rather than large inner voids; (ii) micropores or mesopores to restrain polysulfides; (iii) high conductivity to enhance the insulating sulfur; (iv) flexible and robust physical properties to buffer volume expansion during cycling; (v) low cost and ease to scale-up.

By rationally designing a mesoporous Rubik's cube architecture and adopting a dual confinement strategy, we successfully synthesized PEDOT coated mesoporous carbon nanocube-sulfur (P@CNC-S) composites. The hierarchical mesoporous Rubik's carbon nanocubes have a high surface area of 2425 m^2/g and large pore volume of 3.27 cm^3/g, which provide sufficient voids to accommodate sulfur. When applied as cathodes in Li-S batteries, P@CNC-S composites delivered a high capacity of 1398 mAh/g, and stable cycling capability at 0.1 C (1 C= 1673 mA/g). The electrodes also showed an excellent cyclability, extending to 1000 cycles, and a high remained reversible capacity of 925 mAh/g at 1 C current rate.

11.2 Experimental Section

11.2.1 Preparation of mesoporous MnO nanocube template and mesoporous carbon nanocube:

In a typical synthesis procedures, the mesoporous MnO nanocubes were prepared using a moderate method: 35 mmol $Mn(AC)\cdot H_2O$, 35 mL ethanol and 100 mmol $(NH_4)_2SO_4$ were dissolved in 350 mL of de-ionized water in a round flask with strong stirring and then placed into a preheated oil-bath tank (50 °C). 100 mmol $(NH_4)_2CO_3$ was dissolved in 350 mL of de-ionized water with strong stirring for 10 min. Then, the second solution was added drop-wised into the former solution under vigorous stirring and maintained for 12 h. After that, white precipitation of $MnCO_3$ was collected by filtration, washed with copious de-ionized water and dried at 80 °C. The precursor was annealed at 600 °C with a temperature ramp of 2 °C/min and maintained for 4 h in air. Mesoporous MnO was placed in a quartz tube furnace and heated to 750 °C at a temperature ramp of 2 °C/min in Ar. Then, acetylene (10% in Ar) was introduced with a flow rate of 100 sccm for 30 min. Carbon coated MnO nanocubes (C@MnO) were prepared. Afterward, micro/mesoporous CNC were obtained by etching C@MnO with 1 M HCl, washing and drying at 80 °C in a vacuum oven overnight.

11.2.2 Preparation of P@CNC-S nanocomposites:

50 mg of the as-synthesized micro/mesoporous CNC were transferred into a mixed solution of sodium sulfite solution (3.2 mmol, 10 mL de-ionized water and 10 mL ethanol)

and sodium sulfide (1.65 mmol) with strong stirring for 30 min. Hydrochloric acid (1M, 10 mL) solution was then drop-wised added into the dark suspension and stirred for 12 h. Afterward, the suspension was evenly divided to compare the electrochemical performances without further treatments. Meanwhile, 0.06 mL 3, 4-ethylenedioxythiophene (EDOT) monomer, 10 mL 1 M HCl and 0.307 g $K_2S_2O_8$ were added in one of previously obtained suspension, and stirring for 12 h. Then, the two suspensions were washed with de-ionized water and dried overnight. Finally, the two composites were placed into a preheated horizontal furnace (155 °C) with a flow of Ar (100 sccm) for 12 h, and then cooled to room temperature.

11.2.3 Structural and phase characterization:

The materials were characterized by X-ray diffraction (Rigaku D/max-2550V with Cu Kα radiation) operated at 40 KV and 30 mA, Raman spectra by a Renishaw inVia Raman spectrometer system (Gloucestershire, UK). A thermogravimetric analyzer (TGA, SDT 2960) was used to measure the weight percentage of S. The morphologies and crystal structure of materials were analyzed by a field emission scanning electron microscope (JSM-6700F, 20kV) and transmission electron microscope (TEM, JEOL JEM-2010F) equipped with an energy-dispersive X-ray spectroscopy (EDX).

11.2.4 Electrochemical measurement:

The working electrodes were made from 80 wt.% of active materials, 10 wt.% of carbon black, and 10 wt.% of the binder (PVDF). The mixture was pasted on aluminum current collectors using a medical blade. The work electrodes were dried in a vacuum oven at 80℃ overnight. CR2032 coin cells were assembled in an argon-filled glove box (Mbraun, Unilab, Germany), in which both the moisture and oxygen contents were controlled to be less than 0.1 ppm. Lithium foil was used as the counter electrode. The electrolyte was composed of 1 M lithium bis(trifluoromethanesulfonyl) imide and 0.1M lithium nitrate ($LiNO_3$) in 1,3-dioxolane and 1,2-dimethoxy-ethane (volume ratio 1:1). Electrochemical measurements were performed using a LAND-CT2001C battery test system. The cells were galvanostatically discharged and charged in a voltage range of 1.7–2.6 V at a current density of 167.3 $mA \cdot g^{-1}$ (0.1 C). Higher current rates (0.5 C, 1 C, 5 C and 10 C) were also applied to evaluate the rate capabilities. The CV was measured on a CHI 660E electrochemical workstation at a scan rate of 0.1 $mV \cdot S^{-1}$.

11.3 Results and discussion

Figure 11-1 illustrates the procedures for the synthesis of the P@CNC-S composites. Mesoporous MnO nanocubes were obtained by heat treatment of rhombic $MnCO_3$ at 600 ℃ in air, and then coated with a thin layer of carbon via chemical vapor deposition (CVD). Micro/mesoporous carbon nanocubes with many tiny hollow carbon nanocubes and micro-cavities were obtained after etching MnO templates. After then, sulfur was loaded into micro/mesoporous carbon nanocubes by an *in situ* precipitation. Then, the suspension is equally divided into two for comparison. The reference sample is directly followed by heat treatment for 12h, and the other was first coated with a thin PEDOT polymer layer through the polymerization of monomer EDOT with the assistance of hydrochloric acid and oxidant ($K_2S_2O_8$) and then also experienced the heat treatment in Ar. The architecture of the P@CNC-S composites mimics Rubik's cube (as shown in Figure 11-1), in which individual large cube contains many small nanocubes. The corresponding X-ray diffraction patterns and Raman spectra of the products obtained in different steps are presented in Figure 11-2a and b.

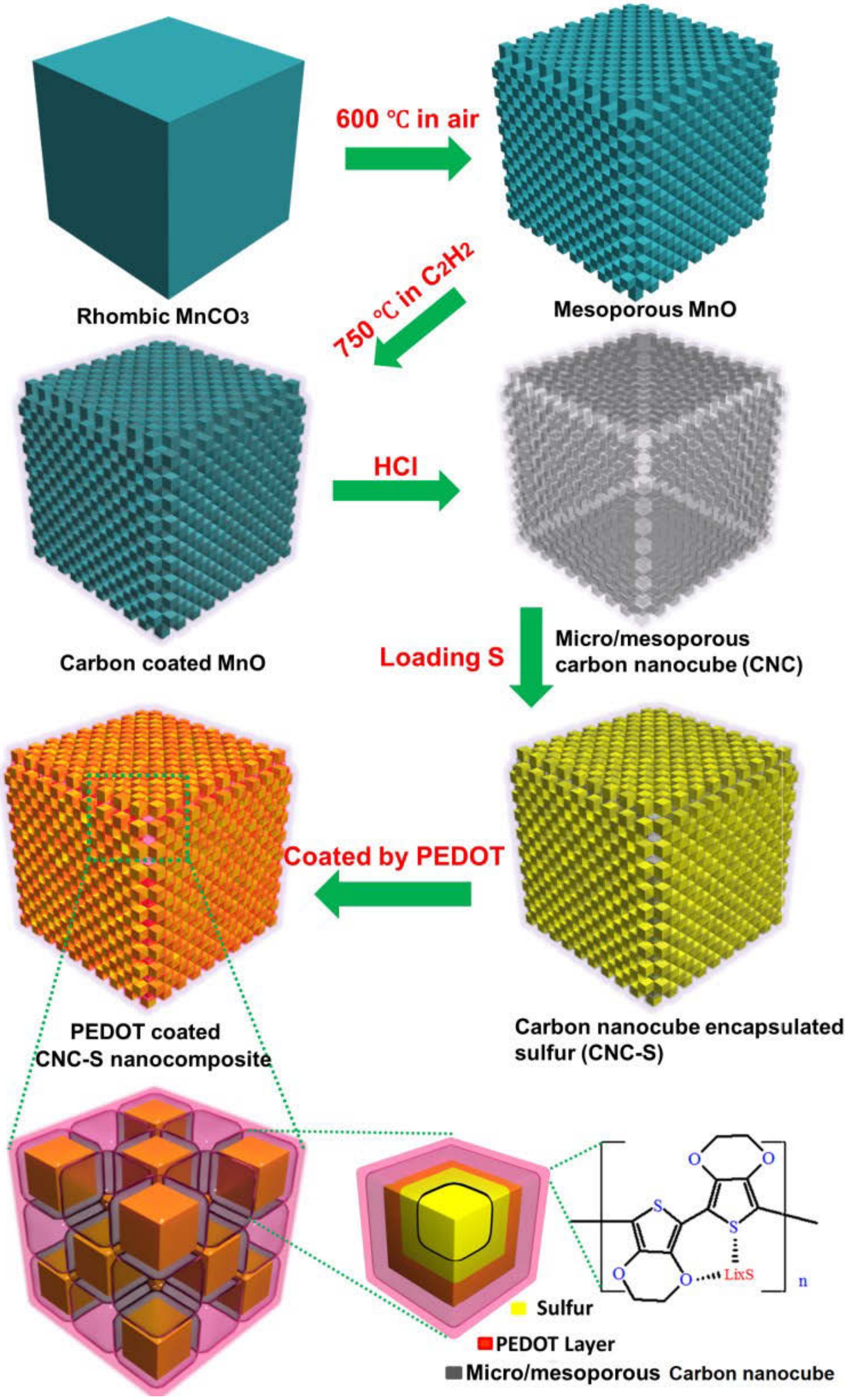

Figure 11- 1 A schematic illustration for preparing PEDOT coated Rubik's micro/mesoporous carbon nanocube-sulfur composites.

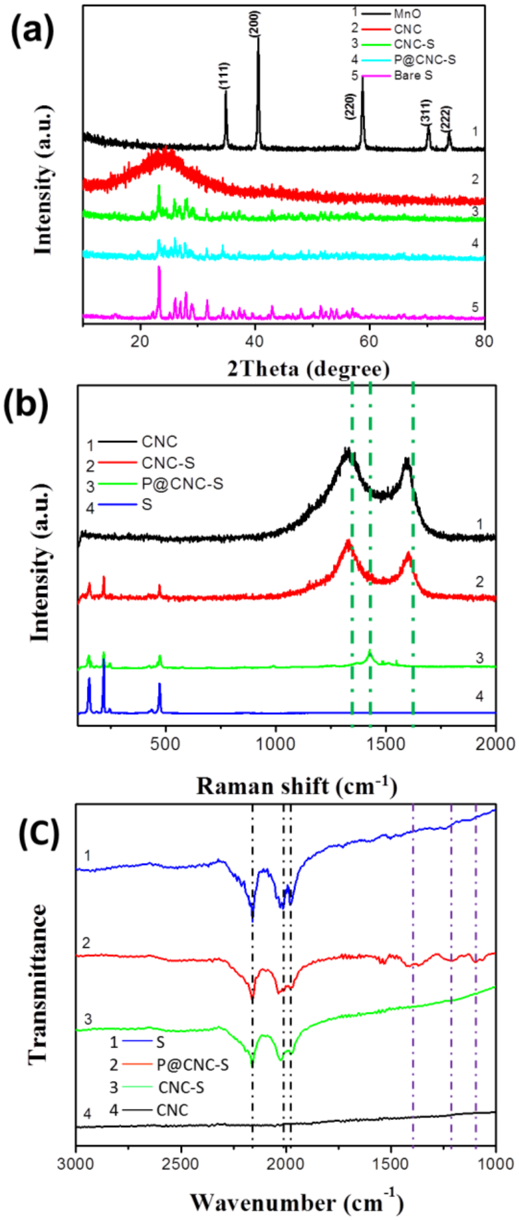

Figure 11- 2 (a) X-ray diffraction patterns of MnO, CNC, CNC-S, P@CNC-S and bare S. (b) Raman spectra of CNC, CNC-S, P@CNC-S and bare S. (c) Fourier transform infrared spectra of CNC, CNC-S, P@CNC-S and bare S.

Typical field-emission scanning electron microscopy (FESEM) images of $MnCO_3$ nanocubes are shown in Figure 11-3a-d, exhibiting smooth surface and regular structure. After heated in air, mesoporous MnO nanocubes (Figure 11-4a-d) were obtained. The corresponding specific surface area measured by nitrogen adsorption/desorption isotherm is 20.1 m^2/g with an average pore size distribution of 45 nm (Figure 11-5). The carbon coating process (Figure 11-6a-d) was achieved by CVD method using acetylene as carbon soure.[94, 265, 415-416] Figure 11-7a-d shows the FESEM images and transmission electron microscopy (TEM) images of micro/mesoporous CNC. To further confirm the micro/mesoporous architecture, low and high magnification TEM images are presented in Figure 11-7b-d. It should be clarified that the TEM electron beam is focused on the carbon layer near the copper grid, and the height of the entire carbon nanocube is around 600 nm. Therefore, the middle of the carbon nanocube is obscure. Micro/mesoporous CNC consists of many small hollow carbon nanocubes, which connect with adjacent small carbon nanocubes. The wall thickness of small carbon nanocubes is measured to be 1.4 nm (The insert profile in Figure 11-7d actually shows the thickness of double layers of CNC). More FESEM images are presented in Figure 11-8a-d. The unique micro/mesoporous CNC exhibited a high specific surface area of 2425 m^2/g and a pore volume of 3.72 cm^3/g (Fig. 1e).[146, 280] The pore size distribution of micro/mesoporous CNC is shown in Figure 11-7e as the insert image, exhibiting both mesopores at around 39 nm, 18 nm, 8 nm and 3 nm, and micropores at 0.8 nm and 1.9 nm, respectively. The abundant micropores and micro-cavities on CNC are generated during CVD. Compared to mesoporous MnO with thick and heavier mass, the thin and lighter carbon layers (1.4 nm) make the high specific surface area possible. According to previous reports,[64, 236, 417] micropores are facilitated to absorbing short sulfur chains (S_{2-4}) due to the limited rooms for cyclo-octasulfur (S_8) and mesopores are benefitted to store more sulfur. The special structure of micro/mesoporous CNC can not only provide physical barrier to restrain the dissolution of lithium polysulfides, but also supply sufficient rooms for both sulfur loading and volume expansions during discharge. More SEM images are presented in Figure 11-8a-d.

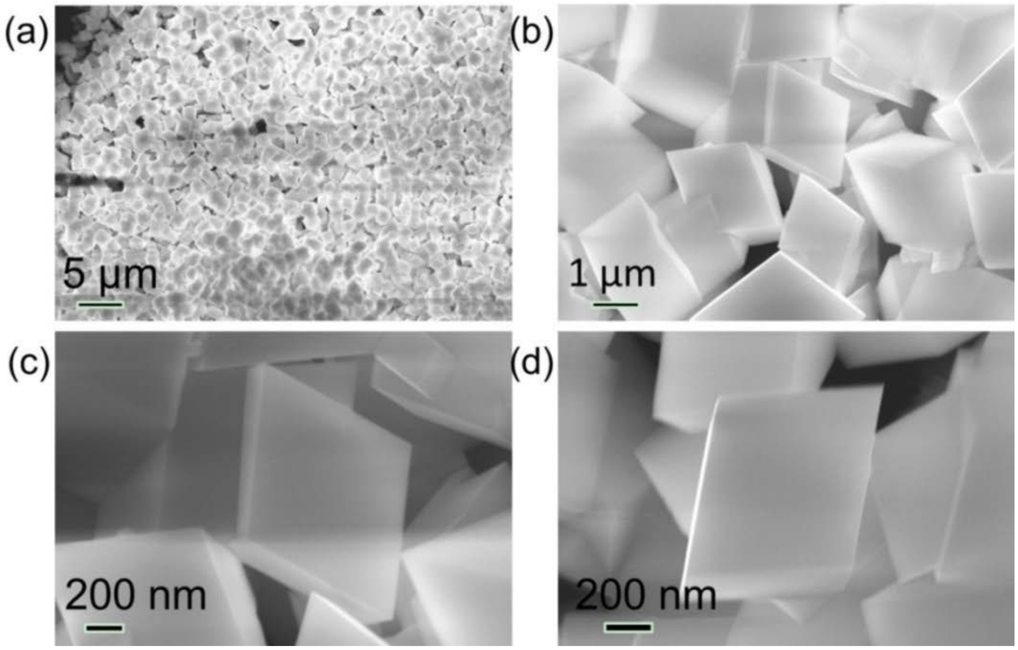

Figure 11- 3 (a-d) Low and high magnification SEM images of rhombic $MnCO_3$ nanocubes.

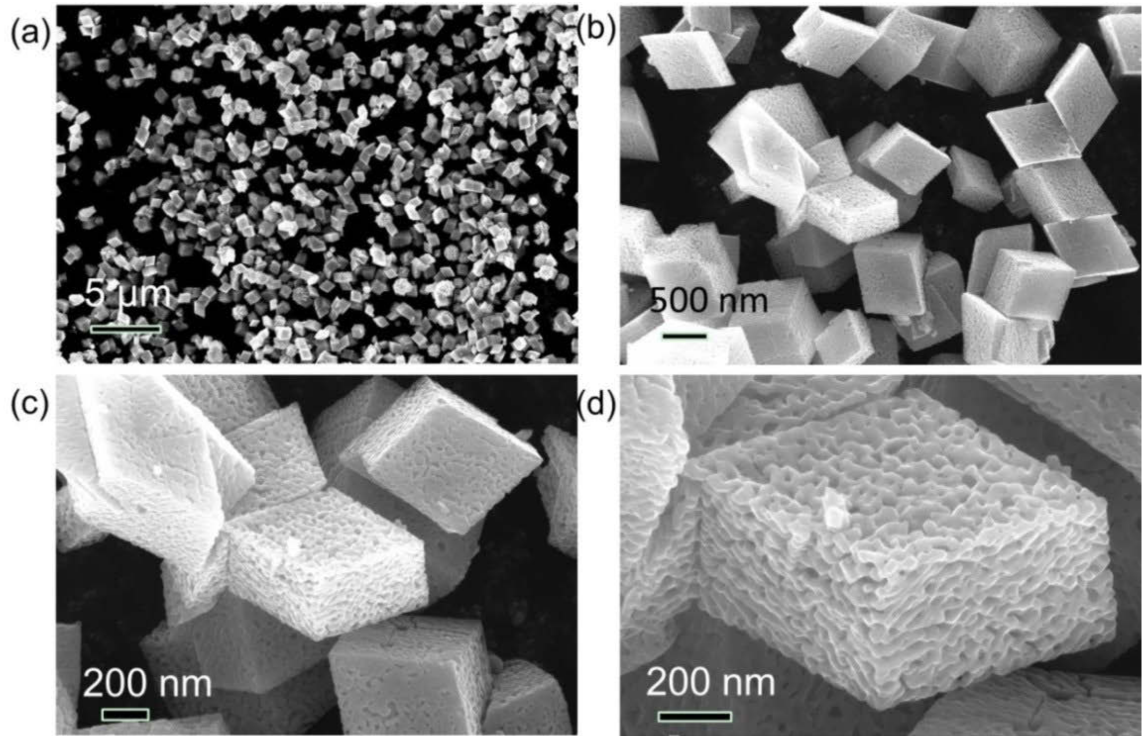

Figure 11- 4 (a-d) Low and high magnification SEM images of mesoporous rhombic MnO nanocubes.

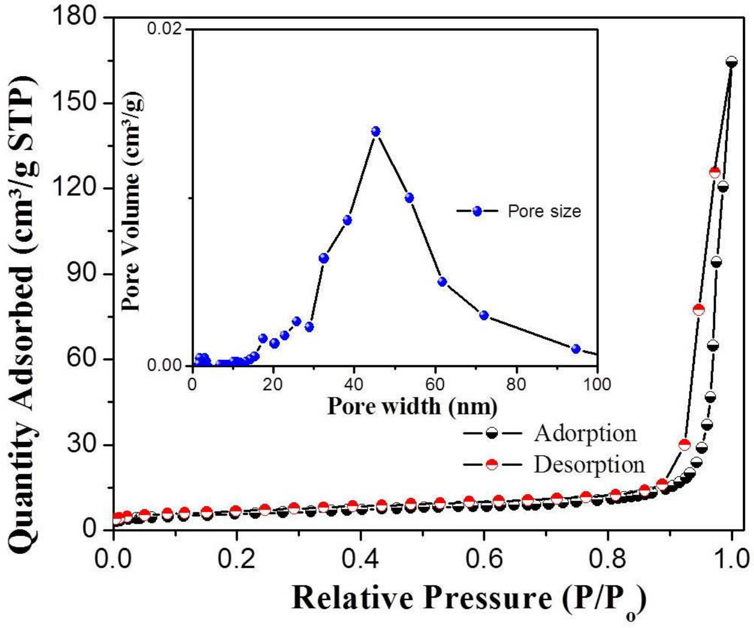

Figure 11- 5 Nitrogen absorption-desorption isotherm plots and pore size distribution information of mesoporous MnO nanocubes.

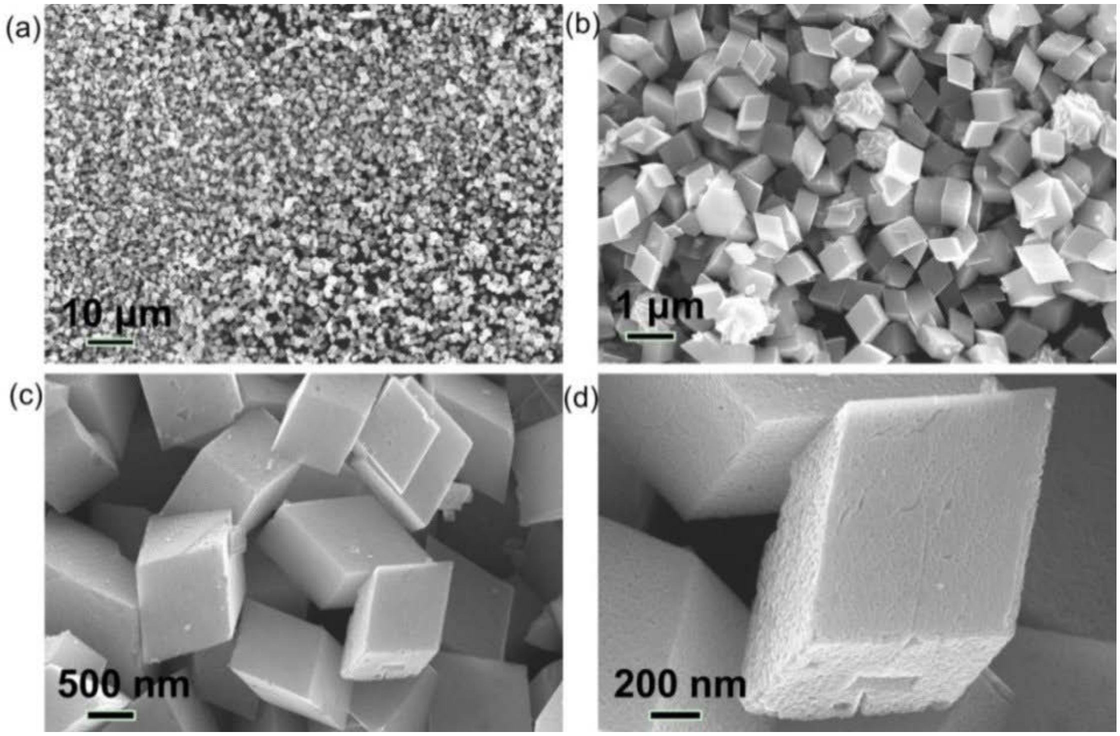

Figure 11- 6 (a-d) Low and high magnification SEM images of carbon coated MnO nanocubes.

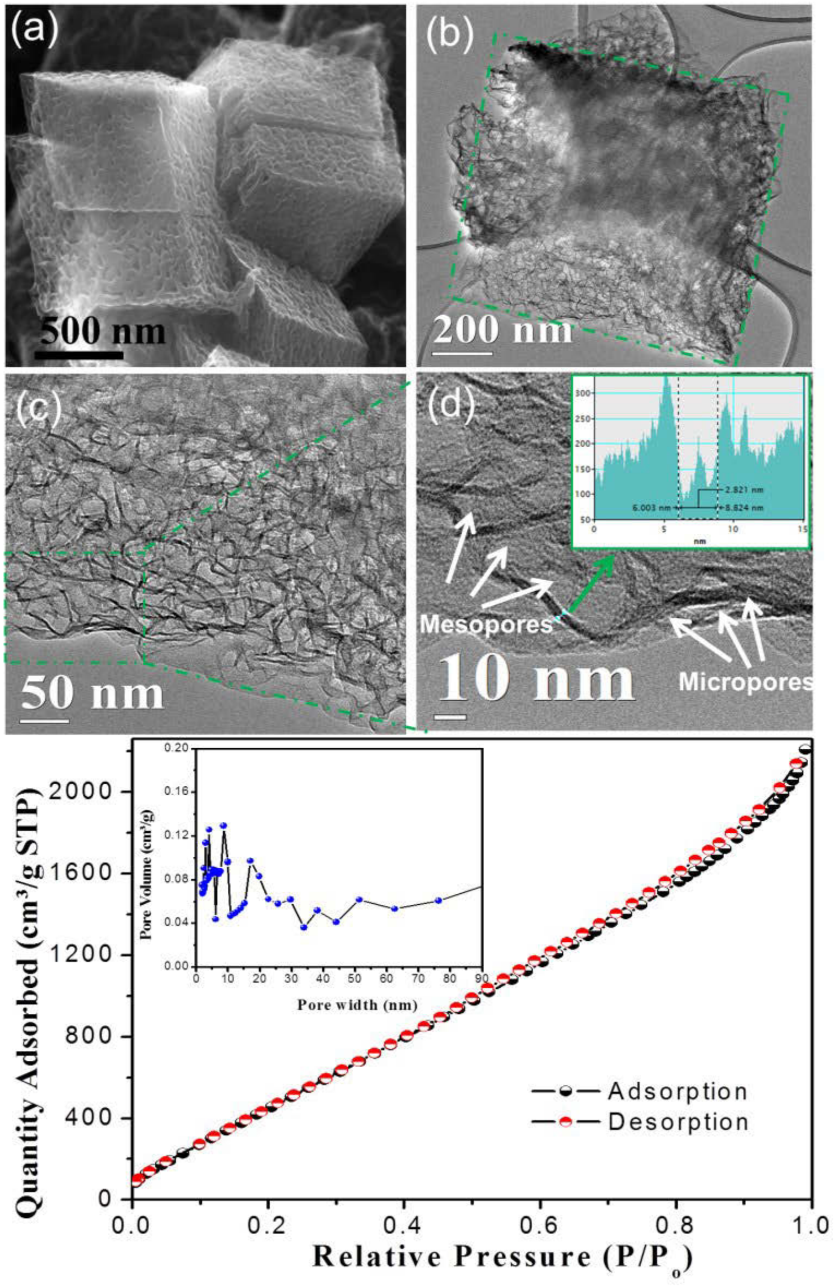

Figure 11- 7 (a) Scanning electron microscopy (SEM) image of mesoporous carbon nanocubes. (b) Transmission electron microscopy (TEM) image of mesoporous CNC. (c-d) High-resolution TEM images of CNC with a thickness profile image of CNC in (d). (e) Nitrogen adsorption-desorption isotherm and pore size distribution (insert image) of micro/mesoporous carbon nanocubes.

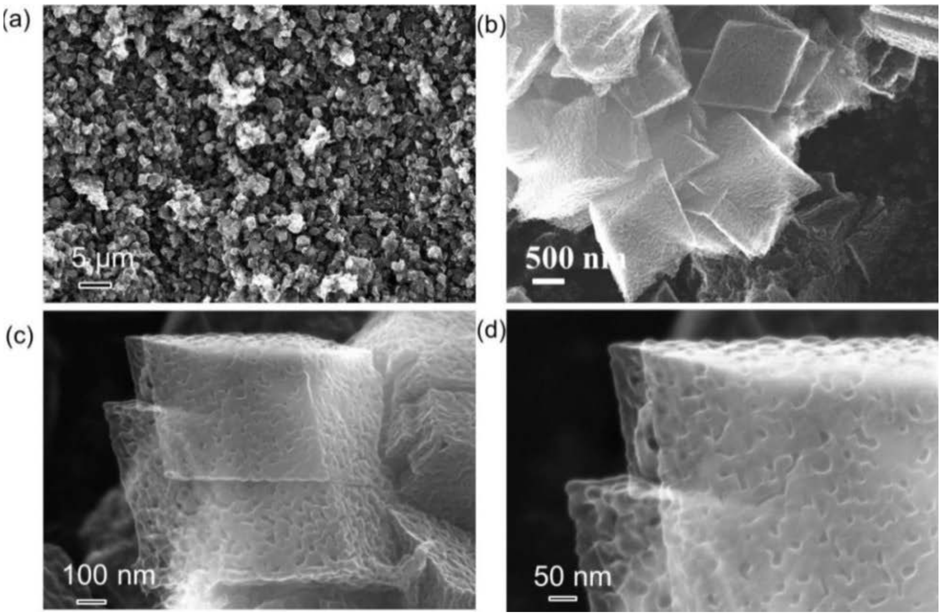

Figure 11- 8 (a-d) Low and high magnification SEM images of mesoporous hollow carbon nanocubes.

Sulfur was impregnated in hollow CNC *via* a disproportionate reaction, which can be described as: $2Na_2S + Na_2SO_3 + 6HCl \rightarrow 3S\downarrow + 6NaCl + 3H_2O$. During heat treatment at 155 ℃ for 12 h, sulfur with the lowest viscosity was absorbed into mesopores and micropores of CNC though the capillary force, forming CNC-S composites.[54] As comparison, PEDOT coated CNC-S composites are also prepared through wet-precipitation and melting-diffusion method. After loaded sulfur, partially transparent micro/mesoporous carbon CNC became opaque (Fig. 11-9a). The TEM image in Figure 11-9b shows that sulfur is distributed in individual carbon nanocubes, yet not all micro/mesoporous CNC are filled, leaving sufficient spaces to buffer the volume expansion during discharge and contraction during charge. The corresponding TEM elemental mapping image is shown in Figure 11-9c, in which sulfur in blue is clearly observed. Green spots, representing micro/mesoporous CNC, overlap with blue spots, indicating sulfur is encapsulated in micro/mesoporous CNC. More SEM and TEM images of CNC-S composites are presented in Figure 11-10a-d and Figure 11-12a. The corresponding elemental mapping image and EDX spectrum are shown in Figure 11-13a-e.

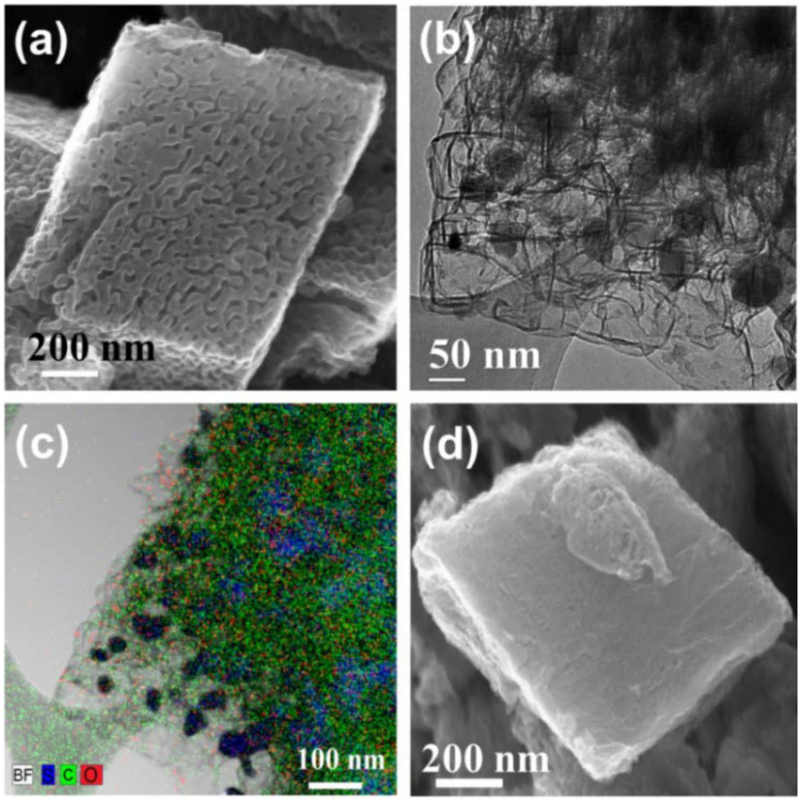

Figure 11- 9 (a) SEM images of CNC-S composites. (b) TEM image of CNC-S composites. (c) Elemental mapping image of CNC-S composites. (d) SEM images of P@CNC-S composites.

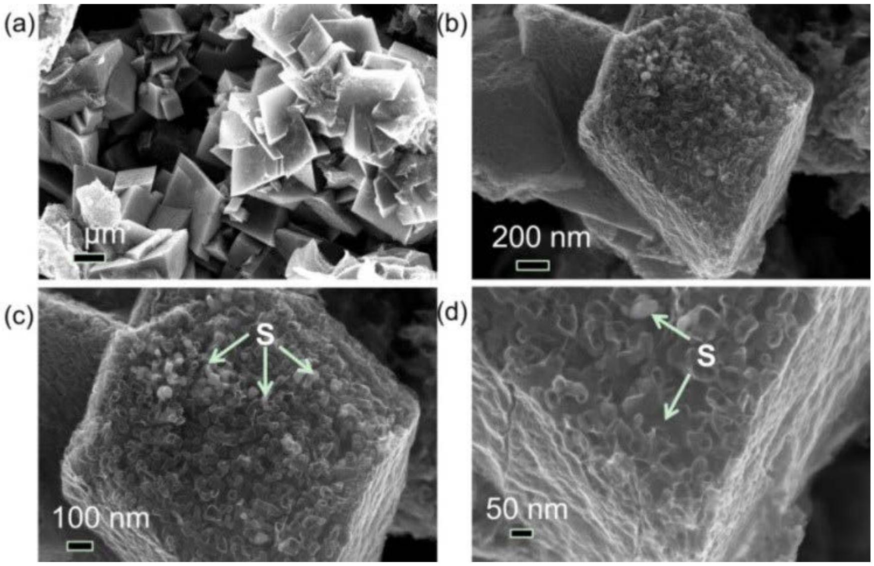

Figure 11- 10 (a-d) Low and high magnification SEM images of hollow carbon nanocubes with vast mesopores encapsulated sulfur into individual small hollow carbon nanocubes. Sulfur is labeled with white arrows in the image c and d.

The rhombic architecture of P@CNC-S composites is shown in Figure 11-9d and Figure 11-11a-d. The high magnification views of the TEM image are presented in Figure 11-12a, exhibiting that sulfur is dispersedly stored in mirco/mesoporous CNC and PEDOT polymer covers on the surface of CNC-S nanocomposites. After coated PEDOT polymer, the porous surface of CNC is filled with PEDOT polymer, turning into smooth surface, which can be clearly observed from the obvious differences of TEM images (Figure 11-9b and Figure 11-12b) and SEM images (Figure 11-9a and Figure 11-9d). Moreover, the transparent carbon nanocube layer becomes translucence, which is a sign for polymer coated carbon nanocube. The Fourier transform infrared spectra about CNC-S and P@CNC-S composites are shown in Figure 11-2c. The absorption peaks at 2203 cm^{-1}, 2002 cm^{-1}, and 1987 cm^{-1} are attributed to the stretching and bending vibrations of sulfur. The absorption peaks at 1533 cm^{-1} originate from the C=C stretching of quinoid structure. The peaks at 1355 cm^{-1} and 1199 cm^{-1} come from the C-C ring stretching of thiophene in PEDOT polymer. Additionally, the peak at 1087 cm^{-1} is ascribed to the stretching vibration of C-S bond. Those characterization peaks in P@CNC-S composites illustrate the presence of PEDOT polymer.

Assisted by the conductive polymer, individual P@CNC-S nanocubes with smooth surfaces aggregate together, which can improve the robust property and integrity of the P@CNC-S nanocomposites. The elemental mapping SEM and TEM images vividly exhibit the distribution of sulfur (red) and carbon (green) in the nanocomposites in Figure 11-14a-d. No sulfur is observed on the outside of P@CNC host, which demonstrates the good absorption capability and provides superior prerequisite for the further electrochemical measurements. The sulfur contents in CNC-S (76%) and P@CNC-S composites (72%) were determined by thermal gravimetry analysis (TGA) in air and presented in Figure 11-15. Compared to the direct weight loss curve of bare sulfur (from 180 ℃ to 280℃), both CNC-S and P@CNC-S nanocomposites show two-stage of sulfur loss (The first wave sulfur loss appears at 180℃, and ends at 220 ℃ for CNC-S nanocomposites and 250 ℃ for P@CNC-S nanocomposites. The second wave of sulfur further loss for CNC-S nanocomposites ends at 390 ℃, yet for P@CNC-S nanocomposites stops at 420 ℃). The first stage weight loss is ascribed to the evaporation of sulfur stored in mesopores and the second stage weight loss is attributed to sulfur absorbed in micropores. It should be noted that the sulfur loss rate in the second stage is much lower than that of both bare sulfur and the first stage sulfur loss, due to the physical confinement of micropores in CNC. Moreover, the sulfur loss temperature of P@CNC-S nanocomposites in both two stages exhibits at least 30 ℃ higher than that of CNC-S nanocomposites, implying the additional strong chemical bonding combination force from PEDOT polymer. The advantages of the dual protection and stabilization strategy are more obvious in the subsequent electrochemical measurements.

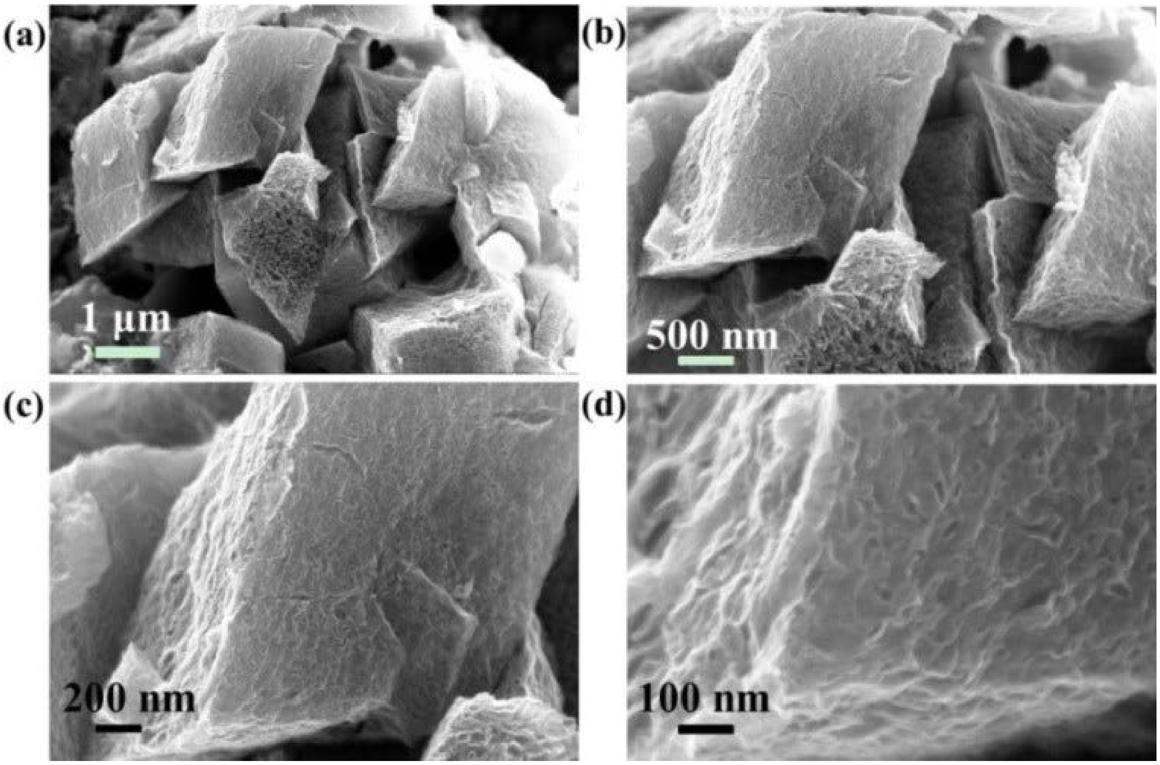

Figure 11- 11 Low and high magnification SEM images of PEDOT coated CNC-S composites. Mesopores on CNC-S composites were covered by PEDOT conductive polymers.

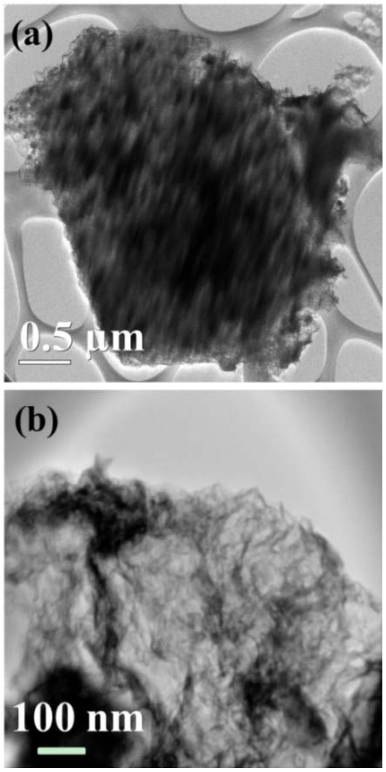

Figure 11- 12 (a) TEM images of rhombic CNC-S composites in which sulfur was encapsulated. (b) TEM images of PEDOT coated CNC-S composites.

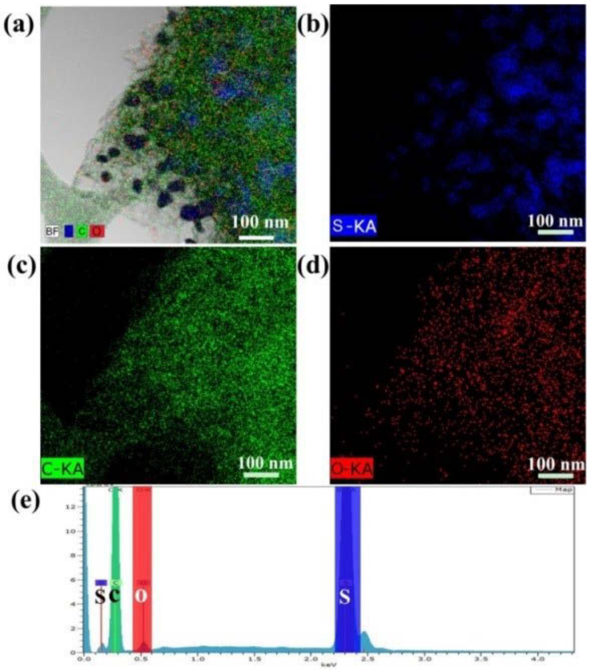

Figure 11- 13 (a-d) Elemental mapping TEM images of CNC-S composites. (e) Energy dispersive X-ray (EDX) spectrum of CNC-S composites.

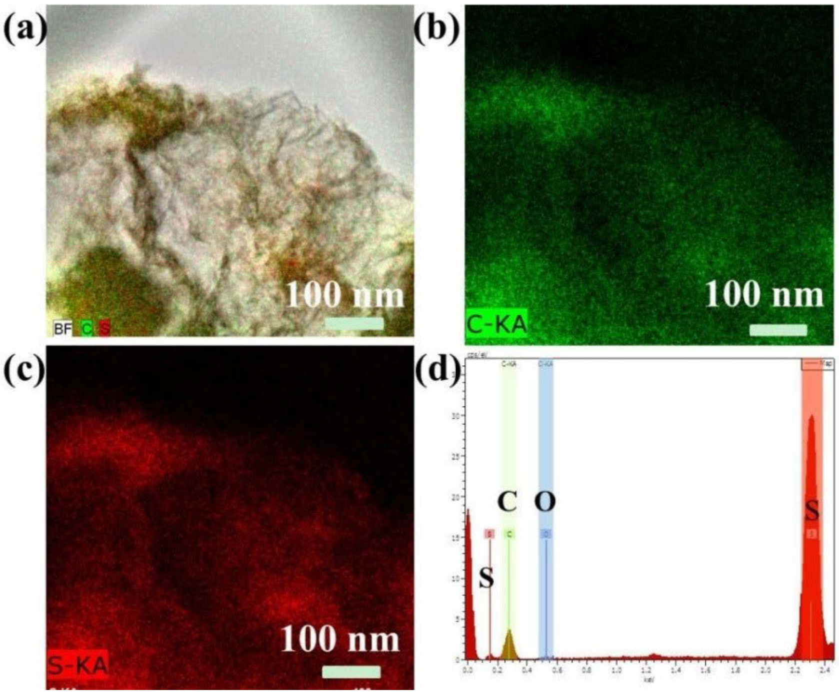

Figure 11- 14 (a-c) High resolution elemental mapping images of P@CNC-S composites. (d) The corresponding EDX spectrum.

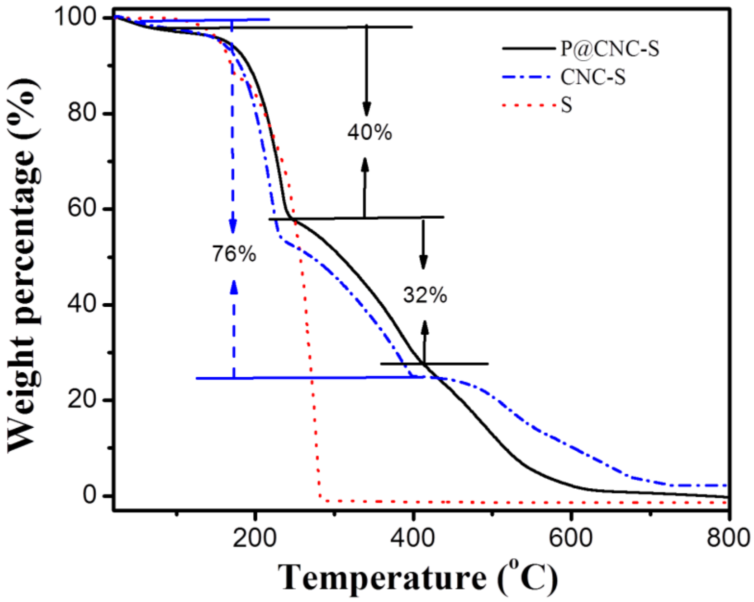

Figure 11- 15 Thermogravimetric analysis of bare sulfur, CNC-S and P@CNC-S composites.

To evaluate electrochemical performances of CNC-S and P@CNC-S composites, Figure 11-16a-b show the cyclic voltammogram (CV) curves in five cycles at a scan rate of

5 mV/s. Apparently, both electrodes show two similar cathodic peaks at around 2.3 V and 2.05 V, which agrees well with previous reports on two main stages of reduction reactions.[397-398, 418-423] The peak at 2.3 V is ascribed to the transformation of cyclo-octasulfur to long-chain soluble lithium polysulfides, and the second peak at 2.05 V is associated with the further decomposition of lithium polysulfides to insoluble short-chain lithium sulfides. However, the first anodic peak of P@CNC-S composites is at 2.45 V, and shifted to 2.38 V in the subsequent scanning cycles. The differences between the two anode peaks of the two sulfur composites are ascribed to the coating of PEDOT conductive polymers and the arousal of slow oxidation kinetics from lithium sulfides to lithium polysulfides and cyclo-octasulfur. In the subsequent CV cycles, there are no changes of shape and position of the redox peaks for the P@CNC-S composites. However, the redox peaks of the CNC-S composites slightly decrease, indicating that the reversibility and stability of electrodes are both improved after coated with PEDOT conductive polymer. Furthermore, according to the previous reports,[26, 424] the shuttling reaction can be predicted by the presences of high anodic based current at around 2.6V and the decreases of redox reaction peaks during cycling, which is a sign for the reactions of dissolved lithium polysulfides. Even though there are flat baselines for CNC-S nanocomposites, the decrease redox reaction peaks still can be distinguished, indicating that the shuttle effect is not fully confined. On contrast, the CV curves of P@CNC-S nanocomposites exhibit the flat baselines and highly reversible redox reaction peaks after 1st cycle, implying that the shuttle effect is well suppressed.

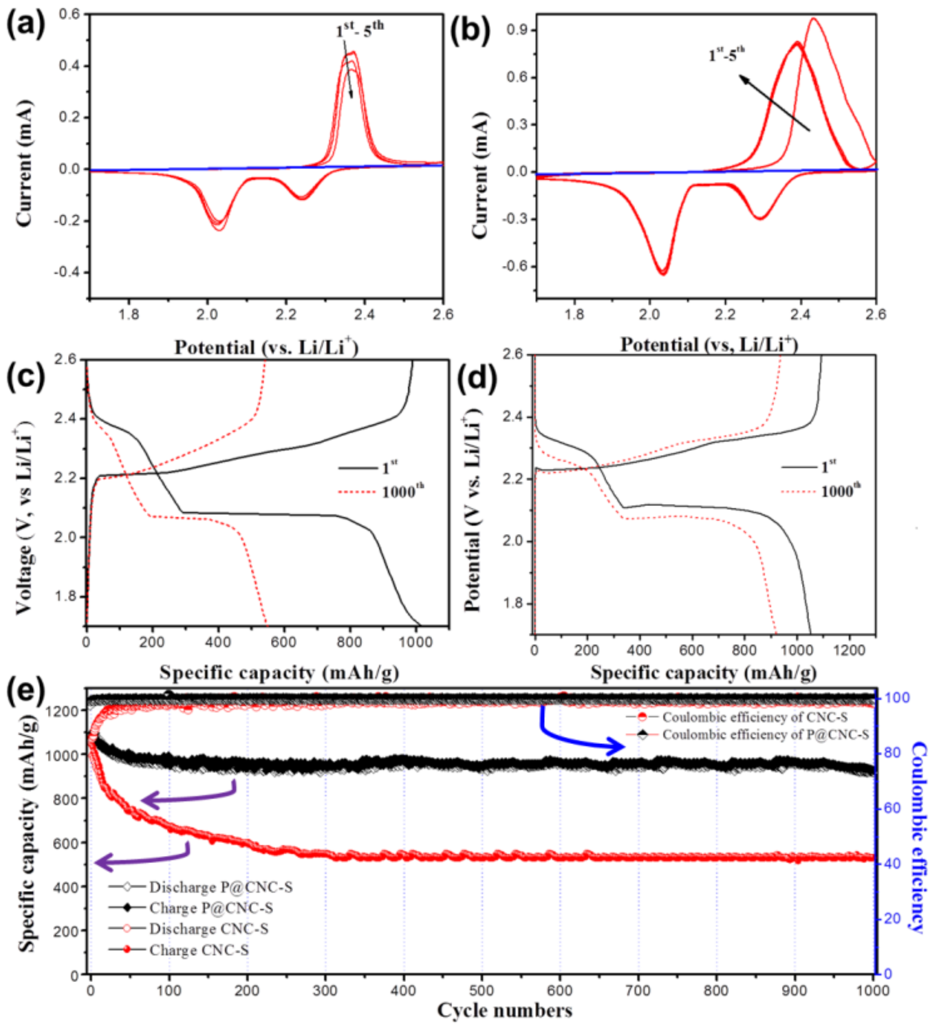

Figure 11- 16 Cyclic voltammogram (CV) plots of CNC-S (a) and P@CNC-S (b) composites. The charge/discharge profiles of CNC-S (c) and P@CNC-S (d) composites in 1st and 1000th cycles at 1 C current rate. (e) Cycling performances of CNC-S and P@CNC-S composites at 1 C for 1000 cycles (1 C = 1673 mA/g).

Typical discharge/charge profiles in the first and 1000th cycles of two sulfur composites are presented in Figure 11-16c-d at 1 C. The two discharge/charge profiles exhibited two main plateaus of typical sulfur cathode and are followed with the “solid-liquid-solid” mechanism,[417] which coincide well with the aforementioned CV curves. Moreover, the CNC-S composites also exhibit a small discharge plateaus at around 1.7V. The electrochemical behavior is similar to the reports about micro/mesoporous carbon nanosphere/nanotubes-sulfur composites from Huang’s group and Guo’s group.[236, 417] The small plateau is corresponding to the reduction of small sulfur chains (S_{2-4}) confined in CNC micropores and formation of solid lithium sulfides (Li_2S_2/Li_2S), which is followed the "solid-solid" reaction mechanism. The cycling performances and corresponding Coulombic efficiencies of the two composites are shown in Figure 11-16e. The CNC-S and P@CNC-S composites delivered high initial reversible specific capacities of 993 and 1086 mAh/g, respectively (It should be noted that the capacity calculation is based on the mass of sulfur on each electrode). Compared with the bare sulfur in the previous reports,[398] both the capacity and cycling performance were improved, which was attributed to the physical confinements from micro/mesoporous carbon layers and the enhanced conductivity of both CNC-S and P@CNC-S composites. Unlike previous reported sulfur host materials with large hollow cavities, like hollow carbon spheres or hollow TiO_2 nanospheres,[42, 326, 425] the micro/mesoporous carbon nanocubes provide hundreds of small carbon chambers to accommodate sulfur and offer sufficient inner spaces to alleviate mechanical stress during charge/discharge. After 1000 cycles, the reversible capacity of CNC-S maintained at 530 mAh/g (53% of initial capacity). On the contrary, the capacity of P@CNC-S composites stabilized at 927 mAh/g (85% of initial capacity) with a capacity decay ratio of 0.015% per cycle. Besides of an additional physical barrier, the PEDOT conductive polymer also supply chemical absorptions forming a chelated coordination structure with discharged products (Li_2S: 1.08 eV, and Li_2S_2: 1.22 eV) due to the strong electronegative atoms (S and O) in PEDOT polymers.[58] $LiNO_3$ as an additive is believed to confine the dissolution of lithium polysulfides and passivate the active lithium metal, which also contribute to the cycling stabilities.[426] The charge/discharge profile and cycling performances of P@CNC-S composites without adding $LiNO_3$ additive are given in Figure 11-17a-b. The unstable cycling performances and low Coulombic efficiency in the first 40 cycles imply that without the assistance of $LiNO_3$ additive, P@CNC-S composites take longer time to reach a stable cycliability and high Coulombic efficiency.

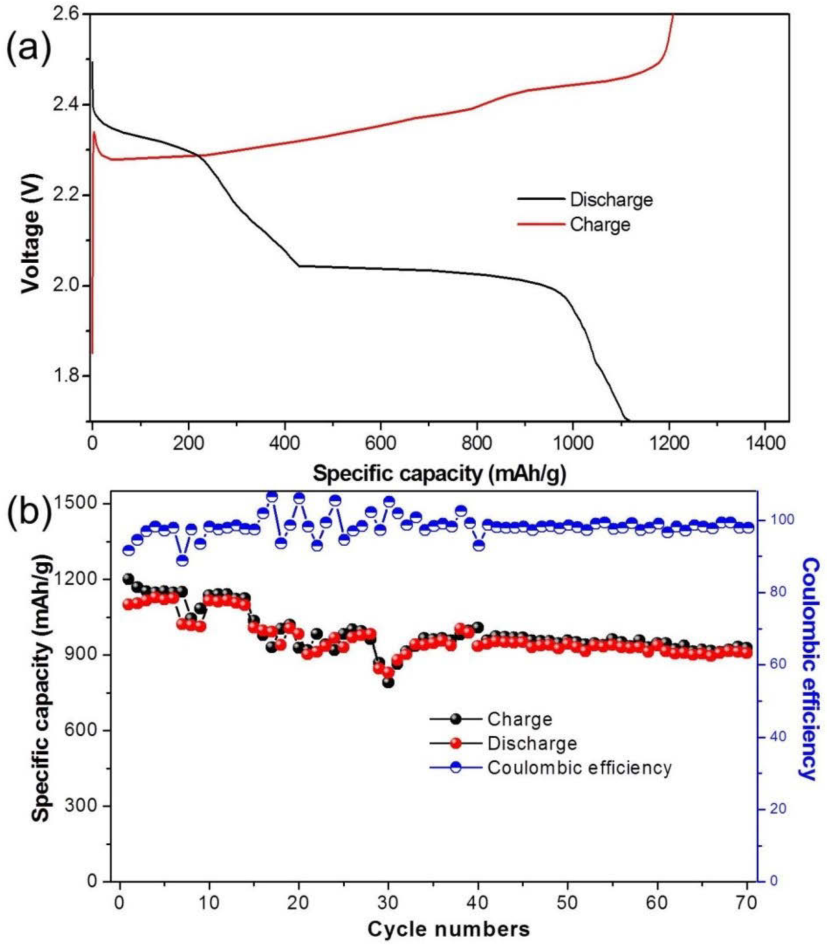

Figure 11- 17 (a) Typical discharge/charge voltage profiles of P@CNC-S composites without the addition of $LiNO_3$ at 1 C in the 1st cycle. (b) Cycling performance and corresponding Coulombic efficiency of P@CNC-S composites without the addition of $LiNO_3$ at 1 C in 70 cycles.

Aiming to examine the tolerance to high current rates, both CNC-S and P@CNC-S composites were cycled at step-wise current rates (Figure 11-18a). CNC-S composites delivered a high reversible capacity of 1316 mAh/g at 0.1 C, further experienced gradually increased current rates 0.5 C (1045 mAh/g), 1 C (902 mAh/g), 5 C (593 mAh/g) and 10 C (460 mAh/g), finally reversed to 0.1 C (1298 mAh/g). After coating with PEDOT, the P@CNC-S cathode delivered a better electrochemical performance. For example, it achieved a high initial reversible specific capacity of 1407 mAh/g at 0.1 C. When the current rates increased to 10 C and gradually declined to 0.1 C, P@CNC composites exhibited high reversible capacities of 1156 mAh/g (0.5 C), 1070 mAh/g (1 C), 896 mAh/g (5 C) and 711 mAh/g (10 C), respectively. The corresponding Coulombic efficiencies exceeded 96%. The discharge/charge profiles of P@CNC-S composites and the cycling performance at 0.1 C are shown in Figure 11-19a-b. It should be noted that the reversible capacity of P@CNC-S is 1407 mAh/g with a Coulombic efficiency of 99.4% in the first cycle, indicating that the shuttle effect originating from the dissolution of lithium polysulfides in cathode has been effectively restrained. After 150 cycles, the reversible capacity of P@CNC-S composites is stabilized at 1259 mAh/g with a capacity retention ratio of 89.9%. The corresponding Coulombic efficiencies are shown in Figure 11-19b.

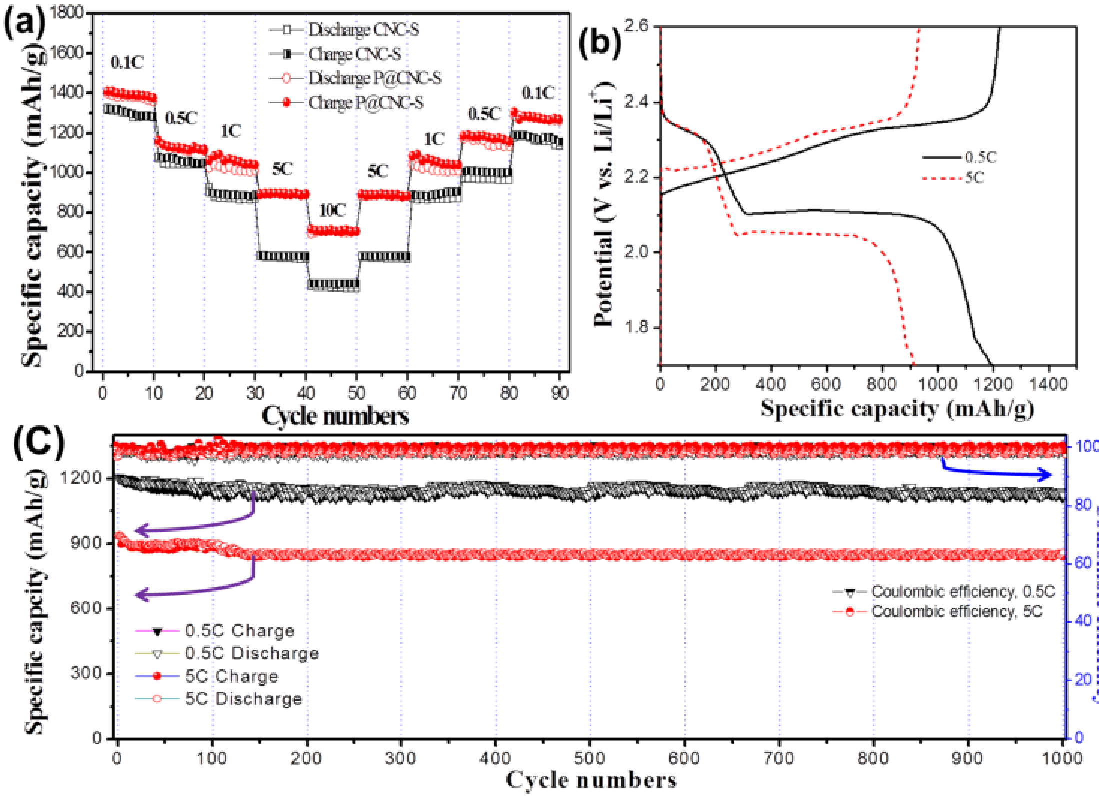

Figure 11- 18 (a) Rate capability of rhombic CNC-S and P@CNC-S composites measured at various current rates for C/10 to 10 C. (b) Typical discharge/charge profiles of P@CNC-S composites at C/2, 5 C and 10 C. (c) Cycling performance of P@CNC-S composites at C/2, 5 C and 10 C (1 C= 1673 mA/g) and the corresponding Coulombic efficiencies.

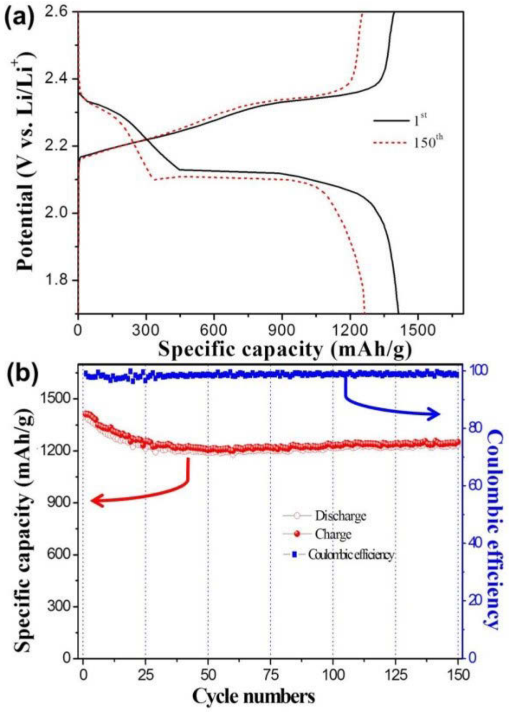

Figure 11- 19 (a) Typical discharge/charge voltage profiles of P@CNC-S composites at C/10 in the 1st and 150th cycles. (b) Cycling performance and corresponding Coulombic efficiency of P@CNC-S composites at C/10 for 150 cycles.

The discharge/charge profiles, cycling performances and the corresponding Coulombic efficiencies of P@CNC-S composites at higher current rates (0.5 C, 5 C and 10 C) are shown in Figure 11-18b-c and Figure 11-20a-b. The composites demonstrated an initial reversible capacity of 1078 mAh/g at 0.5 C rate, with a capacity retention ratio of 93.2% after 1000 cycles (0.07% per cycle). When the current rates were increased to 5 C and 10 C, P@CNC-S composites achieved a high reversible capacity of 851 mAh/g and 530 mA/g after 1000 cycles, with capacity retention ratios of 91.5% and 74.5%, respectively. The enhanced electrochemical performances indicate that P@CNC-S composites can tolerate high current densities and maintain excellent electrochemical performances even after the electrodes experienced long-term cycling, thereby exhibiting the features of excellent robustness, fast kinetics and high reversibility. The electrochemical performances of P@CNC-S materials are compared with other carbon-sulfur based materials, which are shown in Table11-1.

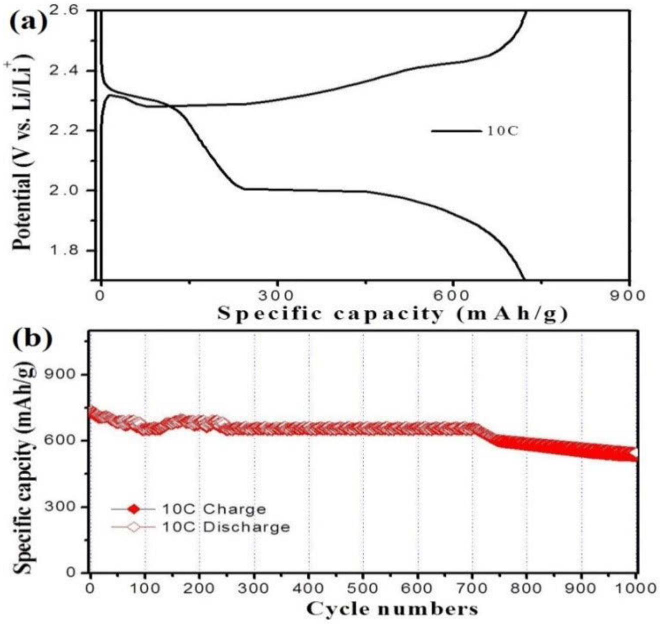

Figure 11- 20 (a) Typical discharge/charge voltage profile of P@CNC-S composites at 10 C at the first cycle. (b) Cycling performance of P@CNC-S composites at 10 C for 1000 cycles.

In order to investigate the dual protective effect of PEDOT and CNC, the fully discharged P@CNC-S electrode after 1000 cycles at 1 C, washed with 1,3-dioxolane and 1,2-dimethoxyethane, was examined by *ex-situ* TEM and HRTEM observation, which further confirmed the sulfur distribution by elemental mapping (as shown in Figure 11-21a-d). Compared to micro/mesoporous carbon nanocube partially filled with sulfur in Figure 11-9b, the rhombic P@CNC was completely occupied by the insoluble discharge product (Li_2S) in Figure 11-21a due to the volume expansion after discharge. This illustrates the successful confinement of volume changes by dual protective layers during cycling, which can significantly improve the cyclabilities of sulfur electrodes. The sulfur distribution in Figure 11-21b demonstrates that Li_2S was well confined in P@CNC composites and the corresponding EDX spectrum, which also confirmed the effective restraining of the dissolution of lithium polysulfides. The enlarged view of the discharged product Li_2S encapsulated in P@CNC is shown in Figure 11-21c and the HRTEM image in Figure 11-21d illustrates the lattice of Li_2S. The corresponding fast fourier transform (FFT) image inserted in Figure 11-21d also verified the crystallization of Li_2S, exhibiting crystal planes of (111) and (222).

Table 11- 1 The electrochemical performances of P@CNC-S materials are compared with other carbon-sulfur based materails.

Sulfur cathode Ref.	Sulfur percentage	Rate capacity based on sulfur mass (mAh/g)	Rate capacity at 0.1 C based on entire electrode mass (mAh/g)	Cycle life	Remained capacity at 0.1 C based on sulfur mass (mAh/g)	Remained capacity at 0.1 C based on entire electrode mass (mAh/g)
Highly ordered carbon fibers-S[30]	75%	1100(0.2 C)	825(0.2 C)	150	730(0.2 C)	547(0.2 C)
Porous graphene[363]	66%	1068(0.5 C)	704(0.5 C)	35	653(0.5 C)	430(0.5 C)
N-doped mesoporous carbon-S[55]	60%	1172(0.2 C)	703(0.2 C)	100	874(0.2 C)	524(0.2 C)
Amylopectin warped grapheme oxide-S[63]	52%	817(0.125 C)	424(0.125 C)	175	441(0.125 C)	229(0.125 C)
The P@CNC-S in the Thesis	76%	1156(0.5 C)	878(0.5 C)	500	1078(0.5 C)	819(0.5 C)

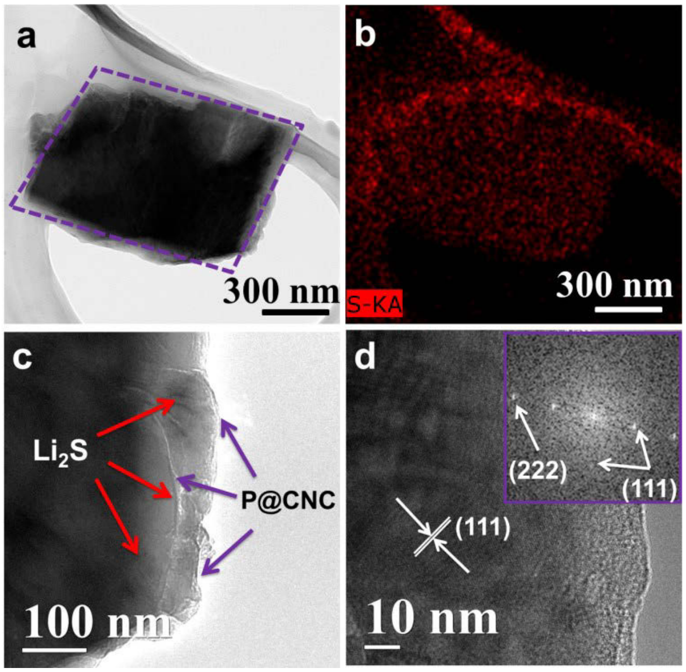

Figure 11- 21 (a) TEM image of discharge product (Li_2S) of P@CNC-S composites after 1000 cycles at 1 C. (b) The elemental mapping image of sulfur (red) in the discharged electrode. (c) TEM image of the Li_2S completely encapsulated by P@CNC shells. (d) HRTEM image of the discharged product and its corresponding FFT image.

The SEM images in Figure 11-22a-d demonstrated that typical rhombic architecture was well-preserved after 1000 cycles under charged state. High resolution TEM elemental mapping images (Figure 11-23a-c) show that sulfur particles are still confined in PEDOT coated CNC. Based on the aforementioned characterizations and analysis, the superior electrochemical performances of P@CNC-S could be associated with the unique rhombic micro/mesoporous CNC architecture and homogenous PEDOT coating, which provide sufficient spaces to encapsulate sulfur in mesopores and a cushion effect for large volume changes, as well as strict physical barriers from micropores of CNC and strong chemical bondings from PEDOT to the soluble lithium polysulfides.

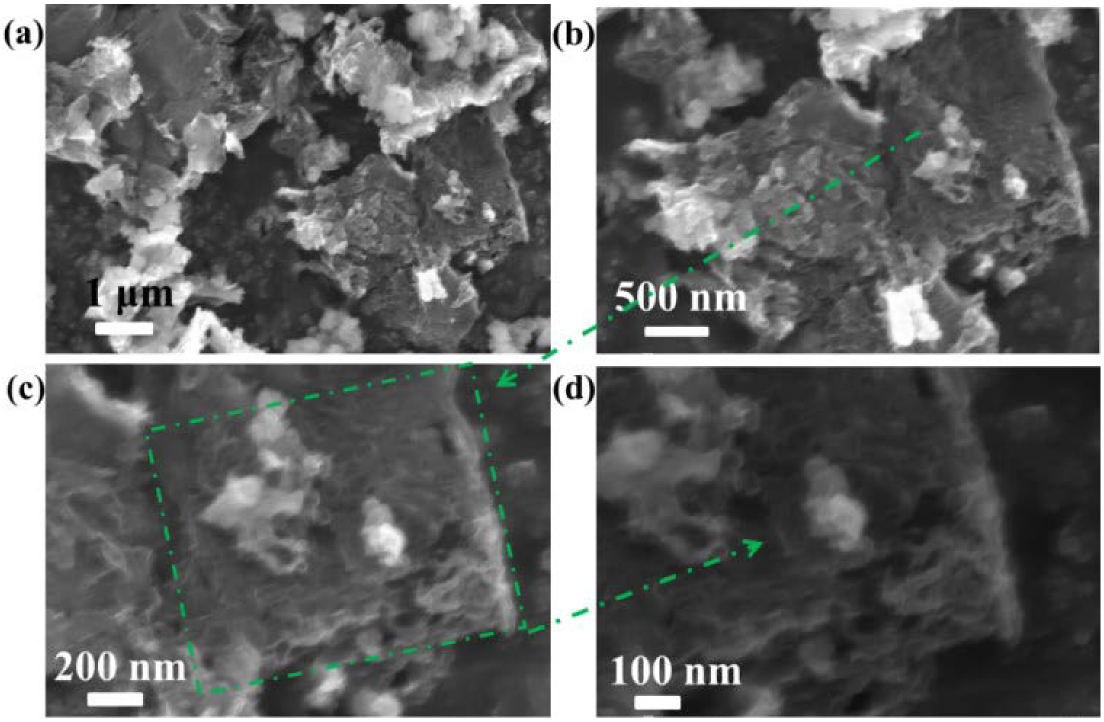

Figure 11- 22 (a-d) Low and high magnification SEM images of P@CNC-S electrode after 1000 cycles at 1 C. Typical rhombic structure was well maintained and marked by dashed square in (c).

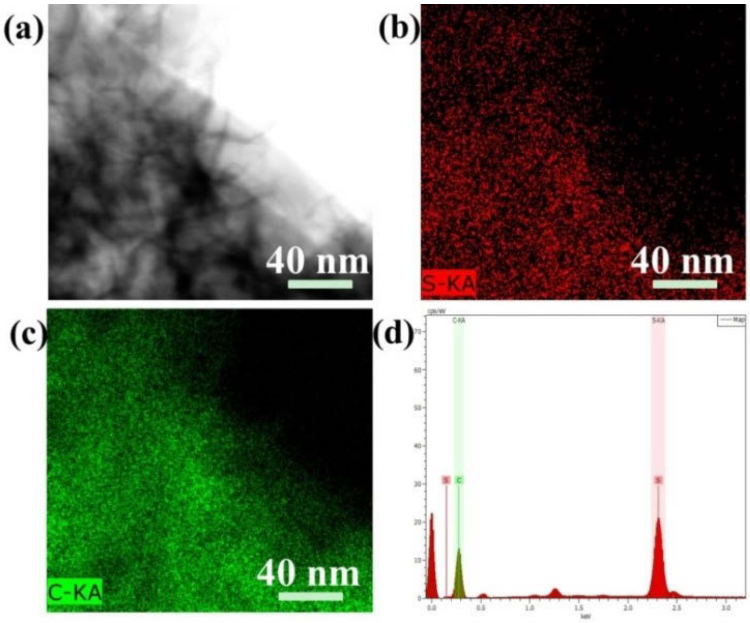

Figure 11- 23 (a-c) High resolution TEM elemental mapping images of P@CNC-S electrode after 1000 cycles at 1 C. (d) The corresponding EDX spectrum.

To further explore the mechanism of the enhanced electrochemical performances of the P@CNC-S composites, we performed electrochemical impedance spectroscopy (EIS) measurement at different discharge and charge states, *ex situ* SEM and TEM characterizations. Figure 11-24a shows a typical discharge/charge voltage profile of P@CNC-S composites at 0.1 C, where sign A and B represent the EIS states recorded before cycling and after 150 cycles, and sign C, D and E reflect the changes of electrode's impedances during discharge/charge processes. The EIS data in Figure 11-24b shows the impedance changes before and after 150 cycles. The Nyquist plots consist of a depressed semicircle in the high frequency region and an oblique line in the medium frequency region. The little increase in radius of the semicircle at the high frequency region means the slight changes of charge-transfer resistance, indicating that the electrode had little inner electrochemical resistance. The impedance changes during discharge/charge are shown in Figure 11-24c. The radius values of three semicircles increase in the order of E > D > C, implying the changes of resistance of the electrode during discharge/charge. This coincides with the transformation of intermediates from soluble lithium polysulfides to insulating insoluble lithium sulfides during discharge, and the reverse process during charge.

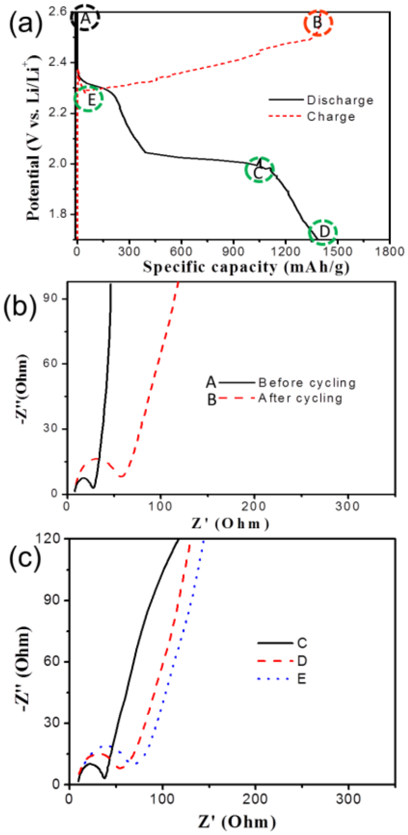

Figure 11- 24 (a) Discharge/charge voltage profiles of P@CNC-S electrode at C/10 current rate. Nyquist plots of P@CNT-S electrode measured at different states: (b) EIS obtained before (A) and after cycling (B). (c) EIS obtained at C, D and E stages marked in (a).

11.4 Conclusions

In summary, we have successfully synthesised mesoporous Rubik's CNC with a high surface area of 2425 m^2/g. With further PEDOT coating, P@CNC-S composites offer a dual confinement of both physical trapping and chemical bonding to lithium polysulfides. When applied as cathodes in Li-S batteries, P@CNC-S composites delivered a high capacity of 1086 mAh/g at 1 C rate extending to 1000 cycles. The electrodes also exhibited high rate capabilities of 842 mAh/g and 530 mAh/g after 1000 cycles at 5 C and 10 C, respectively. The superior performances could be ascribed to the well-preserved Rubik's nanocube architecture and the dual confinement strategy. Moreover, the unique mesoporous Rubik's carbon nanocube architecture can also be applied in the other fields, such as lithium air battery, sodium ion battery, hydrogen storage, drug delivery, catalysis.

CHAPTER 12 CONCLUSIONS

12.1 Graphene and Graphene Nanocomposites as Anode Materials for Lithium-Ion Batteries

We have developed a microwave hydrothermal synthesis and hydrogen gas reduction approach for the preparation of Sn-GNS nanocomposites with different weight ratios. Altering the weight ratios between tin and graphene has critical influences on their morphologies. Field emission scanning electron microscope and transmission electron microscope analysis reveals that tin nanoparticles homogeneously distribute on the surface of graphene nanosheets. There is no apparent pulverization and cracking of Sn nanoparticles for Sn-graphene nanosheets nanocomposite after cycling tests. The Sn-graphene nanosheets with a weight ratio of 1:4 (Sn-GNS-2) exhibit a high initial reversible specific capacity of 946 mAh g^{-1} at a large current density of 1600 mA g^{-1}, and a high specific capacity of 542 mAh g^{-1}, that is maintained after 30 cycles, which demonstrates that the Sn-GNS-2 electrode has an excellent high rate capacity and a stable cycle performance. The superior electrochemical performance should be attributed to the high specific surface area of tin nanoparticles and the synergetic effect of the combination of Sn nanoparticles and highly conductive graphene nanosheets.

Graphene nanosheet/carbon nanotube hybrid materials were successfully prepared by the π- π interaction without using any chemical reagent. The different ratios between graphene oxide and carbon nanotubes had critical influences on their states in aqueous solution and the final products' morphologies. FESEM and TEM analysis confirmed the 3D nanoarchitecture with the wrapping of graphene nanosheets around individual carbon nanotubes. The GNS-CNT-2 sample exhibited a high initial reversible specific capacity of 439 mAh g^{-1} at a current density of 372 mA g^{-1}, and that a high capacity of 429 mAh g^{-1} had been maintained after 100 cycles with a high Coulombic efficiency of 98.5% (from the 2nd to 100th cycles). The good electrochemical performance could be attributed to the homogeneous three-dimensional nanostructure and the synergistic effect of the combination between graphene nanosheets and carbon nanotubes.

Monolayer to triple-layer graphene sheets have been successfully prepared by APCVD deposition using acetylene gas as the carbon source and coral-like iron as catalyst. The process can be scaled up for large scale production at a low cost. The optimum CVD temperature has been identified to be 850 °C, which is much lower than other methods with other metals. TEM, AFM, Raman spectroscopy and XPS characterizations show the single crystalline and high quality nature of the as-prepared graphene produced by the bottom-up APCVD approach. A new horizontal “dissolution-deposition-growth” mechanism is proposed and verified by TEM and HRTEM analyses. When applied as anode materials in lithium ion batteries, graphene sheets exhibit high initial rechargeable capacity and stable multi-current rate cycling performance. Large scale production of graphene could pave the way for a wide range of applications of graphene materials.

Mesoporous C@Si@GF nanoarchitectures were successfully synthesized by a thermal bubble ejection assisted chemical-vapor-deposition and magnesiothermic reduction method. Mesoporous Si nanospheres were coated with a nanolayer carbon and embedded in graphene foam, which provided sufficient voids to cushion the large volume changes of Si during lithiation and de-lithiation processes and enhance electronic conductivity for semi-insulating Si nanoparticles. When applied as anode materials for lithium storage in lithium ion batteries, C@Si@GF nanocomposites exhibited superior electrochemical performances, including a high lithium storage capacity of 1200 mAh/g at current density of 1 A/g, excellent tolerances to high current densities and outstanding cyclability. The as-developed approach could also be extended to synthesize other 3D materials.

Fe_2O_3-CNT-GNS hybrid materials consisting of bamboo-like CNTs and Fe_2O_3 nanorings were successfully prepared by a chemical vapor deposition synthesis method. Fe nanorings play critical roles in forming bamboo-like carbon nanotubes. A modified “tip-growth” mechanism of carbon nanotubes and a unique lithiation process were proposed. When applied as anode materials in lithium ion batteries, the Fe_2O_3-CNT-GNS-2 hybrid materials exhibited a high specific capacity of 984 $mAh \cdot g^{-1}$ with a superior cycling stability and high rate capacity. This could be credited to the facile Li^+ ions diffusion through the open tips of CNTs and cracks on the outside walls of CNTs, and extra lithium storage sites provided by arc-like graphene layers inside CNTs. Flexible and highly conductive GNS and open 3D architecture also contribute to the superior electrochemical performance. The carbon-based hybrid materials with 3D structure could also be applied for lithium-air batteries, supercapacitors and fuel cells.

12.2 Nanostructure Transition Metal Oxides for Lithium-Ion Batteries

Mesoporous Co_3O_4 with interconnected architecture was synthesized by means of a microwave-assisted hydrothermal and low-temperature conversion method, which exhibited excellent electrochemical performances as anode materials in lithium ion batteries and as catalyst in oxygen evolution reaction under alkaline solutions. FESEM and TEM images show the unique interconnected and mesoporous structure. When employed as anode materials for lithium ion batteries, mesoporous Co_3O_4 delivered a high specific capacity of 883 mAh/g at 0.1 C current rate and stable cycling performances even at higher current rates. Post-mortem analysis of ex-situ FESEM images reveal that the particular structure has been well maintained after long-term charge/discharge cycling and verifies the robust properties of mesoporous Co_3O_4 nanoflakes electrodes. The mesoporous Co_3O_4 material also exhibited OER active properties, showing an onset potential towards OER of 0.529 V (vs. Ag/AgCl) in alkaline solution and smaller Tafel slopes of $b = 49$ mV/decade in 1 M KOH and $b = 60$ mV/decade in 0.1 M KOH. This implies that the synthesized mesoporous Co_3O_4 is an efficient catalyst to the OER. Meanwhile, the mesoporous Co_3O_4 exhibited good catalytic stability during OER, even when cycled 1000 times, which is attributed to the stability of the unique mesoporous structure and exposed highly reactive energy facets on the edges.

12.3 Novel Carbon Nanomaterials as Sulfur Carriers for Lithium-Sulfur Batteries

Graphitic hyperbranched hollow carbon nanorods were well-designed and synthesized to encapsulate sulfur as the cathode materials for lithium sulfur batteries. FESEM and TEM characterization confirmed the hierarchical 3D nanomaze-like architecture, in which sulfur was confined inside hollow and interconnected carbon nanorods. When applied as cathodes in lithium-sulfur batteries, CNR-S composites delivered a high specific capacity of 1378 mAh/g at 0.1 C current rate and a stable cycling performance. The CNR-S composites also demonstrated high capacities of 990 mAh/g, 861 mAh/g and 663 mAh/g at 1 C, 5 C and 10 C with capacity retentions of 94.4%, 95.5% and 85.5% after 500 cycles, respectively. Post-mortem FESEM analysis illustrates that the integrity of the CNR-S composite electrode had been well preserved after long-term cycling. The superior electrochemical performances of CNR-S composites should be ascribed to the unique graphitic hyperbranched hollow carbon nanorods architecture, which can effectively suppress the dissolution of sulfur during charge/discharge cycling. The approach and strategy developed in this paper could also be applied to other battery systems, such as lithium-air batteries and sodium-ion batteries.

The sulfur-rich (86 wt. %) MHCS composites were successfully synthesised by an aqueous emulsion approach and *in-situ* impregnation method. Multi-shelled hollow carbon nanospheres and PVP polymers were employed as a dual sulfur confining strategy. When applied as cathodes in lithium sulfur batteries, multi-shelled hollow carbon nanosphere-sulfur composites delivered a high specific capacity of 1350 mAh/g, and excellent cycling stability at the current density of 0.1 C. Reversible curves from cyclic voltammogram curves validate successful suppression of the shuttle effect. The electrode delivered 1003 mAh/g and 541 mAh/g at 1 C and 5 C in the initial cycle, respectively. After 200 cycles, specific capacities of the MHCS composites at 1 C and 5 C still maintained 846 mAh/g and 452 mAh/g with capacity retention ratios of 84% and 83.5%, respectively, which demonstrates enhanced cyclability and good capacity retentions.

Mesoporous Rubik's hollow carbon nanocubes (CNC) with a high surface area of 2425 m^2/g were successfully prepared and employed as sulfur host to immobilize the sulfur cathode. With further PEDOT coating, P@CNC-S composites offer a dual confinement of both physical trapping and chemical bonding to lithium polysulfides. When applied as cathodes in Li-S batteries, P@CNC-S composites delivered a high capacity of 1086 mAh/g at 1 C rate extending to 1000 cycles. The electrodes also exhibited high rate capabilities of 842 mAh/g and 530 mAh/g after 1000 cycles at 5 C and 10 C, respectively. The superior performances could be ascribed to sufficient spaces to encapsulate sulfur in mesopores and a cushion effect for large volume changes, as well as the successful dual confinement strategy through strict physical barriers from micro/mesopores of CNC and strong chemical bondings from PEDOT to the soluble lithium polysulfide. *Ex-situ* TEM analysis also proved the successful confinement of the dissolution of lithium polysulfides and volume expansion of the discharged product (Li_2S). Moreover, the unique micro/mesoporous rhombic carbon nanocube architecture can also be applied in other fields, such as the lithium air battery, sodium ion battery, hydrogen storage, drug delivery and catalysis.

12.4 Outlook

The thesis mainly concentrates on the synthesis of deliberately designed nanomaterials with novel architectures and their applications for electrodes of Li-ion batteries or Li-S batteries. Various synthesis methods and preparation concepts reported in this thesis have large potentials to synthesize other similar nanomaterials or utilize the specifically mentioned electrochemical measuring techniques, including galvanostatic charge and discharge, cyclic voltammetry and electrochemical impedance spectroscopy.

The modified Hummer method for preparing graphene oxide and subsequent reduction can be applied to the production of high quality graphene on a large scale, which also has extensive potential in developing applications for graphene and its nanocomposites (graphene-CNT, graphene-Sn, graphene-Si and graphene-transition metal oxides with different morphologies) in Li-ion batteries, Na-ion batteries or Li-O_2 batteries. The chemical vapor deposition method can be extended to prepare various materials with appropriate catalysts and templates. This technique can also be upgraded to sophisticated CVD with the assistance of high-vacuum, water-assisted or plasma-enhanced techniques.

The dual protective strategy reported in the thesis is of significant importance in the confining of the dissolution of lithium polysulfides in Li-S batteries. Mesoporous carbon materials and multi-shelled carbon nanospheres used as sulfur carriers can also be employed as hollow host to encapsulate Li_2S or lithium polysulfides for the novel configuration of Li-S batteries. Conductive polymers synthesized in this work can also be applied as chemical absorptions of lithium polysulfides in the novel configuration of Li-S batteries with Li metal-free electrodes, which is very important for the safety of practical applications of Li-S batteries (avoiding the formation of lithium dendrites). New electrolytes with high concentration play a significant role in Li-S batteries on stabilizing cycling performance and improving Coulombic effieciency. For future Li-S batteries, developing new sulfur cathodes with advanced features (like a high percentage of sulfur, high electronic and ionic conductivities, high capacity and long cycle life) are extremely important for practical applications, such as meeting the vast requirements of the EV and HEV market, and balancing the off-peak in large-scale grid stations. Moreover, a smart charging/discharging technique that stabilizes the redox reactions in highly reversible trace polysulfide shuttle zones is also effective in significantly enhancing the cycling performance and increasing the Coulombic efficiency of Li-S batteries.

REFERENCES

1. Chen, J., Recent Progress in Advanced Materials for Lithium Ion Batteries. *Mater.* **2013,** *6* (1), 156-183.

2. Liu, J., Addressing the Grand Challenges in Energy Storage. *Adv. Funct. Mater.* **2013,** *23* (8), 924-928.

3. Bruce, P. G.; Scrosati, B.; Tarascon, J. M., Nanomaterials for rechargeable lithium batteries. *Angew. Chem. Int. Ed.* **2008,** *47* (16), 2930-2946.

4. BrucePeter, G.; FreunbergerStefan, A.; HardwickLaurence, J.; TarasconJean, M., Li-O_2 and Li-S Batteries with High Energy Storage. *Nat. Mater.* **2012,** *11* (02), 172-172.

5. Pan, H.; Hu, Y.-S.; Chen, L., Room-temperature stationary sodium-ion batteries for large-scale electric energy storage. *Energ. Environ. Sci.* **2013,** *6* (8), 2338-2360.

6. Choi, N.-S.; Chen, Z.; Freunberger, S. A.; Ji, X.; Sun, Y.-K.; Amine, K.; Yushin, G.; Nazar, L. F.; Cho, J.; Bruce, P. G., Challenges Facing Lithium Batteries and Electrical Double-Layer Capacitors. *Angew. Chem. Int. Ed.* **2012,** *51* (40), 9994-10024.

7. Das, S. K.; Lau, S.; Archer, L. A., Sodium-oxygen batteries: a new class of metal-air batteries. *J. Mater. Chem. A* **2014,** *2* (32), 12623-12629.

8. Liu, B.; Luo, T.; Mu, G.; Wang, X.; Chen, D.; Shen, G., Rechargeable Mg-Ion Batteries Based on WSe_2 Nanowire Cathodes. *ACS Nano* **2013,** *7* (9), 8051-8058.

9. Nagaura, T.; Tozawa, K., Lithium ion rechargeable battery. *Prog. Batteries Solar Cells* **1990,** *9*, 209-217.

10. Goodenough, J. B.; Park, K.-S., The Li-Ion Rechargeable Battery: A Perspective. *J. Am. Chem. Soc.* **2013,** *135* (4), 1167-1176.

11. Nozu, R.; Nakamura, M.; Banno, K.; Maruo, T.; Sato, T., Studying a Phenomenon during Overcharge of a Lithium-Ion Battery with Methacrylate Additives for the Gel Electrolyte. *J Electrochem Soc* **2006,** *153* (6), A1031-A1037.

12. Tarascon, J. M.; Armand, M., Issues and challenges facing rechargeable lithium batteries. *Nature* **2001,** *414* (6861), 359-367.

13. Manthiram, A.; Choi, J., Chemical and structural instabilities of lithium ion battery cathodes. *J Power Sources* **2006,** *159* (1), 249-253.

14. Xu, B.; Qian, D.; Wang, Z.; Meng, Y. S., Recent progress in cathode materials research for advanced lithium ion batteries. *Mater. Sci. Eng. R-Rep.* **2012,** *73* (5–6), 51-65.

15. Morgan, D.; Van der Ven, A.; Ceder, G., Li Conductivity in $Li_x MPO_4$ $(M = Mn , Fe , Co , Ni)$ Olivine Materials. *Electrochem. Solid St.* **2004,** *7* (2), A30-A32.

16. Fisher, C. A. J.; Hart Prieto, V. M.; Islam, M. S., Lithium Battery Materials $LiMPO_4$ (M = Mn, Fe, Co, and Ni): Insights into Defect Association, Transport Mechanisms, and Doping Behavior. *Chem. Mater.* **2008,** *20* (18), 5907-5915.

17. Kim, J. H.; Myung, S. T.; Yoon, C. S.; Kang, S. G.; Sun, Y. K., Comparative Study of $LiNi_{0.5}Mn_{1.5}O_{4-\delta}$ and $LiNi_{0.5}Mn_{1.5}O_4$ Cathodes Having Two Crystallographic Structures: Fd$\bar{3}$m and P4332. *Chem. Mater.* **2004,** *16* (5), 906-914.

18. Winter, M.; Besenhard, J. O.; Spahr, M. E.; Novák, P., Insertion Electrode Materials for Rechargeable Lithium Batteries. *Adv. Mater.* **1998,** *10* (10), 725-763.

19. Geim, A. K.; Novoselov, K. S., The rise of graphene. *Nat. Mater.* **2007,** *6* (3), 183-191.

20. Kubiak, P.; Fröschl, T.; Hüsing, N.; Hörmann, U.; Kaiser, U.; Schiller, R.; Weiss, C. K.; Landfester, K.; Wohlfahrt-Mehrens, M., TiO_2 Anatase Nanoparticle Networks: Synthesis, Structure, and Electrochemical Performance. *Small* **2011,** *7* (12), 1690-1696.

21. Yang, Y.; Zheng, G.; Cui, Y., Nanostructured sulfur cathodes. *Chem. Soc. Rev.* **2013,** *42* (7), 3018-3032.

22. Kumaresan, K.; Mikhaylik, Y.; White, R. E., A Mathematical Model for a Lithium–Sulfur Cell. *J. Electrochem. Soc.* **2008,** *155* (8), A576-A582.

23. Wang, L.; Zhang, T.; Yang, S.; Cheng, F.; Liang, J.; Chen, J., A quantum-chemical study on the discharge reaction mechanism of lithium-sulfur batteries. *J. Energy Chem.* **2013,** *22* (1), 72-77.

24. Fronczek, D. N.; Bessler, W. G., Insight into lithium–sulfur batteries: Elementary kinetic modeling and impedance simulation. *J. Power Sources* **2013,** *244* (0), 183-188.

25. Wang, D.-W.; Zeng, Q.; Zhou, G.; Yin, L.; Li, F.; Cheng, H.-M.; Gentle, I. R.; Lu, G. Q. M., Carbon-sulfur composites for Li-S batteries: status and prospects. *J. Mater. Chem. A* **2013,** *1* (33), 9382-9394.

26. Xiao, L.; Cao, Y.; Xiao, J.; Schwenzer, B.; Engelhard, M. H.; Saraf, L. V.; Nie, Z.; Exarhos, G. J.; Liu, J., A Soft Approach to Encapsulate Sulfur: Polyaniline Nanotubes for Lithium-Sulfur Batteries with Long Cycle Life. *Adv. Mater.* **2012,** *24* (9), 1176-1181.

27. Guo, J.; Xu, Y.; Wang, C., Sulfur-Impregnated Disordered Carbon Nanotubes Cathode for Lithium–Sulfur Batteries. *Nano Lett.* **2011,** *11* (10), 4288-4294.

28. Li, G.-C.; Li, G.-R.; Ye, S.-H.; Gao, X.-P., A Polyaniline-Coated Sulfur/Carbon Composite with an Enhanced High-Rate Capability as a Cathode Material for Lithium/Sulfur Batteries. *Adv. Energy Mater.* **2012,** *2* (10), 1238-1245.

29. Wang, B.; Li, K.; Su, D.; Ahn, H.; Wang, G., Superior Electrochemical Performance of Sulfur/Graphene Nanocomposite Material for High-Capacity Lithium–Sulfur Batteries. *Chem. Asian J.* **2012,** *7* (7), 1637-1643.

30. Zheng, G.; Yang, Y.; Cha, J. J.; Hong, S. S.; Cui, Y., Hollow Carbon Nanofiber-Encapsulated Sulfur Cathodes for High Specific Capacity Rechargeable Lithium Batteries. *Nano Lett.* **2011,** *11* (10), 4462-4467.

31. Jayaprakash, N.; Shen, J.; Moganty, S. S.; Corona, A.; Archer, L. A., Porous Hollow Carbon@Sulfur Composites for High-Power Lithium–Sulfur Batteries. *Angew. Chem. Int. Ed.* **2011,** *50* (26), 5904-5908.

32. Bucur, C. B.; Muldoon, J.; Lita, A.; Schlenoff, J. B.; Ghostine, R. A.; Dietz, S.; Allred, G., Ultrathin tunable ion conducting nanomembranes for encapsulation of sulfur cathodes. *Energ. Environ. Sci.* **2013,** *6* (11), 3286-3290.

33. Yin, L.; Wang, J.; Lin, F.; Yang, J.; Nuli, Y., Polyacrylonitrile/graphene composite as a precursor to a sulfur-based cathode material for high-rate rechargeable Li-S batteries. *Energ. Environ. Sci.* **2012,** *5* (5), 6966-6972.

34. Cao, Y.; Li, X.; Aksay, I. A.; Lemmon, J.; Nie, Z.; Yang, Z.; Liu, J., Sandwich-type functionalized graphene sheet-sulfur nanocomposite for rechargeable lithium batteries. *Phys. Chem. Chem. Phys.* **2011,** *13* (17), 7660-7665.

35. Li, W.; Zheng, G.; Yang, Y.; Seh, Z. W.; Liu, N.; Cui, Y., High-performance hollow sulfur nanostructured battery cathode through a scalable, room temperature, one-step, bottom-up approach. *Proc. Natl. Acad. Sci.* **2013,** *110* (18), 7148-7153.

36. Huang, J.-Q.; Liu, X.-F.; Zhang, Q.; Chen, C.-M.; Zhao, M.-Q.; Zhang, S.-M.; Zhu, W.; Qian, W.-Z.; Wei, F., Entrapment of sulfur in hierarchical porous graphene for lithium–

sulfur batteries with high rate performance from −40 to 60 °C. *Nano Energy* **2013,** *2* (2), 314-321.

37. Morozov, S. V.; Novoselov, K. S.; Katsnelson, M. I.; Schedin, F.; Ponomarenko, L. A.; Jiang, D.; Geim, A. K., Strong Suppression of Weak Localization in Graphene. *Physical Review Letters* **2006,** *97* (1).

38. Wu, F.; Chen, J.; Li, L.; Zhao, T.; Liu, Z.; Chen, R., Polyethylene-Glycol-Doped Polypyrrole Increases the Rate Performance of the Cathode in Lithium–Sulfur Batteries. *ChemSusChem* **2013,** *6* (8), 1438-1444.

39. Li, K.; Wang, B.; Su, D.; Park, J.; Ahn, H.; Wang, G., Enhance electrochemical performance of lithium sulfur battery through a solution-based processing technique. *J Power Sources* **2012,** *202* (0), 389-393.

40. Xiao, L.; Cao, Y.; Xiao, J.; Schwenzer, B.; Engelhard, M. H.; Saraf, L. V.; Nie, Z.; Exarhos, G. J.; Liu, J., Molecular structures of polymer/sulfur composites for lithium-sulfur batteries with long cycle life. *J. Mater. Chem. A* **2013,** *1* (33), 9517-9526.

41. Song, M.-K.; Zhang, Y.; Cairns, E. J., A Long-Life, High-Rate Lithium/Sulfur Cell: A Multifaceted Approach to Enhancing Cell Performance. *Nano Lett.* **2013,** *13* (12), 5891-5899.

42. Zhang, C.; Wu, H. B.; Yuan, C.; Guo, Z.; Lou, X. W., Confining Sulfur in Double-Shelled Hollow Carbon Spheres for Lithium–Sulfur Batteries. *Angew. Chem. Int. Ed.* **2012,** *51* (38), 9592-9595.

43. Zhang, K.; Zhao, Q.; Tao, Z.; Chen, J., Composite of sulfur impregnated in porous hollow carbon spheres as the cathode of Li-S batteries with high performance. *Nano Res.* **2013,** *6* (1), 38-46.

44. Zhang, B.; Qin, X.; Li, G. R.; Gao, X. P., Enhancement of long stability of sulfur cathode by encapsulating sulfur into micropores of carbon spheres. *Energ. Environ. Sci.* **2010,** *3* (10), 1531-1537.

45. Su, Y.-S.; Manthiram, A., Lithium–sulphur batteries with a microporous carbon paper as a bifunctional interlayer. *Nat. Commun.* **2012,** *3*, 1166.

46. Chen, R.; Zhao, T.; Lu, J.; Wu, F.; Li, L.; Chen, J.; Tan, G.; Ye, Y.; Amine, K., Graphene-Based Three-Dimensional Hierarchical Sandwich-type Architecture for High-Performance Li/S Batteries. *Nano Lett.* **2013,** *13* (10), 4642-4649.

47. Zu, C.; Manthiram, A., Hydroxylated Graphene–Sulfur Nanocomposites for High-Rate Lithium–Sulfur Batteries. *Adv. Energy Mater.* **2013,** *3* (8), 1008-1012.

48. Snyman, I.; Beenakker, C., Ballistic transmission through a graphene bilayer. *Physical Review B* **2007,** *75* (4).

49. Malini, R.; Uma, U.; Sheela, T.; Ganesan, M.; Renganathan, N. G., Conversion reactions: a new pathway to realise energy in lithium-ion battery-review. *Ionics* **2009,** *15* (3), 301-307.

50. Dorfler, S.; Hagen, M.; Althues, H.; Tubke, J.; Kaskel, S.; Hoffmann, M. J., High capacity vertical aligned carbon nanotube/sulfur composite cathodes for lithium-sulfur batteries. *Chem. Commun.* **2012,** *48* (34), 4097-4099.

51. Moon, S.; Jung, Y. H.; Jung, W. K.; Jung, D. S.; Choi, J. W.; Kim, D. K., Encapsulated Monoclinic Sulfur for Stable Cycling of Li–S Rechargeable Batteries. *Adv. Mater.* **2013,** *25* (45), 6547-6553.

52. Zhang, Y.; Jiang, Z.; Small, J. P.; Purewal, M. S.; Tan, Y. W.; Fazlollahi, M.; Chudow, J. D.; Jaszczak, J. A.; Stormer, H. L.; Kim, P., Landau-Level Splitting in Graphene in High Magnetic Fields. *Physical Review Letters* **2006,** *96* (13).

53. Vozmediano, M. A. H.; López-Sancho, M. P.; Stauber, T.; Guinea, F., Local defects and ferromagnetism in graphene layers. *Physical Review B* **2005,** *72* (15).

54. Ji, X.; Lee, K. T.; Nazar, L. F., A highly ordered nanostructured carbon-sulphur cathode for lithium-sulphur batteries. *Nat. Mater.* **2009,** *8* (6), 500-506.

55. Sun, F.; Wang, J.; Chen, H.; Qiao, W.; Ling, L.; Long, D., Bottom-Up Catalytic Approach towards Nitrogen-Enriched Mesoporous Carbons/Sulfur Composites for Superior Li-S Cathodes. *Sci. Rep.* **2013,** *3*, 2823-2831.

56. Tan, Y. W.; Zhang, Y.; Bolotin, K.; Zhao, Y.; Adam, S.; Hwang, E. H.; Das Sarma, S.; Stormer, H. L.; Kim, P., Measurement of Scattering Rate and Minimum Conductivity in Graphene. *Physical Review Letters* **2007,** *99* (24).

57. Xu, G.; Ding, B.; Nie, P.; Shen, L.; Wang, J.; Zhang, X., Porous Nitrogen-Doped Carbon Nanotubes Derived from Tubular Polypyrrole for Energy-Storage Applications. *Chem. Eur. J.* **2013,** *19* (37), 12306-12312.

58. Li, W.; Zhang, Q.; Zheng, G.; Seh, Z. W.; Yao, H.; Cui, Y., Understanding the Role of Different Conductive Polymers in Improving the Nanostructured Sulfur Cathode Performance. *Nano Lett.* **2013,** *13* (11), 5534-5540.

59. Esquinazi, P.; Spemann, D.; Höhne, R.; Setzer, A.; Han, K. H.; Butz, T., Induced Magnetic Ordering by Proton Irradiation in Graphite. *Physical Review Letters* **2003,** *91* (22).

60. Demir-Cakan, R.; Morcrette, M.; Nouar, F.; Davoisne, C.; Devic, T.; Gonbeau, D.; Dominko, R.; Serre, C.; Férey, G.; Tarascon, J.-M., Cathode Composites for Li–S Batteries via the Use of Oxygenated Porous Architectures. *J. Am. Chem. Soc.* **2011,** *133* (40), 16154-16160.

61. Nilsson, J.; Castro Neto, A.; Peres, N.; Guinea, F., Electron-electron interactions and the phase diagram of a graphene bilayer. *Physical Review B* **2006,** *73* (21).

62. Yang, Y.; Yu, G.; Cha, J. J.; Wu, H.; Vosgueritchian, M.; Yao, Y.; Bao, Z.; Cui, Y., Improving the Performance of Lithium–Sulfur Batteries by Conductive Polymer Coating. *ACS Nano* **2011,** *5* (11), 9187-9193.

63. Zhou, W.; Chen, H.; Yu, Y.; Wang, D.; Cui, Z.; DiSalvo, F. J.; Abruña, H. D., Amylopectin Wrapped Graphene Oxide/Sulfur for Improved Cyclability of Lithium–Sulfur Battery. *ACS Nano* **2013,** *7* (10), 8801-8808.

64. He, G.; Evers, S.; Liang, X.; Cuisinier, M.; Garsuch, A.; Nazar, L. F., Tailoring Porosity in Carbon Nanospheres for Lithium–Sulfur Battery Cathodes. *ACS Nano* **2013,** *7* (12), 10920-10930.

65. Huang, C.; Xiao, J.; Shao, Y.; Zheng, J.; Bennett, W. D.; Lu, D.; Saraf, L. V.; Engelhard, M.; Ji, L.; Zhang, J.; Li, X.; Graff, G. L.; Liu, J., Manipulating surface reactions in lithium–sulphur batteries using hybrid anode structures. *Nat. Commun.* **2014,** *5*, 3015-3022.

66. Su, Y.-S.; Fu, Y.; Cochell, T.; Manthiram, A., A strategic approach to recharging lithium-sulphur batteries for long cycle life. *Nat. Commun.* **2013,** *4*, 2985.

67. Wu, F.; Lee, J. T.; Magasinski, A.; Kim, H.; Yushin, G., Solution-Based Processing of Graphene–Li_2S Composite Cathodes for Lithium-Ion and Lithium–Sulfur Batteries. *Part. Part. Syst. Char.* **2014,** *31* (6), 639-644.

68. Cai, K.; Song, M.-K.; Cairns, E. J.; Zhang, Y., Nanostructured Li_2S–C Composites as Cathode Material for High-Energy Lithium/Sulfur Batteries. *Nano Lett.* **2012,** *12* (12), 6474-6479.

69. Fu, Y.; Su, Y.-S.; Manthiram, A., Li_2S-Carbon Sandwiched Electrodes with Superior Performance for Lithium-Sulfur Batteries. *Adv. Energy Mater.* **2014,** *4* (1), 1300655.

70. Nan, C.; Lin, Z.; Liao, H.; Song, M.-K.; Li, Y.; Cairns, E. J., Durable Carbon-Coated Li_2S Core–Shell Spheres for High Performance Lithium/Sulfur Cells. *J. Am. Chem. Soc.* **2014,** *136* (12), 4659-4663.

71. Hildebrandt, G., The Discovery of the Diffraction of X-rays in Crystals — A Historical Review. *Cryst. Res. Technol.* **1993,** *28* (6), 747-766.

72. Brunauer, S.; Emmett, P. H.; Teller, E., Adsorption of Gases in Multimolecular Layers. *J. Am. Chem. Soc.* **1938,** *60* (2), 309-319.

73. Cui, L. F.; Ruffo, R.; Chan, C. K.; Peng, H. L.; Cui, Y., Crystalline-Amorphous Core-Shell Silicon Nanowires for High Capacity and High Current Battery Electrodes. *Nano Lett.* **2009,** *9* (1), 491-495.

74. Lucas, I. T.; Pollak, E.; Kostecki, R., In situ AFM studies of SEI formation at a Sn electrode. *Electrochem Commun* **2009,** *11* (11), 2157-2160.

75. Wu, F. D.; Wu, M. H.; Wang, Y., Antimony-doped tin oxide nanotubes for high capacity lithium storage. *Electrochem Commun* **2011,** *13* (5), 433-436.

76. Wang, Y.; Lee, J. Y.; Chen, B. H., Microemulsion Syntheses of Sn and SnO_2-Graphite Nanocomposite Anodes for Li-ion Batteries. *J Electrochem Soc* **2004,** *151* (4), A563-A570.

77. Tao, F. F.; Gao, C. L.; Wen, Z. H.; Wang, Q.; Li, J. H.; Xu, Z., Cobalt oxide hollow microspheres with micro- and nano-scale composite structure: Fabrication and electrochemical performance. *J Solid State Chem* **2009,** *182* (5), 1055-1060.

78. Cheng, H.; Lu, Z. G.; Deng, J. Q.; Chung, C. Y.; Zhang, K.; Li, Y. Y., A facile method to improve the high rate capability of Co_3O_4 nanowire array electrodes. *Nano Res.* **2010,** *3* (12), 895-901.

79. Kim, D. Y.; Ahn, H. J.; Kim, J. S.; Kim, I. P.; Kweon, J. H.; Nam, T. H.; Kim, K. W.; Ahn, J. H.; Hong, S. H., The Electrochemical Properties of Nano-Sized Cobalt Powder as an Anode Material for Lithium Batteries. *Electron Mater Lett* **2009,** *5* (4), 183-186.

80. Do, J. S.; Dai, R. F., Cobalt oxide thin film prepared by an electrochemical route for Li-ion battery. *J Power Sources* **2009,** *189* (1), 204-210.

81. Huang, X. H.; Tu, J. P.; Xia, X. H.; Wang, X. L.; Xiang, J. Y.; Zhang, L.; Zhou, Y., Morphology effect on the electrochemical performance of NiO films as anodes for lithium ion batteries. *J Power Sources* **2009,** *188* (2), 588-591.

82. Wang, Y.; Lee, J. Y.; Deivaraj, T. C., Tin nanoparticle loaded graphite anodes for Li-ion battery applications. *J Electrochem Soc* **2004,** *151* (11), A1804-A1809.

83. Wang, Y.; Lee, J. Y., Microwave-assisted synthesis of SnO_2-graphite nanocomposites for Li-ion battery applications. *J Power Sources* **2005,** *144* (1), 220-225.

84. Wang, Y.; Lee, J. Y., Preparation of SnO_2-graphite nanocomposite anodes by urea-mediated hydrolysis. *Electrochem. Commun.* **2003,** *5* (4), 292-296.

85. Han, S. J.; Jang, B. C.; Kim, T.; Oh, S. M.; Hyeon, T., Simple synthesis of hollow tin dioxide microspheres and their application to lithium-ion battery anodes. *Adv. Funct. Mater.* **2005,** *15* (11), 1845-1850.

86. Paek, S.-M.; Yoo, E.; Honma, I., Enhanced Cyclic Performance and Lithium Storage Capacity of SnO_2/Graphene Nanoporous Electrodes with Three-Dimensionally Delaminated Flexible Structure. *Nano Lett.* **2009,** *9* (1), 72-75.

87. Hassoun, J.; Derrien, G.; Panero, S.; Scrosati, B., A nanostructured Sn-C composite lithium battery electrode with unique stability and high electrochemical performance. *Adv. Mater.* **2008,** *20* (16), 3169-3175.

88. Derrien, G.; Hassoun, J.; Panero, S.; Scrosati, B., Nanostructured Sn-C composite as an advanced anode material in high-performance lithium-ion batteries. *Adv. Mater.* **2007,** *19* (17), 2336-2340.

89. Zhang, H.-X.; Feng, C.; Zhai, Y.-C.; Jiang, K.-L.; Li, Q.-Q.; Fan, S.-S., Cross-Stacked Carbon Nanotube Sheets Uniformly Loaded with SnO_2 Nanoparticles: A Novel Binder-Free and High-Capacity Anode Material for Lithium-Ion Batteries. *Adv. Mater.* **2009,** *21* (22), 2299-2304.

90. Wu, F. D.; Wang, Y., Self-assembled Echinus-like Nanostructures of Mesoporous CoO Nanorod@CNT for Lithium-ion Batteries. *J. Mater. Chem.* **2011,** *21* (18), 6636-6641.

91. Wu, F.; Chen, J. Z.; Chen, R. J.; Wu, S. X.; Li, L.; Chen, S.; Zhao, T., Sulfur/Polythiophene with a Core/Shell Structure: Synthesis and Electrochemical Properties of the Cathode for Rechargeable Lithium Batteries. *J. Phys. Chem. C* **2011,** *115* (13), 6057-6063.

92. Basch, A.; Albering, J. H., Preparation and characterization of core-shell battery materials for Li-ion batteries manufactured by substrate induced coagulation. *J Power Sources* **2011,** *196* (6), 3290-3295.

93. Chen, Z. X.; Cao, Y. L.; Qian, J. F.; Ai, X. P.; Yang, H. X., Facile synthesis and stable lithium storage performances of Sn- sandwiched nanoparticles as a high capacity anode material for rechargeable Li batteries. *J. Mater. Chem.* **2010,** *20* (34), 7266-7271.

94. Chen, S.; Chen, P.; Wu, M.; Pan, D.; Wang, Y., Graphene supported Sn–Sb@carbon core-shell particles as a superior anode for lithium ion batteries. *Electrochem Commun* **2010,** *12* (10), 1302-1306.

95. Yang, Z. L.; Cao, C.; Liu, F. F.; Chen, D. R.; Jiao, X. L., Core-shell $Li(Ni_{1/3}Co_{1/3}Mn_{1/3})O_2/Li(Ni_{1/2}Mn_{1/2})O_2$ fibers: Synthesis, characterization and electrochemical properties. *Solid State Ionics* **2010,** *181* (15-16), 678-683.

96. Pirkle, A.; Chan, J.; Venugopal, A.; Hinojos, D.; Magnuson, C. W.; McDonnell, S.; Colombo, L.; Vogel, E. M.; Ruoff, R. S.; Wallace, R. M., The effect of chemical residues on the physical and electrical properties of chemical vapor deposited graphene transferred to SiO_2. *Appl. Phys. Lett.* **2011,** *99* (12), 122108-122111.

97. Alicea, J.; Fisher, M. P. A., Graphene integer quantum Hall effect in the ferromagnetic and paramagnetic regimes. *Phys. Rev. B* **2006,** *74* (7), 075422-075435.

98. Elias, D. C.; Nair, R. R.; Mohiuddin, T. M. G.; Morozov, S. V.; Blake, P.; Halsall, M. P.; Ferrari, A. C.; Boukhvalov, D. W.; Katsnelson, M. I.; Geim, A. K.; Novoselov, K. S., Control of Graphene's Properties by Reversible Hydrogenation: Evidence for Graphane. *Science* **2009,** *323* (5914), 610-613.

99. Wang, G.; Kim, Y.; Choe, M.; Kim, T. W.; Lee, T., A New Approach for Molecular Electronic Junctions with a Multilayer Graphene Electrode. *Adv. Mater.* **2011,** *23* (6), 755-760.

100. Sun, B.; Wang, B.; Su, D. W.; Xiao, L. D.; Ahn, H.; Wang, G. X., Graphene nanosheets as cathode catalysts for lithium-air batteries with an enhanced electrochemical performance. *Carbon* **2012,** *50* (2), 727-733.

101. Abanin, D. A.; Morozov, S. V.; Ponomarenko, L. A.; Gorbachev, R. V.; Mayorov, A. S.; Katsnelson, M. I.; Watanabe, K.; Taniguchi, T.; Novoselov, K. S.; Levitov, L. S.; Geim, A. K., Giant Nonlocality Near the Dirac Point in Graphene. *Science* **2011,** *332* (6027), 328-330.

102. Zhang, Y.; Tan, Y.-W.; Stormer, H. L.; Kim, P., Experimental observation of the quantum Hall effect and Berry's phase in graphene. *Nature* **2005,** *438* (7065), 201-204.

103. Xu, K.; Cao, P.; Heath, J. R., Graphene Visualizes the First Water Adlayers on Mica at Ambient Conditions. *Science* **2010,** *329* (5996), 1188-1191.

104. Zhang, M.; Lei, D.; Yin, X.; Chen, L.; Li, Q.; Wang, Y.; Wang, T., Magnetite/graphene composites: microwave irradiation synthesis and enhanced cycling and rate performances for lithium ion batteries. *J. Mater. Chem.* **2010,** *20* (26), 5538.

105. Wang, G. X.; Wang, B.; Wang, X. L.; Park, J.; Dou, S. X.; Ahn, H.; Kim, K., Sn/graphene nanocomposite with 3D architecture for enhanced reversible lithium storage in lithium ion batteries. *J. Mater. Chem.* **2009,** *19* (44), 8378-8384.

106. Ji, L. W.; Tan, Z. K.; Kuykendall, T.; An, E. J.; Fu, Y. B.; Battaglia, V.; Zhang, Y. G., Multilayer nanoassembly of Sn-nanopillar arrays sandwiched between graphene layers for high-capacity lithium storage. *Energ. Environ. Sci.* **2011,** *4* (9), 3611-3616.

107. Li, Y. M.; Lv, X. J.; Lu, J.; Li, J. H., Preparation of SnO_2-Nanocrystal/Graphene-Nanosheets Composites and Their Lithium Storage Ability. *J. Phys. Chem. C* **2010,** *114* (49), 21770-21774.

108. Kim, H.; Kim, S. W.; Park, Y. U.; Gwon, H.; Seo, D. H.; Kim, Y.; Kang, K., SnO_2/Graphene Composite with High Lithium Storage Capability for Lithium Rechargeable Batteries. *Nano Res.* **2010,** *3* (11), 813-821.

109. Harrison, K. L.; Manthiram, A., Microwave-Assisted Solvothermal Synthesis and Characterization of Metastable $LiFe_{1-x}(VO)_xPO_4$ Cathodes. *Inorg Chem* **2011,** *50* (8), 3613-3620.

110. Yoon, S.; Manthiram, A., Microwave-hydrothermal synthesis of $W_{0.4}Mo_{0.6}O_3$ and carbon-decorated WO_x-MoO_2 nanorod anodes for lithium ion batteries. *J. Mater. Chem.* **2011,** *21* (12), 4082-4085.

111. Zhong, C.; Wang, J. Z.; Chen, Z. X.; Liu, H. K., SnO_2-Graphene Composite Synthesized via an Ultrafast and Environmentally Friendly Microwave Autoclave Method and Its Use as a Superior Anode for Lithium-Ion Batteries. *J. Phys. Chem. C* **2011,** *115* (50), 25115-25120.

112. Zhu, X.; Zhu, Y.; Murali, S.; Stoller, M. D.; Ruoff, R. S., Reduced graphene oxide/tin oxide composite as an enhanced anode material for lithium ion batteries prepared by homogenous coprecipitation. *J Power Sources* **2011,** *196* (15), 6473-6477.

113. Chen, S. Q.; Wang, Y., Microwave-assisted Synthesis of a Co_3O_4–Graphene Sheet-on-sheet Nanocomposite as a Superior Anode Material for Li-ion Batteries. *J. Mater. Chem.* **2010,** *20* (43), 9735-9739.

114. Hummers, W. S.; Offeman, R. E., Preparation of Graphitic Oxide. *J. Am. Chem. Soc.* **1958,** *80* (6), 1339-1339.

115. Wang, X. Y.; Zhou, X. F.; Yao, K.; Zhang, J. G.; Liu, Z. P., A SnO_2/graphene composite as a high stability electrode for lithium ion batteries. *Carbon* **2011,** *49* (1), 133-139.

116. Liang, S. Z.; Zhu, X. F.; Lian, P. C.; Yang, W. S.; Wang, H. H., Superior cycle performance of Sn@C/graphene nanocomposite as an anode material for lithium-ion batteries. *J Solid State Chem* **2011,** *184* (6), 1400-1404.

117. Zhang, M.; Lei, D.; Du, Z. F.; Yin, X. M.; Chen, L. B.; Li, Q. H.; Wang, Y. G.; Wang, T. H., Fast synthesis of SnO_2/graphene composites by reducing graphene oxide with stannous ions. *J. Mater. Chem.* **2011,** *21* (6), 1673-1676.

118. Murugan, A. V.; Muraliganth, T.; Manthiram, A., Rapid, Facile Microwave-Solvothermal Synthesis of Graphene Nanosheets and Their Polyaniline Nanocomposites for Energy Strorage. *Chem. Mater.* **2009,** *21* (21), 5004-5006.

119. Guo, B. K.; Shu, J.; Tang, K.; Bai, Y.; Wang, Z. X.; Chen, L. Q., Nano-Sn/hard carbon composite anode material with high-initial coulombic efficiency. *J Power Sources* **2008,** *177* (1), 205-210.

120. Li, Y. M.; Lv, X. J.; Lu, J.; Li, J. H., Preparation of SnO_2-Nanocrystal/Graphene-Nanosheets Composites and Their Lithium Storage Ability. *J. Phys. Chem. C* **2010,** *114* (49), 21770-21774.

121. Iijima, S., Helical Microtubules of Graphitic Carbon. *Nature* **1991,** *354* (6348), 56-58.

122. Sun, Y. P.; Huang, W. J.; Lin, Y.; Fu, K. F.; Kitaygorodskiy, A.; Riddle, L. A.; Yu, Y. J.; Carroll, D. L., Soluble dendron-functionalized carbon nanotubes: Preparation, characterization, and properties. *Chem. Mater.* **2001,** *13* (9), 2864-2869.

123. Hudson, J. L.; Casavant, M. J.; Tour, J. M., Water-soluble, exfoliated, nonroping single-wall carbon nanotubes. *J. Am. Chem. Soc.* **2004,** *126* (36), 11158-11159.

124. Zu, S. Z.; Sun, X. X.; Zhou, D.; Han, B. H., Supramolecular modification of single-walled carbon nanotubes with a water-soluble triptycene derivative. *Carbon* **2011,** *49* (15), 5339-5347.

125. Matsuzawa, Y.; Kato, H.; Ohyama, H.; Nishide, D.; Kataura, H.; Yoshida, M., Photoinduced Dispersibility Tuning of Carbon Nanotubes by a Water-Soluble Stilbene as a Dispersant. *Adv. Mater.* **2011,** *23* (34), 3922-5.

126. Baughman, R. H., Carbon Nanotubes--the Route Toward Applications. *Science* **2002,** *297* (5582), 787-792.

127. Deng, X. Y.; Wu, F.; Liu, Z.; Luo, M.; Li, L.; Ni, Q. S.; Jiao, Z.; Wu, M. H.; Liu, Y. F., The splenic toxicity of water soluble multi-walled carbon nanotubes in mice. *Carbon* **2009,** *47* (6), 1421-1428.

128. Amorim, R. G.; Fazzio, A.; Antonelli, A.; Novaes, F. D.; da Silva, A. J. R., Divacancies in Graphene and Carbon Nanotubes. *Nano Lett.* **2007,** *7* (8), 2459-2462.

129. Zhi, L. J.; Wu, J. S.; Li, J. X.; Kolb, U.; Mullen, K., Carbonization of disclike molecules in porous alumina membranes: Toward carbon nanotubes with controlled graphene-layer orientation. *Angew. Chem. Int. Ed.* **2005,** *44* (14), 2120-2123.

130. Chen, Z. Y.; Kobashi, K.; Rauwald, U.; Booker, R.; Fan, H.; Hwang, W. F.; Tour, J. M., Soluble ultra-short single-walled carbon nanotubes. *J. Am. Chem. Soc.* **2006,** *128* (32), 10568-10571.

131. Buh, G. H.; Hwang, J. H.; Jeon, E. K.; So, H. M.; Lee, J. O.; Kong, K. J.; Chang, H., On-Chip Electrical Breakdown of Metallic Nanotubes for Mass Fabrication of Carbon-Nanotube-Based Electronic Devices. *Ieee T Nanotechnol* **2008,** *7* (5), 624-627.

132. Simon, F.; Peterlik, H.; Pfeiffer, R.; Bernardi, J.; Kuzmany, H., Fullerene release from the inside of carbon nanotubes: A possible route toward drug delivery. *Chem Phys Lett* **2007,** *445* (46), 288-292.

133. Chaban, V. V.; Prezhdo, O. V., Water Boiling Inside Carbon Nanotubes: Toward Efficient Drug Release. *ACS Nano* **2011,** *5* (7), 5647-5655.

134. Sankaran, M.; Viswanathan, B., The role of heteroatoms in carbon nanotubes for hydrogen storage. *Carbon* **2006,** *44* (13), 2816-2821.

135. Assfour, B.; Leoni, S.; Seifert, G.; Baburin, I. A., Packings of Carbon Nanotubes - New Materials for Hydrogen Storage. *Adv. Mater.* **2011,** *23* (10), 1237-41.

136. Zhang, D. W.; Zhao, Y. B.; Goodenough, J. B.; Lu, Y. H.; Chen, C. H.; Wang, L.; Liu, J. W., Exfoliation from carbon nanotubes versus tube size on lithium insertion. *Electrochem Commun* **2011,** *13* (2), 125-128.

137. Tung, V. C.; Chen, L. M.; Allen, M. J.; Wassei, J. K.; Nelson, K.; Kaner, R. B.; Yang, Y., Low-Temperature Solution Processing of Graphene-Carbon Nanotube Hybrid Materials for High-Performance Transparent Conductors. *Nano Lett.* **2009,** *9* (5), 1949-1955.

138. Gaspar, H.; Pereira, C.; Rebelo, S. L. H.; Pereira, M. F. R.; Figueiredo, J. L.; Freire, C., Understanding the silylation reaction of multi-walled carbon nanotubes. *Carbon* **2011,** *49* (11), 3441-3453.

139. Ausman, K. D.; Piner, R.; Lourie, O.; Ruoff, R. S.; Korobov, M., Organic solvent dispersions of single-walled carbon nanotubes: Toward solutions of pristine nanotubes. *J. Phys. Chem. B* **2000,** *104* (38), 8911-8915.

140. Torrens, F., Calculations of organic-solvent dispersions of single-wall carbon nanotubes. *Int J Quantum Chem* **2006,** *106* (3), 712-718.

141. Sreekumar, T. V.; Liu, T.; Kumar, S.; Ericson, L. M.; Hauge, R. H.; Smalley, R. E., Single-wall carbon nanotube films. *Chem. Mater.* **2003,** *15* (1), 175-178.

142. Fischer, J. E.; Zhou, W.; Vavro, J.; Llaguno, M. C.; Guthy, C.; Haggenmueller, R.; Casavant, M. J.; Walters, D. E.; Smalley, R. E., Magnetically aligned single wall carbon nanotube films: Preferred orientation and anisotropic transport properties. *J Appl Phys* **2003,** *93* (4), 2157-2163.

143. Wassei, J. K.; Tung, V. C.; Jonas, S. J.; Cha, K.; Dunn, B. S.; Yang, Y.; Kaner, R. B., Stenciling Graphene, Carbon Nanotubes, and Fullerenes Using Elastomeric Lift-Off Membranes. *Adv. Mater.* **2010,** *22* (8), 897-901.

144. Aizawa, M.; Shaffer, M. S. P., Silylation of multi-walled carbon nanotubes. *Chem Phys Lett* **2003,** *368* (1-2), 121-124.

145. Hummers, W. S.; Offeman, R. E., Preparation of Graphitic Oxide. *J Am Chem Soc* **1958,** *80* (6), 1339-1339.

146. Geim, A. K., Graphene: Status and Prospects. *Science* **2009,** *324* (5934), 1530-1534.

147. Novoselov, K. S.; Geim, A. K.; Morozov, S. V.; Jiang, D.; Zhang, Y.; Dubonos, S. V.; Grigorieva, I. V.; Firsov, A. A., Electric field effect in atomically thin carbon films. *Science* **2004,** *306* (5696), 666-669.

148. Novoselov, K. S.; Jiang, Z.; Zhang, Y.; Morozov, S. V.; Stormer, H. L.; Zeitler, U.; Maan, J. C.; Boebinger, G. S.; Kim, P.; Geim, A. K., Room-temperature quantum hall effect in graphene. *Science* **2007,** *315* (5817), 1379-1379.

149. Nair, R. R.; Blake, P.; Grigorenko, A. N.; Novoselov, K. S.; Booth, T. J.; Stauber, T.; Peres, N. M. R.; Geim, A. K., Fine structure constant defines visual transparency of graphene. *Science* **2008,** *320* (5881), 1308-1308.

150. Mayorov, A. S.; Elias, D. C.; Mucha-Kruczynski, M.; Gorbachev, R. V.; Tudorovskiy, T.; Zhukov, A.; Morozov, S. V.; Katsnelson, M. I.; Fal'ko, V. I.; Geim, A. K.; Novoselov, K. S., Interaction-Driven Spectrum Reconstruction in Bilayer Graphene. *Science* **2011,** *333* (6044), 860-863.

151. Zou, Y.; Kan, J.; Wang, Y., Fe_2O_3-Graphene Rice-on-Sheet Nanocomposite for High and Fast Lithium Ion Storage. *J. Phys. Chem. C* **2011,** *115* (42), 20747–20753.

152. Fan, Z. J.; Yan, J.; Zhi, L. J.; Zhang, Q.; Wei, T.; Feng, J.; Zhang, M. L.; Qian, W. Z.; Wei, F., A Three-Dimensional Carbon Nanotube/Graphene Sandwich and Its Application as Electrode in Supercapacitors. *Adv. Mater.* **2010,** *22* (33), 3723-3728.

153. Rolison, D. R.; Long, R. W.; Lytle, J. C.; Fischer, A. E.; Rhodes, C. P.; McEvoy, T. M.; Bourga, M. E.; Lubers, A. M., Multifunctional 3D nanoarchitectures for energy storage and conversion. *Chem. Soc. Rev.* **2009,** *38* (1), 226-252.

154. Kim, U. J.; Lee, I. L. H.; Bae, J. J.; Lee, S.; Han, G. H.; Chae, S. J.; Güneş, F.; Choi, J. H.; Baik, C. W.; Kim, S. I.; Kim, J. M.; Lee, Y. H., Graphene/Carbon Nanotube Hybrid-Based Transparent 2D Optical Array. *Adv. Mater.* **2011,** *23* (33), 3809-3814.

155. Xu, Z. X.; Gao, H. Y.; Guoxin, H., Solution-based synthesis and characterization of a silver nanoparticle-graphene hybrid film. *Carbon* **2011,** *49* (14), 4731-4738.

156. Wang, Y.; Wu, Y. P.; Huang, Y.; Zhang, F.; Yang, X.; Ma, Y. F.; Chen, Y. S., Preventing Graphene Sheets from Restacking for High-Capacitance Performance. *J. Phys. Chem. C* **2011,** *115* (46), 23192-23197.

157. Qiu, L.; Yang, X. W.; Gou, X. L.; Yang, W. R.; Ma, Z. F.; Wallace, G. G.; Li, D., Dispersing Carbon Nanotubes with Graphene Oxide in Water and Synergistic Effects between Graphene Derivatives. *Chem. Eur. J.* **2010,** *16* (35), 10653-10658.

158. Xu, Y. X.; Sheng, K. X.; Li, C.; Shi, G. Q., Self-Assembled Graphene Hydrogel via a One-Step Hydrothermal Process. *ACS Nano* **2010,** *4* (7), 4324-4330.

159. Li, Y. Q.; Yang, T. Y.; Yu, T.; Zheng, L. X.; Liao, K., Synergistic effect of hybrid carbon nantube-graphene oxide as a nanofiller in enhancing the mechanical properties of PVA composites. *J. Mater. Chem.* **2011,** *21* (29), 10844-10851.

160. Graf, D.; Molitor, F.; Ensslin, K.; Stampfer, C.; Jungen, A.; Hierold, C.; Wirtz, L., Spatially resolved raman spectroscopy of single- and few-layer graphene. *Nano Lett.* **2007,** *7* (2), 238-242.

161. Ferrari, A. C.; Meyer, J. C.; Scardaci, V.; Casiraghi, C.; Lazzeri, M.; Mauri, F.; Piscanec, S.; Jiang, D.; Novoselov, K. S.; Roth, S.; Geim, A. K., Raman spectrum of graphene and graphene layers. *Phys Rev Lett* **2006,** *97* (18), 187401-187404.

162. Ni, Z. H.; Wang, Y. Y.; Yu, T.; Shen, Z. X., Raman Spectroscopy and Imaging of Graphene. *Nano Res.* **2008,** *1* (4), 273-291.

163. Zdrojek, M.; Gebicki, W.; Jastrzebski, C.; Melin, T.; Huczko, A., Studies of multiwall carbon nanotubes using Raman spectroscopy and atomic force microscopy. *Sol St Phen* **2004,** *99*, 265-268.

164. Duesberg, G. S.; Loa, I.; Burghard, M.; Syassen, K.; Roth, S., Polarized Raman spectroscopy on isolated single-wall carbon nanotubes. *Phys Rev Lett* **2000,** *85* (25), 5436-5439.

165. Fan, Z.-J.; Yan, J.; Wei, T.; Ning, G.-Q.; Zhi, L.-J.; Liu, J.-C.; Cao, D.-X.; Wang, G.-L.; Wei, F., Nanographene-Constructed Carbon Nanofibers Grown on Graphene Sheets by Chemical Vapor Deposition: High-Performance Anode Materials for Lithium Ion Batteries. *ACS Nano* **2011,** *5* (4), 2787-2794.

166. Guo, P.; Song, H.; Chen, X., Electrochemical performance of graphene nanosheets as anode material for lithium-ion batteries. *Electrochem Commun* **2009,** *11* (6), 1320-1324.

167. Wu, Z.-S.; Ren, W.; Xu, L.; Li, F.; Cheng, H.-M., Doped Graphene Sheets As Anode Materials with Superhigh Rate and Large Capacity for Lithium Ion Batteries. *ACS Nano* **2011,** *5* (7), 5463-5471.

168. Armand, M.; Tarascon, J. M., Building better batteries. *Nature* **2008,** *451* (7179), 652-657.

169. Etacheri, V.; Marom, R.; Elazari, R.; Salitra, G.; Aurbach, D., Challenges in the development of advanced Li-ion batteries: a review. *Energ. Environ. Sci.* **2011,** *4* (9), 3243-3262.

170. Bruce, P. G.; Freunberger, S. A.; Hardwick, L. J.; Tarascon, J. M., Li-O_2 and Li-S batteries with high energy storage. *Nat. Mater.* **2012,** *11* (02), 172-172.

171. Girishkumar, G.; McCloskey, B.; Luntz, A. C.; Swanson, S.; Wilcke, W., Lithium−Air Battery: Promise and Challenges. *J. Phys. Chem. Lett.* **2010,** *1* (14), 2193-2203.

172. Song, M.-K.; Park, S.; Alamgir, F. M.; Cho, J.; Liu, M., Nanostructured electrodes for lithium-ion and lithium-air batteries: the latest developments, challenges, and perspectives. *Mater. Sci. Eng. R-Rep.* **2011,** *72* (11), 203-252.

173. Wang, G.; Zhang, L.; Zhang, J., A review of electrode materials for electrochemical supercapacitors. *Chem. Soc. Rev.* **2012,** *41* (2), 797-828.

174. Cavaliere, S.; Subianto, S.; Savych, I.; Jones, D. J.; Roziere, J., Electrospinning: designed architectures for energy conversion and storage devices. *Energ. Environ. Sci.* **2011,** *4* (12), 4761-4785.

175. Rakhi, R. B.; Chen, W.; Cha, D.; Alshareef, H. N., High performance supercapacitors using metal oxide anchored graphene nanosheet electrodes. *J. Mater. Chem.* **2011,** *21* (40), 16197-16204.

176. Shin, W. H.; Jeong, H. M.; Kim, B. G.; Kang, J. K.; Choi, J. W., Nitrogen-Doped Multiwall Carbon Nanotubes for Lithium Storage with Extremely High Capacity. *Nano Lett.* **2012,** *12* (5), 2283-2288.

177. Sivakkumar, S. R.; Pandolfo, A. G., Evaluation of lithium-ion capacitors assembled with pre-lithiated graphite anode and activated carbon cathode. *Electrochim Acta* **2012,** *65* (0), 280-287.

178. Park, M.-S.; Lim, Y.-G.; Kim, J.-H.; Kim, Y.-J.; Cho, J.; Kim, J.-S., A Novel Lithium-Doping Approach for an Advanced Lithium Ion Capacitor. *Adv. Energy Mater.* **2011,** *1* (6), 1002-1006.

179. Castro Neto, A. H.; Peres, N. M. R.; Novoselov, K. S.; Geim, A. K., The electronic properties of graphene. *Rev. Mod. Phys.* **2009,** *81* (1), 109-162.

180. Zhu, Y.; Murali, S.; Cai, W.; Li, X.; Suk, J. W.; Potts, J. R.; Ruoff, R. S., Graphene and Graphene Oxide: Synthesis, Properties, and Applications. *Adv. Mater.* **2010,** *22* (35), 3906-3924.

181. Li, X.; Geng, D.; Zhang, Y.; Meng, X.; Li, R.; Sun, X., Superior cycle stability of nitrogen-doped graphene nanosheets as anodes for lithium ion batteries. *Electrochem Commun* **2011,** *13* (8), 822-825.

182. Jin, C.; Suenaga, K.; Iijima, S., Direct evidence for lip-lip interactions in multi-walled carbon nanotubes. *Nano Res.* **2010,** *1* (5), 434-439.

183. Li, X.; Liu, J.; Zhang, Y.; Li, Y.; Liu, H.; Meng, X.; Yang, J.; Geng, D.; Wang, D.; Li, R.; Sun, X., High concentration nitrogen doped carbon nanotube anodes with superior Li^+ storage performance for lithium rechargeable battery application. *J Power Sources* **2012,** *197* (0), 238-245.

184. Li, X.; Yang, J.; Hu, Y.; Wang, J.; Li, Y.; Cai, M.; Li, R.; Sun, X., Novel approach toward a binder-free and current collector-free anode configuration: highly flexible nanoporous carbon nanotube electrodes with strong mechanical strength harvesting improved lithium storage. *J. Mater. Chem.* **2012,** *22* (36), 18847-18853.

185. Yao, Y.; McDowell, M. T.; Ryu, I.; Wu, H.; Liu, N.; Hu, L.; Nix, W. D.; Cui, Y., Interconnected Silicon Hollow Nanospheres for Lithium-Ion Battery Anodes with Long Cycle Life. *Nano Lett.* **2011,** *11* (7), 2949-2954.

186. Wang, Y.; Wu, M.; Jiao, Z.; Lee, J. Y., Sn@CNT and Sn@C@CNT nanostructures for superior reversible lithium ion storage. *Chem. Mater.* **2009,** *21* (14), 3210-3215.

187. Song, T.; Cheng, H.; Choi, H.; Lee, J.-H.; Han, H.; Lee, D. H.; Yoo, D. S.; Kwon, M.-S.; Choi, J.-M.; Doo, S. G.; Chang, H.; Xiao, J.; Huang, Y.; Park, W. I.; Chung, Y.-C.; Kim, H.; Rogers, J. A.; Paik, U., Si/Ge Double-Layered Nanotube Array as a Lithium Ion Battery Anode. *ACS Nano* **2011,** *6* (1), 303-309.

188. Zhu, X.; Zhu, Y.; Murali, S.; Stoller, M. D.; Ruoff, R. S., Nanostructured Reduced Graphene Oxide/Fe_2O_3 Composite As a High-Performance Anode Material for Lithium Ion Batteries. *ACS Nano* **2011,** *5* (4), 3333-3338.

189. Li, X.; Meng, X.; Liu, J.; Geng, D.; Zhang, Y.; Banis, M. N.; Li, Y.; Yang, J.; Li, R.; Sun, X.; Cai, M.; Verbrugge, M. W., Tin Oxide with Controlled Morphology and Crystallinity by Atomic Layer Deposition onto Graphene Nanosheets for Enhanced Lithium Storage. *Adv. Funct. Mater.* **2012,** *22* (8), 1647-1654.

190. Qian, Y.; Lu, S.; Gao, F., Preparation of MnO_2/graphene composite as electrode material for supercapacitors. *J. Mater. Sci.* **2011,** *46* (10), 3517-3522.

191. Lu, L. Q.; Wang, Y., Facile synthesis of graphene-supported shuttle- and urchin-like CuO for high and fast Li-ion storage. *Electrochem Commun* **2012,** *14* (1), 82-85.

192. Xiang, J. Y.; Tu, J. P.; Yuan, Y. F.; Wang, X. L.; Huang, X. H.; Zeng, Z. Y., Electrochemical investigation on nanoflower-like CuO/Ni composite film as anode for lithium ion batteries. *Electrochim Acta* **2009,** *54* (4), 1160-1165.

193. Wu, C.; Yin, P.; Zhu, X.; OuYang, C.; Xie, Y., Synthesis of Hematite (α-Fe_2O_3) Nanorods: Diameter-Size and Shape Effects on Their Applications in Magnetism, Lithium Ion Battery, and Gas Sensors. *J. Phys. Chem. B* **2006,** *110* (36), 17806-17812.

194. Liu, S.; Zhang, L.; Zhou, J.; Xiang, J.; Sun, J.; Guan, J., Fiberlike Fe_2O_3 Macroporous Nanomaterials Fabricated by Calcinating Regenerate Cellulose Composite Fibers. *Chem. Mater.* **2008,** *20* (11), 3623-3628.

195. Sun, B.; Horvat, J.; Kim, H. S.; Kim, W.-S.; Ahn, J.; Wang, G., Synthesis of Mesoporous α-Fe_2O_3 Nanostructures for Highly Sensitive Gas Sensors and High Capacity Anode Materials in Lithium Ion Batteries. *J. Phys. Chem. C* **2010,** *114* (44), 18753-18761.
196. Zou, Y.; Kan, J.; Wang, Y., Fe_2O_3-Graphene Rice-on-Sheet Nanocomposite for High and Fast Lithium Ion Storage. *J. Phys. Chem. C* **2011,** *115* (42), 20747-20753.
197. Song, P.; Cao, Z.; Cai, Y.; Zhao, L.; Fang, Z.; Fu, S., Fabrication of exfoliated graphene-based polypropylene nanocomposites with enhanced mechanical and thermal properties. *Polymer* **2011,** *52* (18), 4001-4010.
198. Wang, G.; Liu, T.; Luo, Y. J.; Zhao, Y.; Ren, Z. Y.; Bai, J. B.; Wang, H., Preparation of Fe_2O_3/graphene composite and its electrochemical performance as an anode material for lithium ion batteries. *J Alloy Compd* **2011,** *509* (24), L216-L220.
199. Kovalevski, V. V.; Safronov, A. N., Pyrolysis of hollow carbons on melted catalyst. *Carbon* **1998,** *36* (7–8), 963-968.
200. Chou, S.-L.; Wang, J.-Z.; Wexler, D.; Konstantinov, K.; Zhong, C.; Liu, H.-K.; Dou, S.-X., High-surface-area [small alpha]-Fe_2O_3/carbon nanocomposite: one-step synthesis and its highly reversible and enhanced high-rate lithium storage properties. *J. Mater. Chem.* **2010,** *20* (11), 2092-2098.
201. Chen, J.; Xu, L.; Li, W.; Gou, X., α-Fe2O3 Nanotubes in Gas Sensor and Lithium-Ion Battery Applications. *Adv. Mater.* **2005,** *17* (5), 582-586.
202. Reddy, M. V.; Yu, T.; Sow, C. H.; Shen, Z. X.; Lim, C. T.; Rao, G. V. S.; Chowdari, B. V. R., alpha-Fe_2O_3 nanoflakes as an anode material for Li-ion batteries. *Adv. Funct. Mater.* **2007,** *17* (15), 2792-2799.
203. Liu, H.; Wang, G.; Park, J.; Wang, J.; Liu, H.; Zhang, C., Electrochemical performance of α-Fe_2O_3 nanorods as anode material for lithium-ion cells. *Electrochim Acta* **2009,** *54* (6), 1733-1736.
204. Xiao, L.; Wu, D.; Han, S.; Huang, Y.; Li, S.; He, M.; Zhang, F.; Feng, X., Self-Assembled Fe_2O_3/Graphene Aerogel with High Lithium Storage Performance. *ACS Appl. Mater. Interfaces* **2013,** *5* (9), 3764-3769.
205. Zhou, G.-W.; Wang, J.; Gao, P.; Yang, X.; He, Y.-S.; Liao, X.-Z.; Yang, J.; Ma, Z.-F., Facile Spray Drying Route for the Three-Dimensional Graphene-Encapsulated Fe_2O_3 Nanoparticles for Lithium Ion Battery Anodes. *Ind. Eng. Chem. Res.* **2013,** *52* (3), 1197-1204.
206. Zhang, M.; Qu, B.; Lei, D.; Chen, Y.; Yu, X.; Chen, L.; Li, Q.; Wang, Y.; Wang, T., A green and fast strategy for the scalable synthesis of Fe_2O_3/graphene with significantly enhanced Li-ion storage properties. *J. Mater. Chem.* **2012,** *22* (9), 3868-3874.
207. Li, Y.; Lv, X.; Lu, J.; Li, J., Preparation of SnO_2-Nanocrystal/Graphene-Nanosheets Composites and Their Lithium Storage Ability. *J. Phys. Chem. C* **2010,** *114* (49), 21770-21774.
208. Chen, D.; Wei, W.; Wang, R.; Zhu, J.; Guo, L., [small alpha]-Fe_2O_3 nanoparticles anchored on graphene with 3D quasi-laminated architecture: in situ wet chemistry synthesis and enhanced electrochemical performance for lithium ion batteries. *New J. Chem.* **2012**.
209. Lee, K. K.; Deng, S.; Fan, H. M.; Mhaisalkar, S.; Tan, H. R.; Tok, E. S.; Loh, K. P.; Chin, W. S.; Sow, C. H., [small alpha]-Fe_2O_3 nanotubes-reduced graphene oxide composites as synergistic electrochemical capacitor materials. *Nanoscale* **2012,** *4* (9), 2958-2961.

210. Novoselov, K. S.; McCann, E.; Morozov, S. V.; Fal'ko, V. I.; Katsnelson, M. I.; Zeitler, U.; Jiang, D.; Schedin, F.; Geim, A. K., Unconventional quantum Hall effect and Berry's phase of 2π in bilayer graphene. *Nat. Phys.* **2006,** *2* (3), 177-180.
211. Huang, Y.; Liang, J.; Chen, Y., An Overview of The Applications of Graphene-Based Materials in Supercapacitors. *Small* **2012,** *8* (12), 1805-1834.
212. Yang, L.-X.; Zhu, Y.-J.; Li, L.; Zhang, L.; Tong, H.; Wang, W.-W.; Cheng, G.-F.; Zhu, J.-F., A Facile Hydrothermal Route to Flower-Like Cobalt Hydroxide and Oxide. *European Journal of Inorganic Chemistry* **2006,** *2006* (23), 4787-4792.
213. Xiao, J.; Mei, D.; Li, X.; Xu, W.; Wang, D.; Graff, G. L.; Bennett, W. D.; Nie, Z.; Saraf, L. V.; Aksay, I. A.; Liu, J.; Zhang, J.-G., Hierarchically Porous Graphene As A Lithium–Air Battery Electrode. *Nano Lett.* **2011,** *11* (11), 5071-5078.
214. Stoller, M. D.; Park, S.; Zhu, Y.; An, J.; Ruoff, R. S., Graphene-Based Ultracapacitors. *Nano Lett.* **2008,** *8* (10), 3498-3502.
215. Robinson, J. T.; Perkins, F. K.; Snow, E. S.; Wei, Z.; Sheehan, P. E., Reduced Graphene Oxide Molecular Sensors. *Nano Lett.* **2008,** *8* (10), 3137-3140.
216. Bae, S.; Kim, H.; Lee, Y.; Xu, X.; Park, J.-S.; Zheng, Y.; Balakrishnan, J.; Lei, T.; Ri Kim, H.; Song, Y. I.; Kim, Y.-J.; Kim, K. S.; Ozyilmaz, B.; Ahn, J.-H.; Hong, B. H.; Iijima, S., Roll-to-Roll Production of 30-Inch Graphene Films for Transparent Electrodes. *Nat. Nanotechnol.* **2010,** *5* (8), 574-578.
217. Li, X.; Cai, W.; An, J.; Kim, S.; Nah, J.; Yang, D.; Piner, R.; Velamakanni, A.; Jung, I.; Tutuc, E.; Banerjee, S. K.; Colombo, L.; Ruoff, R. S., Large-Area Synthesis of High-Quality and Uniform Graphene Films on Copper Foils. *Science* **2009,** *324* (5932), 1312-1314.
218. Gao, L.; Ren, W.; Zhao, J.; Ma, L.-P.; Chen, Z.; Cheng, H.-M., Efficient Growth of High-Quality Graphene Films on Cu Foils by Ambient Pressure Chemical Vapor Deposition. *App. Phys. Lett.* **2010,** *97* (18), 183109.
219. Yu, Q.; Jauregui, L. A.; Wu, W.; Colby, R.; Tian, J.; Su, Z.; Cao, H.; Liu, Z.; Pandey, D.; Wei, D.; Chung, T. F.; Peng, P.; Guisinger, N. P.; Stach, E. A.; Bao, J.; Pei, S.-S.; Chen, Y. P., Control and Characterization of Individual Grains and Grain Boundaries in Graphene Grown by Chemical Vapour Deposition. *Nat. Mater.* **2011,** *10* (6), 443-449.
220. Ismach, A.; Druzgalski, C.; Penwell, S.; Schwartzberg, A.; Zheng, M.; Javey, A.; Bokor, J.; Zhang, Y., Direct Chemical Vapor Deposition of Graphene on Dielectric Surfaces. *Nano Lett.* **2010,** *10* (5), 1542-1548.
221. Chen, Z.; Ren, W.; Gao, L.; Liu, B.; Pei, S.; Cheng, H.-M., Three-Dimensional Flexible and Conductive Interconnected Graphene Networks Grown by Chemical Vapour Deposition. *Nat. Mater.* **2011,** *10* (6), 424-428.
222. Reina, A.; Jia, X.; Ho, J.; Nezich, D.; Son, H.; Bulovic, V.; Dresselhaus, M. S.; Kong, J., Large Area, Few-Layer Graphene Films in Arbitrary Substrates by Chemical Vapor Deposition. *Nano Lett.* **2008,** *9* (1), 30-35.
223. Sutter, P. W.; Flege, J.-I.; Sutter, E. A., Epitaxial Graphene on Ruthenium. *Nat. Mater.* **2008,** *7* (5), 406-411.
224. Pan, Y.; Zhang, H.; Shi, D.; Sun, J.; Du, S.; Liu, F.; Gao, H.-j., Highly Ordered, Millimeter-Scale, Continuous, Single-Crystalline Graphene Monolayer Formed on Ru (0001). *Adv. Mater.* **2009,** *21* (27), 2777-2780.
225. Shu, H.; Chen, X.; Tao, X.; Ding, F., Edge Structural Stability And Kinetics Of Graphene Chemical Vapor Deposition Growth. *ACS Nano* **2012,** *6* (4), 3243-3250.

226. Edwards, R. S.; Coleman, K. S., Graphene Film Growth on Polycrystalline Metals. *Acc. Chem. Res.* **2012,** *46* (1), 23-30.

227. Xue, Y.; Wu, B.; Guo, Y.; Huang, L.; Jiang, L.; Chen, J.; Geng, D.; Liu, Y.; Hu, W.; Yu, G., Synthesis of large-area, few-layer graphene on iron foil by chemical vapor deposition. *Nano Res.* **2011,** *4* (12), 1208-1214.

228. Ramón, M. E.; Gupta, A.; Corbet, C.; Ferrer, D. A.; Movva, H. C. P.; Carpenter, G.; Colombo, L.; Bourianoff, G.; Doczy, M.; Akinwande, D.; Tutuc, E.; Banerjee, S. K., CMOS-Compatible Synthesis of Large-Area, High-Mobility Graphene by Chemical Vapor Deposition of Acetylene on Cobalt Thin Films. *ACS Nano* **2011,** *5* (9), 7198-7204.

229. Zhan, N.; Wang, G.; Liu, J., Cobalt-assisted large-area epitaxial graphene growth in thermal cracker enhanced gas source molecular beam epitaxy. *Appl. Phys. A* **2011,** *105* (2), 341-345.

230. Wang, S. M.; Pei, Y. H.; Wang, X.; Wang, H.; Meng, Q. N.; Tian, H. W.; Zheng, X. L.; Zheng, W. T.; Liu, Y. C., Synthesis of graphene on a polycrystalline Co film by radio-frequency plasma-enhanced chemical vapour deposition. *J. Phys. D: Appl. Phys.* **2010,** *43* (45), 455402.

231. Dreyer, D. R.; Park, S.; Bielawski, C. W.; Ruoff, R. S., The Chemistry of Graphene Oxide. *Chem. Soc. Rev.* **2010,** *39* (1), 228-240.

232. Loh, K. P.; Bao, Q.; Eda, G.; Chhowalla, M., Graphene Oxide As A Chemically Tunable Platform for Optical Applications. *Nat. Chem.* **2010,** *2* (12), 1015-1024.

233. Zhang, X.; Coleman, A. C.; Katsonis, N.; Browne, W. R.; van Wees, B. J.; Feringa, B. L., Dispersion of Graphene in Ethanol Using A Simple Solvent Exchange Method. *Chem. Commun.* **2010,** *46* (40), 7539-7541.

234. Jiao, L.; Zhang, L.; Ding, L.; Liu, J.; Dai, H., Aligned graphene nanoribbons and crossbars from unzipped carbon nanotubes. *Nano Res.* **2010,** *3* (6), 387-394.

235. Jiao, L.; Zhang, L.; Wang, X.; Diankov, G.; Dai, H., Narrow graphene nanoribbons from carbon nanotubes. *Nature* **2009,** *458* (7240), 877-880.

236. Xin, S.; Gu, L.; Zhao, N.-H.; Yin, Y.-X.; Zhou, L.-J.; Guo, Y.-G.; Wan, L.-J., Smaller Sulfur Molecules Promise Better Lithium–Sulfur Batteries. *J. Am. Chem. Soc.* **2012,** *134* (45), 18510-18513.

237. Chen, S. Q.; Wang, Y., Microwave-assisted synthesis of a Co_3O_4-graphene sheet-on-sheet nanocomposite as a superior anode material for Li-ion batteries. *J. Mater. Chem.* **2010,** *20* (43), 9735-9739.

238. Shao, Y.; Wang, J.; Wu, H.; Liu, J.; Aksay, I. A.; Lin, Y., Graphene Based Electrochemical Sensors and Biosensors: A Review. *Electroanal.* **2010,** *22* (10), 1027-1036.

239. Huang, X.; Sun, B.; Li, K.; Chen, S.; Wang, G., Mesoporous graphene paper immobilised sulfur as a flexible electrode for lithium-sulfur batteries. *Journal of Materials Chemistry A* **2013,** *1* (43), 13484-13489.

240. Geng, D.; Wu, B.; Guo, Y.; Huang, L.; Xue, Y.; Chen, J.; Yu, G.; Jiang, L.; Hu, W.; Liu, Y., Uniform Hexagonal Graphene Flakes and Films Grown on Liquid Copper Surface. *Proc. Natl. Acad. Sci. U.S.A.* **2012,** *109* (21), 7992-7996.

241. Li, X.; Magnuson, C. W.; Venugopal, A.; Tromp, R. M.; Hannon, J. B.; Vogel, E. M.; Colombo, L.; Ruoff, R. S., Large-Area Graphene Single Crystals Grown by Low-Pressure Chemical Vapor Deposition of Methane on Copper. *J. Am. Chem. Soc.* **2011,** *133* (9), 2816-2819.

242. Zhang, Y.; Zhang, L.; Kim, P.; Ge, M.; Li, Z.; Zhou, C., Vapor Trapping Growth of Single-Crystalline Graphene Flowers: Synthesis, Morphology, and Electronic Properties. *Nano Lett.* **2012,** *12* (6), 2810-2816.

243. Chae, S. J.; Güneş, F.; Kim, K. K.; Kim, E. S.; Han, G. H.; Kim, S. M.; Shin, H.-J.; Yoon, S.-M.; Choi, J.-Y.; Park, M. H.; Yang, C. W.; Pribat, D.; Lee, Y. H., Synthesis of Large-Area Graphene Layers on Poly-Nickel Substrate by Chemical Vapor Deposition: Wrinkle Formation. *Adv. Mater.* **2009,** *21* (22), 2328-2333.

244. Hesjedal, T., Continuous roll-to-roll growth of graphene films by chemical vapor deposition. *Appl. Phys. Lett.* **2011,** *98* (13), 133106.

245. Bhaviripudi, S.; Jia, X.; Dresselhaus, M. S.; Kong, J., Role of Kinetic Factors in Chemical Vapor Deposition Synthesis if Uniform Large Area Graphene Using Copper Catalyst. *Nano Lett.* **2010,** *10* (10), 4128-4133.

246. Zhang, Y.; Gao, T.; Gao, Y.; Xie, S.; Ji, Q.; Yan, K.; Peng, H.; Liu, Z., Defect-Like Structures of Graphene on Copper Foils for Strain Relief Investigated by High-Resolution Scanning Tunneling Microscopy. *ACS Nano* **2011,** *5* (5), 4014-4022.

247. Wang, Y.-Q.; Gu, L.; Guo, Y.-G.; Li, H.; He, X.-Q.; Tsukimoto, S.; Ikuhara, Y.; Wan, L.-J., Rutile-TiO2 Nanocoating for a High-Rate Li4Ti5O12 Anode of a Lithium-Ion Battery. *Journal of the American Chemical Society* **2012,** *134* (18), 7874-7879.

248. Zhang, Y.; Gomez, L.; Ishikawa, F. N.; Madaria, A.; Ryu, K.; Wang, C.; Badmaev, A.; Zhou, C., Comparison of Graphene Growth on Single-Crystalline and Polycrystalline Ni by Chemical Vapor Deposition. *J. Phys. Chem. Lett.* **2010,** *1* (20), 3101-3107.

249. Sinclair, R.; Itoh, T.; Chin, R., In Situ TEM Studies of Metal–Carbon Reactions. *Microsc. Microanal.* **2002,** *8* (04), 288-304.

250. Mattevi, C.; Kim, H.; Chhowalla, M., A review of chemical vapour deposition of graphene on copper. *J. Mater. Chem.* **2011,** *21* (10), 3324-3334.

251. Zhang, Y.; Zhang, L.; Zhou, C., Review of Chemical Vapor Deposition of Graphene and Related Applications. *Acc. Chem. Res.* **2013,** *46* (10), 2329-2339.

252. Sutter, P.; Sadowski, J. T.; Sutter, E., Graphene on Pt(111): Growth and Substrate Interaction. *Phys. Rev. B* **2009,** *80* (24), 245411.

253. Wang, Y.; Zheng, Y.; Xu, X.; Dubuisson, E.; Bao, Q.; Lu, J.; Loh, K. P., Electrochemical Delamination of CVD-Grown Graphene Film: Toward The Recyclable Use of Copper Catalyst. *ACS Nano* **2011,** *5* (12), 9927-9933.

254. Gao, L.; Ren, W.; Xu, H.; Jin, L.; Wang, Z.; Ma, T.; Ma, L.-P.; Zhang, Z.; Fu, Q.; Peng, L.-M.; Bao, X.; Cheng, H.-M., Repeated Growth and Bubbling Transfer of Graphene With Millimetre-Size Single-Crystal Grains Using Platinum. *Nat. Commun.* **2012,** *3*, 699.

255. Li, N.; Chen, Z.; Ren, W.; Li, F.; Cheng, H.-M., Flexible graphene-based lithium ion batteries with ultrafast charge and discharge rates. *Proc. Natl. Acad. Sci. U.S.A.* **2012,** *109* (43), 17360-17365.

256. Zhou, M.; Cai, T.; Pu, F.; Chen, H.; Wang, Z.; Zhang, H.; Guan, S., Graphene/Carbon-Coated Si Nanoparticle Hybrids as High-Performance Anode Materials for Li-Ion Batteries. *ACS Appl. Mater. Inter.* **2013,** *5* (8), 3449-3455.

257. Wang, C.; Ju, J.; Yang, Y.; Tang, Y.; Lin, J.; Shi, Z.; Han, R. P. S.; Huang, F., In situ grown graphene-encapsulated germanium nanowires for superior lithium-ion storage properties. *J. Mater. Chem. A* **2013,** *1*, 8897-8902.

258. Bai, S.; Chen, S.; Shen, X.; Zhu, G.; Wang, G., Nanocomposites of Hematite ([small alpha]-Fe_2O_3) Nanospindles with Crumpled Reduced Graphene Oxide Nanosheets

as High-performance Anode Material for Lithium-ion Batteries. *RSC Adv.* **2012,** *2* (29), 10977-10984.

259. Zou, Y.; Wang, Y., NiO nanosheets grown on graphene nanosheets as superior anode materials for Li-ion batteries. *Nanoscale* **2011,** *3* (6), 2615-2620.

260. Häglund, J., Fixed-Spin-Moment Calculations on bcc and fcc Iron Using The Generalized Gradient Approximation. *Phys. Rev. B* **1993,** *47* (1), 566-569.

261. Kondo, D.; Sato, S.; Yagi, K.; Harada, N.; Sato, M.; Nihei, M.; Yokoyama, N., Low-Temperature Synthesis of Graphene and Fabrication of Top-Gated Field Effect Transistors without Using Transfer Processes. *App. Phys. Express* **2010,** *3* (2), 1-3.

262. Kondo, D.; Yagi, K.; Sato, M.; Nihei, M.; Awano, Y.; Sato, S.; Yokoyama, N., Selective synthesis of carbon nanotubes and multi-layer graphene by controlling catalyst thickness. *Chem Phys Lett* **2011,** *514* (4–6), 294-300.

263. An, H.; Lee, W.-J.; Jung, J., Graphene synthesis on Fe foil using thermal CVD. *Curr. App. Phys.* **2011,** *11* (4), S81-S85.

264. He, Z.; Maurice, J.-L.; Gohier, A.; Lee, C. S.; Pribat, D.; Cojocaru, C. S., Iron Catalysts for The Growth of Carbon Nanofibers: Fe, Fe_3C or Both? *Chem. Mater.* **2011,** *23* (24), 5379-5387.

265. Chen, S.; Chen, P.; Wang, Y., Carbon Nanotubes Grown in situ on Graphene Nanosheets as Superior Anodes for Li-ion Batteries. *Nanoscale* **2011,** *3* (10), 4323-9.

266. Xue, D.-J.; Xin, S.; Yan, Y.; Jiang, K.-C.; Yin, Y.-X.; Guo, Y.-G.; Wan, L.-J., Improving the Electrode Performance of Ge through Ge@C Core–Shell Nanoparticles and Graphene Networks. *J. Am. Chem. Soc.* **2012,** *134* (5), 2512-2515.

267. Charlier, J. C.; Amara, H.; Lambin, P., Catalytically Assisted Tip Growth Mechanism For Single-Wall Carbon Nanotubes. *ACS Nano* **2007,** *1* (3), 202-207.

268. Guzmán de Villoria, R.; Hart, A. J.; Wardle, B. L., Continuous High-Yield Production Of Vertically Aligned Carbon Nanotubes On 2D and 3D Substrates. *ACS Nano* **2011,** *5* (6), 4850-4857.

269. Cui, Y.; Fu, Q.; Zhang, H.; Tan, D.; Bao, X., Dynamic Characterization of Graphene Growth and Etching by Oxygen on Ru(0001) by Photoemission Electron Microscopy. *J. Phys. Chem. C* **2009,** *113* (47), 20365-20370.

270. Girit, Ç. Ö.; Meyer, J. C.; Erni, R.; Rossell, M. D.; Kisielowski, C.; Yang, L.; Park, C.-H.; Crommie, M. F.; Cohen, M. L.; Louie, S. G.; Zettl, A., Graphene at The Edge: Stability and Dynamics. *Science* **2009,** *323* (5922), 1705-1708.

271. Chen, S.; Yeoh, W.; Liu, Q.; Wang, G., Chemical-free Synthesis of Graphene–Carbon Nanotube Hybrid Materials for Reversible Lithium Storage in Lithium-ion Batteries. *Carbon* **2012,** *50* (12), 4557-4565.

272. Malard, L. M.; Pimenta, M. A.; Dresselhaus, G.; Dresselhaus, M. S., Raman Spectroscopy in Graphene. *Phys. Rep.* **2009,** *473* (5–6), 51-87.

273. Choucair, M.; Thordarson, P.; Stride, J. A., Gram-Scale Production of Graphene Based on Solvothermal Synthesis and Sonication. *Nat. Nanotechnol.* **2009,** *4* (1), 30-33.

274. Ansari, S.; Kelarakis, A.; Estevez, L.; Giannelis, E. P., Oriented Arrays of Graphene in a Polymer Matrix by in situ Reduction of Graphite Oxide Nanosheets. *Small* **2010,** *6* (2), 205-209.

275. Tang, W.; Hou, Y.; Wang, F.; Liu, L.; Wu, Y.; Zhu, K., $LiMn_2O_4$ Nanotube as Cathode Material of Second-Level Charge Capability for Aqueous Rechargeable Batteries. *Nano Lett.* **2013,** *13* (5), 2036-2040.

276. Qu, Q.; Fu, L.; Zhan, X.; Samuelis, D.; Maier, J.; Li, L.; Tian, S.; Li, Z.; Wu, Y., Porous $LiMn_2O_4$ as cathode material with high power and excellent cycling for aqueous rechargeable lithium batteries. *Energ. Environ. Sci.* **2011,** *4* (10), 3985-3990.

277. Luo, J.; Zhao, X.; Wu, J.; Jang, H. D.; Kung, H. H.; Huang, J., Crumpled Graphene-Encapsulated Si Nanoparticles for Lithium Ion Battery Anodes. *J. Phys. Chem. Lett.* **2012,** *3* (13), 1824-1829.

278. Wu, H.; Yu, G.; Pan, L.; Liu, N.; McDowell, M. T.; Bao, Z.; Cui, Y., Stable Li-ion battery anodes by in-situ polymerization of conducting hydrogel to conformally coat silicon nanoparticles. *Nat. Commun.* **2013,** *4*.

279. Wang, G.; Wang, B.; Wang, X.; Park, J.; Dou, S.; Ahn, H.; Kim, K., Sn/graphene nanocomposite with 3D architecture for enhanced reversible lithium storage in lithium ion batteries. *J. Mater. Chem.* **2009,** *19* (44), 8378-8384.

280. Chen, S.; Bao, P.; Xiao, L.; Wang, G., Large-Scale and Low Cost Synthesis of Graphene as High Capacity Anode Materials for Lithium-Ion Batteries. *Carbon* **2013,** *64* (0), 158-169.

281. Wu, H.; Cui, Y., Designing nanostructured Si anodes for high energy lithium ion batteries. *Nano Today* **2012,** *7* (5), 414-429.

282. Kim, H.; Han, B.; Choo, J.; Cho, J., Three-Dimensional Porous Silicon Particles for Use in High-Performance Lithium Secondary Batteries. *Angew. Chem. Int. Ed.* **2008,** *47* (52), 10151-10154.

283. Ge, M.; Rong, J.; Fang, X.; Zhang, A.; Lu, Y.; Zhou, C., Scalable preparation of porous silicon nanoparticles and their application for lithium-ion battery anodes. *Nano Res.* **2013,** *6* (3), 174-181.

284. Liu, N.; Yao, Y.; Cha, J.; McDowell, M.; Han, Y.; Cui, Y., Functionalization of silicon nanowire surfaces with metal-organic frameworks. *Nano Res.* **2012,** *5* (2), 109-116.

285. Zhu, X.; Chen, H.; Wang, Y.; Xia, L.; Tan, Q.; Li, H.; Zhong, Z.; Su, F.; Zhao, X. S., Growth of silicon/carbon microrods on graphite microspheres as improved anodes for lithium-ion batteries. *J. Mater. Chem. A* **2013,** *1* (14), 4483-4489.

286. Kong, J.; Yee, W. A.; Wei, Y.; Yang, L.; Ang, J. M.; Phua, S. L.; Wong, S. Y.; Zhou, R.; Dong, Y.; Li, X.; Lu, X., Silicon nanoparticles encapsulated in hollow graphitized carbon nanofibers for lithium ion battery anodes. *Nanoscale* **2013,** *5* (7), 2967-2973.

287. Kim, H.; Seo, M.; Park, M.-H.; Cho, J., A Critical Size of Silicon Nano-Anodes for Lithium Rechargeable Batteries. *Angew. Chem. Int. Ed.* **2010,** *49* (12), 2146-2149.

288. Zhou, X.; Cao, A.-M.; Wan, L.-J.; Guo, Y.-G., Spin-coated silicon nanoparticle/graphene electrode as a binder-free anode for high-performance lithium-ion batteries. *Nano Res.* **2012,** *5* (12), 845-853.

289. Kovalenko, I.; Zdyrko, B.; Magasinski, A.; Hertzberg, B.; Milicev, Z.; Burtovyy, R.; Luzinov, I.; Yushin, G., A Major Constituent of Brown Algae for Use in High-Capacity Li-Ion Batteries. *Science* **2011,** *334* (6052), 75-79.

290. Koo, B.; Kim, H.; Cho, Y.; Lee, K. T.; Choi, N.-S.; Cho, J., A Highly Cross-Linked Polymeric Binder for High-Performance Silicon Negative Electrodes in Lithium Ion Batteries. *Angew. Chem. Int. Ed.* **2012,** *51* (35), 8762-8767.

291. Magasinski, A.; Zdyrko, B.; Kovalenko, I.; Hertzberg, B.; Burtovyy, R.; Huebner, C. F.; Fuller, T. F.; Luzinov, I.; Yushin, G., Toward Efficient Binders for Li-Ion Battery Si-Based Anodes: Polyacrylic Acid. *ACS Appl. Mater. Inter.* **2010,** *2* (11), 3004-3010.

292. Guy, D.; Lestriez, B.; Guyomard, D., New Composite Electrode Architecture and Improved Battery Performance from the Smart Use of Polymers and Their Properties. *Adv. Mater.* **2004,** *16* (6), 553-557.
293. Guo, J.; Wang, C., A polymer scaffold binder structure for high capacity silicon anode of lithium-ion battery. *Chem. Commun.* **2010,** *46* (9), 1428-1430.
294. Kim, J. W.; Ryu, J. H.; Lee, K. T.; Oh, S. M., Improvement of silicon powder negative electrodes by copper electroless deposition for lithium secondary batteries. *J Power Sources* **2005,** *147* (1–2), 227-233.
295. Chen, D.; Mei, X.; Ji, G.; Lu, M.; Xie, J.; Lu, J.; Lee, J. Y., Reversible Lithium-Ion Storage in Silver-Treated Nanoscale Hollow Porous Silicon Particles. *Angew. Chem. Int. Ed.* **2012,** *51* (10), 2409-2413.
296. Yu, Y.; Gu, L.; Zhu, C.; Tsukimoto, S.; van Aken, P. A.; Maier, J., Reversible Storage of Lithium in Silver-Coated Three-Dimensional Macroporous Silicon. *Adv. Mater.* **2010,** *22* (20), 2247-2250.
297. Yang, Z.; Guo, J.; Xu, S.; Yu, Y.; Abruña, H. D.; Archer, L. A., Interdispersed silicon–carbon nanocomposites and their application as anode materials for lithium-ion batteries. *Electrochem Commun* **2013,** *28* (0), 40-43.
298. Cui, L.-F.; Hu, L.; Choi, J. W.; Cui, Y., Light-Weight Free-Standing Carbon Nanotube-Silicon Films for Anodes of Lithium Ion Batteries. *ACS Nano* **2010,** *4* (7), 3671-3678.
299. Chen, P.-C.; Xu, J.; Chen, H.; Zhou, C., Hybrid silicon-carbon nanostructured composites as superior anodes for lithium ion batteries. *Nano Res.* **2011,** *4* (3), 290-296.
300. Deng, J.; Ji, H.; Yan, C.; Zhang, J.; Si, W.; Baunack, S.; Oswald, S.; Mei, Y.; Schmidt, O. G., Naturally Rolled-Up C/Si/C Trilayer Nanomembranes as Stable Anodes for Lithium-Ion Batteries with Remarkable Cycling Performance. *Angew. Chem. Int. Ed.* **2013,** *52* (8), 2326-2330.
301. Magasinski, A.; Dixon, P.; Hertzberg, B.; Kvit, A.; Ayala, J.; Yushin, G., High-performance lithium-ion anodes using a hierarchical bottom-up approach. *Nat. Mater.* **2010,** *9* (4), 353-358.
302. Park, M. S.; Wang, G. X.; Liu, H. K.; Dou, S. X., Electrochemical properties of Si thin film prepared by pulsed laser deposition for lithium ion micro-batteries. *Electrochim Acta* **2006,** *51* (25), 5246-5249.
303. Xin, X.; Zhou, X.; Wang, F.; Yao, X.; Xu, X.; Zhu, Y.; Liu, Z., A 3D porous architecture of Si/graphene nanocomposite as high-performance anode materials for Li-ion batteries. *J. Mater. Chem.* **2012,** *22* (16), 7724-7730.
304. Lee, J. K.; Smith, K. B.; Hayner, C. M.; Kung, H. H., Silicon nanoparticles-graphene paper composites for Li ion battery anodes. *Chem. Commun.* **2010,** *46* (12), 2025-2027.
305. Hu, Y.-S.; Demir-Cakan, R.; Titirici, M.-M.; Müller, J.-O.; Schlögl, R.; Antonietti, M.; Maier, J., Superior Storage Performance of a Si@SiO$_x$/C Nanocomposite as Anode Material for Lithium-Ion Batteries. *Angew. Chem. Int. Ed.* **2008,** *47* (9), 1645-1649.
306. Huang, X.; Qian, K.; Yang, J.; Zhang, J.; Li, L.; Yu, C.; Zhao, D., Functional Nanoporous Graphene Foams with Controlled Pore Sizes. *Adv. Mater.* **2012,** *24* (32), 4419-4423.
307. Ranjbartoreh, A. R.; Wang, B.; Shen, X.; Wang, G., Advanced mechanical properties of graphene paper. *J Appl Phys* **2011,** *109* (1), 014306.

308. Hu, H.; Zhao, Z.; Wan, W.; Gogotsi, Y.; Qiu, J., Ultralight and Highly Compressible Graphene Aerogels. *Adv. Mater.* **2013,** *25* (15), 2219-2223.

309. Su, D.; Ford, M.; Wang, G., Mesoporous NiO Crystals with Dominantly Exposed {110} Reactive Facets for Ultrafast Lithium Storage. *Sci. Rep.* **2012,** *2*, 924.

310. Qiu, L.; Liu, J. Z.; Chang, S. L. Y.; Wu, Y.; Li, D., Biomimetic superelastic graphene-based cellular monoliths. *Nat. Commun.* **2012,** *3*, 1241.

311. Zhao, Y.; Hu, C.; Hu, Y.; Cheng, H.; Shi, G.; Qu, L., A Versatile, Ultralight, Nitrogen-Doped Graphene Framework. *Angew. Chem. Int. Ed.* **2012,** *51* (45), 11371-11375.

312. Li, D.; Muller, M. B.; Gilje, S.; Kaner, R. B.; Wallace, G. G., Processable aqueous dispersions of graphene nanosheets. *Nat. Nanotechnol.* **2008,** *3* (2), 101-105.

313. Vickery, J. L.; Patil, A. J.; Mann, S., Fabrication of Graphene–Polymer Nanocomposites With Higher-Order Three-Dimensional Architectures. *Adv. Mater.* **2009,** *21* (21), 2180-2184.

314. Xu, Y.; Sheng, K.; Li, C.; Shi, G., Self-Assembled Graphene Hydrogel via a One-Step Hydrothermal Process. *ACS Nano* **2010,** *4* (7), 4324-4330.

315. Kim, K. H.; Oh, Y.; Islam, M. F., Graphene coating makes carbon nanotube aerogels superelastic and resistant to fatigue. *Nat. Nanotechnol.* **2012,** *7* (9), 562-566.

316. Liang, H.-W.; Guan, Q.-F.; Chen, L.-F.; Zhu, Z.; Zhang, W.-J.; Yu, S.-H., Macroscopic-Scale Template Synthesis of Robust Carbonaceous Nanofiber Hydrogels and Aerogels and Their Applications. *Angew. Chem. Int. Ed.* **2012,** *51* (21), 5101-5105.

317. Mecklenburg, M.; Schuchardt, A.; Mishra, Y. K.; Kaps, S.; Adelung, R.; Lotnyk, A.; Kienle, L.; Schulte, K., Aerographite: Ultra Lightweight, Flexible Nanowall, Carbon Microtube Material with Outstanding Mechanical Performance. *Adv. Mater.* **2012,** *24* (26), 3437-3437.

318. Bao, Z.; Weatherspoon, M. R.; Shian, S.; Cai, Y.; Graham, P. D.; Allan, S. M.; Ahmad, G.; Dickerson, M. B.; Church, B. C.; Kang, Z.; Abernathy Iii, H. W.; Summers, C. J.; Liu, M.; Sandhage, K. H., Chemical reduction of three-dimensional silica micro-assemblies into microporous silicon replicas. *Nature* **2007,** *446* (7132), 172-175.

319. Saint, J.; Morcrette, M.; Larcher, D.; Laffont, L.; Beattie, S.; Pérès, J. P.; Talaga, D.; Couzi, M.; Tarascon, J. M., Towards a Fundamental Understanding of the Improved Electrochemical Performance of Silicon–Carbon Composites. *Adv. Funct. Mater.* **2007,** *17* (11), 1765-1774.

320. Lu, Z.; Zhu, J.; Sim, D.; Shi, W.; Tay, Y. Y.; Ma, J.; Hng, H. H.; Yan, Q., In situ growth of Si nanowires on graphene sheets for Li-ion storage. *Electrochim Acta* **2012,** *74* (0), 176-181.

321. Ji, J.; Ji, H.; Zhang, L. L.; Zhao, X.; Bai, X.; Fan, X.; Zhang, F.; Ruoff, R. S., Graphene-Encapsulated Si on Ultrathin-Graphite Foam as Anode for High Capacity Lithium-Ion Batteries. *Adv. Mater.* **2013,** *25* (33), 4673-4677.

322. Wen, Y.; Zhu, Y.; Langrock, A.; Manivannan, A.; Ehrman, S. H.; Wang, C., Graphene-Bonded and -Encapsulated Si Nanoparticles for Lithium Ion Battery Anodes. *Small* **2013,** *9* (16), 2810-2816.

323. Chen, S.; Wang, Y.; Ahn, H.; Wang, G., Microwave Hydrothermal Synthesis of High Performance Tin–Graphene Nanocomposites for Lithium Ion Batteries. *J Power Sources* **2012,** *216* (0), 22-27.

324. Mondal, A. K.; Wang, B.; Su, D.; Wang, Y.; Chen, S.; Zhang, X.; Wang, G., Graphene/MnO_2 Hybrid Nanosheets as High Performance Electrode Materials for Supercapacitors. *Mater. Chem. Phys.* **2014,** *143* (2), 740-746.
325. Chen, S.; Bao, P.; Huang, X.; Sun, B.; Wang, G., Hierarchical 3D Mesoporous Silicon@Graphene Nanoarchitectures for Lithium Ion Batteries with Superior Performance. *Nano Res.* **2014,** *7* (1), 85-94.
326. Wei Seh, Z.; Li, W.; Cha, J. J.; Zheng, G.; Yang, Y.; McDowell, M. T.; Hsu, P.-C.; Cui, Y., Sulphur–TiO_2 Yolk–Shell Nanoarchitecture with Internal Void Space for Long-Cycle Lithium–Sulphur Batteries. *Nat. Commun.* **2013,** *4*, 1331.
327. Wang, Y.; Zeng, H. C.; Lee, J. Y., Highly Reversible Lithium Storage in Porous SnO_2 Nanotubes with Coaxially Grown Carbon Nanotube Overlayers. *Adv. Mater.* **2006,** *18* (5), 645-649.
328. Lukowski, M. A.; Jin, S., Improved Synthesis and Electrical Properties of Si-Doped α-Fe_2O_3 Nanowires. *J. Phys. Chem. C* **2011,** *115* (25), 12388-12395.
329. Huang, X.; Sun, B.; Chen, S.; Wang, G., Self-Assembling Synthesis of Free-standing Nanoporous Graphene–Transition-Metal Oxide Flexible Electrodes for High-Performance Lithium-Ion Batteries and Supercapacitors. *Chem. Asian J.* **2014,** *9* (1), 206-211.
330. Zhuang, Z.; Sheng, W.; Yan, Y., Synthesis of Monodispere Au@Co_3O_4 Core-Shell Nanocrystals and Their Enhanced Catalytic Activity for Oxygen Evolution Reaction. *Adv. Mater.* **2014,** *26* (23), 3950-3955.
331. Koza, J. A.; He, Z.; Miller, A. S.; Switzer, J. A., Electrodeposition of Crystalline Co_3O_4—A Catalyst for the Oxygen Evolution Reaction. *Chem. Mater.* **2012,** *24* (18), 3567-3573.
332. Liu, D.; Wang, X.; Wang, X.; Tian, W.; Bando, Y.; Golberg, D., Co_3O_4 Nanocages with Highly Exposed {110} Facets for High-Performance Lithium Storage. *Sci. Rep.* **2013,** *3*, 2543.
333. Lou, X. W.; Deng, D.; Lee, J. Y.; Feng, J.; Archer, L. A., Self-Supported Formation of Needlelike Co_3O_4 Nanotubes and Their Application as Lithium-Ion Battery Electrodes. *Adv. Mater.* **2008,** *20* (2), 258-262.
334. Lou, X. W.; Deng, D.; Lee, J. Y.; Archer, L. A., Thermal formation of mesoporous single-crystal Co_3O_4 nano-needles and their lithium storage properties. *J. Mater.Chem.* **2008,** *18* (37), 4397-4401.
335. Du, N.; Zhang, H.; Chen, B. D.; Wu, J. B.; Ma, X. Y.; Liu, Z. H.; Zhang, Y. Q.; Yang, D. R.; Huang, X. H.; Tu, J. P., Porous Co_3O_4 Nanotubes Derived From $Co_4(CO)_{12}$ Clusters on Carbon Nanotube Templates: A Highly Efficient Material For Li-Battery Applications. *Adv. Mater.* **2007,** *19* (24), 4505-4509.
336. Jeong, S.; Park, S.; Cho, J., High-Performance, Layered, 3D-$LiCoO_2$ Cathodes with a Nanoscale Co_3O_4 Coating via Chemical Etching. *Adv. Energy Mater.* **2011,** *1* (3), 368-372.
337. Lai, L.; Zhu, J.; Li, Z.; Yu, D. Y. W.; Jiang, S.; Cai, X.; Yan, Q.; Lam, Y. M.; Shen, Z.; Lin, J., Co_3O_4/Nitrogen Modified Graphene Electrode as Li-ion Battery Anode with High Reversible Capacity and Improved Initial Cycle Performance. *Nano Energy* **2014,** *3* (1), 134-143.

338. Zhang, G.; Wang, T.; Yu, X.; Zhang, H.; Duan, H.; Lu, B., Nanoforest of Hierarchical Co_3O_4@$NiCo_2O_4$ Nanowire Arrays for High-Performance Supercapacitors. *Nano Energy* **2013,** *2* (5), 586-594.

339. Gao, M.-R.; Xu, Y.-F.; Jiang, J.; Zheng, Y.-R.; Yu, S.-H., Water Oxidation Electrocatalyzed by an Efficient Mn_3O_4/$CoSe_2$ Nanocomposite. *J. Am. Chem. Soc.* **2012,** *134* (6), 2930-2933.

340. Cowin, P. I.; Petit, C. T. G.; Lan, R.; Irvine, J. T. S.; Tao, S., Recent Progress in the Development of Anode Materials for Solid Oxide Fuel Cells. *Adv. Energy Mater.* **2011,** *1* (3), 314-332.

341. Masa, J.; Xia, W.; Sinev, I.; Zhao, A.; Sun, Z.; Grützke, S.; Weide, P.; Muhler, M.; Schuhmann, W., Mn_xO_y/NC and Co_xO_y/NC Nanoparticles Embedded in a Nitrogen-Doped Carbon Matrix for High-Performance Bifunctional Oxygen Electrodes. *Angew. Chem. Int. Ed.* **2014,** *53* (32), 8508-8512.

342. Liang, Y.; Wang, H.; Diao, P.; Chang, W.; Hong, G.; Li, Y.; Gong, M.; Xie, L.; Zhou, J.; Wang, J.; Regier, T. Z.; Wei, F.; Dai, H., Oxygen Reduction Electrocatalyst Based on Strongly Coupled Cobalt Oxide Nanocrystals and Carbon Nanotubes. *J. Am. Chem. Soc.* **2012,** *134* (38), 15849-15857.

343. Pickrahn, K. L.; Park, S. W.; Gorlin, Y.; Lee, H.-B.-R.; Jaramillo, T. F.; Bent, S. F., Active MnO_x Electrocatalysts Prepared by Atomic Layer Deposition for Oxygen Evolution and Oxygen Reduction Reactions. *Adv. Energy Mater.* **2012,** *2* (10), 1269-1277.

344. Esswein, A. J.; McMurdo, M. J.; Ross, P. N.; Bell, A. T.; Tilley, T. D., Size-Dependent Activity of Co_3O_4 Nanoparticle Anodes for Alkaline Water Electrolysis. *J. Phys. Chem. C* **2009,** *113* (33), 15068-15072.

345. Wu, J.; Xue, Y.; Yan, X.; Yan, W.; Cheng, Q.; Xie, Y., Co_3O_4 Nanocrystals on Single-Walled Carbon Nanotubes as a Highly Efficient Oxygen-Evolving Catalyst. *Nano Res.* **2012,** *5* (8), 521-530.

346. Wang, Y.; Zhang, H. J.; Wei, J.; Wong, C. C.; Lin, J.; Borgna, A., Crystal-Match Guided Formation of Single-Crystal Tricobalt Tetraoxygen Nanomesh as Superior Anode for Electrochemical Energy Storage. *Energy Environ. Sci.* **2011,** *4* (5), 1845-1854.

347. Farhadi, S.; Pourzare, K.; Sadeghinejad, S., Simple Preparation of Ferromagnetic Co_3O_4 Nanoparticles by Thermal Dissociation of the $[CoII(NH_3)_6](NO_3)_2$ Complex at Low Temperature. *J. Nanostruct. Chem.* **2013,** *3* (1), 1-7.

348. Zhang, Q.; Zhao, M.-Q.; Tang, D.-M.; Li, F.; Huang, J.-Q.; Liu, B.; Zhu, W.-C.; Zhang, Y.-H.; Wei, F., Carbon-Nanotube-Array Double Helices. *Angew. Chem. Inter. Ed.* **2010,** *49* (21), 3642-3645.

349. Poizot, P.; Laruelle, S.; Grugeon, S.; Dupont, L.; Tarascon, J. M., Nano-sized transition-metal oxides as negative-electrode materials for lithium-ion batteries. *Nature* **2000,** *407* (6803), 496-499.

350. Lu, Y.; Wang, Y.; Zou, Y.; Jiao, Z.; Zhao, B.; He, Y.; Wu, M., Macroporous Co_3O_4 Platelets with Excellent Rate Capability as Anodes for Lithium Ion Batteries. *Electrochem Commun* **2010,** *12* (1), 101-105.

351. Wu, Z.-S.; Ren, W.; Wen, L.; Gao, L.; Zhao, J.; Chen, Z.; Zhou, G.; Li, F.; Cheng, H.-M., Graphene Anchored with Co_3O_4 Nanoparticles as Anode of Lithium Ion Batteries with Enhanced Reversible Capacity and Cyclic Performance. *ACS Nano* **2010,** *4* (6), 3187-3194.

352. Wang, J. Q.; Niu, B.; Du, G. D.; Zeng, R.; Chen, Z. X.; Guo, Z. P.; Dou, S. X., Microwave homogeneous synthesis of porous nanowire Co_3O_4 arrays with high capacity and rate capability for lithium ion batteries. *Mater. Chem. Phys.* **2011,** *126* (3), 747-754.

353. Ramírez, A.; Bogdanoff, P.; Friedrich, D.; Fiechter, S., Synthesis of $Ca_2Mn_3O_8$ films and their electrochemical studies for the oxygen evolution reaction (OER) of water. *Nano Energy* **2012,** *1* (2), 282-289.

354. Rafailović, L. D.; Gammer, C.; Rentenberger, C.; Trišović, T.; Kleber, C.; Peter Karnthaler, H., Enhanced oxygen evolution and reduction reactions of porous ternary NiCoFe foam electrodes prepared by dynamic hydrogen template deposition. *Nano Energy* **2013,** *2* (4), 523-529.

355. Zou, X.; Su, J.; Silva, R.; Goswami, A.; Sathe, B. R.; Asefa, T., Efficient Oxygen Evolution Reaction Catalyzed by Low-Density Ni-Doped Co_3O_4 Nanomaterials Derived from Metal-Embedded Graphitic C_3N_4. *Chem. Commun.* **2013,** *49* (68), 7522-7524.

356. Wang, D.; Chen, X.; Evans, D. G.; Yang, W., Well-Dispersed Co_3O_4/Co_2MnO_4 Nanocomposites as a Synergistic Bifunctional Catalyst for Oxygen Reduction and Oxygen Evolution Reactions. *Nanoscale* **2013,** *5* (12), 5312-5315.

357. Wang, Y.; Cui, X.; Chen, L.; Wei, C.; Cui, F.; Yao, H.; Shi, J.; Li, Y., One-Step Replication and Enhanced Catalytic Activity for Cathodic Oxygen Reduction of the Mesostructured Co_3O_4/Carbon Composites. *Dalton Trans.* **2014,** *43* (10), 4163-4168.

358. Ma, T. Y.; Dai, S.; Jaroniec, M.; Qiao, S. Z., Metal–Organic Framework Derived Hybrid Co_3O_4-Carbon Porous Nanowire Arrays as Reversible Oxygen Evolution Electrodes. *J. Am. Chem. Soc.* **2014,** *136* (39), 13925-13931.

359. Liang, Y.; Li, Y.; Wang, H.; Zhou, J.; Wang, J.; Regier, T.; Dai, H., Co_3O_4 Nanocrystals on Graphene as a Synergistic Catalyst for Oxygen Reduction Reaction. *Nat. Mater.* **2011,** *10* (10), 780-786.

360. Singh, R. N.; Hamdani, M.; Koenig, J. F.; Poillerat, G.; Gautier, J. L.; Chartier, P., Thin Films of Co_3O_4 and $NiCo_2O_4$ Obtained by the Method of Chemical Spray Pyrolysis for Electrocatalysis III. The Electrocatalysis of Oxygen Evolution. *J. Appl. Electrochem.* **1990,** *20* (3), 442-446.

361. Wang, Y.; Zhou, T.; Jiang, K.; Da, P.; Peng, Z.; Tang, J.; Kong, B.; Cai, W.-B.; Yang, Z.; Zheng, G., Reduced Mesoporous Co_3O_4 Nanowires as Efficient Water Oxidation Electrocatalysts and Supercapacitor Electrodes. *Adv. Energy Mater.* **2014,** *4* (16), 1400696.

362. Peres, N.; Guinea, F.; Castro Neto, A., Electronic properties of disordered two-dimensional carbon. *Physical Review B* **2006,** *73* (12).

363. Huang, J.-Q.; Liu, X.-F.; Zhang, Q.; Chen, C.-M.; Zhao, M.-Q.; Zhang, S.-M.; Zhu, W.; Qian, W.-Z.; Wei, F., Entrapment of sulfur in hierarchical porous graphene for lithium–sulfur batteries with high rate performance from −40 to 60°C. *Nano Energy* **2013,** *2* (2), 314-321.

364. Pereira, V.; Guinea, F.; Lopes dos Santos, J.; Peres, N.; Castro Neto, A., Disorder Induced Localized States in Graphene. *Physical Review Letters* **2006,** *96* (3).

365. Li, W.; Zheng, G.; Yang, Y.; Seh, Z. W.; Liu, N.; Cui, Y., High-performance hollow sulfur nanostructured battery cathode through a scalable, room temperature, one-step, bottom-up approach. *Proc. Natl. Acad. Sci. U.S.A.* **2013,** *110* (18), 7148-7153.

366. McCann, E.; Fal'ko, V., Landau-Level Degeneracy and Quantum Hall Effect in a Graphite Bilayer. *Physical Review Letters* **2006,** *96* (8).

367. Liu, Y.; Zhan, H.; Zhou, Y., Investigation of S/C composite synthesized by solvent exchange method. *Electrochim Acta* **2012,** *70* (0), 241-247.

368. Lin, Z.; Liu, Z.; Fu, W.; Dudney, N. J.; Liang, C., Lithium Polysulfidophosphates: A Family of Lithium-Conducting Sulfur-Rich Compounds for Lithium–Sulfur Batteries. *Angew. Chem. Int. Ed.* **2013,** *52* (29), 7460-7463.

369. Fuchs, J.-N.; Lederer, P., Spontaneous Parity Breaking of Graphene in the Quantum Hall Regime. *Physical Review Letters* **2007,** *98* (1).

370. Joshi, R.; Engstler, J.; Houben, L.; Bar Sadan, M.; Weidenkaff, A.; Mandaliev, P.; Issanin, A.; Schneider, J. J., Catalyst Composition, Morphology and Reaction Pathway in the Growth of "Super-Long" Carbon Nanotubes. *ChemCatChem* **2010,** *2* (9), 1069-1073.

371. Wang, D.; Qian, F.; Yang, C.; Zhong, Z.; Lieber, C. M., Rational Growth of Branched and Hyperbranched Nanowire Structures. *Nano Lett.* **2004,** *4* (5), 871-874.

372. Bierman, M. J.; Lau, Y. K. A.; Kvit, A. V.; Schmitt, A. L.; Jin, S., Dislocation-Driven Nanowire Growth and Eshelby Twist. *Science* **2008,** *320* (5879), 1060-1063.

373. Lao, J. Y.; Huang, J. Y.; Wang, D. Z.; Ren, Z. F., ZnO Nanobridges and Nanonails. *Nano Lett.* **2002,** *3* (2), 235-238.

374. Lao, J. Y.; Wen, J. G.; Ren, Z. F., Hierarchical ZnO Nanostructures. *Nano Lett.* **2002,** *2* (11), 1287-1291.

375. Hao, Y.; Meng, G.; Ye, C.; Zhang, X.; Zhang, L., Kinetics-Driven Growth of Orthogonally Branched Single-Crystalline Magnesium Oxide Nanostructures. *J. Phys. Chem. B* **2005,** *109* (22), 11204-11208.

376. Klug, K. L.; Dravid, V. P., Observation of two- and three-dimensional magnesium oxide nanostructures formed by thermal treatment of magnesium diboride powder. *App. Phys. Lett.* **2002,** *81* (9), 1687-1689.

377. Pan, Z. W.; Dai, Z. R.; Wang, Z. L., Nanobelts of Semiconducting Oxides. *Science* **2001,** *291* (5510), 1947-1949.

378. Sneha, G.; Cameron, B.; Siping, G.; Keisuke, F.; Peter, A. D.; Jeffry, A. K., Direct graphene growth on MgO: origin of the band gap. *J. Phys.: Condens. Matter* **2011,** *23* (7), 072204.

379. Yu, Y.; Gu, L.; Wang, C.; Dhanabalan, A.; van Aken, P. A.; Maier, J., Encapsulation of Sn@carbon Nanoparticles in Bamboo-like Hollow Carbon Nanofibers as an Anode Material in Lithium-Based Batteries. *Angew. Chem. Int. Ed.* **2009,** *48* (35), 6485-6489.

380. Ning, G.; Fan, Z.; Wang, G.; Gao, J.; Qian, W.; Wei, F., Gram-scale synthesis of nanomesh graphene with high surface area and its application in supercapacitor electrodes. *Chem. Commun.* **2011,** *47* (21), 5976-5978.

381. Chan, C. K.; Peng, H.; Liu, G.; McIlwrath, K.; Zhang, X. F.; Huggins, R. A.; Cui, Y., High-performance lithium battery anodes using silicon nanowires. *Nat. Nanotechnol.* **2008,** *3* (1), 31-35.

382. Yi, R.; Dai, F.; Gordin, M. L.; Sohn, H.; Wang, D., Influence of Silicon Nanoscale Building Blocks Size and Carbon Coating on the Performance of Micro-Sized Si–C Composite Li-Ion Anodes. *Adv. Energy Mater.* **2013,** *3* (11), 1507-1515.

383. Yang, Y.; Zheng, G.; Cui, Y., A membrane-free lithium/polysulfide semi-liquid battery for large-scale energy storage. *Energ. Environ. Sci.* **2013,** *6* (5), 1552-1558.

384. Gao, J.; Abruña, H. D., Key Parameters Governing the Energy Density of Rechargeable Li/S Batteries. *J. Phys. Chem. Lett.* **2014,** *5* (5), 882-885.

385. Wang, L.; Zhang, T.; Yang, S.; Cheng, F.; Liang, J.; Chen, J., A quantum-chemical study on the discharge reaction mechanism of lithium-sulfur batteries. *J. Energ. Chem.* **2013,** *22* (1), 72-77.

386. Dong, Z.; Lai, X.; Halpert, J. E.; Yang, N.; Yi, L.; Zhai, J.; Wang, D.; Tang, Z.; Jiang, L., Accurate Control of Multishelled ZnO Hollow Microspheres for Dye-Sensitized Solar Cells with High Efficiency. *Adv. Mater.* **2012,** *24* (8), 1046-1049.

387. Wang, J.; Yang, N.; Tang, H.; Dong, Z.; Jin, Q.; Yang, M.; Kisailus, D.; Zhao, H.; Tang, Z.; Wang, D., Accurate Control of Multishelled Co_3O_4 Hollow Microspheres as High-Performance Anode Materials in Lithium-Ion Batteries. *Angew. Chem. Int. Ed.* **2013,** *52* (25), 6417-6420.

388. Xu, S.; Hessel, C. M.; Ren, H.; Yu, R.; Jin, Q.; Yang, M.; Zhao, H.; Wang, D., [small alpha]-Fe_2O_3 multi-shelled hollow microspheres for lithium ion battery anodes with superior capacity and charge retention. *Energ. Environ. Sci.* **2014,** *7* (2), 632-637.

389. Du, J.; Qi, J.; Wang, D.; Tang, Z., Facile synthesis of Au@TiO_2 core-shell hollow spheres for dye-sensitized solar cells with remarkably improved efficiency. *Energ. Environ. Sci.* **2012,** *5* (5), 6914-6918.

390. Lai, X.; Halpert, J. E.; Wang, D., Recent advances in micro-/nano-structured hollow spheres for energy applications: From simple to complex systems. *Energ. Environ. Sci.* **2012,** *5* (2), 5604-5618.

391. Qi, J.; Zhao, K.; Li, G.; Gao, Y.; Zhao, H.; Yu, R.; Tang, Z., Multi-shelled CeO_2 hollow microspheres as superior photocatalysts for water oxidation. *Nanoscale* **2014,** *6* (8), 4072-4077.

392. Su, F.; Poh, C. K.; Chen, J. S.; Xu, G.; Wang, D.; Li, Q.; Lin, J.; Lou, X. W., Nitrogen-containing microporous carbon nanospheres with improved capacitive properties. *Energ. Environ. Sci.* **2011,** *4* (3), 717-724.

393. Yi, L.; Liu, Y.; Yang, N.; Tang, Z.; Zhao, H.; Ma, G.; Su, Z.; Wang, D., One dimensional $CuInS_2$-ZnS heterostructured nanomaterials as low-cost and high-performance counter electrodes of dye-sensitized solar cells. *Energ. Environ. Sci.* **2013,** *6* (3), 835-840.

394. Gu, D.; Bongard, H.; Deng, Y.; Feng, D.; Wu, Z.; Fang, Y.; Mao, J.; Tu, B.; Schüth, F.; Zhao, D., An Aqueous Emulsion Route to Synthesize Mesoporous Carbon Vesicles and Their Nanocomposites. *Adv. Mater.* **2010,** *22* (7), 833-837.

395. Zhou, G.; Yin, L.-C.; Wang, D.-W.; Li, L.; Pei, S.; Gentle, I. R.; Li, F.; Cheng, H.-M., Fibrous Hybrid of Graphene and Sulfur Nanocrystals for High-Performance Lithium–Sulfur Batteries. *ACS Nano* **2013,** *7* (6), 5367-5375.

396. Lin, Z.; Liu, Z.; Dudney, N. J.; Liang, C., Lithium Superionic Sulfide Cathode for All-Solid Lithium–Sulfur Batteries. *ACS Nano* **2013,** *7* (3), 2829-2833.

397. Zhang, C.; Lv, W.; Zhang, W.; Zheng, X.; Wu, M.-B.; Wei, W.; Tao, Y.; Li, Z.; Yang, Q.-H., Reduction of Graphene Oxide by Hydrogen Sulfide: A Promising Strategy for Pollutant Control and as an Electrode for Li-S Batteries. *Adv. Energy Mater.* **2014,** *4* (7), 1301565.

398. Chen, S.; Huang, X.; Liu, H.; Sun, B.; Yeoh, W.; Li, K.; Zhang, J.; Wang, G., 3D Hyperbranched Hollow Carbon Nanorod Architectures for High-Performance Lithium-Sulfur Batteries. *Adv. Energy Mater.* **2014,** *4* (8), 1301761.

399. Zheng, S.; Chen, Y.; Xu, Y.; Yi, F.; Zhu, Y.; Liu, Y.; Yang, J.; Wang, C., In Situ Formed Lithium Sulfide/Microporous Carbon Cathodes for Lithium-Ion Batteries. *ACS Nano* **2013,** *7* (12), 10995-11003.

400. Wei, S.; Zhang, H.; Huang, Y.; Wang, W.; Xia, Y.; Yu, Z., Pig bone derived hierarchical porous carbon and its enhanced cycling performance of lithium-sulfur batteries. *Energ. Environ. Sci.* **2011,** *4* (3), 736-740.

401. Schuster, J.; He, G.; Mandlmeier, B.; Yim, T.; Lee, K. T.; Bein, T.; Nazar, L. F., Spherical Ordered Mesoporous Carbon Nanoparticles with High Porosity for Lithium–Sulfur Batteries. *Angew. Chem. Int. Ed.* **2012,** *51* (15), 3591-3595.

402. Li, Z.; Yuan, L.; Yi, Z.; Liu, Y.; Xin, Y.; Zhang, Z.; Huang, Y., A dual coaxial nanocable sulfur composite for high-rate lithium-sulfur batteries. *Nanoscale* **2014,** *6* (3), 1653-1660.

403. Ji, X.; Nazar, L. F., Advances in Li-S batteries. *J. Mater. Chem.* **2010,** *20* (44), 9821-9826.

404. Yamin, H.; Gorenshtein, A.; Penciner, J.; Sternberg, Y.; Peled, E., Lithium Sulfur Battery: Oxidation/Reduction Mechanisms of Polysulfides in THF Solutions. *J. Electrochem. Soc.* **1988,** *135* (5), 1045-1048.

405. Xu, R.; Belharouak, I.; Li, J. C. M.; Zhang, X.; Bloom, I.; Bareño, J., Role of Polysulfides in Self-Healing Lithium–Sulfur Batteries. *Adv. Energy Mater.* **2013,** *3* (7), 833-838.

406. Huang, C.; Xiao, J.; Shao, Y.; Zheng, J.; Bennett, W. D.; Lu, D.; Laxmikant, S. V.; Engelhard, M.; Ji, L.; Zhang, J.; Li, X.; Graff, G. L.; Liu, J., Manipulating surface reactions in lithium–sulphur batteries using hybrid anode structures. *Nat Commun* **2014,** *5*.

407. Wang, C.; Chen, J.-j.; Shi, Y.-n.; Zheng, M.-s.; Dong, Q.-f., Preparation and performance of a core–shell carbon/sulfur material for lithium/sulfur battery. *Electrochim. Acta* **2010,** *55* (23), 7010-7015.

408. Li, Z.; Yuan, L.; Yi, Z.; Sun, Y.; Liu, Y.; Jiang, Y.; Shen, Y.; Xin, Y.; Zhang, Z.; Huang, Y., Insight into the Electrode Mechanism in Lithium-Sulfur Batteries with Ordered Microporous Carbon Confined Sulfur as the Cathode. *Adv. Energy Mater.* **2014,** *4* (7), 1301473.

409. Huang, X.; Sun, B.; Li, K.; Chen, S.; Wang, G., Mesoporous graphene paper immobilised sulfur as a flexible electrode for lithium-sulfur batteries. *J. Mater. Chem. A* **2013,** *1* (43), 13484-13489.

410. Chen, H.; Dong, W.; Ge, J.; Wang, C.; Wu, X.; Lu, W.; Chen, L., Ultrafine Sulfur Nanoparticles in Conducting Polymer Shell as Cathode Materials for High Performance Lithium/Sulfur Batteries. *Sci. Rep.* **2013,** *3*, 1910.

411. Fu, Y.; Su, Y.-S.; Manthiram, A., Sulfur-Polypyrrole Composite Cathodes for Lithium-Sulfur Batteries. *J. Electrochemi. Soc.* **2012,** *159* (9), A1420-A1424.

412. Yin, L.; Wang, J.; Lin, F.; Yang, J.; Nuli, Y., Polyacrylonitrile/graphene composite as a precursor to a sulfur-based cathode material for high-rate rechargeable Li-S batteries. *Energy Environ. Sci.* **2012,** *5* (5), 6966-6972.

413. Huang, J.-Q.; Zhang, Q.; Peng, H.-J.; Liu, X.-Y.; Qian, W.-Z.; Wei, F., Ionic shield for polysulfides towards highly-stable lithium-sulfur batteries. *Energy Environ. Sci.* **2014,** *7* (1), 347-353.

414. Yin, Z.; Zheng, Q., Controlled Synthesis and Energy Applications of One-Dimensional Conducting Polymer Nanostructures: An Overview. *Adv. Energy Mater.* **2012,** *2* (2), 179-218.

415. Chen, S.; Bao, P.; Wang, G., Synthesis of Fe_2O_3–CNT–graphene hybrid materials with an open three-dimensional nanostructure for high capacity lithium storage. *Nano Energy* **2013,** *2* (3), 425-434.

416. Taylor, C. A.; Chiu, W. K. S., Characterization of CVD carbon films for hermetic optical fiber coatings. *Surf. Coat. Tech.* **2003,** *168* (1), 1-11.

417. Li, Z.; Jiang, Y.; Yuan, L.; Yi, Z.; Wu, C.; Liu, Y.; Strasser, P.; Huang, Y., A Highly Ordered Meso@Microporous Carbon-Supported Sulfur@Smaller Sulfur Core–Shell Structured Cathode for Li–S Batteries. *ACS Nano* **2014,** *8* (9), 9295-9303.

418. Su, Y.-S.; Manthiram, A., A new approach to improve cycle performance of rechargeable lithium-sulfur batteries by inserting a free-standing MWCNT interlayer. *Chem. Commun.* **2012,** *48* (70), 8817-8819.

419. Yin, L.; Wang, J.; Yu, X.; Monroe, C. W.; NuLi, Y.; Yang, J., Dual-mode sulfur-based cathode materials for rechargeable Li-S batteries. *Chem. Commun.* **2012,** *48* (63), 7868-7870.

420. Chen, S.; Dai, F.; Gordin, M. L.; Wang, D., Exceptional electrochemical performance of rechargeable Li-S batteries with a polysulfide-containing electrolyte. *RSC Adv.* **2013,** *3* (11), 3540-3543.

421. He, G.; Ji, X.; Nazar, L., High "C" rate Li-S cathodes: sulfur imbibed bimodal porous carbons. *Energy Environ. Sci.* **2011,** *4* (8), 2878-2883.

422. Lin, T.; Tang, Y.; Wang, Y.; Bi, H.; Liu, Z.; Huang, F.; Xie, X.; Jiang, M., Scotch-tape-like exfoliation of graphite assisted with elemental sulfur and graphene-sulfur composites for high-performance lithium-sulfur batteries. *Energy Environ. Sci.* **2013,** *6* (4), 1283-1290.

423. Wei, S.; Zhang, H.; Huang, Y.; Wang, W.; Xia, Y.; Yu, Z., Pig bone derived hierarchical porous carbon and its enhanced cycling performance of lithium-sulfur batteries. *Energy Environ. Sci.* **2011,** *4* (3), 736-740.

424. Shim, J.; Striebel, K. A.; Cairns, E. J., The Lithium/Sulfur Rechargeable Cell: Effects of Electrode Composition and Solvent on Cell Performance. *J Electrochem Soc* **2002,** *149* (10), A1321-A1325.

425. Wang, B.; Wen, Y.; Ye, D.; Yu, H.; Sun, B.; Wang, G.; Hulicova-Jurcakova, D.; Wang, L., Dual Protection of Sulfur by Carbon Nanospheres and Graphene Sheets for Lithium–Sulfur Batteries. *Chem. Eur. J.* **2014,** *20* (18), 5224-5230.

426. Zheng, G.; Zhang, Q.; Cha, J. J.; Yang, Y.; Li, W.; Seh, Z. W.; Cui, Y., Amphiphilic Surface Modification of Hollow Carbon Nanofibers for Improved Cycle Life of Lithium Sulfur Batteries. *Nano Lett.* **2013,** *13* (3), 1265-1270.